Understanding the Early Stages of Crystallisation of $CaCO_3$ Using Advanced Electron Microscopy Techniques

Maryam Afzali Haji Dela

School of Chemical and Process Engineering

University of Leeds

Thesis submitted in accordance with the requirements for the degree of

Doctor of Philosophy

Clarification

The candidate confirms that the work submitted is her own, except where work which has formed part of jointly authored publications has been included. The contribution of the candidate and the other authors to this work has been explicitly indicated. The candidate confirms that appropriate credit has been given within the thesis where reference has been made to the work of others.

Publications:

The work in **chapter 4** of this thesis is drafted and will be published in the Journal of Microscopy:

Studying Crystallisation Processes using Electron Microscopy: the importance of sample preparation*, M. Ilett1*, M. Afzali1, B. Abdulkarim1, Z. Aslam1, S. Foster, M. Burgos-Ruiz, Y-Y. Kim, F.C. Meldrum and R.M.D. Brydson,* the final draft has been submitted to the Journal of Microscopy and is scheduled for publication in 2024.

The candidate conducted all experimental work and performed data analysis of any calcium carbonate related work. M lett carried out all the experimental and data analysis of calcium sulphate work. The manuscript was written by the candidate, M Ilett and R Brydson.

Analysis of complex, beam-sensitive materials by transmission electron microscopy and associated techniques*, Martha Ilett, Mark S'ari, Helen Freeman, Zabeada Aslam, Natalia Koniuch, Maryam Afzali, James Cattle, Robert Hooley, Teresa Roncal-Herrero, Sean M. Collins, Nicole Hondow, Andy Brown and Rik Brydson, Philosophical Transactions A, 26 October 2020.*

All authors contributed to writing the final manuscript.

Oral presentation:

mmc2023, Manchester, Impact of sample preparation on the early stages of crystallisation of $CaCO_3$ using advanced electron microscopies, Maryam Afzali, 4-6 July 2023.

Bragg centre PhD Colloquium 2023, Leeds University, Study the early stages of crystallisation of $CaCO_3$ using advanced electron microscopies, Maryam Afzali, 6 June 2023.

Goldschmidt2021, Online, Study the early stages of crystallisation of $CaCO_3$ using advanced electron microscopies, Maryam Afzali, 6 July 2021.

Poster presentation:

The Bragg exchange 2023 Leeds, Investigating the effect of sample preparation on the observed crystallisation of $CaCO_3$, 25 January 2023.

Microscience Microscopy Congress 2021 (mmc2021), online, Understanding the early stages of crystallisation of $CaCO_3$ using electron microscopy, 5-9 July 2021.

Leeds Doctoral College Online poster conference, Understanding the early stages of crystallisation of $CaCO_3$ using electron microscopy, 9 June 2020.

The Bragg Centre Research Symposium- understanding the early stages of crystallisation of $CaCO_3$ using electron microscopy, 17 January 2020.

Acknowledgement

I would like to take this opportunity to express my sincere gratitude to my supervisor, Professor Rik Brydson, with whom I had the honour of working. There are no words that can adequately convey how thankful I am for the invaluable experience of working under his guidance. Rik has been an exceptional supervisor, providing unwavering support, and I have learned immensely from him. Every moment of working with him has been truly enjoyable.

I extend a huge thank you to Dr Martha llett, for her assistance and invaluable contributions throughout my PhD journey and I am grateful for the mentorship and inspiration she provided. Special thanks are due to Dr Zabeada for her patience and support in training on the TEMs, and appreciation to all the staff at LEMAS. I am also grateful to Dr Alexander Kulak for his assistance in creating outstanding SEM images. I would like to acknowledge Dr Yifei Xu, whose scientific leadership and input greatly impacted my research. Furthermore, my gratitude extends to Professor Meldrum and Dr Yi-Yeoun Kim for their support and guidance. Thanks go to Dario Fernandez, whom I supervised during his MSc and whose PHREEQC data was incorporated into my thesis.

I am grateful to Dr Natalia Koniuch, both as a colleague and a dear friend. Her constant motivation, exceptional support, have greatly impacted my PhD journey.

I extend my deepest gratitude to my beloved father, who dreamt of me pursuing my PhD even though he's not here, his strength and support stay with me every step of the way. I want to express heartfelt appreciation to my mother, who went above and beyond by traveling all the way from Iran to stay with me, providing unwavering support during the challenging journey of completing my PhD. My gratitude also extends to my brother, whose consistent presence and support have been my pillars of strength through every challenge. My thanks also go to all my friends who have consistently been there for me when help was needed. I want to express my heartfelt gratitude to my son, Liam, who brought light into my life and gave me the strength to continue, especially after the loss of my father. Finally, I extend my sincere and profound appreciation to my partner,

who has constantly supported me. I am grateful for the dedicated assistance provided by him to support me in the completion of my thesis.

Abstract

There are three recognized crystalline polymorphs of calcium carbonate ($CaCO_3$): calcite, aragonite, and vaterite, along with an amorphous Calcium Carbonate (ACC) phase. Interestingly, nature uses the distinct characteristics of these phases effectively by somehow choosing the appropriate one for a given purpose. A notable example is found in aquatic organisms like oysters, mussels, and abalones. These creatures produce $CaCO_3$ shells with a unique structure—layers of calcite form the outer part, providing protection to the soft body from enemies, while the inner surface is crafted from a shiny and smooth nanoscale aragonite, known as nacre or mother-of-pearl.
To gain insight into how nature selectively chooses a polymorph, it will help us mimic natural processes and gain control over crystallisation. This requires a deep understanding of the mechanisms involved. Studying the early stages of crystallisation in the laboratory in bulk solutions is challenging because it occurs rapidly at the atomic scale. To address this issue, the crystallization of $CaCO_3$ was studied at very low levels of supersaturation, as existing literature primarily focuses on higher supersaturations.

In this thesis the early stages of crystallisation of $CaCO_3$ in bulk solutions was investigated at room temperature. For this purpose, $CaCO_3$ crystallisation was monitored at different times and different supersaturation levels for two different systems: equimolar reactant concentrations (0.5, 1.0, 2.5 and 4.5 mM) and carbonate rich conditions (Na_2CO_3:$CaCl_2$ in a 200:1 molar ratio). The shape (polymorph) and size of the crystals were studied as a function of reaction time and supersaturation by scanning electron microscopy (SEM), transmission electron microscopy (TEM) and Cryogenic (cryo)-TEM. Energy dispersive x-ray spectroscopy and electron diffraction patterns were used to confirm the presence of $CaCO_3$ and determine the polymorphs.

At higher supersaturated concentrations, nano-sized crystals of spherical vaterite and rhombohedral calcite were observed with well-defined morphologies which grew over time (minutes), together with the presence of some ACC at the shortest reaction time (5 seconds) of the crystallisation process, but no evidence was found for the presence of aragonite. As super-

saturation decreases to 1.0 and 0.5 mM, there is an increased proportion of ACC and crystalline particles were smaller due to slower reaction kinetics. At the concentration of 0.5 mM after 5 minutes, a diffuse region of higher contrast was observed from TEM, which was not seen at any other concentrations. We attribute this to potentially the remains of a dense liquid-like precursor structure. Interestingly, a carbonate-rich environment led to the formation of aragonite at room temperature, with no vaterite or calcite observed.

Additionally, a range of different sample preparation methods including air-drying, vacuum filtering, ethanol quenching and plunge freezing-vacuum drying as well as plunge freezing and direct examination in cryo-TEM, were investigated. Significant differences have been observed especially in terms of the amount and size of ACC particles in ethanol quenching techniques since ethanol is known to affect both the polymorphs and morphologies in crystallization solutions. Notably, in ethanol quenching techniques, the formation of a network of ACC particles was observed, leading to the conclusion that ethanol contributed to the formation of this network.

Overall, the process of $CaCO_3$ polymorph crystallisation is highly complex, and modifying a specific parameter can result in the preferential formation of a different polymorph. The research findings of this thesis demonstrate that electron microscopy techniques such as TEM and particularly Cryo-TEM are robust, offering insights into the complex nature of $CaCO_3$ polymorph crystallisation, allowing the study of crystallization in its native state.

Table of Contents

List of tables

List of Figures

Abbreviations

ACC	Amorphous calcium carbonate
ADF	Annular dark field
BF	Bright field
$CaCO_3$	Calcium carbonate
CNT	Classical nucleation theory
Cryo-TEM	Cryogenic transmission electron microscopy
CTEM	Conventional transmission electron microscopy
DF	Dark Field
DLP	Dense liquid phase
DLS	Dynamic light scattering
EDX	Energy dispersive X-ray
EM	Electron microscopy
HAADF	High angle annular dark field
HRTEM	High resolution transmission electron microscope
LCTEM	Liquid cell transmission electron microscopy
LLPS	Liquid- liquid Phase Separation
PNC	Prenucleation clusters
SAED	Selected area electron diffraction pattern
SEM	Scanning electron microscope
SI	Saturation Index
STEM	Scanning transmission electron microscope
TEM	Transmission electron microscope
XRD	X-ray diffraction

Chapter 1 Introduction

Crystallisation is a phase transition from a gaseous, or more usually a liquid state, to the solid state. It plays a key role in many natural phenomena and chemical processes. For example, from the technological point of view, many food and pharmaceutical sectors use the crystallisation process as a separation and purification step. Also, within the natural world, the formation of ice crystals in the atmosphere, bio-mineralization and scaling are typical phenomena occurring via a crystallisation process. The importance of crystallisation over a wide range of scientific disciplines including geology, biology and materials science has motivated researchers to seek a fundamental understanding of the initial nucleation of crystals and their subsequent growth.

In many studies the formation of crystals can be successfully explained by the so-called classical nucleation and growth model. This theory was originally developed from the study of water droplet formation in a supersaturated vapour (Feder et al., 1966). This was then subsequently applied to the solidification of pure metals from the melt (Thompsont & Spaepen., 1983). In the classical theory of nucleation, crystallization is categorized into nucleation and crystal growth. Nucleation relies on the level of supersaturation in the solution, whereas crystal growth is influenced by the movement of atoms or ions to and across the surface of the nuclei, eventually integrating into the lattice (Ueckert et al., 2020) . In contrast, non-classical theories of crystallization were developed to account for phenomena such as crystallization through amorphous precursors or the creation of mesocrystals (Ueckert et al., 2020). Despite numerous studies carried out on the mechanisms of crystallisation in many materials systems, often there is still a poor understanding as to how nucleation and crystal growth occurs, and which factors can preferentially create a specific type of morphology (shape and structure of a substance) or crystal polymorph (the occurrence of various crystalline forms of a substance) as well as the exact mechanisms for this selection. According to the literature, uncertainty exists regarding whether the nucleation process occurs within the solution through either a single-step or multi-step pathway. In the case of a multi-step pathway,

it is unclear whether the transformation of one phase to another occurs through the dissolution of the original phase or through the nucleation of the more stable phase. One reason for this is that crystallisation occurs at the nanoscale and significant changes can occur over extremely short time scales, both of which mean that it is very difficult to study experimentally. Furthermore, even though the conditions that lead to the formation of different crystal polymorphs may be known, the exact mechanisms may yet remain to be clearly identified.

Figure 1 shows a schematic comparison of classical and non-classical routes (Gebauer and Cölfen, 2011; Gebauer et al., 2018), which can both lead to the formation of a single crystal. The bottom route illustrates a classical nucleation pathway, where metastable clusters of critical size form, and nucleation proceeds in a single step, with monomer by monomer, ultimately resulting in the formation of a final crystalline structure (grey arrow). Here, importantly the structure of the critical nucleus is assumed to be the same as the final crystal. However, alternative non-classical pathways (black arrows) explain the nucleation mechanism as proceeding via a series of multiple steps. specific example of nonclassical crystallisation is where nucleation of a salt in an aqueous phase solution occurs via the association of stable, pre-critical clusters which eventually lead to the formation of droplets. These droplets then undergo dehydration, resulting in the formation of a crystal (Rodriguez-Navarro et al., 2015).

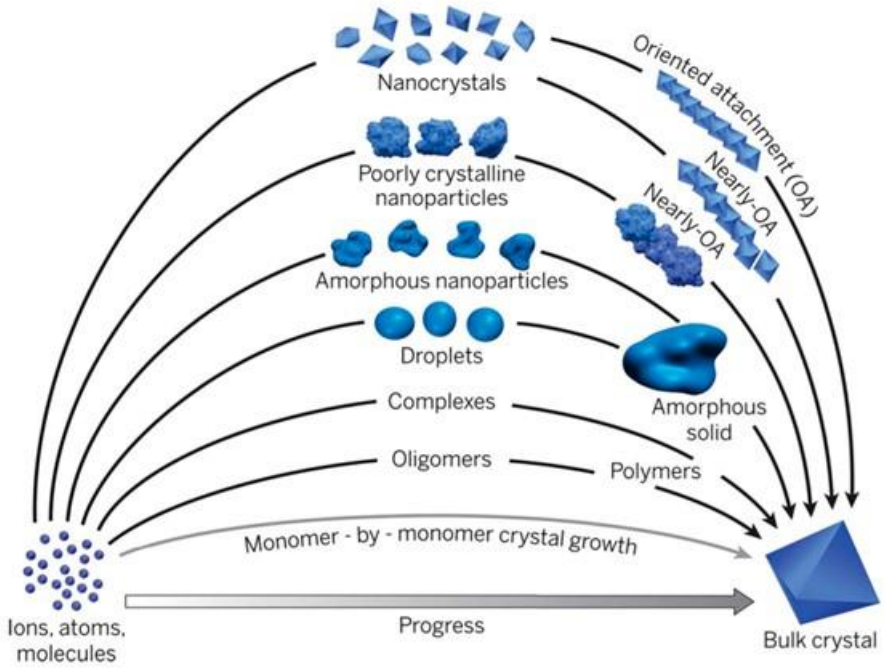

Figure 1 Schematic illustration of classical and non-classical crystallisation (De Yoreo et al., 2015)**.**

$CaCO_3$ can exist in many different forms: amorphous phase (ACC), two hydrated polymorphs and three anhydrous forms. Anhydrous $CaCO_3$ exists in three crystalline forms: calcite, aragonite, and vaterite, with their thermodynamic stability decreasing in aqueous ambient conditions in the order calcite > aragonite > vaterite (Xu and Sommerdijk, 2018). Calcite is the most stable $CaCO_3$ mineral, while aragonite is more soluble than pure calcite (Sulpis et al., 2022). Calcite is known for its rhombohedral structure, while aragonite has an orthorhombic symmetry, giving rise to needle-like crystal morphologies. Vaterite, an intermediate stage between non-crystalline ACC and the more stable calcite and aragonite polymorphs, lacks a well-defined structure and typically forms spherical polycrystalline particles. Early literature suggests that the crystallisation of $CaCO_3$ occurs via a classical process (Karthika et al., 2016). However, more recently, the existence of an amorphous precursor has led to the suggestion of a non-classical route (Gebauer and Cölfen., 2011). ACC is now commonly considered to be a precursor to the anhydrous polymorphs in aqueous solutions, existing as spherical nanoparticles. The formation of ACC is believed to involve the association of stable pre-nucleation

clusters (PNCs) in the solution, followed by an intermediate step of liquid-liquid phase separation (LLPS) (Gebauer et al., 2014; Wallace et al., 2013). In light of the many studies conducted on $CaCO_3$ crystallisation, the mechanism via which crystallisation occurs and the polymorphic behaviour of $CaCO_3$ continues to pose a significant scientific question.

The inorganic system $CaCO_3$ was chosen for this study, as it is a ubiquitous mineral abundantly present in limestone and marble, as well as serving as a fundamental component in the bio-mineralization processes of various organisms, including the formation of pearls, nacre in seashells, and the skeletal structures of sea urchins (Xu and Sommerdijk, 2018). $CaCO_3$ crystallisation occurs in a variety of processes such as bio-mineralisation in shellfish, the production of personal health products, and the production of construction materials. Equally important is the prevention of unwanted deposition of $CaCO_3$ in the form of mineral scales in the oil and water industries causing major operational difficulties from clogging pipes to increasing the amount of energy needed to remove them. Therefore, understanding the early stages of $CaCO_3$ crystallisation would not only allow the ability to control undesirable scale formation, but would also enable us to mimic biocompatible structures for bio-applications such as bone replacement implants.

The focus of this research study is to attempt to understand the early stages of crystallisation of a model inorganic system, $CaCO_3$. For this purpose, a series of experiments were designed, and high spatial resolution advanced electron microscopy techniques were used to visualise and capture the initial stages of the nucleation and growth process. Both conventional scanning electron microscopy (SEM) and transmission electron microscopy (TEM) techniques were employed to investigate the presence of crystallinity within crystallising solutions and the selection of the various polymorphic forms. Relatively new techniques including liquid cell and cryo-TEM were also used for the visualisation of the early stages of crystallisation of $CaCO_3$ in liquid and frozen environments, representative of the native state of the crystallising solution.

Crystallisation of $CaCO_3$ from aqueous solution is influenced by many factors, including the degree of supersaturation, additives, temperature, alcohols, pH, the degree of confinement (Meldrum and O'Shaughnessy, 2020). Whilst many

of these factors have been extensively researched, this study aims to address certain gaps in our understanding.

Most previous studies focused on concentrations of equimolar precursor components which give rise to high supersaturation levels for $CaCO_3$, however there is not much information about crystallisation at very low concentrations. Under reduced supersaturation conditions, the thermodynamic driving force slows down, resulting in a decrease in the precipitation rate, which, in turn, allows for enhanced visibility of the initial stages of the crystallisation process.

Two different solution conditions have also been investigated, leading to the selection and formation of the aragonite polymorph rather than the more usual calcite polymorph. Aragonite is a relatively uncommon crystalline form of $CaCO_3$ commonly found in seawater. The formation of $CaCO_3$ was investigated in a synthetic carbonate-rich system, leading to the formation of the aragonite structure at room temperature. In addition, the effect of magnesium ions in solution was examined and it was observed that magnesium promotes the formation of aragonite. In both scenarios, there was no formation of calcite or vaterite and the early stages. In the scenario of carbonate-rich conditions, the mechanism proposes the formation of small amorphous nanoclusters, which organize into a linear structure of nanowires, ultimately leading to the creation of aragonite.

Additionally, many studies of crystallisation processes that have employed electron microscopy have primarily concentrated on the use of dry sample preparation techniques, and ethanol has been a common choice to halt reactions for both TEM and SEM studies. In this work I have investigated and compared a number of different sample preparation methods which have been utilized in the literature. This approach is driven by the need to investigate the early stages of crystallisation in the hydrated and native state, which provides a more representative view of the actual state of the crystallising solution. Importantly, distinct differences between different sample preparation methods were observed which suggests that a re-evaluation of much of the literature data is required.

The thesis is arranged as follows: first the background science and the literature concerning the initial phases of $CaCO_3$ crystallization and the techniques capable of capturing this phenomenon, such as TEM, SEM, and cryo-TEM (Chapter 2); followed by the methods and materials employed in this study (Chapter 3). This is then followed by the experimental results relating to: the study of the crystallisation of $CaCO_3$ in equimolar aqueous solutions of $CaCl_2$ to Na_2CO_3 as a function of time (Chapter 4), the in-situ study of $CaCO_3$ formed from equimolar aqueous solutions of $CaCl_2$ and Na_2CO_3 in real time (Chapter 5) and $CaCO_3$ polymorph selection during the crystallisation process (Chapter 6). Finally, the overall conclusions of this PhD alongside suggestions of future work are presented (Chapter 7).

Chapter 2 Background Science

2.1 Fundamentals of Crystallisation

Crystallization can be defined as a process by which the atoms or molecules arrange themselves in a liquid phase, leading to the formation of a highly ordered 3-dimensional solid consisting of repeating unit cells. Crystallisation is of significant importance in various fields of science and technology ranging from natural and life sciences, *e.g.*, mineralisation, food science, biology and medicine, to engineering and geology (Gebauer, 2018). However, there has been a debate regarding the understanding of crystallization phenomena, particularly in the fields of bio- and biomimetic mineralization. This debate aims to determine which framework (classical or non-classical) would be the most appropriate for describing the crystallization pathway, specifically concerning the process of nucleation from an aqueous solution (Gebauer et al., 2014).

2.1.1 Classical nucleation theory (CNT)

Crystallization is known to occur in two main steps: the first step is nucleation, which is a primary phase transition involving the creation of solid particles from atoms, ions, or large molecules, and the second step is crystal growth (Florence and Attwood, 2015). Nucleation is the most fundamental step in crystallisation which can be defined via two different frameworks: classical nucleation theory (CNT) and non-classical nucleation theory. According to CNT, nucleation is based on the formation of critical nuclei which have the same structural form as the final crystal and which are induced by stochastic association of ions or molecules in solution, which acts as transition states separating the solid phase from the supersaturated solution (Gebauer, 2018). The spontaneous formation of nuclei from the solution results in the release of heat to the surroundings, attributed to the increased enthalpy (H) resulting from bond formation. This process is accompanied by a decrease in entropy when crystals are formed. Moreover, the transition of nuclei into the crystal leads to a lower energy state compared to that of the solution, as described by the equation (Eq.1). The Gibbs free energy change (ΔG) in equilibrium can be expressed as:

$$\Delta G = \Delta H - T\Delta S \qquad (1)$$

Where, ΔH represents the enthalpy change with a negative ΔH indicating the release of heat as the reaction progresses from reactants to products, while a positive ΔH indicates heat absorption, *ΔS* represents the entropy change of the system during the reaction. A positive *ΔS* signifies an increase in disorder within the system, while a negative *ΔS* implies a greater degree of order. The overall free energy change of the reaction is influenced by both *ΔS* and *ΔH*, with the relative impacts determined by the temperature (*T*) in Kelvin (*K*). Crystal growth is then initiated by ions adsorbing onto the sites of the resultant nuclei and leads to a final crystalline state (Gebauer and Cölfen, 2011; Gebauer et al., 2018).

From the CNT point of view, nucleation can be explained by Gibbs free energy change, *ΔG*, associated with the formation of a nucleus in the solution (Karthika et al., 2016). The change in the Gibbs free energy during the nucleation of a spherical nucleus of radius r can be expressed as (Eq. 2):

$$\Delta G = \underbrace{\frac{-4\pi r^3}{3\,\mathrm{v}}\, kT \ln S}_{\Delta G_v} + \underbrace{4\pi r^2\ \ Y}_{\Delta G_s} \qquad (2)$$

Where the first term, ΔG_v, is the change in volume free energy (J mol^{-1}) related to the phase transition of aqueous phase to solid state which is a negative quantity, $4\pi r^3/ (3\ v)$ represents the number of molecules in a cluster of radius *r* with the volume of single molecule as *v, k* is the Boltzmann constant, and *T* is the temperature and *S* is the supersaturation ratio. The second term, ΔG_s, is the change in surface (interfacial) free energy (J mol^{-1}) associated with the formation of the aggregates and represents a positive quantity, with *Y* as the interfacial energy (Urphy, 1999). As shown in Figure 2, when r is larger, the value of ΔG_v dominates which gives rise to a decrease in the free energy of the system. When r is less, the second term dominates implying the formation of new surfaces, which leads to an increased *ΔG* value (Karthika et al., 2016).

During homogeneous nucleation clusters grow and decay by gaining and losing monomers until they become stable (Kashchiev, 2000). Upon the formation of stable clusters, they will grow in size until the nucleus reaches a critical size (r*) upon which the Gibbs free energy of the system begins to decrease. In other words, for nuclei with a radius larger than the critical size, the probability of

formation of a new nucleus decreases (Karthika et al., 2016). The ΔG value corresponding to this critical size is called the critical nucleation barrier (or the activation free energy of nucleation); denoted as ΔG^* as shown in (Eq.3- 4) (Figure 2).

$$r^* = \frac{2Y}{KT} lnS \qquad (3)$$

$$\Delta\, G^* = 16\,\pi Y^3 v^2 / K^2 T^2 \ln S^2 \qquad (4)$$

Upon the formation of nuclei, which are stable and have the same structure as the growing crystals, the growth units (e.g., atoms, ions, or molecules) can move via diffusion from the bulk solution to the surface of the nuclei, leading to the formation of ordered crystalline structures of defined size and shape. Crystal growth involves dissolution of smaller particles and their attachment to larger ones. Smaller particles are thermodynamically less stable and have a tendency to diffuse through the solution and eventually dissolve. Larger particles grow at the expense of small particles and consequently grow in size which is accompanied by a reduction in the population of small nano-sized particles a phenomenon known as Ostwald ripening (Fiona C Meldrum and Cölfen, 2008; Vedantam and Ranade, 2013).

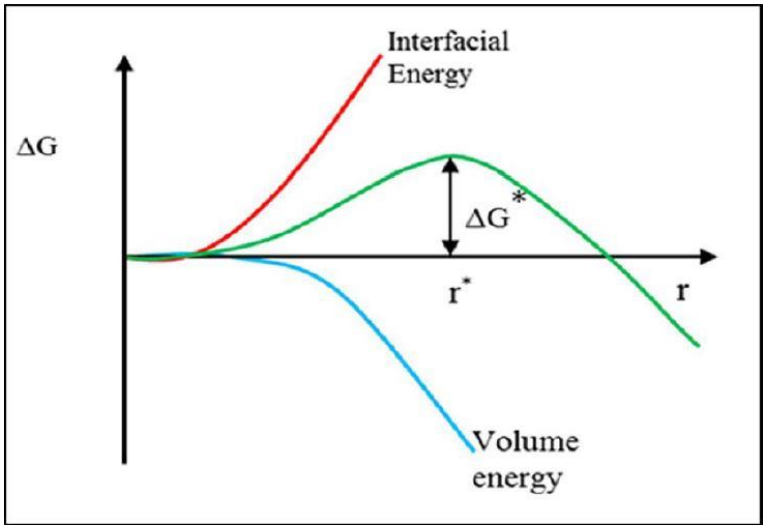

Figure 2 The dependence of the total free energy (in green) on the nuclei radius, r, showing the free energy barrier for nucleation at a critical radius r* (Karthika et al., 2016).

The change in free Gibbs energy, ΔG, associated with the formation of a crystal from a homogeneous supersaturated solution can also be quantified in terms of N, the number of molecules or ions in the crystal, ф the reaction affinity, A the surface area of the crystal, and ϒ the surface tension, as given by (Eq.5) (Karpiński and Bałdyga, 2019):

$$\Delta G = -N\,\varphi + YA \qquad (5)$$

A general expression for the affinity φ is defined by (Eq. 6) where a is the activity of the solute in solution, and a^* is the activity of the pure solute in a crystal.

$$\varphi = kT \ln\left(\frac{a}{a^*}\right) \qquad (6)$$

By assuming the activity coefficients to be unity, the supersaturation ratio, *S*, is thus:

$$(a/a^*) = (c/c^*) = S \qquad (7)$$

$$\varphi - \varphi^* = kT\ ln\ S \qquad (8)$$

$$\Delta\varphi = \varphi - \varphi^* = kT\ ln\ S = kT\ ln\ (c/c^*) \qquad (9)$$

Where $\Delta\varphi$ is the change in chemical potential, *c* is the actual concentration of the solute, c^* is the solute concentration at saturation conditions, and S is super saturation ratio.

The driving force for crystallization or precipitation derives from the difference between chemical potential of the solute in equilibrium (saturated) and the chemical potential of the solute at the supersaturated state. The driving force expression using activity coefficient is expressed as (Eq.10):

$$\sigma = \ln(\frac{a}{a_{eq}}) \approx S_a - 1 = \frac{a - a_{eq}}{a_{eq}} \approx S - 1 = \frac{c - c^*}{c^*} \qquad (10)$$

Where σ is the relative or absolute supersaturation, S_a defines the activity based and S the concentration c-based supersaturation ratio (Karpiński and Bałdyga, 2019). However, in practical applications, it is common to express supersaturation in relation to concentration as expressed in (Eq.11):

$$\Delta c = c - c^* \qquad (11)$$

Where c is concentration of solution, *c** the saturation concentration at equilibrium and *Δ c* is termed the 'concentration driving force (Giulietti et al., 2001;. From a thermodynamic perspective the supersaturation ratio *(S)* is the driving force for all crystallisation processes which can be defined as the difference bσetween the actual concentration and the solubility concentration at a given temperature. In other words, the degree of supersaturation is defined as the ratio between the activity of dissolved solid in a supersaturated solution and the activity of the solid in a saturated state. The degree of supersaturation present in a precipitating solution controls the rate of fundamental processes, including nucleation, expansion, and Ostwald ripening (Karpiński and Bałdyga, 2019).

In the case of ionic systems, the definition of driving force becomes more complex because the ionic concentrations are not in a stoichiometric ratio and hence the term solubility product applies which can be defined by the expression in equation (Eq.12) for supersaturation (S). If the saturation index (SI) for a particular mineral is negative, the system is under-saturated with respect to that mineral. If the index is positive, the solution is supersaturated.

$$S_X = IAP/Ksp_X \qquad (12)$$

$$\mathrm{SI} = log_{10}(\frac{IAP}{Ksp})$$

$\mathrm{SI} = 0$ $\quad IAP = Ksp \quad \longrightarrow$ Saturated (in equilibrium)

$\mathrm{SI} < 0$ $\quad IAP < Ksp \quad \longrightarrow$ Under-saturated

$\mathrm{SI} > 0$ $\quad IAP > Ksp \quad \longrightarrow$ Supersaturated

Where I*AP* is the ion activity product and Ksp_x is the solubility product for the mineral salt *x* (Antony et al., 2011). At a constant temperature, for crystallisation to occur the solution concentration is of a primary significance. When a solution becomes supersaturated, nucleation occurs via a phase transition from an aqueous state with high free energy to a solid phase with low

free energy (De Yoreo and Vekilov, 2003). The rate at which crystals grow is also determined by the supersaturation. The higher the supersaturation the higher is the growth rate (Vedantam and Ranade, 2013).

2.1.2 Crystal Growth

After nucleation, crystal growth occurs through two primary processes: 1) ions migrate from the solution to the crystal surface, and 2) these ions integrate into the crystal lattice. Several theories, provide explanations for the growth process such as Volmer, Kossel and Frank's Theory (Liendo et al., 2022). According to Marqusee and Ross, (1983), during the nucleation process, a significant quantity of particles is formed which exhibit a narrow size range distribution. In the subsequent stage, these nuclei undergo rapid growth. As the larger particles grow, the number of nuclei generally decreases from 10^{15} to 10^{6} cm^{-3} or less and smaller particles disappear (Marqusee and Ross, 1983). This can be explained by Ostwald ripening phenomenon which explains that smaller crystals tend to dissolve and diffuse within solutions and adhere to the surface of larger crystals. In general, smaller crystals are energetically less stable than larger particles owing to their higher surface area to volume ratio and tend to reach their thermodynamically lowest energy state more quickly (Fiona C Meldrum and Cölfen, 2008; Vedantam and Ranande, 2013). Hence, small crystals, under the influence of surface tension, undergo dissolution in a supersaturated solution, while larger crystals, lacking sufficient surface tension to counteract the effects of supersaturation, experience growth (Friedman and Ross, 2003). Key factors such as temperature, supersaturation, and impurities significantly influence crystal growth (Liendo et al., 2022). The growth rate of a crystal is defined as the increase in mean size (L) per unit time and can be experimentally estimated using (Eg.13).By monitoring the changes in mean size and saturation level over time, the growth rate can be related to the absolute saturation (s = S-1) through second term of (Eg.13), which describes an empirical power law. In this law, k_g is a kinetics constant related to temperature, and g is the growth order related to the growth-controlling step (Liendo et al., 2022).

$$G = \Delta L_{mean} / \Delta t = k_g S^g \quad (13)$$

According to the classical perspective of crystallisation, crystal growth is a layer-by-layer process by which new crystalline layers are deposited with a well-defined orientation dictated by the crystal packing of the unit cell (Fiona C. Meldrum and Cölfen, 2008; Vedantam and Ranade, 2013). Crystal growth becomes the dominant process responsible for shaping the crystal into a defined size and form (Vedantam and Ranade, 2013). During the process of crystal growth, atoms and molecules migrate from the solution towards the surface of an existing crystal, where they subsequently integrate into the active centre of the crystal lattice. The term "active centre" refers to the specific location on the growth surface of the crystal where the migrating unit exhibits the strongest attraction to the lattice. These active centres typically correspond to steps and kinks on the crystal surface as shown in Figure 3 a and Figure 3 b. The initiation of a new layer begins with the surface nucleation of an island on the flat face of an established crystal, which subsequently grows through the attachment of additional atoms/ions to the steps and kinks of the emerging layer until the surface is fully formed (Figure 3 c). The Kossel model demonstrates the layer-by-layer growth mode of a crystal, as depicted in Figure 4. However, surface growth is typically accompanied by various imperfections in the crystal, such as vacancies (illustrated in parts e and f of Figure 4) or dislocations (Fiona C. Meldrum and Cölfen, 2008).

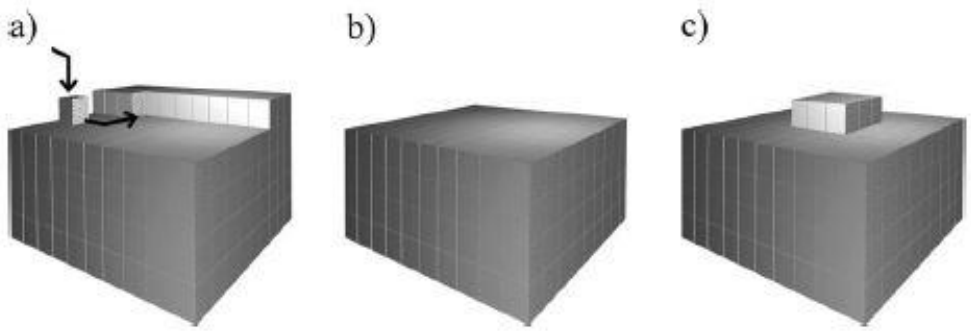

Figure 3 The process of crystal growth occurring layer by layer can be described as follows: (a) migration of a unit towards a surface kink, (b) formation of a fully formed layer, and (c) nucleation of new crystal unit on the crystal surface.

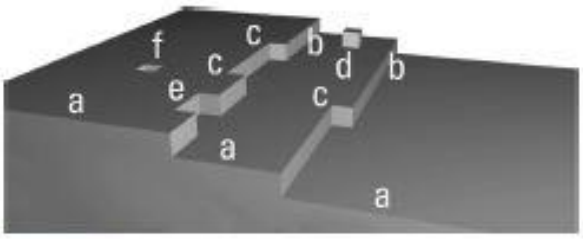

Figure 4 Kossel's model of a developing crystal surface, highlighting various features including: (a) Flat surfaces, (b) steps, (c) kinks, (d) growth units adsorbed on the surface, (e) edge vacancies, and (f) surface vacancies.

2.1.3 Non-classical pathways

In recent years an alternative crystallisation theory has been proposed, based on the concept that thermodynamically stable clusters are formed prior to nucleation (Cölfen & Mann, 2003; Niederberger & Cölfen, 2006). Gebauer and Colfen showed that the stable pre-nucleation cluster concept is truly non-classical and promises a deeper understanding of nucleation (Gebauer and Cölfen, 2011). In non-classical theory, crystal growth can occur via various pathways where preformed building blocks, ranging from multi-ion complexes to fully formed crystals, are arranged through oriented assembly. This process ultimately leads to the formation of a crystallographically single particle (De Yoreo et al., 2015).

Figure 5 shows a comparison of classical and non-classical routes along with their respective energy landscapes (Gebauer and Cölfen, 2011; Gebauer et al., 2018), which can both lead to the formation of a single crystal. The top route represents classical nucleation pathway in which meta-stable clusters of critical size are formed, and nucleation proceeds by the attachment of the basic monomers to a single cluster leading to the formation of a final crystalline structure. However, the alternative non-classical pathway explains the nucleation mechanism as proceeding via association of stable, pre-critical clusters which eventually lead to the formation of droplets. These droplets then undergo dehydration, resulting in the formation of a crystal.

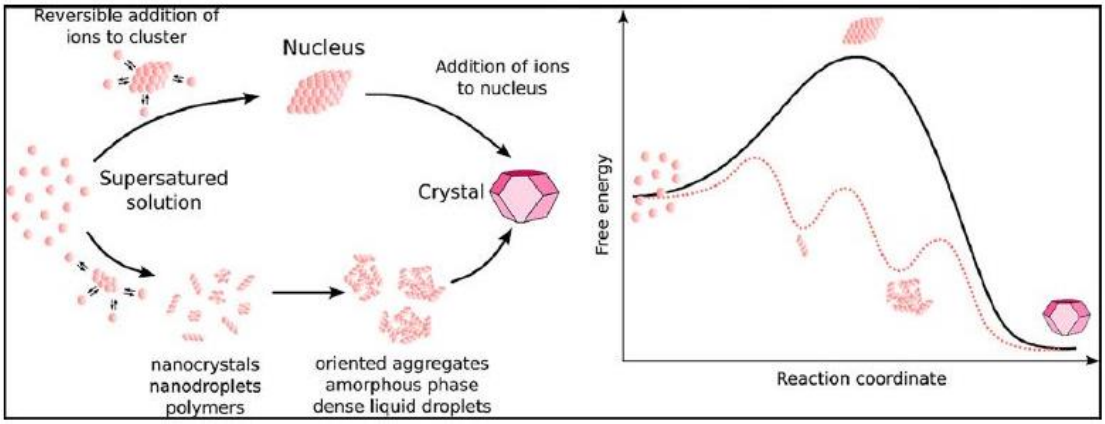

Figure 5 One-step and multi-step pathways for the creation of crystals from solutions that are supersaturated are depicted in a schematic representation (left), along with their respective energy landscapes (right) (Driessche et al., 2019)**.**

Unlike the step-by-step addition of monomers described in classical models, alternative theories for the process of crystallization now acknowledge the occurrence of particle addition, which can involve various entities such as multi-ion complexes to fully developed nanocrystals. An example of a non-classical pathway is the formation of amorphous phases which can initiate nucleation at concentrations significantly lower than that anticipated based on classical models (Yoreo et al., 2015). There is also evidence indicating the occurrence of stable solute species in homogeneous solutions that cannot be rationalized by the classical nucleation theory. Pre-nucleation clusters (PNCs) are thermodynamically stable solutes, which exhibit a high level of dynamic behaviour. The association reactions of ions in a solution are spontaneous, resulting in the formation of PNCs that are generally larger than ion pairs (Gebauer et al., 2018). In non-classical theory, PNCs are considered to be highly hydrated and exhibit properties similar to those of liquids, which is different from the characteristics of classical nuclei (Gebauer et al., 2018). From a classical perspective, the critical size of nuclei is typically within the range of tens of ions, corresponding to a diameter of approximately 3-4 nm or less (Hu et al., 2012). There is evidence showing that PNCs sizes are similar in size to classical nuclei but are thermodynamically stable and more abundant; their size ranges from 0.5 to 3 nm (Kellermeier et al., 2012). These PNCs are capable of participating in the phenomenon of phase separation (Gebauer et al., 2014).

2.1.4 Liquid-liquid phase separation

Liquid-liquid separation has been proposed as an alternative mechanism to classical nucleation for mineralization (Wallace et al., 2013). As for the PNC theory presented by Gebauer, the process of phase separation is initiated through the creation of stable solute species, which are formed as a result of chemical interactions in the solution (Gebauer et al., 2014). In fact, the occurrence of phase separation is primarily attributed to PNCs. When a solution reaches a certain critical composition, which depends on factors such as the IAP or concentration, larger pre-nucleation clusters (PNCs) may form. This critical composition is defined by the point at which the liquid-liquid binodal (coexistence line), which is the boundary between two-phase separation regions, is located. The resulting PNCs subsequently transform into dense liquid nano-droplets by developing interfaces and changing speciation. These nano-droplets then undergo progressive dehydration and aggregate to form larger nano-droplets (Gebauer et al., 2014).

2.1.5 Binodal demixing and Spinodal decomposition

The thermodynamics that govern phase separation can be demonstrated using phase diagrams, as illustrated schematically in Figure 6 for a generic two-phase system with a lower critical solution temperature (LCST). The solution at point A is stable and under-saturated, indicating the absence of any driving force promoting phase separation. However, as the solution composition changes and becomes more concentrated at a constant temperature, it crosses the binodal curve (blue line) and enters the metastable region between points B and C. The binodal region is represented as areas with positive curvature in the free energy landscape, indicating that the system is in a metastable state and can undergo phase separation if fluctuations in composition occur. As the concentration increases further, it eventually reaches the spinodal line (which lies inside the binodal line). At this point, even tiny fluctuations in the density of ions in solution can lead to the formation of clusters that are thermodynamically unstable and will spontaneously grow into the dense liquid phase. This process is known as spinodal decomposition, and it is an irreversible process. At the spinodal boundary, decomposition occurs spontaneously, meaning that the barrier for phase separation disappears (Gebauer et al., 2014). Figure 6 B

shows the spatial patterns resulting from spinodal decomposition in the left image (i.e., continuous regions of de-mixing) and the spatial patterns resulting from binodal de-mixing/nucleation in the right image (i.e., discontinuous regions of de-mixing). Phase separation occurring within the binodal regime relies on significant statistical fluctuations, where solute ions assemble into bulk-like structural units, albeit on a small scale. This results in the stochastic formation of small nuclei, in line with the concepts of Classical Nucleation Theory (CNT). Nucleation becomes more probable as the supersaturation increases, enabling binodal fluctuations to surpass the nucleation barrier. In contrast, spinodal fluctuations are considered to be extremely small in degree but extensive in extent, indicative of a diffusion-limited process of phase separation. Under these conditions, spontaneous and uniform decomposition occurs throughout the entire volume of an unstable system, rather than de-mixing. This can give rise to the formation of distinct channel-like patterns, differing from the stochastic formation of separate nuclei in binodal de-mixing or homogeneous nucleation.

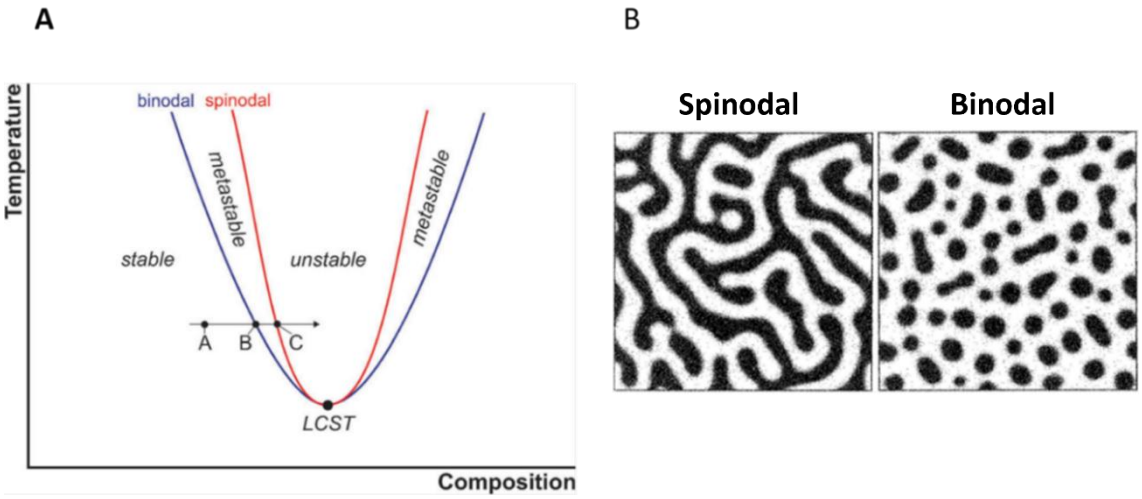

Figure 6 (A) The phase behaviour diagram of a two-phase system. (B) A comparison of spatial patterns resulting from spinodal decomposition (left) and binodal de-mixing/nucleation (right) (Gebauer et al., 2014).

2.2 Material system of interest: Calcium carbonate ($CaCO_3$)

$CaCO_3$ is one of the most versatile and useful inorganic compounds which is widespread throughout nature in its carbonate form as limestone, marble and

chalk and is a major component of biominerals such as shells, coral, pearls, and bones (Weller, 2006; Mukkamala et al., 2006). $CaCO_3$ is widely used for industrial purposes such as paper, plastics, paints, coatings, personal health, food production, building materials and construction (Dae et al., 2020).This inorganic compound possesses characteristics for drug delivery, including biocompatibility, porosity, pH-responsive nature and high encapsulation efficiency (Vidallon et al., 2020). In addition to these highly profitable applications, $CaCO_3$ deposition is one of the most common mineral scales in the oil, gas and water industries causing major operational difficulties from clogging pipes to increasing the amount of energy needed to clear them (Gebauer et al., 2008).

2.2.1 $CaCO_3$ polymorphism

$CaCO_3$ can exist in different polymorphic forms: ACC, two hydrated polymorphs and three anhydrous forms. Hydrous forms are referred to as calcium carbonate monohydrate (MCC) and calcium carbonate hexa-hydrate (ikaite). The latter phase (ikaite) is a metastable form of $CaCO_3$ which can be found at near zero temperature, high alkalinity, and phosphate concentrations (Hu et al., 2015). $CaCO_3$ monohydrate is extremely unstable under normal conditions and is naturally found as a constituent in lake sediments (Kralj, 1995). Major polymorphs such as calcite, vaterite, and aragonite are naturally found as anhydrous polymorphs (Borisov et al., 2021). Calcite, the naturally occurring mineral, is the most thermodynamically stable phase and typically displays rhombohedral shaped crystals expressing their {104} faces. In the calcite structure, each calcium ion is surrounded by six oxygen atoms. Aragonite crystals are thermodynamically less stable than calcite, have orthorhombic symmetry, and typically appear as prisms or needle-like crystals growing along the crystallographic c-axis (Dey et al., 2010). In the aragonite structure each calcium ion is surrounded by nine oxygen atoms (Aydinol et al., 2007; Sun et al., 2015). Vaterite is a metastable phase which exists as an intermediate phase between ACC and more stable polymorphs of calcite (Christy, 2017). Vaterite crystals consist of either a hexagonal or an orthorhombic unit cell, though there is some ambiguity about the details. Vaterite does not display a well-defined morphology and usually agglomerates to form spherical particles (Pouget et al.,

2010). Figure 7 schematically shows the hydrous and anhydrous crystalline polymorphs of $CaCO_3$ (Cartwright et al., 2012) whilst Figures 8 and 9 present my SEM images of the morphologies of the different polymorphs of $CaCO_3$. Figures 9 and 10 demonstrate the structure of the $CaCO_3$ unit cells (and local coordination of calcium ions) of calcite (rhombohedral), aragonite (orthorhombic) and vaterite (hexagonal) (Dhami et al., 2013). Additionally, the crystallographic properties of three $CaCO_3$ phases, are presented in Table 1.

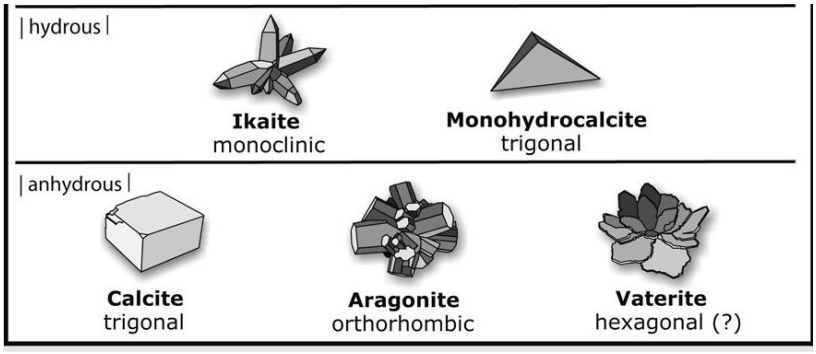

Figure 7 Hydrous and anhydrous polymorphs of $CaCO_3$ (Cartwright et al., 2012)**.**

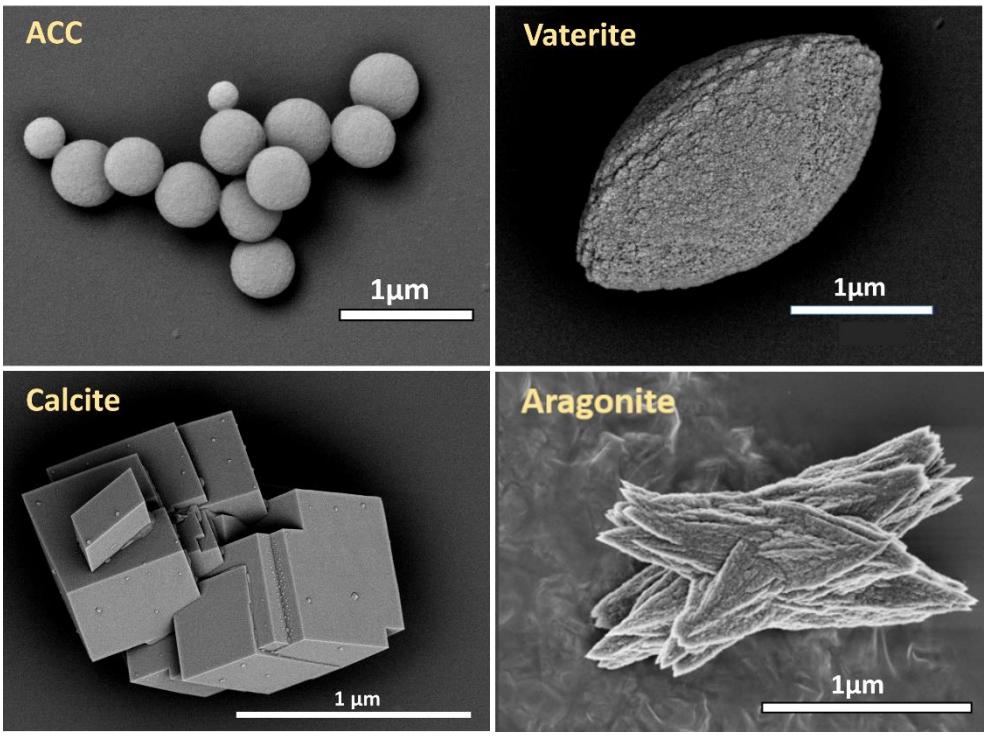

Figure 8 SEM images of ACC particles, along with the morphologies of $CaCO_3$ crystals: vaterite, calcite and aragonite.

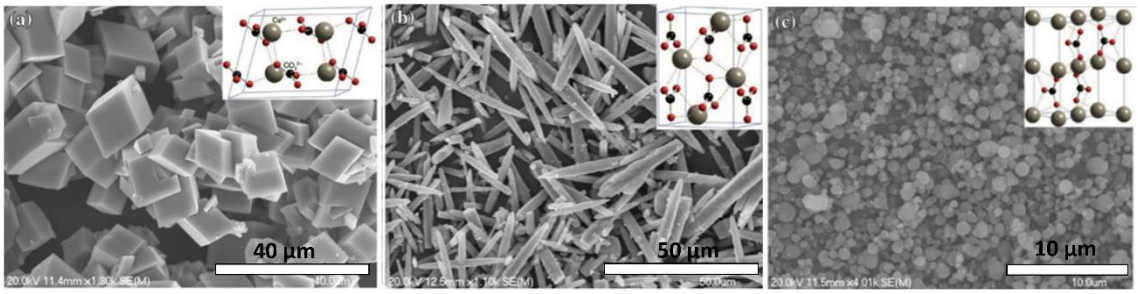

Figure 9 SEM images and the unit cell structures of calcite (rhombohedral), aragonite (orthorhombic) and vaterite (hexagonal). The atoms in the unit cell are as follows: grey represents calcium, black represents carbon, and red represents oxygen (Seifan & Berenjian, 2018).

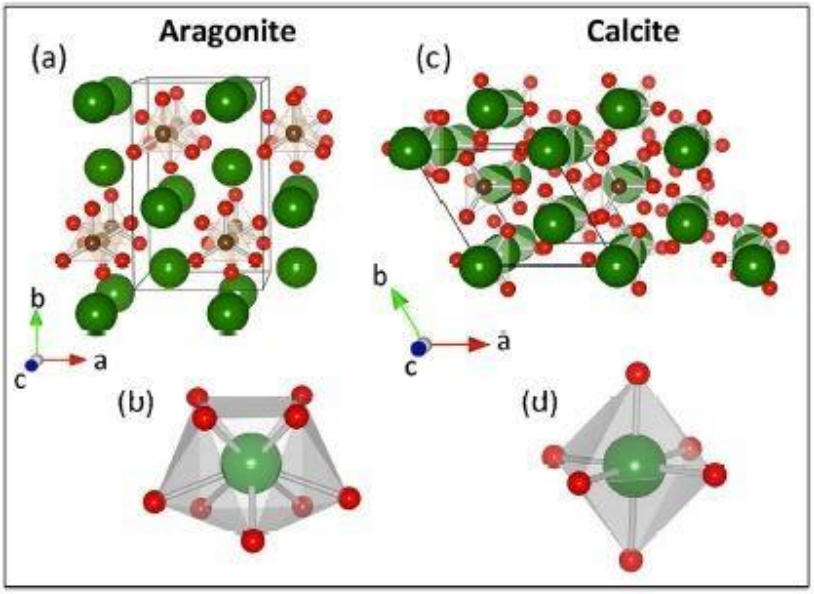

Figure 10 A schematic representation of the crystal structures of two different forms of $CaCO_3$, namely aragonite and calcite. Aragonite (a) exhibits an orthorhombic symmetry and has a crystal structure where the calcium ions are surrounded by nine oxygen ions with a site symmetry denoted as m, as depicted in (b). On the other hand, calcite (c) possesses a trigonal crystal structure. In this case, calcium ions are coordinated by six oxygen ions, forming an octahedral arrangement with a site symmetry of 32, as illustrated in (d). The atoms in the unit cell are as follows: green represents calcium, black represents carbon, and red represents oxygen (Soldati et al., 2016)**.**

Table 1: Characteristics of the three crystalline phases of $CaCO_3$

Parameter	Calcite	Aragonite	Vaterite
Symmetry group	$R\bar{3}c$	*Pmcn*	*C2/c*
Z	6	4	12
Unit cell parameters: *a*, *b*, *c*, Å	4.98, 45.98, 17.192	4.955, 7.9779, 5.742	12.17, 7.12, 9.47
α, β, γ, deg	90, 90, 120	90, 90, 90	90, 118.37, 90

2.3 Literature review

2.3.1 Crystallisation of $CaCO_3$ from solution

Chemicals in an aqueous system can interact to form new dissolved complexes (or species) or precipitate to form solids (Mcavoy, 1992). For precipitation to occur there must be a thermodynamic driving force which can be explained by the degree of supersaturation (Eq. 10). Supersaturation is essentially the disparity between the real concentration and the solubility concentration at a specific temperature. Typically, spontaneous precipitation occurs in solutions with a relatively high degree of supersaturation. For the $CaCO_3$ crystallization process to initiate, it is necessary for the solution to be supersaturated with respect to Ca^{2+} and CO_3^{2-} (Coto et al., 2012). The mass balance equations for $CaCO_3$ precipitation allowing for the saturation ratio is: $CaCO_3 = Ca^{2+} + CO_3^{2-}$ and $SI = (a\,Ca^{2+} + a\,CO_3^{2-}) / Ksp_n$. In these equations, SI represents the saturation ratio, while $a\,Ca^{2+}$ and $a\,CO_3^{2-}$ denote the activity of Ca^{2+} and CO_3^{2-}, respectively (Devau et al., 2018). Furthermore, Ksp_n represents the solubility product of the relevant mineral n, such as ACC or calcite. These equations were developed based on equilibria by Devau et al. (2018).

$CaCO_3$ crystals can form according to the following stoichiometric equation:

$$CaCl_2 + Na_2CO_3 = CaCO_3 + 2NaCl \quad (14)$$

$CaCO_3$ is a complex crystal structure and can be considered as a model system which follows both classical and non-classical crystallisation pathways (Gebauer et al., 2008). In recent years, there has been a considerable amount of interest and research to develop an effective route to control the crystallisation of $CaCO_3$ based on an understanding of its nucleation and growth

mechanisms. Figure 11 shows the precipitation of $CaCO_3$ through classical and non-classical mechanisms (Gebauer, 2018). The difference between classical and non-classical routes has been discussed in section 2.11 and 2.1.3. An overview of the suggested processes for the generation of $CaCO_3$ crystals from an aqueous solution containing Ca^{2+} and CO_3^{2-} ions is shown in Figure 12. The schematic demonstrates that multiple intermediate species, such as PNCs (iii) and liquid precursors, emerge prior to the creation of ACC particles, which ultimately transform into crystal phases (Du and Amstad., 2020). Blanco et al. (2011) studied crystallisation of $CaCO_3$ at the concentration of 0.5 M where they observed the transformation of ACC to calcite via the metastable phase, vaterite. The crystallization process took place in two stages: initially, the ACC particles rapidly dehydrated, leading to the formation of vaterite particles; subsequently, these vaterite particles underwent a transformation into calcite through a dissolution and re-precipitation mechanism, where the reaction rate was influenced by the surface area of calcite (Rodriguez-Blanco et al., 2011)

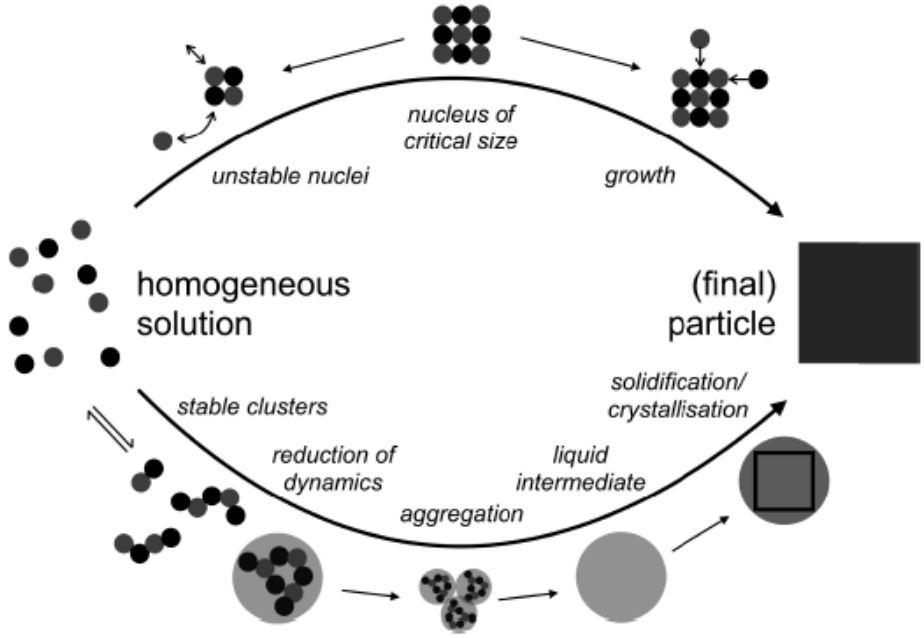

Figure 11 Schematic representation of $CaCO_3$ formation via classical (top) and non-classical (bottom) pathways (Gebauer, 2018; Gebauer & Cölfen, 2011).

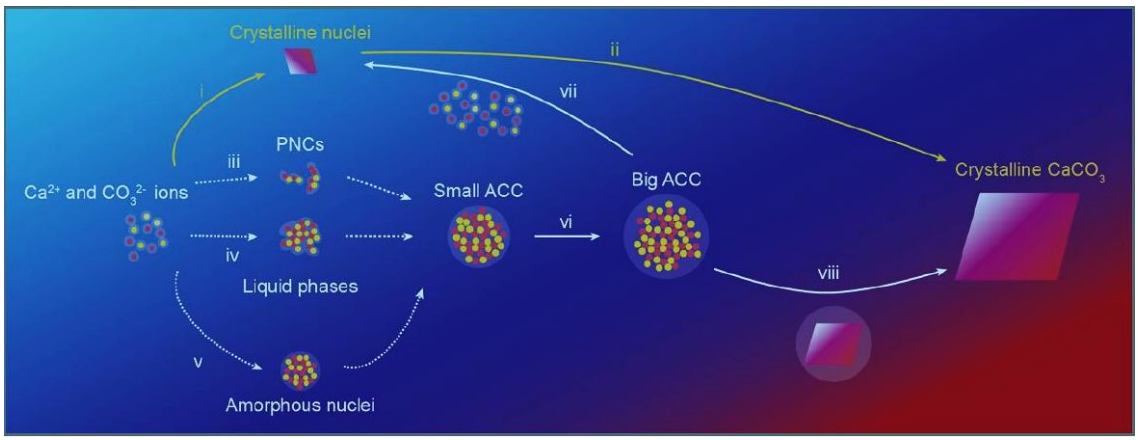

Figure 12 Schematic demonstrating the evolution of $CaCO_3$ through various pathways. (I and ii) illustrates the formation of crystal nuclei and their subsequent growth through ion-by-ion attachment, following the classical nucleation theory (CNT) pathway. Prior to the formation of ACC particles, various intermediate species, including PNCs (iii) and liquid precursors (iv), have been reported. (v) ACC nuclei form directly within the aqueous solution (vi). Small ACC particles then grow and undergo transformation into larger ACC particles (vii), eventually leading to the formation of crystal phases (Du and Amstad., 2020).

Figure 13 shows the change in logarithmic ion activity product (IAP) of $CaCO_3$ at 25º C as a function of time. This plot exhibits three distinct regions: unstable (I), metastable (II) and stable (III) phases (Sawada, 1997). When a solution is supersaturated with Ca^{2+} and CO_3^{2-} ions, $CaCO_3$ immediately starts to appear as ACC during the unstable phase (I). The transition of ACC to crystalline structures (vaterite and calcite) occurs during the metastable phase (II), which is accompanied by a sharp decrease in the IAP value. Eventually all the polymorphs are transformed into the most stable structure (calcite) (Ogino et al., 1987).

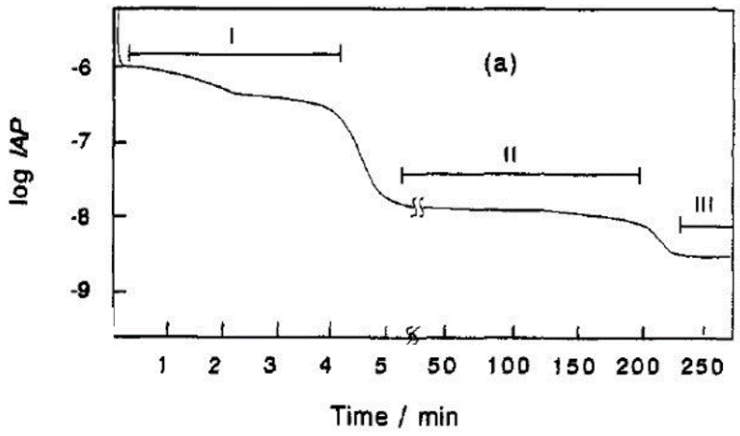

Figure 13 Change in log IAP with time at 25º C. I, unstable phase, II, metastable phase, III, stable phase (Ogino et al., 1987)**.**

ACC is a highly disordered mineral which spontaneously forms in a supersaturated aqueous solution containing Ca^{2+} and CO_3^{2-} ions. ACC is commonly thought to be formed as a precursor to the anhydrous polymorphs in aqueous solution and exists as spherical nanoparticles with a suggested composition of $CaCO_3.xH_2O$, with x in the range 1 to 1.4 (Ihli et al., 2014). In the initial stages of the crystallization process, this hydrated variant of $CaCO_3$ is formed, which does not diffract X-rays due to the absence of a well-defined crystal structure (Addadi et al., 2003). It has been reported that prior to the formation of ACC, various types of intermediate species, including prenucleation clusters (PNCs) and liquid precursors, are formed (Du and Amstad., 2020). The study conducted by Avaro et al. (2017) investigated the mechanisms involved in the formation of liquid or solid amorphous intermediates using potentiometric titrations and attenuated total reflection Fourier-transform infrared spectroscopy (ATR-FTIR). Their findings indicated that solid ACC is formed through the dehydration of liquid precursors, rather than quasi-classical nucleation events occurring within dense liquid droplets (Avaro et al., 2020). The role of water in the ACC structure and its transformation into crystalline polymorphs of $CaCO_3$ were investigated using NMR, as shown in Figure 14. It was found that dehydration of synthetic ACC takes place in three stages: 1) the simultaneous removal of fluid like mobile, restrictedly mobile, and rigid H_2O. 2) The removal of restrictedly mobile and rigid H_2O, 3) The elimination of hydroxyl groups and trapped rigid and mobile

components that cannot be expelled without transforming into crystalline calcium carbonate (Schmidt et al., 2014).

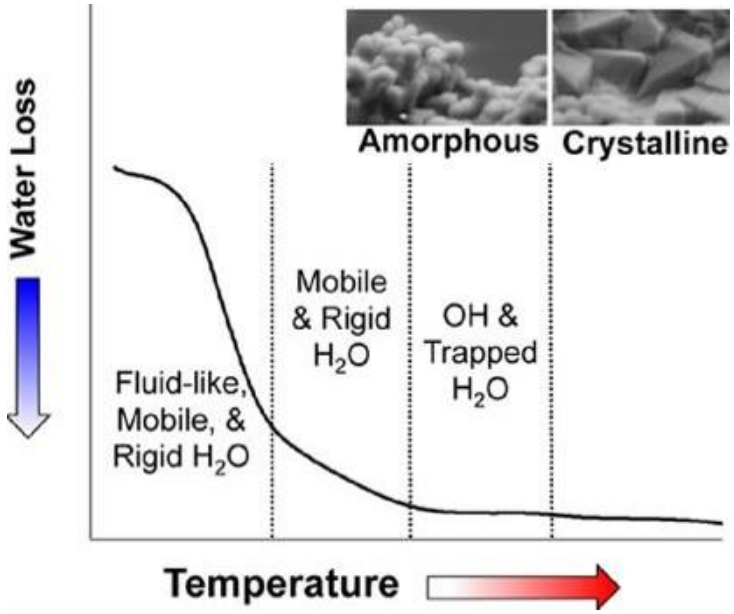

Figure 14 Water loss of ACC particles as a function of temperature (Schmidt et al., 2014)**.**

ACC particles larger than a few nanometres in diameter are metastable and have a tendency to undergo transformation into crystalline forms over time according to Ostwald's rule of stages (ORS) which suggests that when a system has several metastable phases, it follows a sequential progression by transitioning through the nearest thermodynamic state to the most stable phase (Du and Amstad., 2020; Smeets et al., 2017; Cardew, 2023). $CaCO_3$ has three anhydrous crystal polymorphs vaterite, aragonite, and calcite in the order of decreasing solubility, all of which originate from the amorphous form of $CaCO_3$ (ACC) (Mejri et al., 2014; Vidallon et al., 2020). There is evidence showing that, in bulk systems, ACC is transformed to calcite via vaterite within 5 minutes of reaction (Cavanaugh et al., 2019). Von Euw et al., (2020) studied the phase transformation of amorphous calcium magnesium carbonate (ACMC) into a crystalline structure. They developed a model which demonstrated that the amorphous nanoparticles are surrounded by a hydration shell of bound water molecules, as shown in Figure 15 (Von Euw et al., 2020).

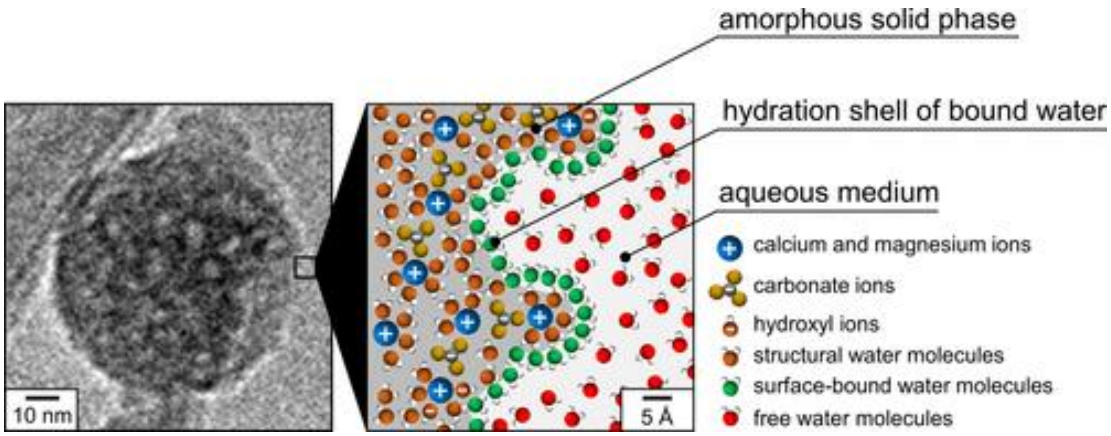

Figure 15 Cryo-TEM micrograph of ACMC along with two-dimensional chemical and structural schematic model of the surface region of the particle dispersed in deionised water (Von Euw et al., 2020)**.**

There has been ongoing debate regarding the mechanisms of nucleation from electrolyte solutions (Michael H.Nielsen, Shaaul Aloni, 2014a). The discovery of amorphous precursors, along with cluster aggregation and liquid–liquid phase separation has challenged the traditional assumptions of classical nucleation theory, which overlooks the possibility of stable ion associates serving as precursors to the formation of critical nuclei (Gebauer et al., 2018). Studies conducted on materials such as calcium carbonates and calcium phosphates have revealed, through the use of titration, that pre-nucleation clusters (PNCs), which are stable solute precursors, can be present in both under-saturated and supersaturated solutions (Du and Amstad., 2020). It was shown that in under-supersaturated solution, PNCs can be detected by potential measurements and constant pH titration. As is shown in Figure 16, Gebauer et al. (2008) used a calcium ion selective electrode to monitor the development of free calcium ions (black line) at a constant pH value of 9.25, against the dosed amount of calcium ions (red line). As supersaturation gradually increased, the amount of free calcium ions (black line) increased at a considerably slower rate. This is due to the binding of a significant portion of free calcium ions with other ions, leading to a decrease in the amount of free calcium ions. The behaviour of calcium binding during the pre-nucleation stage is similar in both under-saturated and supersaturated solutions, as evidenced by the linear development over time. Once a critical threshold is reached, the nucleation process is initiated, resulting in a decrease in the concentration of free calcium ions. The study also revealed

that in a supersaturated solution, it was possible to detect a species with a diameter of 2 nm by analytical ultra-centrifugation (AUC). This size corresponds to a cluster composed of 70 calcium and carbonate ions that are combined into a single cluster. Furthermore, larger cluster species with a diameter of around 5 to 6 nm can be also detected in the early post-nucleation stage, indicating that cluster aggregation is the mechanism responsible for nucleation (Gebauer et al., 2008).

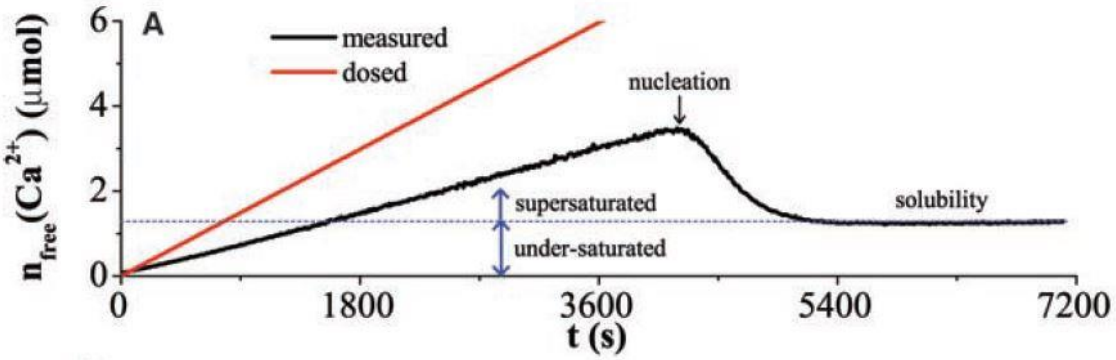

Figure 16 Comparison of dosed calcium ions (red line) and free calcium ions (black line) measured using a calcium ion selective electrode at pH 9.25. The solubility concentration of the precipitated phase determines the undersaturated and supersaturated stages of the prenucleation stage, where calcium ions are bound even in undersaturated solutions (Gebauer et al., 2008).

Pre-nucleation stages of $CaCO_3$ have been studied in real time using liquid cell TEM (LCTEM) where the formation of nano particles of hydrated ACC was visualised through coalescence of dense liquid droplets. The authors reported the presence of these droplets after 5 minutes of the reaction, which coalesced over time (15 minutes) and formed microdroplets of several micrometres in size as show in Figure 17. Additionally, to verify that the observed phenomena were not a result of electron beam effects, the electron dose was computed following the approach outlined by Schneider et al (Ramnarain et al., 2022).

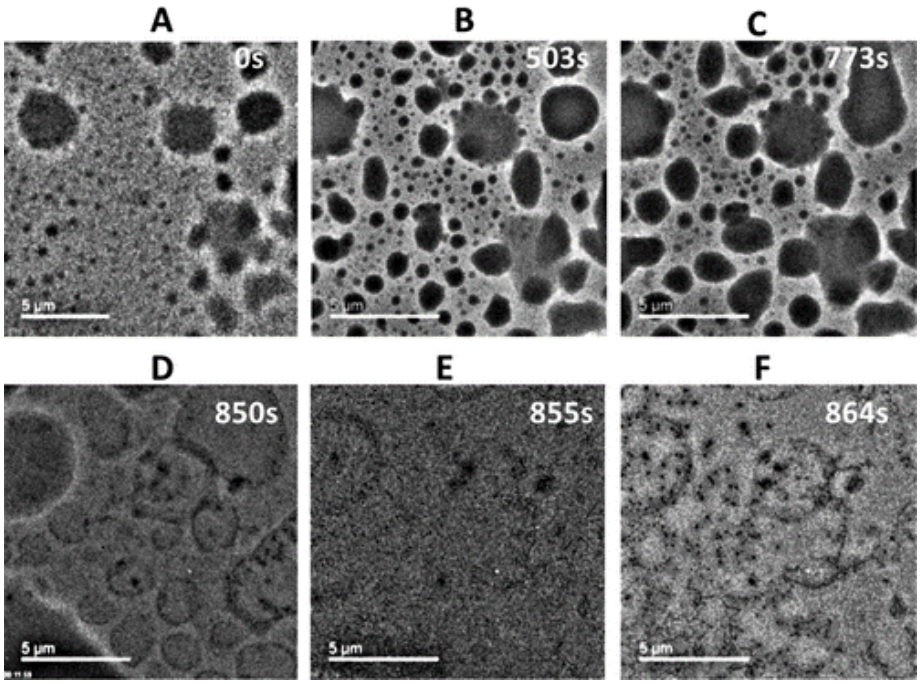

Figure 17 In-situ LC-TEM images of the transformation of dense liquid droplets to ACC in real-time. (A-C) shows evolution of dense liquid droplet through coalescence and their transformation into hydrated amorphous nanoparticles. Reproduced from Ramnarain et.al. (2020).

Sebastiani et al. used THz spectroscopy to study the hydration dynamics, which refers to the interaction of water molecules with calcium ions and carbonate ions in a $CaCO_3$ solution, during the initial stages of $CaCO_3$ formation as shown schematically in Figure 18. It was suggested that water plays an important role during phase separation. Solidification of ACC undergoes an intermediate step called liquid-liquid phase separation (LLPS) which occurs upon crossing the binodal limit (section 2.1.5). PNCs then transform into nanodroplets, which assemble due to a reduction in interfacial surface area. Further dehydration leads to the formation of proto-structured amorphous $CaCO_3$ (proto-ACC, which are different forms of ACC and direct precursors of the anhydrous crystalline structures as detailed in section 2.4.1). These proto-ACC structures are approximately 10–20 nm in size and ultimately lead to the formation of crystals. Thus, from the perspective of a non-classical pathway (PNC), the formation of $CaCO_3$ is proposed to involve a chemical and structural process whereby hydration water is progressively lost, starting from Ca^{2+}/ HCO^{3-}/ CO^{3-} prenucleation clusters and forming dense liquid nanodroplets, liquid amorphous

$CaCO_3$, solid amorphous $CaCO_3$ (ACC), and finally, anhydrous crystalline polymorphs (Gebauer et al., 2014).

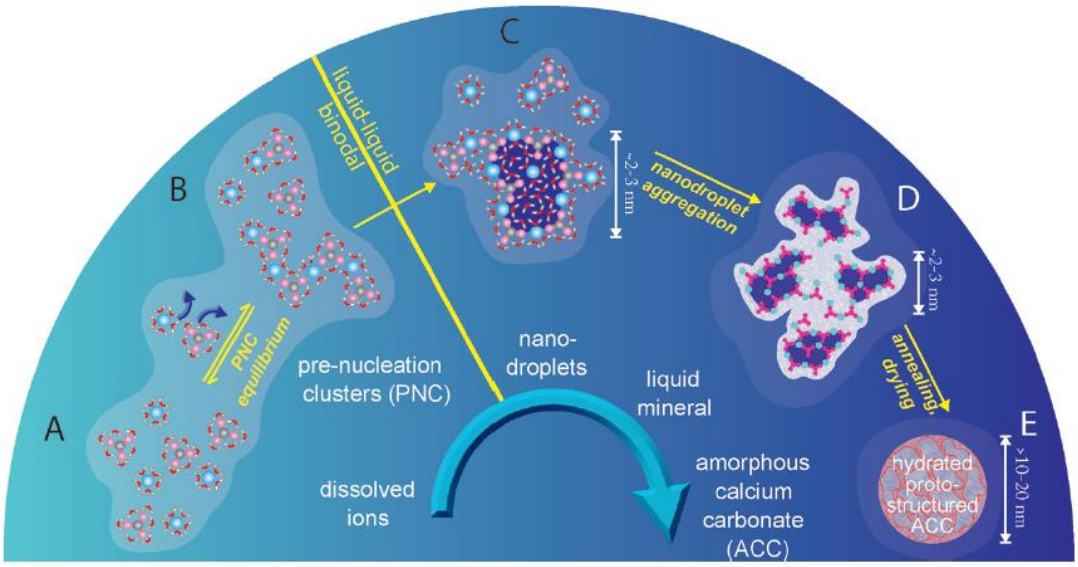

Figure 18 The impact of hydration dynamics on $CaCO_3$ nucleation. A) Shows hydrated calcium and carbonate ions. B) Pre-nucleation ion clustering occurs due to partial dehydration of the individual ions. C) Occurrence of liquid-liquid phase separation. D) Clusters of hydrated $CaCO_3$ nanodroplets that have combined. E) Hydrated proto-ACC with a size of approximately 10–20 nm (Ramnarain et al., 2022)**.**

Through a combination of molecular dynamic (MD) simulations and analysis of experimental data conducted by Demichelis et al. (Demichelis et al., 2011), it has been demonstrated that mineral clusters are composed of an ionic polymer as shown in Figure 19. This polymer consists of alternating calcium and carbonate ions and exhibits a dynamic topology with chains, branches, and rings. In all simulations, the occurrence of chain-like structures was observed, independent of pH and composition. However, what differed under these conditions was the size distribution, the lifetime of a specific length, and the level of branching along the chain. These findings provide an explanation for the formation of liquid-like amorphous phase of $CaCO_3$, as well as the non-classical behaviour observed during the growth of amorphous $CaCO_3$.

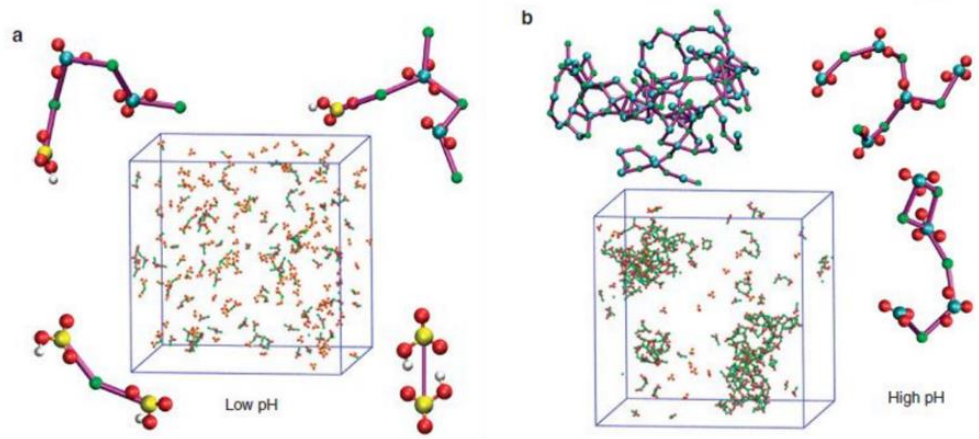

Figure 19 Observed species at low and high pH levels, along with snapshots of the Molecular Dynamics simulation box for a concentration of 0.5 mM. In the illustrations, calcium, carbonate carbon, bicarbonate carbon, oxygen, and hydrogen atoms are colour-coded as green, blue, yellow, red, and white, respectively (Demichelis et al., 2011).

In order to observe the nucleation pathway, Nielsen et al. (2014) studied the early stages of crystallization of $CaCO_3$ by mixing $CaCl_2$ and $NaHCO_3$ (bicarbonate) in a flow cell. The solutions were at concentrations ranging between 10-100 mM, using in-situ LCTEM. Multiple pathways for the formation of $CaCO_3$ were observed, including the direct nucleation and growth of ACC and vaterite, the direct transformation of ACC into crystalline phases such as aragonite and vaterite, and the simultaneous nucleation and growth of calcite crystals directly from the solution. However, the transformation of ACC to calcite was not observed. Figure 20 illustrates the transformation of nucleated ACC to aragonite (A-D) and vaterite (E-H). Shortly after the emergence of the secondary crystalline phases, the size of the ACC particles began to decrease. This reduction in size potentially suggests the removal of water from the amorphous particle or a sudden decrease in concentration that leads to partial dissolution. The subsequent phase grew rapidly, consuming the original amorphous particle (Michael H.Nielsen, Shaaul Aloni, 2014).

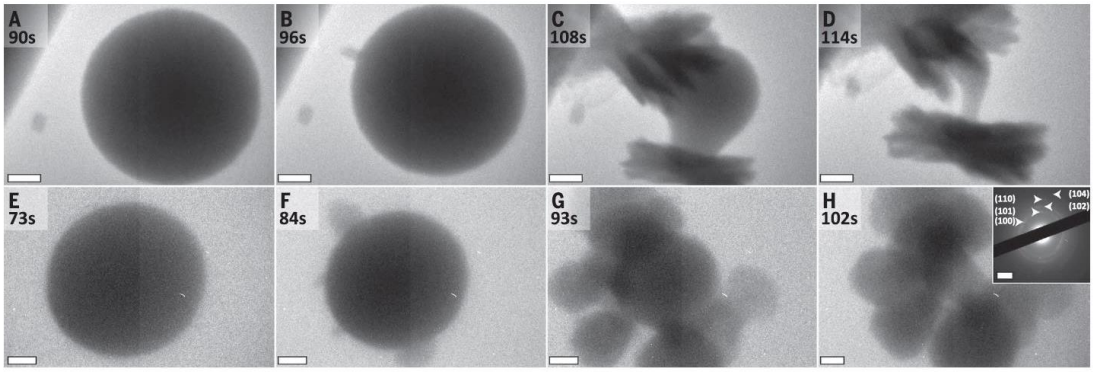

Figure 20 (A-D) The transformation of ACC to aragonite involving concurrent growth of aragonite crystals while ACC undergoes shrinkage and eventual disappearance. (E-F) displays a previously formed ACC particle that has undergone secondary nucleation, resulting in the formation of a crystalline phase either on the surface or within the amorphous particle. (G-H) Growth of vaterite at the expense of ACC particles and the corresponding diffraction pattern (Michael H.Nielsen, Shaaul Aloni, 2014)**.**

Smeets et al. (2017) also utilised cryo-TEM to investigate the morphological and structural evolution of the precipitation of $CaCO_3$ in a dilute solution at a concentration of 1 mM. In this study no evidence was found for the formation of PNCs and solid ACC particles. Instead, the presence of spherical amorphous objects with sizes ranging from 200–400 nm was observed which exhibited a lower contrast in comparison with ACC particles. The observed objects were suggested to be droplets of a dense liquid phase (DLP) embedded in vitrified ice, which later directly transformed into vaterite (Figure 22). In titration experiments, vaterite growth occurs after nucleation, which involves a net transfer of stoichiometric calcium and carbonate ions from the solution. Eventually, this process shows Ostwald ripening, as determined by Dynamic Light Scattering (DLS) measurements. They argue that the nucleation mechanism of $CaCO_3$ could be fully explained by the concepts of classical nucleation in a multiple-step, multiple-phase reaction, starting from predominantly free ions and ion pairs present in the solution (Smeets et al., 2017).

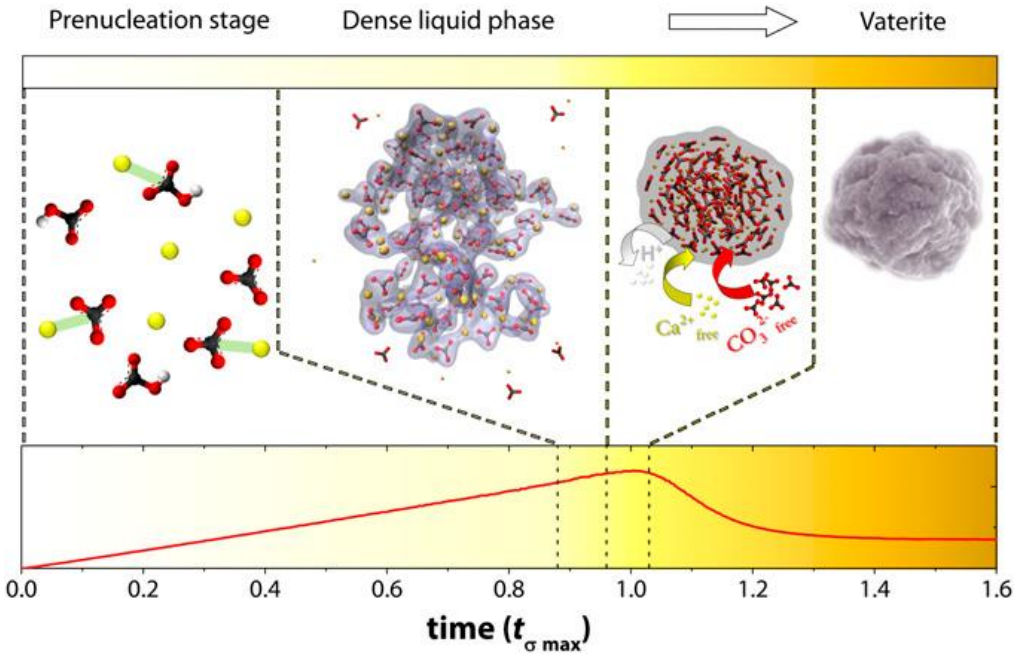

Figure 21 A schematic illustration demonstrating the evolution of the $CaCO_3$ structure during a titration experiment using dilute $CaCO_3$ solutions. In the initial prenucleation stage, the solution primarily consists of $CaCO_3^0$ and $CaHCO_3^+$ ion pairs, alongside free ions. Once the concentration reaches a critical point at approximately 0.90 $t_{\sigma\ max}$ ($t_{\sigma\ max}$ indicates the time point at which the concentration of free calcium ions is at its peak), a liquid-liquid phase separation occurs, resulting in the formation of a dense liquid phase (DLP) and a less concentrated ionic solution containing free ions and ion pairs. At the nucleation point around 0.96 $t_{\sigma\ max}$, the DLP reacts with free Ca^{2+} and free CO_3^{2-} ions, resulting in the release of H^+ ions, and eventually converts to vaterite until equilibrium is achieved (Smeets et al., 2017)**.**

2.4 Effect of variables on the formation of CaCO3

Crystallization of $CaCO_3$ is influenced by physiochemical solution conditions such as the degree of supersaturation (detailed in section 2.1.1), the pH value, temperature, the presence of additives such as ethanol or other ions such as magnesium and the presence of a confined volume.

2.4.1 Effect of pH

In general, a pH change directly affects the precipitation of $CaCO_3$. When pH decreases, the concentration of hydrogen ions ($[H^+]$) increases, shifting the equilibrium towards the formation of carbonic acid H_2CO_3. This makes the system more acidic leading to a decrease in the saturation state of $CaCO_3$. Eq.15-17 illustrate the reversible reactions involved in the carbonic acid equilibrium and the dissolution/precipitation of $CaCO_3$. Within these equilibria,

the combination of water (H_2O) and carbon dioxide (CO_2) results in the formation of H_2CO_3 which can subsequently dissociate into calcium, hydrogen ions (H^+), bicarbonate ions (HCO^{3-}) and carbonate (CO_3^{2-}) ions.

$$H_2O + CO_2 \leftrightarrow H_2CO_3 \leftrightarrow H^+ + HCO_3^- \leftrightarrow CO_3^{-2} + H^+ \quad (15)$$

$$CaCO_3 \leftrightarrow Ca^+ + CO_3^{-2} \quad (16)$$

$$\begin{array}{l} H_2O + CO_2 \\ \quad \| \\ CaCO_3 + H_2CO_3 = Ca^{+2} + 2HCO^-_3 + CO_3^{-2} + H^+ \end{array} \quad (17)$$

In Figure 22, the concentrations of carbonate species (CO_2, HCO_3^-, and CO_3^{2-}) are depicted as a function of pH level. At pH 7.2, the highest proportion of carbonate species is represented by HCO^{3-} (Takahashi, 2016).

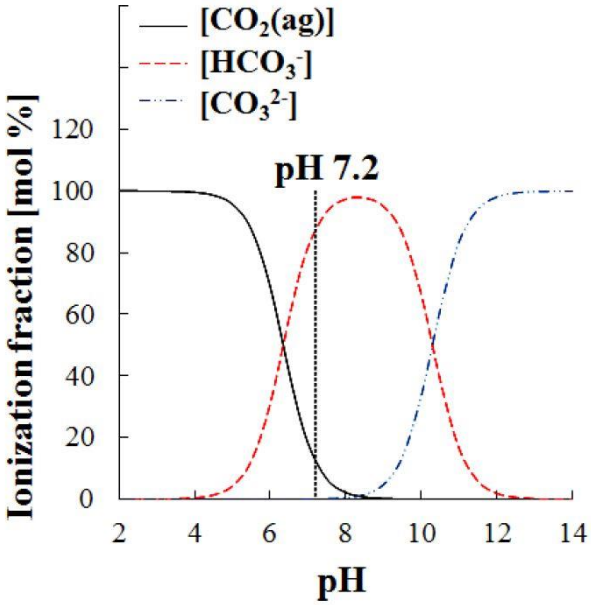

Figure 22 The correlation between the calculated fraction of carbonate species and the corresponding pH levels (Takahashi, 2016).

Gebauer et al. (2008) investigated the effect of different pH levels on the crystallisation of $CaCO_3$ from which they concluded that Ca-CO_3 binding strength during the pre-nucleation stage is governed by the pH value of the carbonate buffer solution. The pH-dependent change of binding strength in clusters is

thought to play a key role in the nucleation of different amorphous forms of $CaCO_3$, which subsequently give rise to the formation of different $CaCO_3$ polymorphs. Solubility products and the time and pH dependencies of the ion activity products of ACC phases are shown in Figure 23. The formation of a more stable, short-range amorphous $CaCO_3$ (ACC I or proto-calcite) at low pH values (pH= 9.0-9.5), corresponding to high binding strength clusters, leads to the formation of calcite. However, the less stable short-range ACC (ACC II or proto-vaterite) formed at higher pH values (9.75-10.0) promotes the formation of vaterite Gebauer et al., 2008; Gebauer et al., 2010). In addition, the formation of different polymorphs has also been shown to be governed by both additives and pH conditions. At near freezing temperature Hu et al. (Hu et al., 2015) investigated the existence of metastable polymorphs (ikaite or vaterite) of calcium carbonate under two pH conditions (pH = 9.0 and 13.4), in the absence and/or presence of phosphate. It was also shown that formation of vaterite is dominant at moderate alkaline conditions (pH = 9.0) in the absence of phosphate. In contrast, it was found that ikaite was predominantly formed at high alkaline conditions (pH 13.4), and/or low pH in the presence of phosphate anions (Hu et al., 2015).

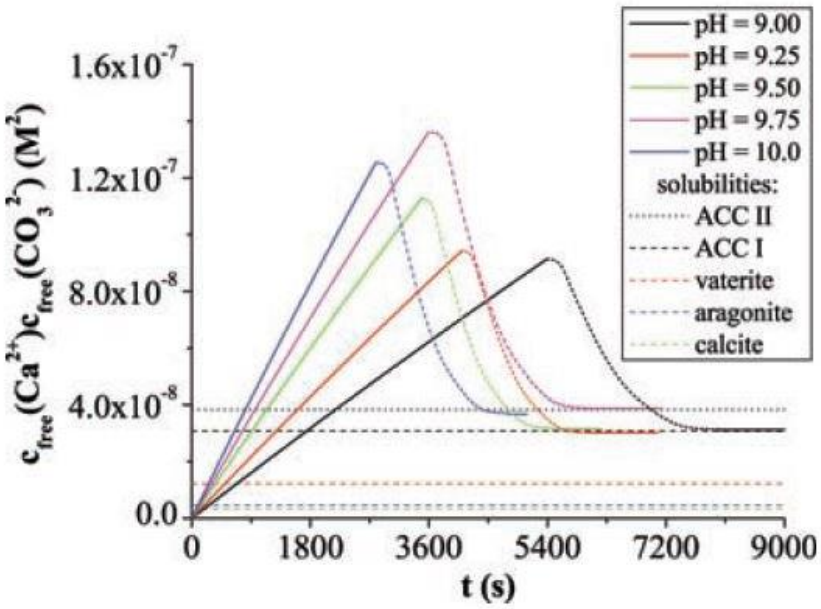

Figure 23 Evolution of the free ion activity product over time. Two distinct ACC phases are observed, denoted as ACC I (~3.1 × 10^{-8} M^2) and ACC II (~3.8 × 10^{-8} M^2), exhibiting different solubility products corresponding to the pH-dependent prenucleation cluster equilibrium. The figure also presents the solubility of vaterite, aragonite, and calcite (Gebauer, 2008).

2.4.2 Effect of CO_2

The presence or absence of carbon dioxide (CO_2) can influence the balance between $CaCO_3$ dissolution and precipitation (Eq.14 and 16). Higher levels of CO_2 promote dissolution, whereas lower levels of CO_2 favour the formation and precipitation of $CaCO_3$. When CO_2 levels are elevated, the concentration of dissolved carbonic acid (H_2CO_3) increases (Eq.14). This higher concentration of H_2CO_3 facilitates the dissolution of $CaCO_3$ by reacting to form soluble bicarbonate ions (HCO^{3-}). This phenomenon is commonly known as carbonation or carbonic acid dissolution. Environmental studies on the influence of dissolved CO_2 in the ocean has revealed that the increased level of dissolved CO_2 causes marine organisms to have difficulties in calcifying their shells and skeletons. In addition, as a result of the pH reduction, fewer carbonate ions are available for corals to form their skeletons from aragonite (Cao et al., 2007). In laboratories, the process of preparing samples is typically conducted under atmospheric conditions that maintain a significantly low level of CO_2, approximately around 1%. According to Le Chatelier's principle, when the concentration of CO_2 decreases, the equilibrium will shift towards the left side to compensate for the loss of CO_2 (Eq.14-16). This shift enhances the recombination of HCO^{3-} and H^+ ions, promoting the preferential production of CO_2. As a result, the pH increases and becomes more alkaline (M. A. Ilett, 2020).

2.4.3 Effect of Temperature

In terms of temperature, in general, the aqueous solubility of minerals increases with increasing temperature except for $CaCO_3$, which shows an inverse trend of decreasing aqueous solubility (Figure 24). This can be explained by Le Chatelier’s principle. In the equilibrium reaction (Eq.18), the forward reaction leading to solid formation is endothermic, whereas the backward reaction involving dissolution is exothermic (Nasser et al., 2016). An increase in temperature will shift the equilibrium towards the endothermic forward reaction, leading to the precipitation of $CaCO_3$. In other words, as the temperature rises, the solubility of CO_2 in water decreases. As a result, the concentration of hydrogen ions (H^+) decreases, promoting the formation of carbonate ions and

facilitating the precipitation of $CaCO_3$. However, a decrease in temperature will favour the backward exothermic reaction, resulting in the dissolution of the carbonate.

$$Ca^{+} + HCO_3^{-} \leftrightarrow CaCO_3 + CO_2 + H_2O \quad (18)$$

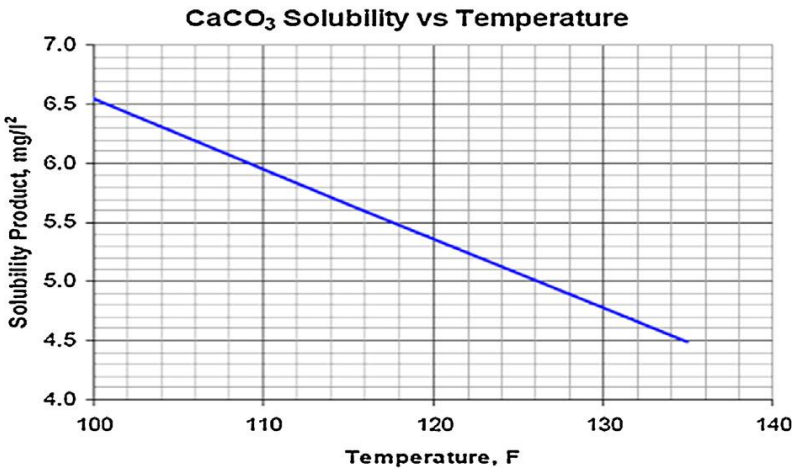

Figure 24 The solubility of $CaCO_3$ exhibits an inverse relationship with temperature at a pressure of 1 bar (Nasser et al., 2016).

(Sawada, 1997) studied the effect of temperature on the formation of different polymorphs of $CaCO_3$. As shown in Figure 25, $CaCO_3$ polymorphism was found to be a temperature-dependent phenomenon. Calcite was the dominant polymorph over a temperature range of~10-20 °C. Considerable vaterite formation was seen at temperatures between 30 °C and~50 °C, which was followed by the formation of aragonite at higher temperatures between 60°C to 80 °C. All crystals are eventually transformed to calcite at any temperature. During the metastable stage, aragonite is the main polymorph formed, accompanied by a smaller amount of calcite. The IAP (Ion Activity Product) value remains constant at the solubility product of aragonite throughout this stage. Towards the end of the metastable stage, the decrease in IAP is linked to the disappearance of aragonite. Consequently, the transformation from aragonite to calcite occurs through a process involving the dissolution of aragonite and the subsequent growth of calcite. Notably, the growth of calcite

represents the rate-determining step in this transformation process (Sawada, 1997).

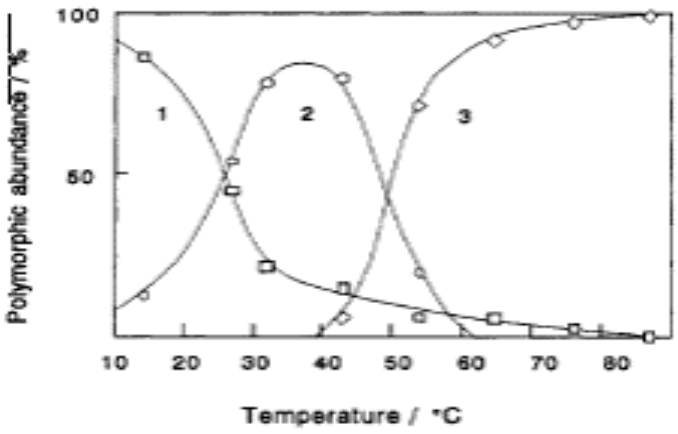

Figure 25 Polymorph abundance of calcium carbonate as a function of temperature. Curve 1, calcite; curve 2, vaterite; curve 3, aragonite (Sawada, 1997)**.**

2.4.4 Effect of Ethanol

In general, alcohols have an impact on the dielectric constant of the medium, interionic attraction, and solute-solvent interaction. Chen et al. (2013) suggested that the addition of alcohol to solutions containing Ca2+ and CO32- ions would raise the saturation index (SI) of the solution (Chen et al., 2013) (Sand et al., 2012). According to a study by Manoli et al. (2000), the presence of ethanol was found to enhance the rate of precipitation of CaCO3, potentially attributed to a slight increase in the solution's supersaturation. It was also found that ethanol has an impact on the morphology and structure of vaterite crystals and acts as a stabilizing agent for this mineral phase, inhibiting its transformation into calcite (Manoli and Dalas, 2000). Although calcite and aragonite have similar surface energies, they may respond differently to changes in the solvent composition. This is because the exposed atomic arrangement on the surface of each mineral is distinct. As a result, aragonite tends to remain stable for a longer period in solutions at room temperature compared to calcite. Nahi et al. investigated how the presence of ethanol affected the precipitation of CaCO3. Their research demonstrated that the introduction of ethanol caused a change in the growth pattern of calcite crystals. Specifically, the crystals shifted from having rhombohedral shapes with smooth {104} faces (up to 25 vol % ethanol)

to developing hopper morphology with pits in the centres of their faces (with ethanol concentrations ranging from 30% to 50%). Moreover, when ethanol concentrations exceeded 50 vol %, the formation of vaterite was observed (Nahi et al., 2021). Walker et al. (2017) conducted a cryo-TEM study of 0.025 M $CaCO_3$ formation in the presence of ethanol. After 3 minutes of the reaction, a network of ACC particles appeared with a size range of 60-120 nm, which then aggregated and grew to a size range of 250-300 nm. Subsequently, non-classical aragonite formation occurred after 1 hour of the reaction as depicted in Figure 26 (Walker, Marzec, & Nudelman, 2017) . Cryo-TEM image of the transformation of ACC to aragonite. (A-B) shows the formation of ACC particles after 3 minutes of the reaction, with a size range of 60-120 nm (B) ACC particles grew and appear with a size range of 250-300 nm after 10 minutes of the reaction. (C-D) fully formed aragonite with the corresponding diffraction pattern after 1 hr of the reaction (Walker et al., 2017).

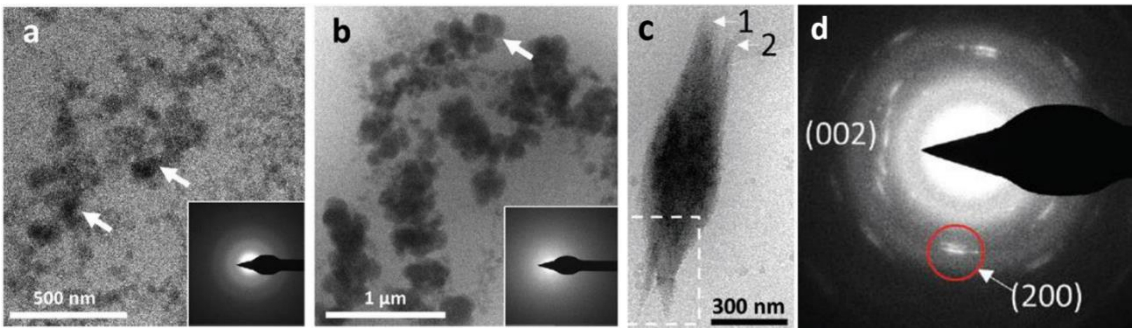

Figure 26. Cryo-TEM image of the transformation of ACC to aragonite. (A-B) shows the formation of ACC particles after 3 minutes of the reaction, with a size range of 60-120 nm (B) ACC particles grew and appear with a size range of 250-300 nm after 10 minutes of the reaction. (C-D) fully formed aragonite with the corresponding diffraction pattern after 1 hr of the reaction (Walker et al., 2017)

2.4.5 Effect of additives on crystallisation of $CaCO_3$

The deposition of $CaCO_3$ is a widespread issue in the oil, gas, and water industries. This phenomenon causes significant operational difficulties, including pipe clogging and an increased demand for energy to clear the deposits. In order to reduce the occurrence of unwanted crystallization of $CaCO_3$, various chemical methods have been employed Gebauer et al. (2008) Mg^{2+} has been reported as one of the influential factors in controlling the polymorphism of

$CaCO_3$. The precipitation of $CaCO_3$ in the presence of Mg^{2+} can lead to the formation of magnesium calcite (Mg-calcite) or aragonite. The ratio of magnesium-to-calcium (Mg: Ca) ions in solution is the primary factor determining the selection of calcite or aragonite polymorphs. In solutions that contains Mg^{2+} in ratios similar to those found in seawater, the barrier for calcite nucleation exceeds that of metastable aragonite. This favours the dominance of aragonite in terms of nucleation kinetics. (Sun et al., 2015). The primary reason for Mg^{2+} inhibiting the formation of calcite is its contribution to an increase in surface energy. When the Mg^{2+}/Ca^{2+} ratio is relatively low, Mg^{2+} ions have access to the surface of $CaCO_3$ and become integrated into the calcite lattice. This incorporation process promotes the selective formation of Mg-calcite (Hong et al., 2022). Mg^{2+} ions promote the formation of aragonite in the solution, but their efficacy relies on a specific calcium-to-magnesium ratio. Loste et al. (2003), conducted a study on the precipitation of $CaCO_3$ at various Mg:Ca ratios, 0:1, 1:1, 2:1, 3:1, 4:1, and 10:1. It was found that the initial phase precipitated consistently consisted of ACC, and the magnesium content within ACC increased as the Mg:Ca ratio in the solution rose. The precipitates obtained from the solutions with Mg:Ca ratios of 0:1 and 1:1 were examined during a time span of 0 to 60 minutes. After 2 minutes, the analysis revealed a combination of calcite and vaterite in the precipitates. Samples with an Mg:Ca ratio of 2:1, were found to be in an amorphous state after 2 minutes and transformed to calcite after 30 and 60 minutes. After a period of 24 hours, in addition to calcite, traces of aragonite and calcium carbonate monohydrate were detected. In solutions with an Mg:Ca ratio of 3:1, the primary polymorph that precipitated after 2 minutes was ACC, along with small amounts of calcite. After 24 hours the precipitates consisted of 85% calcite and 15% aragonite. As the Mg: Ca ratio increased to 4:1, the initial precipitation consisted of 50% aragonite and 50% magnesium-calcite. A ratio of 10:1 resulted in a substantial increase in the stability of ACC. After a duration of 14 days, the sample consisted of 6% calcium carbonate dihydrate ($CaCO_3 \cdot H_2O$) and a higher proportion of magnesium carbonate trihydrate ($MgCO_3 \cdot 3H_2O$), which accounted for 83% of the composition. Additionally, 11% of the composition comprised magnesium calcite (Loste et al., 2003).

The influence of the temperature on the scaling rate of $CaCO_3$ when Mg^{2+} or SO_4^{2-} are present in the solution was investigated using the CO_2 degassing method. It was shown that presence of sulphate and magnesium ions increased the induction time to nucleation and decreased the growth rate which led to less formation of $CaCO_3$. However, an increase in temperature from 30 to 60 °C decreases the inhibitory effect of Mg^{2+}on the precipitation of $CaCO_3$ (Mejri et al., 2014).

Sanciolo et.al, (2008) investigated the influence of accelerated seeded precipitation on reducing the formation of $CaCO_3$ scale in treated sewage treatment plant wastewater. Various amounts of $CaCO_3$ were used as seed material, and the pH was adjusted to 9.5, followed by a 1-hour equilibration period. The study revealed that the addition of calcium as seeding agent results in a reduction of calcium content during the desalination of treated sewage water waste. One challenge in using accelerated seed precipitation to decrease calcium in wastewater is the potential interference from substances such as organics and phosphates. These substances can disrupt the mechanisms of $CaCO_3$ precipitation by adsorbing onto or co-precipitating with the calcium carbonate lattice (Sanciolo et al., 2008). Studies have shown that the use of silica inhibitors effectively inhibits the formation of $CaCO_3$. (Weng et al., 1995).

Ramnarain et al. (2020) employed LC-TEM to observe the initial phases of $CaCO_3$ precipitation in real-time, both with L-aspartic acid and without any additives. It was observed that the presence of L-aspartic acid promotes the formation of stable PNCs, which exhibit DOLLOP- like (dynamically ordered liquid-like oxyanion polymer) characteristic after 3 minutes of the reaction. These clusters remain stable for several minutes before undergoing a transformation into amorphous nanoparticles through particle attachment (route A). In the absence of any additives, the crystallization process of $CaCO_3$ takes a different route as shown in the schematic in Figure 27. Without additives, there is a liquid-liquid binodal separation process taking place, resulting in the creation of droplets rich in $CaCO_3$. These droplets primarily grow through coalescence. The dehydration process induces the precipitation of hydrated ACC nanoparticles within these droplets (Ramnarain et al., 2022).

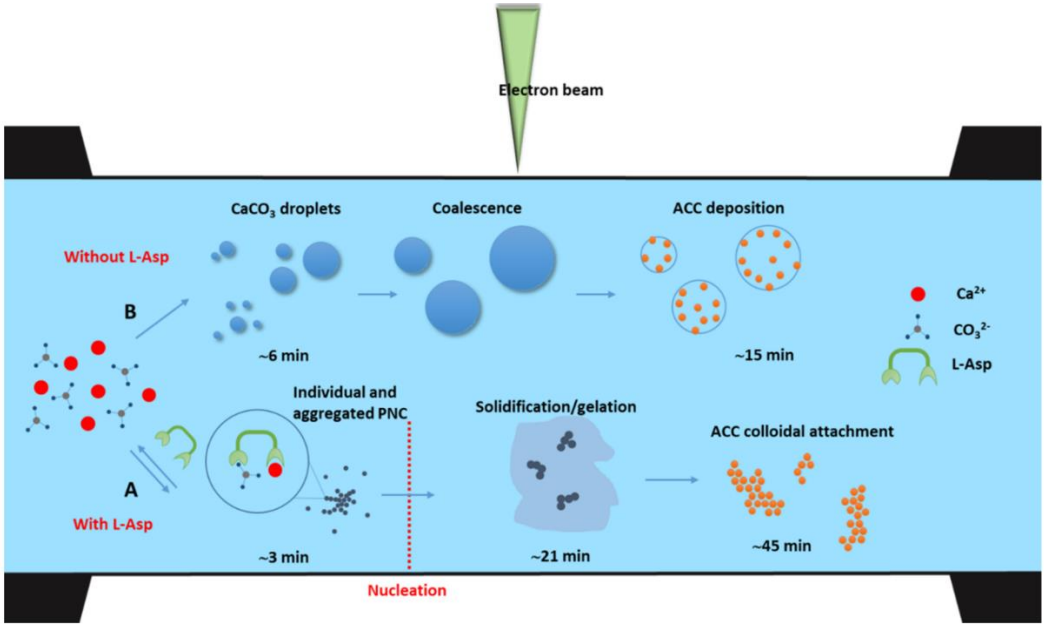

Figure 27 Schematic sequence demonstrating the mineralization of $CaCO_3$ in the presence and the absence of L-Asp (Ramnarain et al., 2022).

2.4.6 Effect of confinement on the crystallisation process

Crystallization can take place within confined volumes in real-world scenarios, which has attracted particular attention in terms of its influence on the bio-mineralisation process and the nucleation and growth of mineral phases in nanometre scale-pore spaces in geochemistry, biology, and tissue engineering (Kim et al., 2018.; Bresme and Cámara, 2006). It has been demonstrated that the nucleation pathways, polymorph selection and morphologies are all controlled by the geometry of confined spaces at which crystallisation occurs. It was also found that confinement generates a thermodynamic barrier that controls the rate of transformation which can significantly impact the dynamics of particle transformation (Cavanaugh et al., 2019). Therefore, in order to acquire a comprehensive understanding of the crystallization process, it is crucial to replicate natural conditions. In this regard, liquid cell chips and microfluidic devices have been employed as controlled platforms for confinement, allowing for the exploration of $CaCO_3$ crystallization and the replication of natural conditions (Meldrum and O'Shaughnessy, 2020). Bone mineralisation (calcification) is an important process consisting of the formation of a collagen matrix and the addition of calcium phosphate nanocrystals to this porous matrix which takes place within a confined volume (Cantaert et al.,

2013). However, calcium phosphate nucleation within the collagenous structure shows different nucleation models in unconfined spaces and confined gap regions. A likely explanation for this different behaviour could be attributed to differences in free energy for nucleation (Kim et al., 2018).

Confinement is recognized for prolonging the time it takes for crystallization to start, which hinders the creation of thermodynamically stable phases like calcite in favour of less stable phases (Xu and Sommerdijk, 2018). Wang et al. (2017) conducted a study on the crystallization of $CaCO_3$ within a confined volume, exploring the potential use of confinement for observing the precursor phase of $CaCO_3$. The authors discovered that intermediate polymorphs, such as vaterite and ACC particles could be observed under confined conditions, whereas their observation in bulk solutions was challenging due to their rapid conversion rate and short lifespan. The study revealed that confining the precipitation space increased the stability of ACC particles and significantly reduced their aggregation state. This effect was attributed to the interplay between surface chemistry and constrained mobility during the crystallization of $CaCO_3$. Consequently, increasing the degree of confinement led to the formation of isolated ACC particles. Furthermore, the study demonstrated that the rate of ACC transformation within confinement was influenced by its aggregation state (Wang et al., 2017). Additionally, Stephens et al. conducted research on the crystallisation of $CaCO_3$ within 10 μm radius microdroplets. Their finding revealed that the constrained volumes of these droplets have a significant impact on the crystallisation process, resulting in the early arrest of growth. It was also found that the morphology, size, and orientation of the calcite crystals were affected (Stephens et al., 2011). Thus overall, it is evident that confinement can control the crystallisation process by modifying the pathway and the kinetics. Zeng et al. (2018) investigated the precipitation of $CaCO_3$ within the cylindrical pores of track-etched membranes, where they examined the relationship between membrane pore diameter and polymorph formation. It was found that as the pore size was decreased, an increasing yield of aragonite was observed. In fact, within 25-nanometer pores in additive-free solution, oriented single crystals of aragonite were exclusively obtained. Even in larger pores, up to 200 nanometres, significant quantities of aragonite emerged in the

presence of low concentrations of magnesium and sulfate ions. This phenomenon can be attributed to the influence of pore size on the ion distribution, which becomes more significant in smaller pores. These intriguing findings suggest that confinement effects may be utilized by living organisms as a means to regulate crystal polymorphs (Zeng et al., 2018).

The time evolution of $CaCO_3$ synthesis, from the earliest stages of nanodroplet precursors to crystalline calcite, was investigated in confinement (Kelly et al., 2021). Globules with a size range of 30-150 nm in diameter were observed shortly after mixing 3.75 mM solutions (the solvent is a mixture of water and isopropyl alcohol in a 3:1 ratio), where liquid-liquid phase separation through spinodal decomposition was observed. These globules then dehydrate (under the electron beam) to form 1-3 nm denser droplets or particles a result of the system moving towards the binodal limit (Kelly et al., 2021).

Summary

This chapter has provided an overview of the key literature relevant to this PhD research project. The review has highlighted the current understanding of $CaCO_3$ crystallization. There is an ongoing debate regarding whether the crystallization process follows a classical route or a non-classical route. The classical route posits that the formation of $CaCO_3$ nucleation is based on the creation of critical nuclei with the same structural form as the final crystal. On the other hand, non-classical routes propose the existence of initial species, such as a dense liquid structure, which later transforms into ACC before eventually crystallizing into its final crystalline structure.

$CaCO_3$ is influenced by physiochemical solution conditions such as the degree of supersaturation (detailed in section 2.1.1), the pH value, temperature, and the presence of additives such ethanol or magnesium ions. These various factors and influences can potentially impact not only the specific pathway through which a crystallization process occurs but also the kinetics governing its progression. Furthermore, these factors may even have the potential to influence the eventual polymorphic structure that emerges as a result.

This research project aims to contribute to the body of research knowledge by investigating and developing methods to study the early stages of crystallisation and polymorph selection of $CaCO_3$.

Chapter 3 Methods and Materials

This chapter presents a comprehensive overview of the methods and materials employed in this research work. Additionally, a thorough discussion of various characterization techniques is provided, offering both an understanding of the general scientific background and the specific application to the project.

3.1 Experimental and Theoretical Methods

3.1.1 Application of electron microscopy to crystallisation processes

Electron microscopes are valuable tools which are used to image nanoparticles in inorganic and biological systems with a high resolution. These techniques have been used to characterise size, the crystal structure, elemental composition, and a variety of other physical information by virtue of interaction of the electrons with the specimen (Goodhew and Humphreys, 2000). In general, the scattering of electrons by atoms of the specimen will produce signals which can be transformed into an image. The key advantages of electron microscopes as compared with their light microscope counterparts are their higher range of magnification and resolution, which enable them to provide clearer and more detailed images at the nanoscale. The better resolution of electron microscopes can be explained by shorter wavelength of electron which is up to 100,000 times smaller than the wavelength of visible light.

There are several experimental techniques that are used for characterisation of nano-crystals: Scanning electron microscopy (SEM), which is based on emitted secondary electrons or back scattered electrons from the surface of the sample, allows for 3-D visualisation and provides images of external morphology, while Transmission electron microscopy (TEM) which is based on transmitted electrons, is a widely used technique for providing information on size, morphology and internal composition of nanocrystals. TEM probes the internal structure of solids and gives good insight into the microstructural and nano-structural detail (Goodhew and Humphreys, 2000). Additional analytical techniques such as selected area electron diffraction (SAED), energy dispersive X-ray spectroscopy (EDX) and electron energy loss spectroscopy (EELS) are also used in combination with TEM. EDX can be used to provide qualitative and

quantitative elemental analysis, whilst SAED is used to identify crystal structure and lattice parameters via *d*-spacing measurements (M. B. Ward, N. Hondow, 2015). However, conventional vacuum TEM cannot be used to study the growth of nano crystals in solutions due to the evaporation of liquids under the vacuum system. For this purpose, liquid cell TEM has been developed to monitor the growth of nanocrystals in real time. Prior to the invention of LC-TEM, cryo-TEM where the liquid is rapidly frozen and examined cold, was one the most common techniques. Even with the introduction of LC-TEM, cryo-TEM continues to be a crucial method for visualizing particle growth, maintaining its significance in the study of biological and colloidal systems. This technique enables the visualization of samples in their frozen state by freezing them at cryogenic temperatures using liquid nitrogen or liquid ethane (Mourdikoudis and Pallares, 2018).

3.1.2 Production and Interaction of Electrons with specimen

Abbe formulated an equation for the resolving power of the microscope which is limited by diffraction shown in Eq (19) (Abbe, 1881). In this context, d represents resolution, λ is wavelength and NA stands for numerical aperture. NA is determined by the formula nsinα, where n represents the refractive index, and α signifies the collection semi-angle of the lens.

$$d = \lambda / 2n \sin \alpha \approx \lambda / 2N \tag{19}$$

Electrons can be used as a radiation source for materials characterization, with wavelengths in the range of 0.001 to 0.01 nanometres. Thus, the electron microscope possesses a remarkably enhanced resolving capability due to the inherent short wavelength of electrons. To utilize electrons in a microscope, it is necessary to evacuate the entire optical path since electron scattering by gases is considerably higher as compared to photons (Goodhew and Humphreys, 2000).

Electron illumination is generated by an electron gun at the top of the instrument. In a thermionic emitter, a tungsten filament acts as the cathode and a current is passed through the filament which causes heating to ~ 2700 K and generates electrons. Alternatively, the electrons can be produced using strong

electric fields near the filament (field emission), or a combination of both heating and electric fields (Schottky emission). The electrons are emitted from a small region at the tip of the filament and are accelerated towards the anode which is held at a certain accelerating voltage with respect to the cathode filament (Goodhew and Humphreys, 2000). The anode receives the flow of electrons released from the cathode and directs the electron flow towards a column operating under vacuum.

When a high energy beam of electrons hits the surface of a thin sample, various interactions can occur, or various ranges of signals can be produced. These signals are used in electron microscopy generating high-resolution images as well as giving us a lot of information about the specimen chemistry and crystallography. In order to get the best signal out of the specimen, it should be thin and transparent to electrons (< 100 nm) (Microscopy, 2012). The electrons striking the specimen are commonly referred to as the incident beam, while those electrons that are deflected by the specimen are termed scattered beams, also known as diffracted beams. A fraction of the electrons will pass through the sample (transmitted beam), and a fraction is scattered into other directions forming the scattered beam (Figure 28) (Williams and Carter, 2009).Scattering can occur with or without loss of energy. Inelastic scattering is produced when the incident beam interacts with the electrons of the atom or the sample and is deflected away with the loss of a fraction of its energy; the scattered electron beam then has a different energy than the incident beam. Elastic scattering occurs when the electron beam interacts with the electrons of an atom inside the specimen without loss of energy and this is the main contribution to diffraction patterns. (Goodhew and Humphreys, 2000; Sigle, 2005). Both transmitted and scattered electron beams carry topographical and structural information about the specimen.

Scattered electrons that do not deviate far from the incident-electron direction usually attract the most interest in TEM. This is because the TEM is designed to primarily collect these electrons, which provide insight into the specimen's internal structure and chemistry. Other forms of scattering, including electrons that are scattered through large angles (e.g., backscattered electrons) and electrons expelled from the specimen such as low energy secondary electrons,

are of greater interest in SEM, where they respectively provide atomic number contrast and yield surface-sensitive, topographical images (Williams & Carter, 2009).

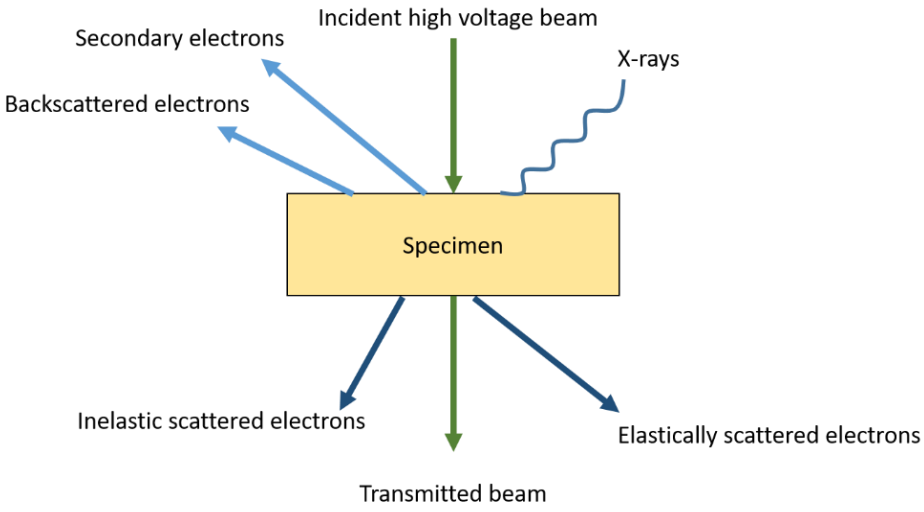

Figure 28 Signals produced when beam of electrons hit the sample (Williams & Carter, 2009).

3.1.3 Scanning electron microscopy (SEM)

SEM is extensively used as a method for imaging the morphology, size, composition, topography, and crystallographic structures of various materials (Ural, 2021). It uses a focused electron beam that is accelerated to energies ranging from 1 keV to 30 keV. Additionally, 2 or 3 condenser lenses are employed to reduce the size of the electron beam before it interacts with the sample (Goodhew and Humphreys, 2000). In SEM, images can be obtained using different detection modes: secondary electron (SE), back-scattered electron (BSE) and energy dispersive x-ray (EDX) spectroscopy (Microscopy, 2012). The secondary electron detector is widely used to analyse particle size, shape and surface morphology. This relies on the detection of low-energy electrons which are produced as the consequence of inelastic scattering interactions between the orbital electrons of the atoms in the specimen and the primary incident electrons. As low-energy electrons are mainly emitted from a few nanometres from the specimen surface, they provide valuable information on surface topography. However, back-scattered imaging relies on the detection of high-energy electrons emitted from below the specimen surface. The signals

are produced as the consequence of elastic interactions with the nuclei of the atoms reflecting the incident electrons from the specimen. The interactions of these primary electrons with heavier elements having higher atomic numbers results in a stronger elastic scatter as compared with light elements, which consequently leads to the projection of brighter areas and hence image contrast (Darwin, 1990). Therefore, back-scattered electron imaging contains valuable information on the composition of the different phases. The intensity of BSE signals is also highly related to the abundance of elements in a specimen. The darker contrast of BSE image indicates a higher electron density region. This allows larger contrast differences between crystals and their background.

The electron beam of the SEM is generated under vacuum, focused to a small diameter, and scanned across the surface of a specimen within the electron column. A specimen chamber is situated in the lower part of the column. The secondary electron detector is located above the sample stage inside the specimen chamber. SEMs are equipped with capabilities to detect both secondary and backscattered electrons, and knowing their location is essential for accurate imaging. Typically, one side of the chamber is designated for the movable X-ray detector, which can be positioned close to the sample during analysis. The energy-dispersive X-ray (EDX) spectrometer uses the X-ray spectrum emitted by a solid sample bombarded with a focused beam of electrons to perform localized chemical analysis and elemental mapping. This allows for both qualitative and quantitative analyses, providing valuable insights (Ural, 2021).

The optimum working resolution of the SEM is determined by the specimen pixel size (p), which relies on the instrument's magnification and the number of points scanned along a line. This resolution is achieved when the diameter of the beam sampling volume does not exceed p, with the size of the sample volume depending on the signal being utilized. Among the signals used, secondary electrons possess the smallest sampling volume, with a diameter slightly larger than the probe diameter. Hence, the ultimate resolution of the SEM is attained when the smallest probe can deliver an adequate signal from the specimen (Goodhew and Humphreys, 2000).

The relative size of the electron probe in relation to the pixel size of the specimen holds significant importance. When the electron probe exceeds the size of the specimen pixel (as shown in Figure 29 on the left), it results in the merging of signals from neighbouring pixels, leading to a degradation in resolution. If the electron probe is smaller in size than the specimen pixel, it will result in a weaker signal (Figure 29 middle). To achieve the best performance from the instrument, it is ideal for the probe diameter to match that of the specimen pixel (as shown in Figure 29 on the right) (Goodhew and Humphreys, 2000).

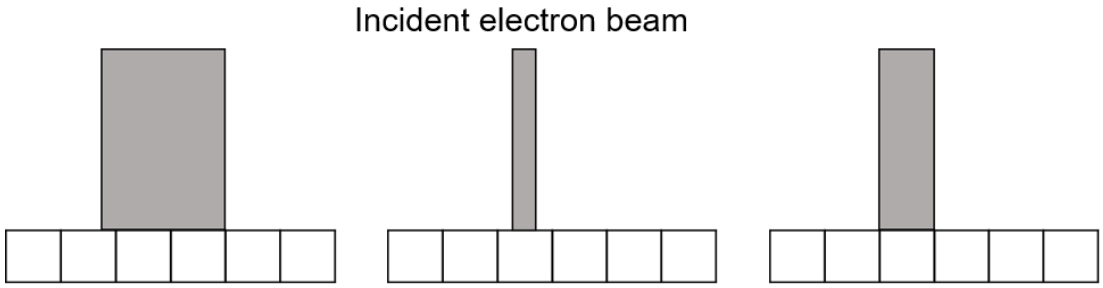

Figure 29 the correlation between the electron beam diameter and the size of the specimen pixels. Reproduced from (Goodhew and Humphreys, 2000)**.**

3.1.4 Transmission electron microscopy (TEM)

3.1.4.1 Principles of TEM

TEM is a widely utilized technique for characterizing the morphology, crystalline structure, and chemical composition of particles at high resolution (Tang and Yang, 2017). TEM serves as a powerful tool for visualizing materials at the nanometre scale, where a high-energy (~100-300 keV) electron beam is directed through a sample. The transmitted electrons are then detected and analysed to generate an image or a diffraction pattern.

The electron beam is guided along the column of the microscope by a series of apertures and electromagnetic lenses. The condenser aperture reduces aberrations and gathers a fraction of the electron beams, and a condenser lens system focuses them onto the specimen. These electromagnetic lenses shape the electron beam which travels in a spiral trajectory. The primary function of the lens involves two main aspects: 1) Gathering all rays originating from an object point and reconstructing a corresponding point in an image. 2)

Converging parallel rays onto a specific point within the lens's focal plane (Williams & Carter, 2009).

TEM images are 2-dimensional projections of a thin sample created by elastically scattered electrons (Brydson et al., 2014) .A conventional TEM image is produced by electrons that pass through the specimen and are collected by an objective lens and an objective aperture located in the back focal plane of the objective lens, and the transmitted portion is then magnified and projected onto an imaging screen. The final image can only be generated by the electrons that pass through the objective aperture not the electrons that stopped by the objective aperture. Therefore, the size and position of objective aperture are important for image contrast (Goodhew and Humphreys, 2000). If the objective aperture is placed on-axis, this is known as bright field imaging. If the aperture collects off-axis electrons then this is dark filed imaging,

There are three major contrast mechanisms contributing to TEM imaging:

1. Mass thickness contrast. The thickness and density of the specimen will affect the image contrast by affecting the angle of electron scattering. For a thicker sample or higher density regions, more scattering will take place through high angles and consequently only small fraction of the electrons will pass through the objective aperture and the image will appear darker. In a thin region only, a few electrons are scattered and the rest of incident electrons remain un-deflected which is why the sample appear brighter (Goodhew and Humphreys, 2000). This is also somewhat dependent on the average atomic number Z of the sample region.

2. Diffraction contrast. An additional contrast mechanism occurs if the sample is crystalline. Coherent elastic scattering from the crystal lattice leads to diffracted beams where the intensity of scattered electrons is very much greater at specific orientations within the crystalline structure. Insertion of an objective aperture allows either the un-deflected beam or a particular diffracted beam to form an image which gives rise to a strong contrast from the areas which are diffracting strongly (Goodhew and Humphreys, 2000).

3. Phase contrast. Phase contrast occurs when a number of different diffracted beams pass through the objective aperture, and this results in an interference

pattern (noticeable at high magnification) which is an indirect representation of the projected crystal lattice.

In contrast to traditional parallel illumination TEM, scanning transmission electron microscopy (STEM) employs a fine electron probe that is scanned across the thin sample, and the magnitude of the transmitted electron signal is quantified through the utilization of one or multiple electron detectors. Various signals can be concurrently measured at each point of the scan. The predominant mode is annular dark field (ADF), where an annular detector captures electrons scattered by the sample at specific angles. This yields a strong signal when electrons scatter from a material's atoms and a weak signal when the beam traverses directly through, i.e., between the atoms. This straightforward interpretation of images, coupled with the capability to simultaneously capture multiple signals (e.g., X-ray spectroscopy), has established ADF STEM as a widely used and standard technique (Peters et al., 2023). In a TEM/STEM microscope, the STEM objective aperture, which forms the probe, is typically identical to the condenser aperture used in TEM mode. The distinction between the two setups lies in the imaging process: in TEM, all pixels in the image are acquired simultaneously in parallel, whereas in STEM, they are obtained one at a time through the scanning of the probe Figure 30 (Pennycook et al., 2007).

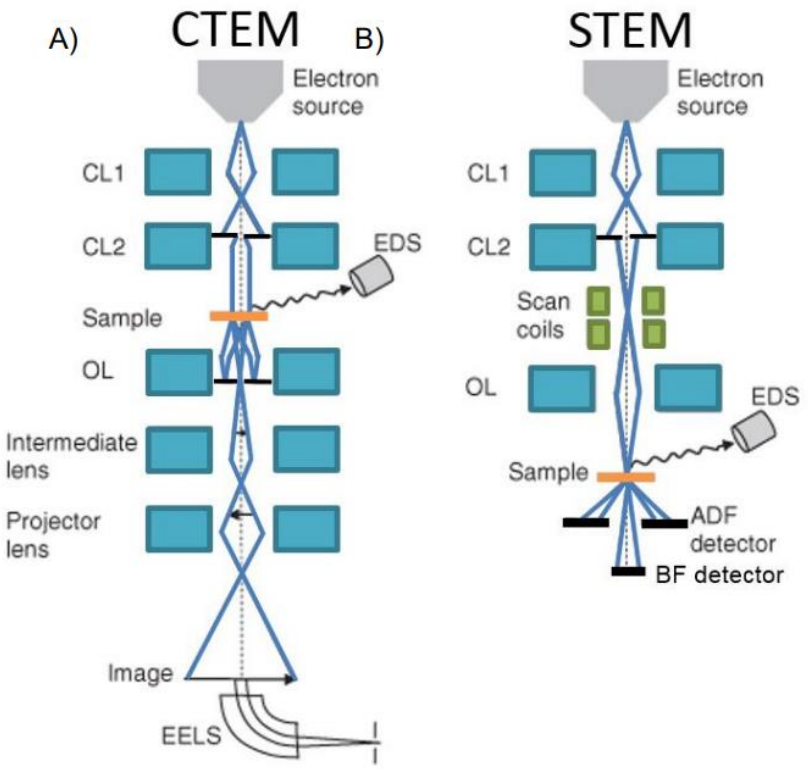

Figure 30 Schematic representation of (A) CTEM and (B) STEM instruments, where the blue line signifies the path of electrons. CL represents the condenser lens, and OL represents the objective lens (William and Hooley, 2019)**.**

3.1.4.2 Lenses

There are limitations associated with electromagnetic lenses that restrict the resolution of the TEM, namely spherical and chromatic aberration, as depicted in Figure 31 (Rose and Wan, 2005). Spherical aberration occurs when lenses are unable to focus all incoming parallel electron waves to a single point. Instead of converging to a precise focal point, the rays converge at different points away from the central region of the optical axis, leading to a blurred or distorted image. Chromatic aberration becomes evident when electrons pass through objects and undergo a loss of velocity. The spatial location of the image is influenced by the accelerating potential (V). Consequently, any deviation in voltage (ΔV) would naturally lead to image blurring. This voltage variation, which is essentially a change in electron velocity, can arise from fluctuations in power sources as well as from the initial voltage or velocity distribution of the emitted electrons (Liu et al., 1944).

The electrons' wavelength is approximately 2.5 picometers (pm) when an acceleration voltage of 200 kV is applied. However, when lens aberrations are included, this results in a resolution limit of around 0.25 (nm), which is insufficient for distinguishing individual atoms in non-periodic objects. Since it is not feasible to significantly increase the acceleration voltage, the focus must shift towards eliminating or effectively reducing spherical and chromatic aberrations. Spherical aberrations can be corrected by additional lenses, known as an aberration corrector (Rose and Wan, 2005) . In addition, one can significantly mitigate chromatic aberration through two methods: (a) using a monochromator to narrow the energy spread of the incident electron beam (e.g. 0.1 eV) and (b) introducing an imaging energy filter positioned between the object and image plane. This filter selectively eliminates inelastically scattered electrons without altering the trajectory of the zero-loss electrons responsible for forming the image (Rose and Wan, 2005).

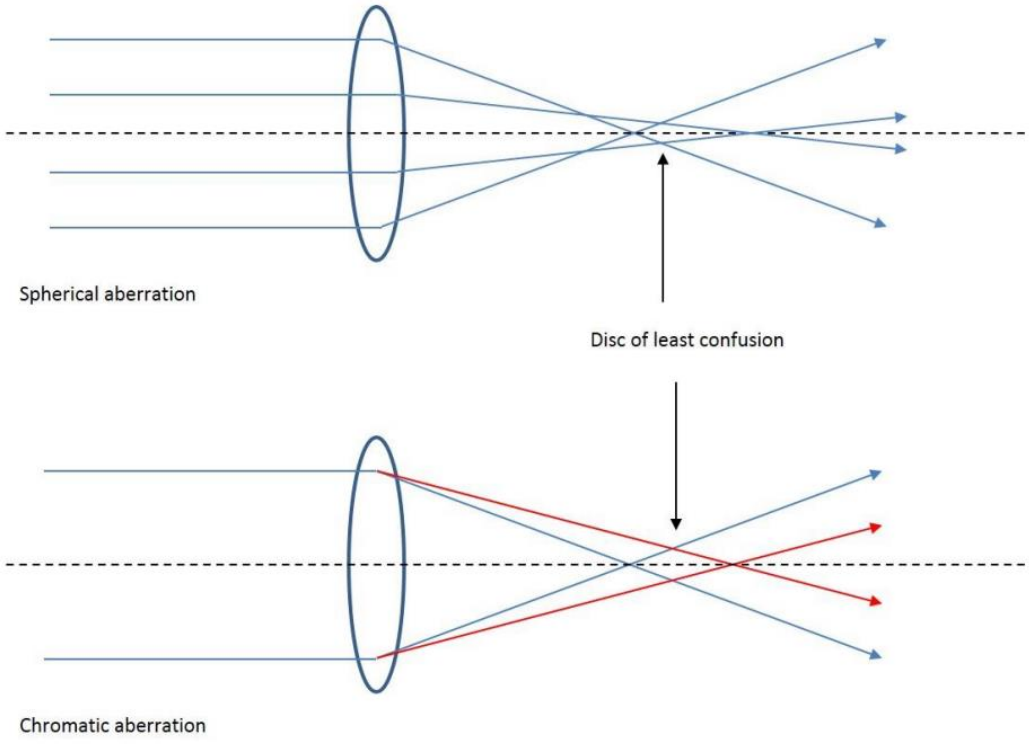

Figure 31 Spherical aberrations (depicted at the top) result in greater bending of electron waves toward the outer edges of the lens. Chromatic aberrations (shown at the bottom) are associated with variations in electron bending caused by differences in energy, with lower-energy electrons experiencing more pronounced bending. Adapted from (Ilett, 2020)**.**

3.1.4.3 Selected area electron diffraction (SAED)

SAED is a TEM technique which can be used to generate diffraction patterns which reflect information about the crystallinity of materials, e.g., whether they are amorphous, crystalline, or polycrystalline. When parallel beam of incident electrons hit the thin crystalline specimen, some of the electrons travel through the specimen and other electrons are diffracted through an angle 2Ɵ by the *d*-spacing of crystal lattice (Goodhew and Humphreys, 2000). For an isolated single crystal, the scattered electrons appear as series of sharp dots around the brightest spot at the centre of diffraction pattern (Lin, 2015). Conversely polycrystalline materials show ring patterns and when the sample is amorphous, diffuse rings are observed. Figure 32 (A-C) shows the diffraction patterns of amorphous, polycrystalline (vaterite) and single crystal (calcite) $CaCO_3$, respectively.

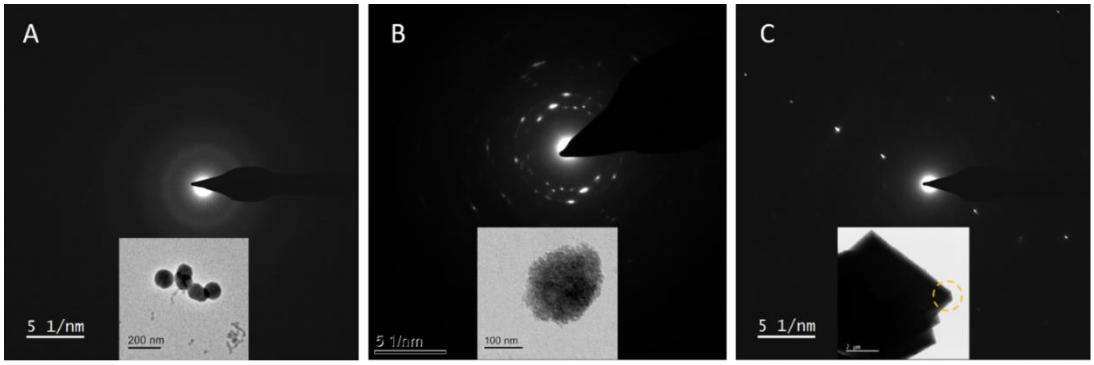

Figure 32 Diffraction patterns of amorphous, polycrystalline (vaterite), and single crystal (calcite) $CaCO_3$, respectively.

3.1.4.4 Energy dispersive X-ray (EDX) spectroscopy:

In EDX technique, the atoms of the specimen are bombarded by high-energy electrons, leading to the ejection of inner-shell electrons of the atoms, which are then replaced by the outer-shell electrons. This electron replacement between the shells having different energy levels, results in the emission of X-ray photons. The energies of the emitted X-rays are unique to the elements which generate them, allowing the elemental analysis of materials (Scoutaris et al., 2014). Transmission electron microscopy (TEM) in conjunction with energy dispersive x-ray spectroscopy (EDX) is an ideal analytical technique to characterize the composition of small particles, as the thickness of the TEM sample is generally small (typically a few hundred nanometres) leading to much less beam

broadening relative to EDX in the SEM where the resolution of the X-ray signal is typically micrometres.

3.1.4.5 Effect of the electron beam on the sample

Inelastic processes and very high-angle elastic scattering can cause damage to the samples, which is a significant concern in electron microscopy when compared to light microscopy. There are two main types of damage:

1) Knock on displacement damage is where lattice atoms are physically displaced from their original position which then leads to mass reduction from the sample (Gu et al., 2017). To avoid radiation-induced damage, it is necessary to maintain the electron energy below the threshold at which atoms can be displaced, which typically falls within the range of 100 to 300 keV for most materials (Rose and Wan, 2005). For example, for carbon the electron beam energy has to be higher than 80keV for that to occur (Terrones, 2010).

2) Ionization arises from ejection of secondary electrons from the sample which can cause breakage of chemical bonds leading to the creation of reactive species which can break up the structure, this is called radiolysis or ionization damage (Chen and Wang, 2019). In addition, charging and heating due to the electron beam bombardment can cause a serious damage such as cracks or holes on the surface or inside the specimen (Liu et al., 1994). This is also dependant on the area of illumination. If the illuminated area is small, heat can escape easily, however, for larger areas this can get trapped which can cause damage to the sample.

To minimize electron beam damage, it is necessary to monitor either the specimen's morphology, its diffraction pattern, or its chemical composition over time. This monitoring helps ascertain if there are any changes in the material, such as a transition from an amorphous state to a crystalline structure and reverse. In general, all materials have a threshold for damage, often known as a critical fluence (electrons per unit area), which tends to be a problem at higher magnifications. Electron fluence can be calculated by the below Eq.20:

$$F(e\text{^}-/\text{Å}\text{^}2) = J \times (t\_(0) + t) \quad (20)$$

Where, J is electron flux (in units of $e\text{^}-/(\text{Å}\text{^}2\ s)$) , t_0 is the time between the area first being exposed on the electron beam and the time taken to record the first data, e.g., diffraction pattern, and t is the acquisition time of the subsequent diffraction pattern. Hooly et.al., (2019) studied electron fluence thresholds for the degradation of calcite nanoparticles under electron irradiation, employing both conventional and scanning transmission electron microscopy (CTEM and STEM). The research, conducted at accelerating voltages of 80 kV and 300 kV, utilized time-resolved phase contrast imaging and EDX spectroscopy. The findings revealed a degradation pathway involving the disruption of the crystal lattice, leading to the formation of pores and transformation into calcium oxide and carbon dioxide. The type of calcium oxide formed (amorphous or crystalline) depends on the irradiation conditions, with hydrocarbon contamination hindering crystalline formation in STEM. At 300 kV, the characteristic lifetime of the calcite lattice is extended, albeit with reduced image contrast and EDX signal. STEM, particularly in the presence of hydrocarbon contamination, increases the fluence threshold for detecting irradiation-induced faults in the calcite lattice. This research lays the foundation for the reliable identification of crystallinity in nominally amorphous nanoscale calcium carbonate particles. It was found that operating at 80 kV did not provide any advantages over operating at 300 kV for phase contrast imaging of calcite nanoparticles. Additionally, there were no benefits observed for energy-dispersive X-ray spectroscopy (EDX), and in fact, the characteristic fluence for mass loss decreased from 1.9×10^7 e^- nm^{2-} at 300 kV to 7.9×10^6 10^7 e^- nm^{2-} at 80 kV operation. In other words, the 300 kV operation was more effective for EDX spectroscopy in this context. For the case of calcite nano particles, it was shown that using 300 kV STEM provides substantial advantages compared to CTEM. This is crucial for fundamental studies of crystallization and process control in synthesizing surfactant-stabilized nanoparticles, particularly for applications like fuel detergents (Hooley et al., 2019).

3.1.5 Cryo-TEM

Prior to development of liquid cell TEM, cryo-TEM has been used as a powerful technique to study a sample of interest in an aqueous environment under cryogenic temperature. Compared to conventional TEM analysis where samples are observed under vacuum, cryo-TEM allows samples to be observed in their native and hydrated state embedded in a layer of rapidly frozen vitreous ice. Upon plunge-freezing of a liquid specimen, all processes are arrested, and the sample becomes immobilised in a fixed state. This includes diffusion-limited damage of the sample caused by radiolysis products generated within the vitreous ice (Ilett et al., 2019).

Cryo-TEM allows a combination of techniques such as electron diffraction, EDX and EELS to be applied to the sample at the same time. Another advantage of Cryo-TEM is the visualisation of 3-D structure of the embedded object by obtaining rapid and high-resolution snapshots at different viewing angles (electron cryo-tomography). For this purpose, the sample is prepared by depositing a droplet of a solution on a grid followed by blotting to remove excess solvent and form a thin film ~ 100 nm (Figure 33). The grid is then plunged into a cryogenic liquid (liquid ethane with the temperature of – 183 ºC) which causes all the components to become fixed in its hydrated state. This rapid immersion of a small specimen (verification process) into liquid ethane guarantees that the liquid sample is preserved in its natural state, free from any undesired effects like drying artifacts such as the redistribution of materials in the suspending medium (Schultz, 1988).

Cryo-STEM/EDX offers a means to achieve precise spatial resolution of elements within a specimen, enabling the examination of a nanoparticle dispersion in its frozen and hydrated condition. However, it is essential to perform any analysis without causing substantial harm to the vitreous ice. Any melting or devitrification would lead to the unintended displacement of nanoparticles within the sample (Ilett et al., 2019; Martha Ilett et al., 2020; Ilett, 2020). Ilett et al., illustrated the application of analytical scanning transmission electron microscopy (STEM) to investigate nanoparticles enclosed within a layer of vitreous ice. By employing STEM-EDX under cryogenic conditions, they successfully identified and distinguished CeO_2, Fe_2O_3, ZnO, and Ag

nanoparticles in suspension within frozen, hydrated samples. The study revealed that electron beam-induced damage of the ice occurred at significantly higher electron fluences in STEM (< 2000 e−/Å^2) when compared to conventional transmission electron microscopy (CTEM) (< 100 e−/Å^2).

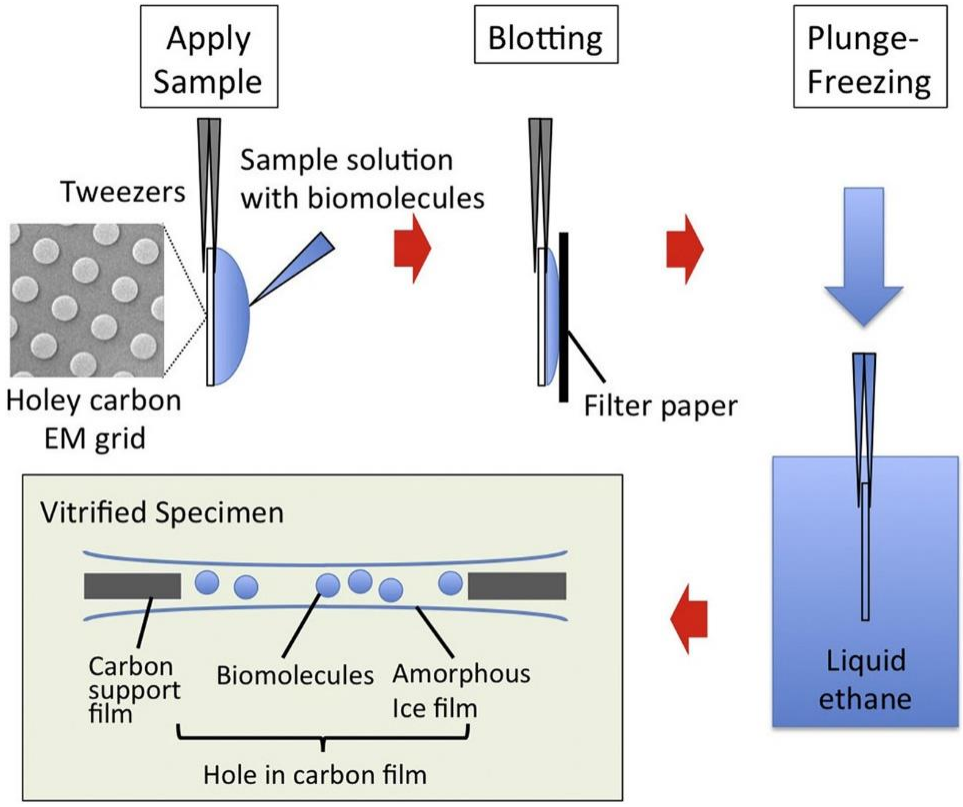

Figure 33 Schematic of sample preparation by plunge-freezing (Murata and Wolf, 2018)**.**

Sample preparation has a significant effect on the final sample observed in the microscope. The Cryo-TEM image of a sample prepared through a plunge freezing process in Figure 34 illustrates how different grid preparation techniques can influence the final sample observed. It also emphasizes that circumstances such as an improper blotting process, inadequate surface hydrophilicity treatment, or poor transfer and handling can significantly impact the results (Grassucci et al., 2007).

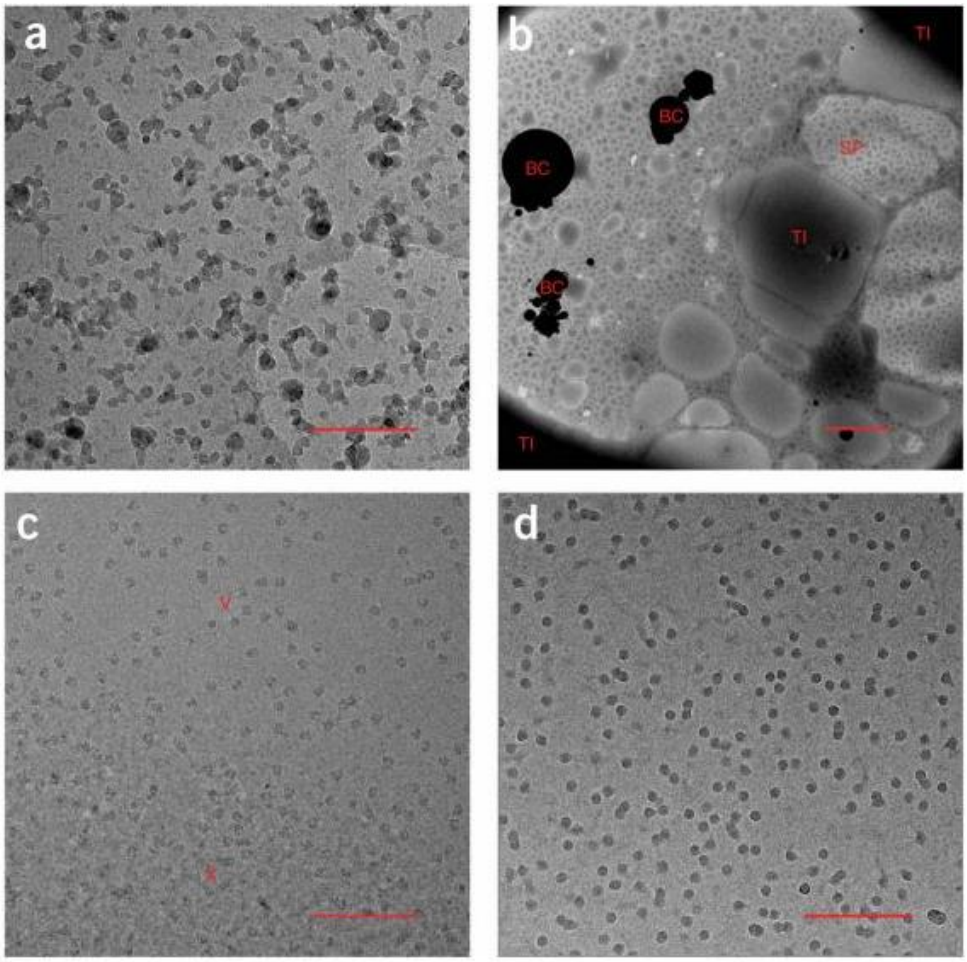

Figure 34 Cryo-TEM Image of a Vitrified Specimen. (a) Reveals ethane contamination on a holey carbon grid. The scale bar represents 250 nm on the object scale. (b) Depicts very thick ice, indicating an insufficient blotting process. BC indicates large ice contaminants that are usually the result of poor handling. SP indicates the uneven ice appearance possibly caused by a hydrophobic grid surface. TI indicates thick ice. The scale bar is 2 µm on the object scale. (c) Exhibits vitreous ice (V) and crystalline ice (X) resulting from improper plunging, along with freeze-dried particles. The scale bar represents 250 nm on the object scale. (d) Freeze-dried particles. The scale bar represents 250 nm on the object scale (Grassucci et al., 2007)**.**

Hondow et al. (2012) suggested an alternative method for analysing samples in their native state which was applied in some of the experiments conducted in this project. This approach involved following the same plunge freezing preparation protocol as described earlier but introduced a warming step under vacuum using a vacuum desiccator after the plunge freezing. This allows imaging of the sample without cooling and use of a cryo-TEM holder. Importantly, this warming step did not affect the original positioning of

nanoparticles within a blotted and frozen dispersion. Consequently, it enabled the imaging of dry samples that remained faithful representations of the nanoparticle dispersion, eliminating the requirement for more intricate in situ TEM techniques.

3.1.6 In situ Liquid Cell (LC-TEM)

As previously mentioned, TEM can only be used to characterise dry solid samples. Recent advancements have given rise to the design of microfluidic liquid cells which allow analysis of a sample within an aqueous environment with nano scale resolution (Schneider et al., 2014). Liquid cell TEM has recently been applied to many areas of research ranging from biology to material science and beyond. The advent of LC-TEM has allowed researchers to study the dynamic mechanisms of nucleation and crystal growth of nanoparticles in a solution and certain biological processes (Martha Ilett et al., 2020). A typical liquid cell consists of two silicon chips between which a liquid cell is sandwiched (Figure 35). The silicon chips are fabricated by etching two thin (typically ~ 30-50 nm) electron-transparent silicon nitride film windows in the centre of a thicker silicon wafer which allows imaging of the flow channel. A spacer layer of a desired thickness creates a gap between the chips and gives a specific thickness for the imaging region. The flow cell device is connected to a syringe which allows for flow of a solution into the liquid cell (Van Driessche et al., 2016).

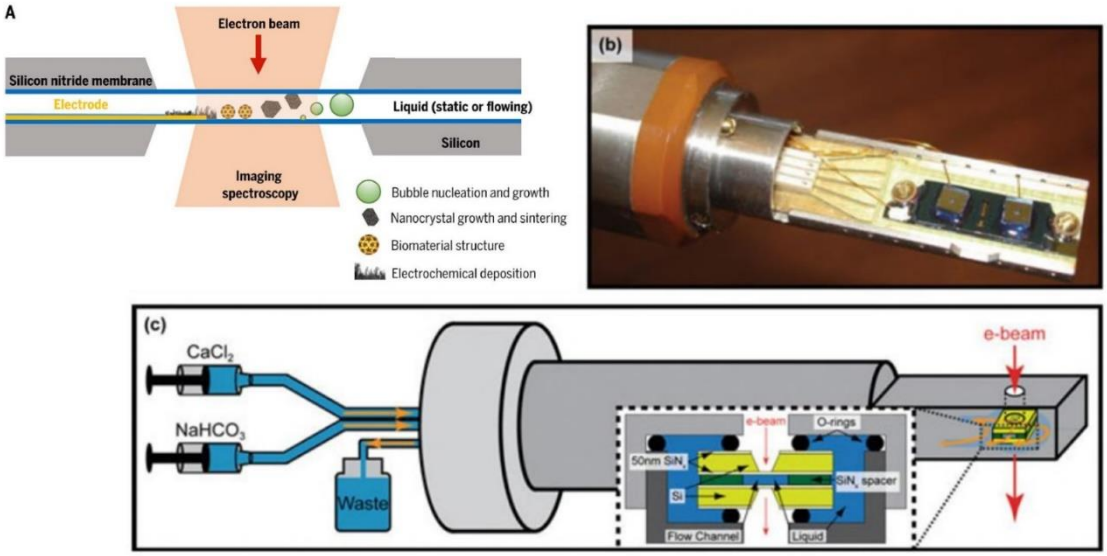

Figure 35 Schematic illustration of the liquid cell holder (Ross, 2015; Van Driessche et al., 2016)**.**

3.1.6.1 The effect of electron beam on LC-TEM

One of the disadvantages associated with LC-TEM is the effect of electron beam. Upon using LC-TEM, there are some factors which influence the quantitative analysis of nanoparticles in a liquid state such as electron beam damage. Radiolytic damage species ($H^{\bullet}$, $OH^{\bullet}$, H^{+}, OH^{-}, H_2O_2, H_2) are formed when incident electrons illuminate an aqueous solution or water. Le Caer separated this process into three primary stages: the physical stage, the physico-chemical stage, and the chemical stage, as shown in Figure 36 (Caër, 2011). Under electron beam irradiation, water molecules undergo instant ionization (H_2O^{+}) and excitation (H_2O^{*}), usually taking place in approximately 1 fs. These reactive radical species have a tendency to react with the sample in the fluid system and generate adverse chemical reactions (Dae et al., 2020). Also, the radiolysis products may change the chemistry of the solution which consequently effects any nucleation and/or crystal growth (Browning et al., 2014). Furthermore, studying the dynamic formation of materials and processes within aqueous systems can negatively impact the image resolution (De Yoreo and Sommerdijk, 2016).

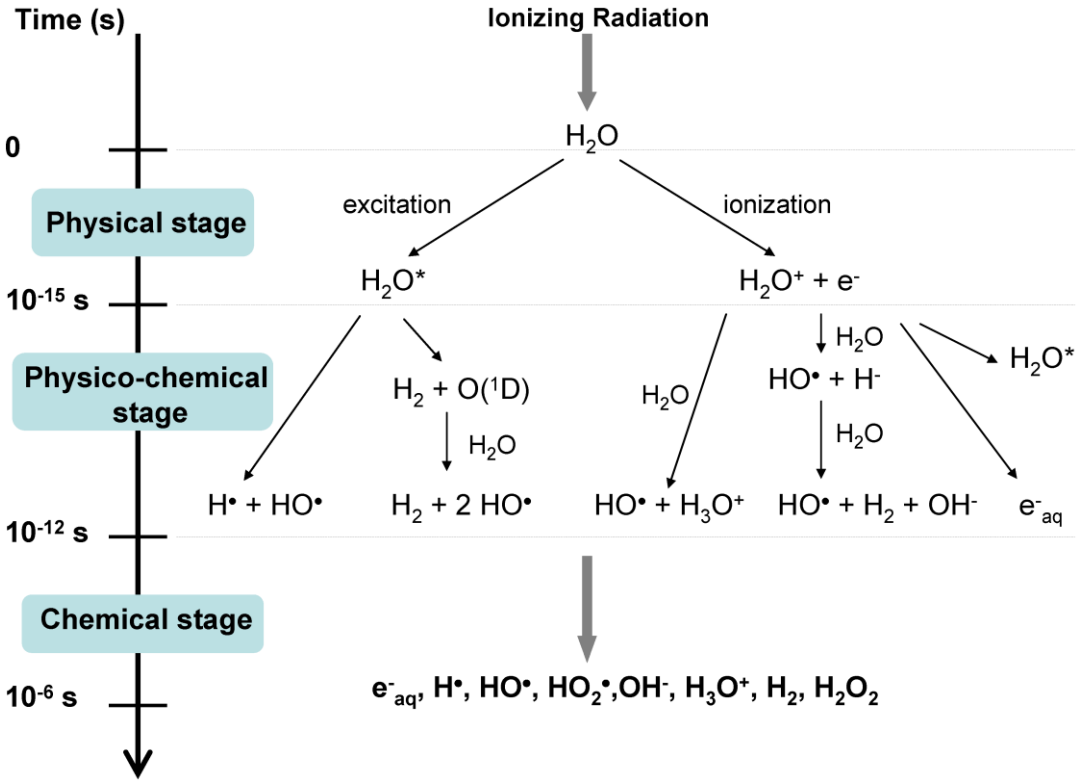

Figure 36 Illustration of the key phases in water radiolysis: The diagram outlines the primary reactions occurring during the three stages of water radiolysis. Upon exposure to beam irradiation, it initiates with the rapid generation of ionized and excited water molecules, commencing the physical stage. Subsequently, these species progress through a series of reactions in the physico-chemical stage, leading to the creation of highly reactive species. These reactive entities can further interact with each other, and any molecules present within vitreous ice or water during the chemical stage (Caër, 2011)**.**

A chemical speciation simulation study was conducted by Schneider, in which deaerated water was exposed to continuous irradiation at a rate of 7.5×10^7 Grays per second (Gy/s) using a 300 keV beam with a radius of 1 µm and a current of 1 nA. Note 1 $e^-/(Å^2\ s)$ is equivalent to between 1.2–3.6 MGy/s when irradiating water in a LCTEM cell at 300 kV. Schneider demonstrated how the concentration of e_h-, H•, H_2, H_2O_2, OH•, and O_2 changed over time as shown in Figure 37. The concentrations of radiolysis products do not increase indefinitely; at some point, these radiolysis products undergo reverse reactions that convert them back into water, ultimately leading to the establishment of a stable equilibrium state (Schneider et al., 2014). The products of radiolysis involve H_3O^+ ions, leading to a change in the solution's pH due to electron beam irradiation. When analysing results from liquid cell experiments, it is crucial to

consider the impact of radiolysis on solution pH. At low dose rates (<10^3 Gy/s), the solution's pH remains largely unaltered by irradiation and is independent of the dose rate. For higher dose rates, the outcome depends on the relative levels of the steady-state H_3O^+ concentration induced by irradiation compared to the initial H_3O^+ concentration in the solution before irradiation. As the dose rate rises, solutions with an initial pH greater than 3 tend to approach a pH value of 3. This phenomenon is particularly noticeable at the dose rates used in electron microscope imaging. Also, alkaline solutions are most strongly affected by radiolysis as shown in Figure 38 (Schneider et al., 2014).

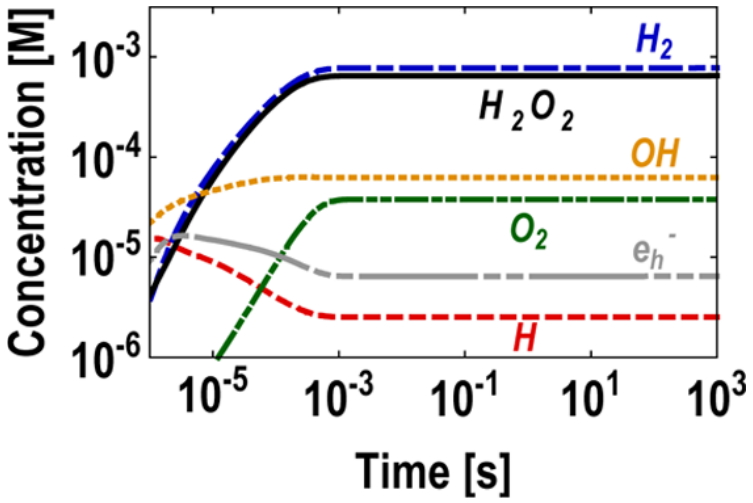

Figure 37 The concentration of eh−, H•, H2, H_2O_2, OH•, and O_2 as a function of time. Reproduced from (Schneider et al., 2014)**.**

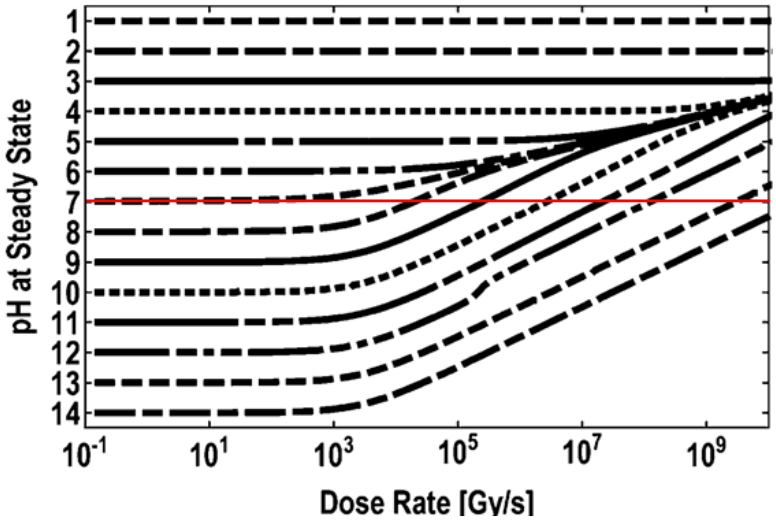

Figure 38 The steady state pH as a function of the dose rate. An increase in the TEM dose rate results in a corresponding change in the pH of the water (Schneider et al., 2014)**.**

3.1.7 PHREEQC Software for Thermodynamic Modelling

PHREEQC (Zhang et al., 2020) enables users to specify thermodynamic data for aqueous species. The software calculates the activity of all potential aqueous species in the solution and assesses the saturation index of solid and gaseous phases. The purpose of these computational calculations is to predict ion speciation, solubility equilibrium and pH calculation in water under thermodynamic equilibrium conditions (Mosley et al., 2015). The results were then compared against the experimental data.

The Davies equation was selected to calculate the activity coefficients of ions in an electrolyte solution and is an extension of the Debye–Hückel equation (this model is adequate at low ionic strength but may break down at high ionic strength) (Parkhurst and Appelo, 1999). The activity coefficient for charged species is calculated using the Davis equation (Eq.21):

$$\log \gamma_i = -Az_i^2 \frac{\sqrt{\mu}}{1+\sqrt{\mu}} - 0.3\mu \qquad (21)$$

Where γ_i is the activity coefficient of species I, z_i is the ionic charge of aqueous species, μ is the ionic strength of species i and A is a constant dependent of temperature (Parkhurst and Appelo, 1999).

The initial PHREEQC database provides information for only a limited number of phases, specifically describing calcite as the sole solid phase for $CaCO_3$. The database underwent modification by the addition of extra aqueous species and solid phases. Hydra/Medusa was employed to identify the phases present in an aqueous system containing Ca^{+2}, CO_3^{-2}, Na^{+}, and Cl^{-} ions, which were subsequently added into the PHREEQC database. Thermodynamic data for these additional phases was primarily sourced from the Wateq4f database, chosen for its compatibility with PHREEQC (Lu et al., 2022). In cases where this was not feasible, thermodynamic data was sourced from empirical studies, with a preference for those studies already included in either database. In the context of the overall crystallization process, gathering thermodynamic data for both hydrated (ACC hydrated) and anhydrous (ACC anhydrous) forms of ACC was deemed essential. The composition and hydration degree of ACC can vary significantly, making it challenging to define. Thermodynamic information for

both hydrated and anhydrous ACC was utilized, considering the distinct enthalpy of formation between the two phases (Radha et al., 2010).

To employ PHREEQC modelling, the initial parameters were derived from the experimental methodology, maintaining the initial concentration of Ca^{+2} and CO_3^{-2} ions at 4.5 mM within a 40 mL water solution, at 25°C, and 1 atm of pressure. CO_3^{-2} ions were introduced gradually through the RACTION command until the molar quantity of CO_3^{-2} ions reached twice the molar quantity of the initial Ca^{+2} ions. The same procedure was replicated with an initial concentration of 4.5 mM of CO_3^{-2} ions. These experiments sought to determine the point at which various $CaCO_3$ polymorphs initiate formation and precipitate from the solution.

3.2 Bulk Material Characterisation

3.2.1 SEM

A Hitachi SU-8230 FEG-SEM was employed to characterise the morphology and size of the $CaCO_3$ particles post-synthesis. Imaging was conducted at 15 kV, utilizing an in-lens secondary electron detector.

3.2.2 TEM, Diffraction and EDX

TEM imaging and diffraction experiments were carried out in using two TEMs: 1) a FEI Tecnai G2 F20 X-TWIN operating at 200 kV, (fitted with a Gatan Orius charge-coupled device (CCD) camera and an Oxford instruments 80 mm2 X – max EDX detector) (Figure 39); and 2) an FEI Titan3 Themis 300: X-FEG operating at 300 kV and fitted with 4 EDX silicon drift detectors, a Gatan One-View CMOS camera and a Gatan quantum ER 965 imaging filter. The Gatan digital micrograph software package was employed to examine diffraction patterns. The analysis involved determining d-spacings by measuring the distance between diffraction spots or the rings. Subsequently, these measurements were halved and converted from 1/nm to angstroms by taking the reciprocal of the distance and multiplying by 10. The resulting spacings were then compared to the known d-spacings of various crystalline calcium carbonate polymorphs. The electron fluence varied between measurements but remained below the damage threshold value reported by Robert Hooley (Hooley et al., 2019). Hooley et al, (2017) conducted a study titled "A Quantitative Evaluation of Electron Beam Sensitivity in Calcite Nanoparticles". In his

research, he proposed that when utilizing 200 kV for bright field imaging, fluences should be kept below 1.9 x 10^6 e^- nm^{-2} (above which pores appear at the edge of calcite) and for diffraction, below 3.9 x 10^6 e^- nm^{-2}. However, at 300 kV, the TEM damage threshold of calcite notably increased from 3.9 x 10^6 e^- nm^{-2} to 5.5 x 10^6 e^- nm^{-2}. This enhancement was attributed to reduced radiolysis damage resulting from a decrease in the inelastic cross-section. Remarkably, STEM imaging at 300 kV could sustain crystallinity and lattice information at higher fluences compared to both 200 kV and 300 kV TEM. Furthermore, no observable degradation into crystalline CaO was observed at STEM fluences up to 1.87 x 10^6 e^- nm^{-2}.

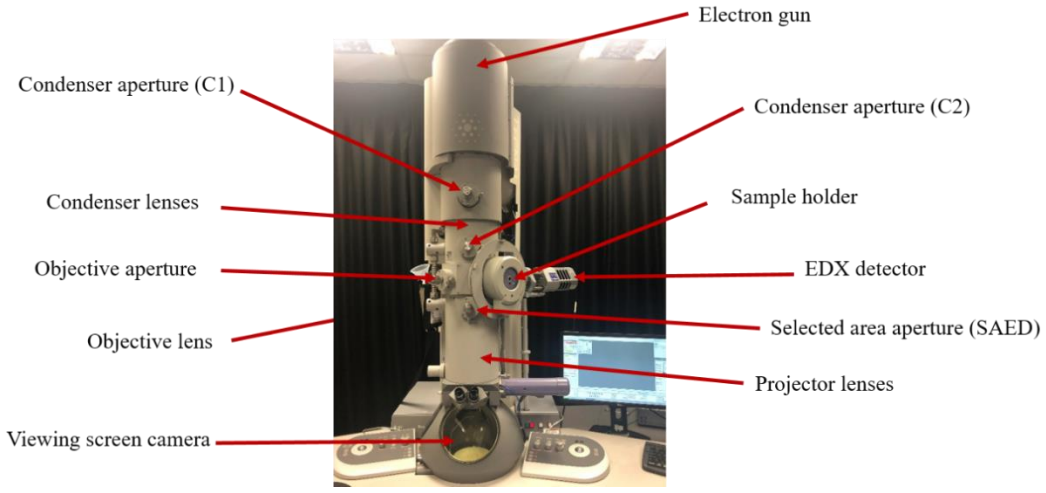

Figure 39 TEM) FEI Tecnai G2 F20 X-Twin (200 KV) at University of Leeds (LEMAS).

3.2.3 Cryo-TEM

Prior to imaging, Quantifoil 300 mesh Cu R2/2 grids were glow-discharged in a Cressington 208 carbon coater with glow discharge unit at 0.1 mbar air, 15 mA for 99 s. A volume of 3 µl of the sample was transferred onto the grid using a FEI Mark IV Vitrobot©. The frozen grids were subsequently transferred to the FEI Titan3 Themis G2 equipped with a monochromator operating at 300 kV. The setup included 4 EDX silicon drift detectors, a Gatan One-View CMOS camera, and a Gatan Quantum ER 965 imaging filter.

3.2.4 Liquid Transmission Electron Microscopy

In situ observation was carried out using FEI Titan3 operating at 300 kV and equipped with a Gatan One-View CMOS camera and a Gatan quantum ER 965 imaging filter. The schematic of the holder and the chips is shown in Figure 40 and 41.

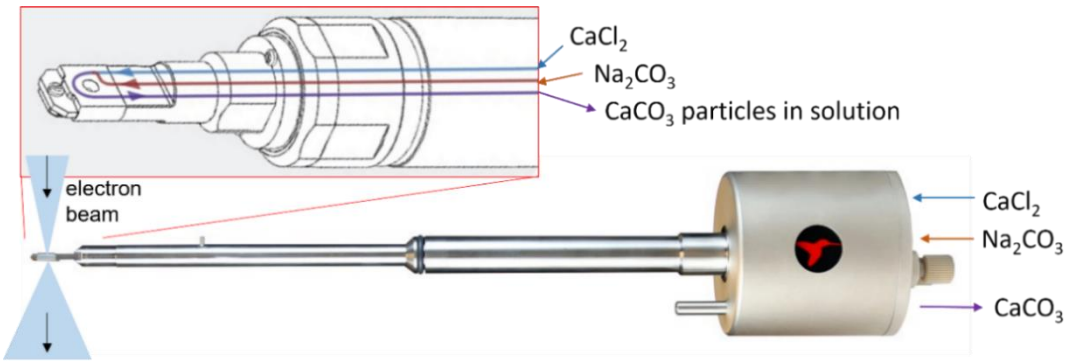

Figure 40 Hummingbird scientific liquid flow TEM holder.

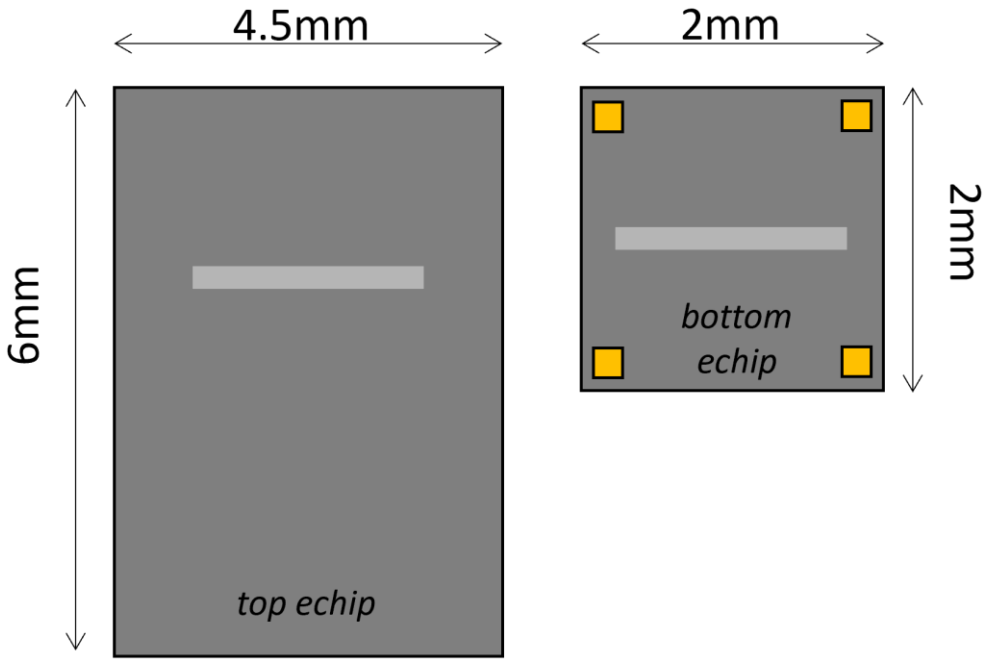

Figure 41 Schematic of the top and bottom chips of the LC used in Lemas with the dimensions of the top chip being 4.5x6 mm and the bottom chip being 2x2 mm. A Gold spacer is utilised, and the window dimension is 50 X 200µm, with a membrane thickness of 50 nm.

3.3 Materials and sample preparation

This section includes detailed procedures for $CaCO_3$ solutions at various concentrations and time points. It also explains how the samples were prepared.

3.3.1 Precipitation of $CaCO_3$ in aqueous solution (equal molar ratio of Ca^{2+} to CO_3^{2-})

3.3.1.1 Sample preparation for SEM and TEM

The crystallisation of $CaCO_3$ was carried out in bulk solution at room temperature. Supersaturated solutions of $CaCO_3$ were prepared by mixing identical molar ratios and volumes (20 mL) of $CaCl_2$ and Na_2CO_3, leading to the final $CaCO_3$ concentrations of 0.5, 1.0, 2.5 and 4.5 mM. Note all these $CaCO_3$ solutions are supersaturated with respect to the solubility of $CaCO_3$, which is 0.013 g/L at 25 º C and equal to 0.13 mM (Rohleder, J.; Kroker, 2001), as the molar mass of $CaCO_3$ is 100.09 g/mol. For sample deposition onto TEM grids (continuous carbon grids), the TEM grids were plasma cleaned for 20 seconds and placed at the bottom of a petri dish, before aqueous solutions of Na_2CO_3 and $CaCl_2$ were added to start the crystallisation. After certain precipitation times (ranging between 15 s and 30 minutes) TEM grids were taken out of the solution and immediately dipped in ethanol to quench the crystallisation process on the TEM grid. The grids were then blotted with filter paper and finally left to dry at room temperature. The presence of ACC and the morphological characteristics of $CaCO_3$ crystalline polymorphs, were analysed using SEM and TEMs. In order to reduce the charging of the samples, all of the SEM samples were coated with a thin layer of iridium prior to SEM analysis, which led to an Iridium signal in EDX from the nanometre-thick coating.

At a concentration of 4.5 mM, the $CaCO_3$ formation using various preparation methods was investigated and the samples were examined using SEM and TEM. These methods include air drying, vacuum filtration, ethanol quenching, plunge freezing, and vacuum drying, as detailed below.

3.3.1.1.1 Samples prepared by air-drying

For the samples prepared using the air-drying method, plasma-cleaned continuous carbon TEM grids were placed in a petri dish and after 5, 15 and 40 minutes, the grids were removed from the crystallising solution, extra water was blotted off by touching the side of the grids on a filter paper and finally dried in ambient air at room temperature (Figure 42).

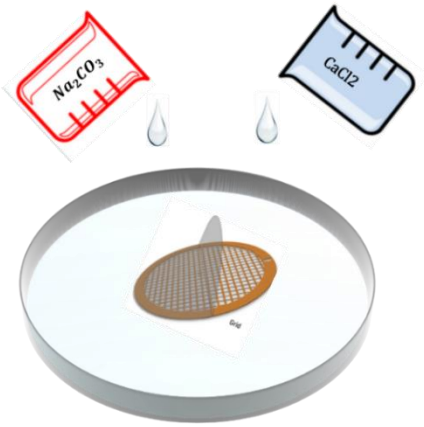

Figure 42 Schematic of the samples prepared by the air-drying method.

3.3.1.1.2 Samples prepared by vacuum filtration

For this technique, the plasma-treated continuous carbon grids were removed from the Petri dish containing crystallisation solution of $CaCO_3$, and then immediately placed on a filter paper in a vacuum- filtration funnel where the drying was carried out under vacuum (Figure 43).

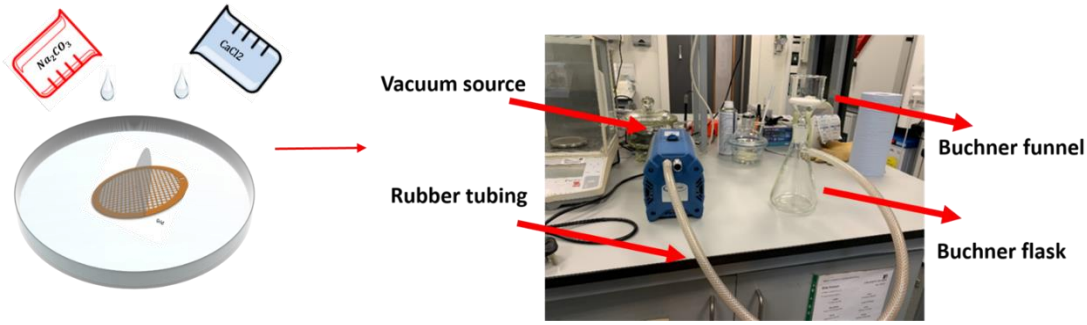

Figure 43 A schematic showing the vacuum-filtration method for preparing samples for imaging analysis.

3.3.1.1.3 Samples prepared by Chemical Quenching in Ethanol

For the ethanol-quenching method, precipitation of $CaCO_3$ in bulk was carried out by placing the plasma-cleaned continuous carbon TEM grids at the bottom of a Petri dish. After a given time point the grids were removed and blotted with a filter paper, then rinsed with ethanol to quench the crystallisation process and finally dried at room temperature (Figure 44).

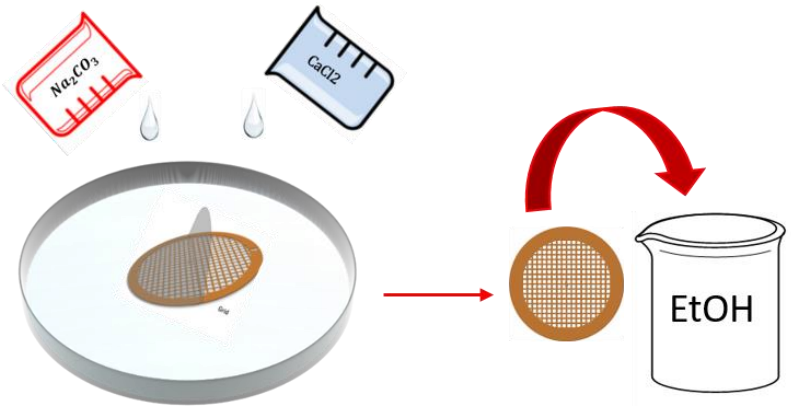

Figure 44 A schematic illustration of samples prepared by ethanol-quenched method.

3.3.1.1.4 Samples prepared by plunge freezing vacuum drying

A $CaCO_3$ solution with a final concentration of 4.5 mM was produced by direct mixing of 9.0 mM $CaCl_2$ and 9.0 mM Na_2CO_3. A 3 µl droplet of the crystallisation solution was transferred onto a plasma-treated continuous TEM grid after set times. It was then blotted for 5 seconds, and the grid was rapidly plunged into liquid ethane using an FEI vitrobot©, which causes the entire specimen to become fixed in its hydrated state with any water rapidly transforming to vitreous ice. Grids were then transferred into a vacuum desiccator overnight where a controlled transition of the vitreous ice from a solid to a gas state (sublimation) occurred as shown in Figure 45 (Hands-portman and Bakker, 2022).

Figure 45 A schematic diagram of samples prepared by the plunge freezing vacuum-drying method.

3.3.1.2 Sample preparation for Cryo-TEM

Supersaturated solutions containing 4.5 and 0.5 mM $CaCO_3$ were prepared through equimolar mixing of $CaCl_2$ and Na_2CO_3 (at 20 mL volumes). The resulting supersaturated solution (a 3 µl droplet of the crystallisation solution) was deposited onto a plasma-treated lacey carbon coated grid or glow discharged Quantifoil TEM grid (EM resolutions) at specific time intervals (4.5 mM: 5 and 40 minutes, and 0.5 mM: 20 and 45 minutes) followed by a 5-second single sided blotting step. The grid was then immediately plunged into liquid ethane (maintained at approximately −180 °C) using an FEI vitrobot©, with 99% humidity (Thompson et al., 2016)©, which causes the entire specimen to become fixed in its hydrated state with any water rapidly transforming to vitreous ice. The vitrified sample was then transferred into a FEI Titan Krios 2 fitted with a direct electron detection (Falcon 4i) camera and was kept at liquid nitrogen temperatures at all times. Upon plunge-freezing of a liquid specimen, all processes are arrested, and the sample becomes immobilised in a fixed state which allows the specimen to be viewed and studied in a layer of vitreous ice.

3.3.1.3 Sample preparation for LC-TEM

LC-TEM involves the use of advanced liquid cell holders, which employ silicon nitride membrane windows to create a sealed environment for the liquid within the TEM. A Hummingbird Scientific liquid flow TEM holder was used for all the experiments. The experimental setup of LC, including the arrangement of components is shown in Figure 46. Additionally, Figure 46 A displays the

sequence of components, while Figures 46 B and 46 C exhibit the LC holder with bottom (2) and top chips (4), respectively.

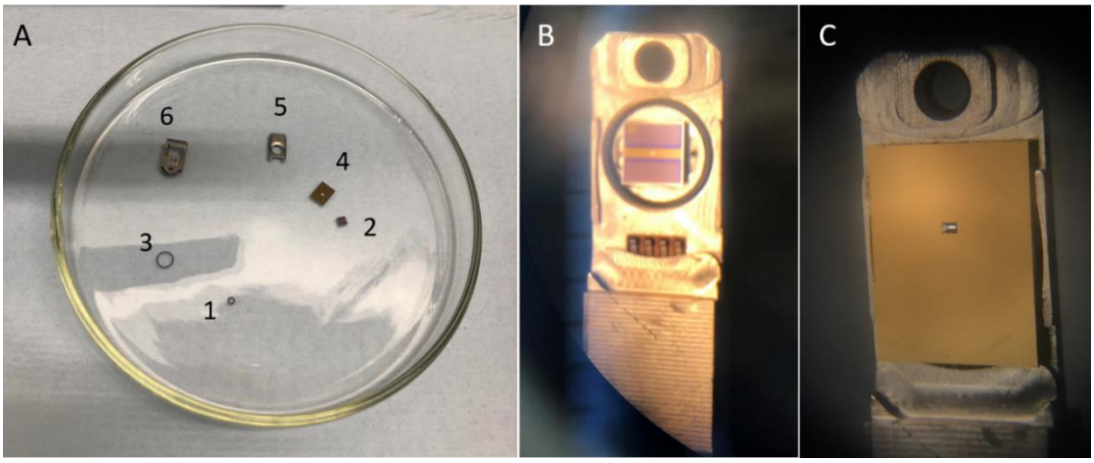

Figure 46 Experimental set-up of a liquid cell holder. A displays the sequence of components, while B and C exhibit the LC holder with small (2) and large chips (4), respectively.

A stock solution comprising equimolar amounts of 9.0 mM $CaCl_2$ and 9.0 mM Na_2CO_3 was prepared to enable real-time observation of the $CaCO_3$ crystallisation process. The $CaCl_2$ and Na_2CO_3 solutions were flowed at a flow rate of 0.5 ml/min through the inlets of liquid cell holder, where the mineralisation process of $CaCO_3$ occurred. As soon as the the reactants were introduced through the inlets, the mineralisation process was probed in real time and images and movies were aquired using FEI Titan3 operating at 300 kV and equipped with a Gatan One-View CMOS camera and a Gatan quantum ER 965 imaging filter. During the crystallisation process, the electron beam was blanked to prevent any changes caused by the prolonged exposure of the electron beam to the sample, and it was then un-blanked after 30 minutes for observation (Tests at 10, 15, 20, and 25 minutes were also conducted, but no observations were made).

3.3.2 Precipitation of $CaCO_3$ in an aqueous solution (unequal molar ratio of Ca^{2+} to CO_3^{2-})

3.3.2.1 Sample preparation for SEM and TEM

Supersaturated solutions of $CaCO_3$ were prepared by mixing $CaCl_2$:Na_2CO_3 in a 1:200 molar ratio, with a volume of 20 ml for each reactant, resulting in final concentrations of 0.5:100 Ca^{2+}: CO_3^{2-} mM. The precipitates of $CaCO_3$ were

collected by placing the plasma- cleaned (20 seconds) continuous carbon grids at the bottom of a petri dish. Aqueous solutions of Na_2CO_3 and $CaCl_2$ were then added to start the crystallisation. After precipitation times of 10, 20 and 30 minutes, the TEM grids were then immediately rinsed with ethanol to quench the crystallisation reaction on the TEM grid. For characterisation, samples were imaged using bright field TEM and SEM. In the solution with concentrations of 0.5:100 Ca^{2+}: CO_3^{2-} mM, the presence of an excess amount of carbonate prevented observation of the early stages of aragonite formation. This was due to the precipitation of an excess sodium carbonate salt on the TEM grid. Therefore, the solution was subjected to centrifugation (at 8000 rpm for 5 min) using a mixture of ethanol and water in a 50%:50% ratio to improve the solution clarity. The reason for centrifuging the carbonate-rich system with a water-ethanol mixture is because sodium carbonate salt is soluble in water and ethanol can slow down any further crystallisation process when we centrifuge, the precipitates will settle at the bottom of the tube, while the supernatant will be separated. The centrifugation process was performed twice, and each time the top layer was carefully removed. This step aimed to dissolve and remove any remaining carbonate salt. Subsequently, a single drop of the resulting solution was transferred onto a plasma-cleaned continuous carbon grid and allowed to dry for 20 and 25 minutes for both TEM and SEM analysis.

Additionally, to confirm quantitatively that the morphology corresponds to aragonite, electron diffraction analysis was performed on the needle-like structure of the aragonite crystals.

3.3.2.2 Sample preparation for Cryo-TEM study:

$CaCl_2$ and Na_2CO_3 solutions were prepared at concentration of 1 mM and 200 mM respectively. Then Na_2CO_3 and $CaCl_2$ solutions were mixed to initiate the crystallisation reaction and centrifuged for 10 minutes at 6000 rpm. At specific time intervals (20 and 25 minutes) a 3 µl droplet of the solution was deposited onto either a Quantifoil or lacey carbon coated grid (EM resolutions) which had been either plasma cleaned for 20 seconds, or glow discharged prior to use. The samples were immediately vitrified by plunging them into a cryogenic liquid (liquid ethane) at a temperature of -183 ºC using a Vitrobot. This process resulted in all the components becoming fixed in their hydrated state. The

prepared grids were then transferred into the TEM for characterisation using a cryo-TEM holder.

3.3.2.3 Sample preparation of calcium-rich solutions

For comparison with the carbonate-rich system, supersaturated solutions of $CaCO_3$ were prepared by mixing $CaCl_2$:Na_2CO_3 in a 200:1 molar ratio, with a volume of 20 ml for each reactant, resulting in final concentrations of 100: 0.5 Ca^{2+}: CO_3^{2-} mM. The precipitates of $CaCO_3$ were collected by dipping the plasma- cleaned (20 seconds duration) continuous carbon grids into the crystallisation solution. After precipitation time of 20 minutes, the TEM grids were then immediately rinsed with ethanol to quench the crystallisation reaction on the TEM grid.

3.3.3 Precipitation of $CaCO_3$ in the presence of Mg^{2+} using Ammonium diffusion method (ADM)

A solution containing 400 mM $MgCl_2$ and 100 mM $CaCl_2$ was prepared in the presence of ammonium carbonate ($(NH_4)_2CO_3$) (Ihli et al., 2013). The precipitation process took place in a multi-well plate, with silicon substrates positioned at the bottom of the wells (Figure 47). The plate was then covered with a gas permeable PDMS thin film. Precipitation of $CaCO_3$ occurs when ammonium carbonate diffuses into the well plate and initiates precipitation of $CaCO_3$ on the surface of the silicon wafer. After specific time intervals of 30 minutes, 1 hour, and 3 hours, the silicon wafer was removed from the solution, washed twice with ethanol, and allowed to dry before being subjected to SEM analysis. For TEM analysis under the same conditions, a gold quantifoil grid was used. Prior to use, the grids were plasma cleaned.

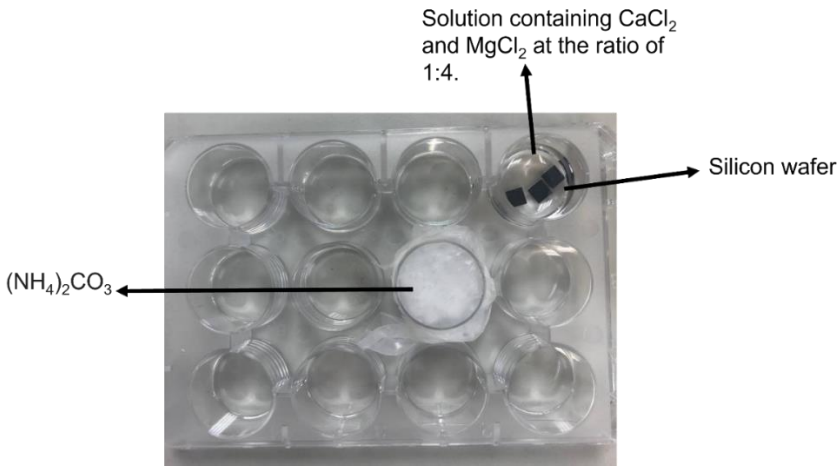

Figure 47 Schematic of experimental preparation of $CaCO_3$ using ADM method.

Chapter 4 Results

4.1 Studying the crystallisation of $CaCO_3$ in equimolar aqueous solutions of $CaCl_2$ to Na_2CO_3 as a function of time

This chapter deals with the early stages of crystallisation of $CaCO_3$ in bulk solution. For this purpose, $CaCO_3$ crystallisation was monitored in solutions with low super-saturations (so as to lower the driving force for crystallisation and so slow the kinetics of the process) and at different time points. Final $CaCO_3$ concentrations were chosen to be 0.5, 1.0, 2.5 and 4.5 mM with an equal concentration ratio of $CaCl_2$:Na_2CO_3. The morphology and size of the crystals were studied as a function of reaction time and degree of supersaturation, using SEM, TEM, and Cryo-TEM. EDX and selected area electron diffraction (SAED) were used to confirm the presence of CaCO3 and determine the respective polymorphs. SAED analysis to differentiate the morphology of ACC, vaterite, and calcite has not been included in all the images, as the shapes of the crystals are already apparent. A comprehensive investigation on this matter has been conducted in literature and also it is detailed in section 2.2.1.

Most previous studies have investigated the crystallisation of $CaCO_3$ at higher supersaturated solutions, (Jessica M Walker et al., 2017; Michael H.Nielsen, Shaaul Aloni, 2014; Shaw and Liane G Benning, 2011) while lower degrees of supersaturation have not received significant attention. Wang et al., (2017) investigated the precipitation of $CaCO_3$ in a dilute system, similar to the concentrations examined in our study (solutions of concentrations $[Ca^{2+}] = [CO_3^{2-}]$ = 0.5, 1.0, 1.5, 2.5, and 4.5 mM). They examined and compared the formation of precipitates and their pathways in both bulk and confined volumes using SEM and TEM.

ACC is an unstable phase (Chen et al., 2013), which has been suggested to be a precursor to all $CaCO_3$ crystalline phases (Cavanaugh et al., 2019; Addadi et al., 2003). ACC particles precipitate from the solution and rapidly convert to crystalline phases. This short lifetime of ACC particles causes difficulties for the visualisation of the early stages of the crystallisation. There is scientific evidence showing that two different ACC phases exist, a more stable phase (ACC I or proto-calcite) and a less stable phase (ACC II or proto-vaterite)

(Gebauer et al., 2010; Gebauer et al., 2008). However, despite extensive research on $CaCO_3$ nucleation and transformation of ACC to crystalline phases, *e.g*., vaterite, aragonite and calcite, the mechanism by which ACC is formed and transformed to their crystalline products, is still under debate. Transformation of ACC particles to the crystalline phases is highly dependent on the solution concentration and whether the reaction occurs in bulk or confined volumes (Cavanaugh et al., 2019). Therefore, this study is focused on the lower supersaturated solutions of $CaCO_3$ which allows easier monitoring of the early stages of the crystallisation in bulk solutions.

4.2 Methodology

4.2.1 Sample preparation

The crystallisation of $CaCO_3$ was carried out in bulk solutions at room temperature. Supersaturated solutions of $CaCO_3$ were prepared by mixing equimolar ratios and volumes (20 mL) of $CaCl_2$ and Na_2CO_3, leading to final $CaCO_3$ concentrations of 0.5, 1.0, 2.5 and 4.5 mM (full detail in section 3.3.1.1)

4.3 Results

4.3.1 Characterisation of 0.5 mM $CaCO_3$ solutions using SEM and TEM

SEM, TEM, EDX and SAED were used to study the emergent structures at the lowest supersaturation level (0.5 mM) in bulk solution. Precipitation of $CaCO_3$ at the concentration of 0.5 mM led to the formation of diffuse regions of higher contrast with an average size of 500 nm after 5 minutes of the reaction as shown in Figure 48 A-D. The amorphous nature of this region was confirmed by electron diffraction, and the EDX spectrum further validates the presence of calcium, carbon, and oxygen in this area respectively as depicted in Figure 48 E and F. There was no evidence of spherical ACC particle formation at the reaction time of 5 minutes. Nonetheless, a single small calcite particle was observed, possibly resulting from heterogeneous nucleation triggered by the presence of impurities within the system.

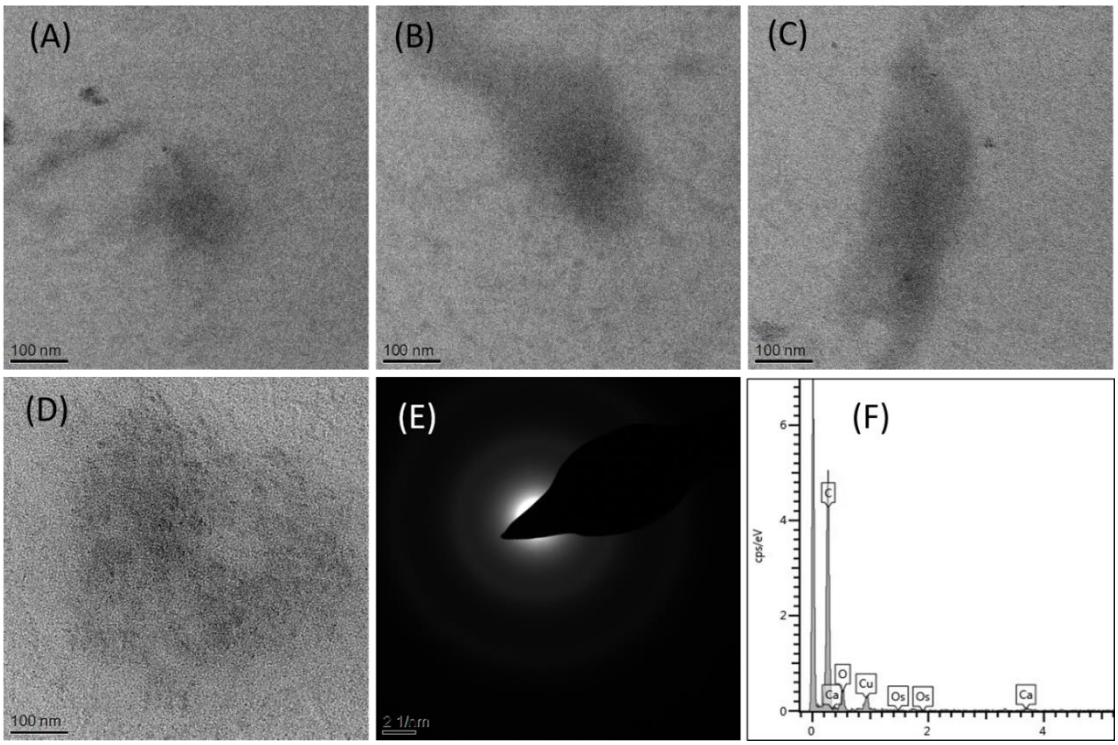

Figure 48 TEM images displaying diffuse regions of higher contrast at the concentration of 0.5 mM after 5 minutes of the reaction (A-D). (E) Electron diffraction of region depicted in D reveals its amorphous nature, and EDX analysis confirms the presence of elemental composition including calcium, carbon, and oxygen. Cupper (Cu) is originated from the grid and osmium (OS) is randomly assigned due to software issue.

TEM and SEM analysis showed that at the concentration of 0.5 mM and after 20 minutes of the reaction, diffuse region of higher contrast on the order of 2.5 µm was observed, as shown in Figure 49 A. Additionally, the formation of spherical ACC particles with sizes ranging from ~5 to 30 nm (Figure 50 A and B) was observed at this time point. However, no crystalline structures were found at this time point. After 30 minutes of the reaction, TEM analysis revealed the presence of diffuse regions of higher contrast, measuring approximately 350 nm in diameter, on the carbon support film, as shown in Figure 51. Additionally, at the 30-minute time point, SEM analysis showed the formation of spherical ACC particles with sizes ranging from ~5 to 25 nm. This was accompanied by the formation of crystalline structures of $CaCO_3$: hexagonal vaterite and rhombohedral calcite (Figure 52 A and B). TEM observations revealed that the disordered diffuse structures were observed only at the lowest concentration of 0.5 mM, which was captured during the quenching and drying method. The

Gray value of these structures, indicating the difference in intensity between the diffuse region of higher contrast and the background ice, was measured (yellow box in Figure 49 A and 51 A).

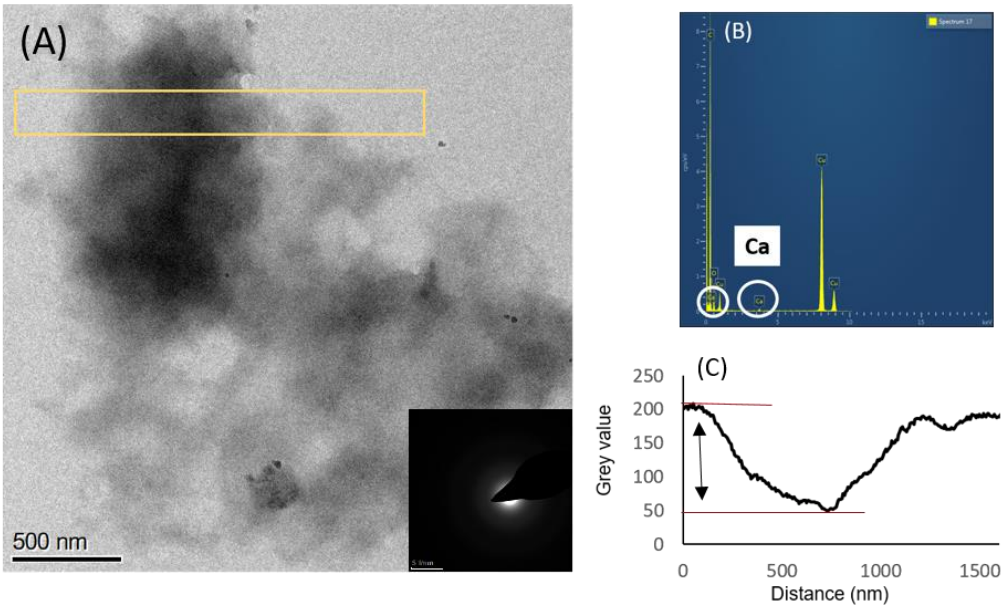

Figure 49 TEM analysis showing: (A) a diffuse region of higher contrast at the concentration of 0.5 mM after 20 min with corresponding diffraction pattern (inset) confirming the amorphous nature of this structure; and (B) EDX conducted in the dense region confirming the presence of calcium, oxygen and carbon. (C) Gray values of diffuse region in A obtained from area in yellow box.

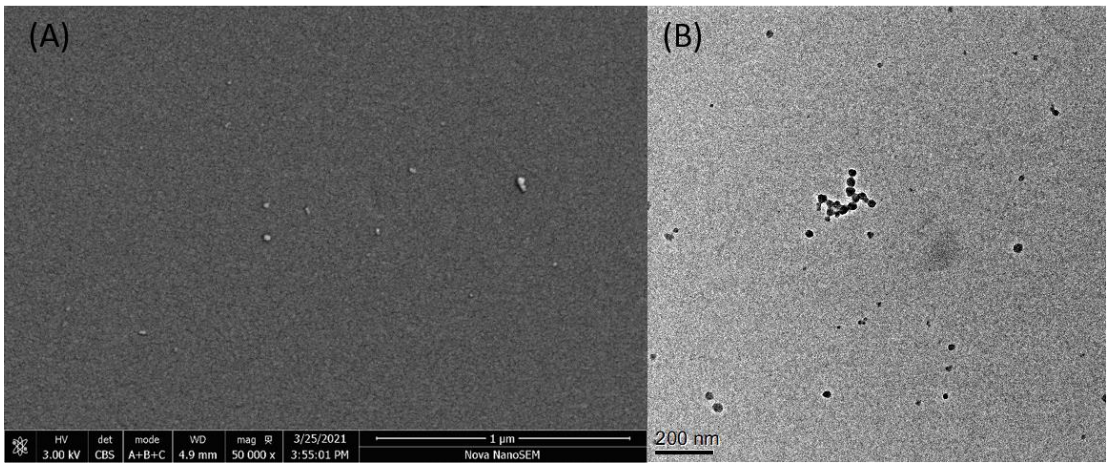

Figure 50 SEM images of $CaCO_3$ particles obtained from the lowest concentration of 0.5 mM in bulk: (A) showing spherical ACC particles after 20 min; (B) TEM image of ACC particles after 20 minutes. No presence of crystalline structures was detected. Both images are taken from the same grid.

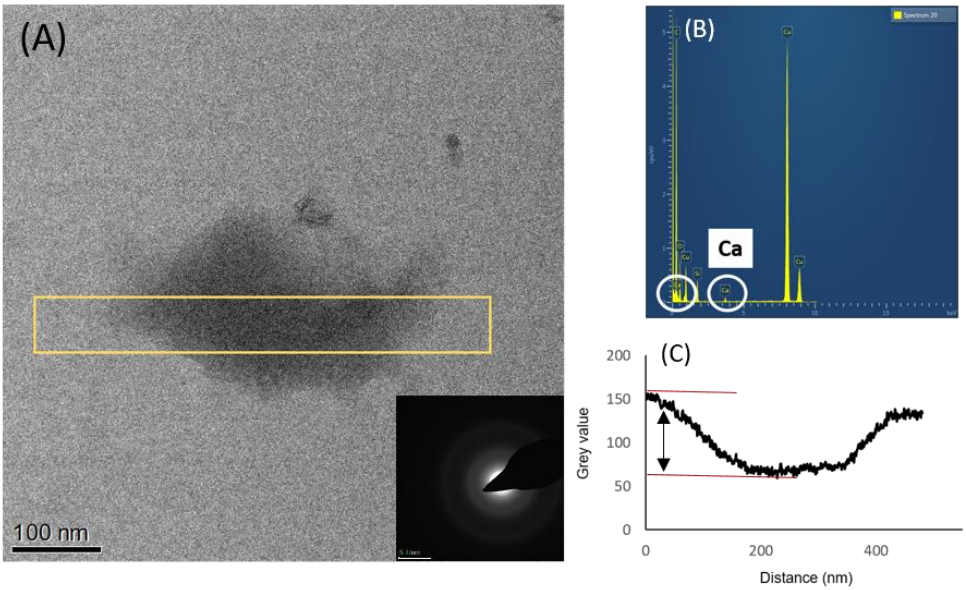

Figure 51 TEM analysis showing: (A) a diffuse region of higher contrast at the concentration of 0.5 mM after 30 min with corresponding diffraction pattern (inset) confirming the amorphous nature of this structure; and (B) EDX conducted in the same region confirming the presence of calcium, oxygen and carbon. (C) Gray values of diffuse region in A obtained from area in yellow box. Copper (Cu) originates from the grid, and the appearance of silicon (Si) elements may be attributed to the samples being prepared in glassware.

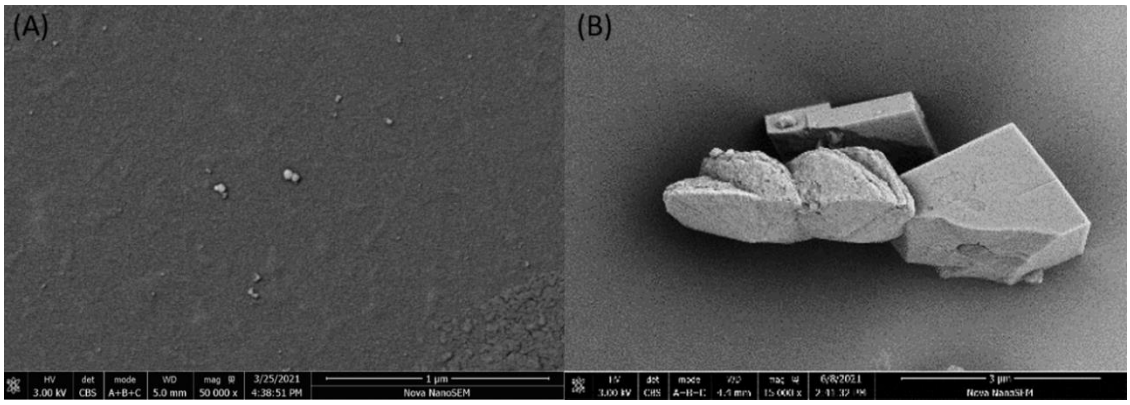

Figure 52 SEM images of precipitates of $CaCO_3$ at a concentration of 0.5 mM after 30 min: (A) shows spherical ACC particles and (B) vaterite and calcite after 30 min. Both images are taken from the same grid.

4.3.2 Characterisation of 1.0 mM $CaCO_3$ solutions using SEM and TEM

Precipitation of $CaCO_3$ in bulk solution at a concentration of 1.0 mM resulted in the formation of spherical ACC particles (~ 15-65 nm), vaterite and calcite after 5 minutes of the reaction (Figure 53 A-C). After 10 and 15 minutes of reaction time,

SEM images (Figures 54 and 55) show a variety of $CaCO_3$ morphologies including spherical ACC particles (Figure 54 C and 55 B), as well as larger crystals of hexagonal vaterite (Figure 54 A and 55 C) and rhombohedral calcite (Figure 54 B and 55A). ACC particles exhibit a size range of ~ 30-85 nm after being subjected to a reaction time of 10 minutes, which subsequently decreases to a size range of ~ 17-55 nm after 15 minutes of the reaction time. The results indicate that the prolonging the reaction time to 10 or 15 minutes resulted in a higher yield of crystalline structures in comparison to the 5 minutes reaction time.

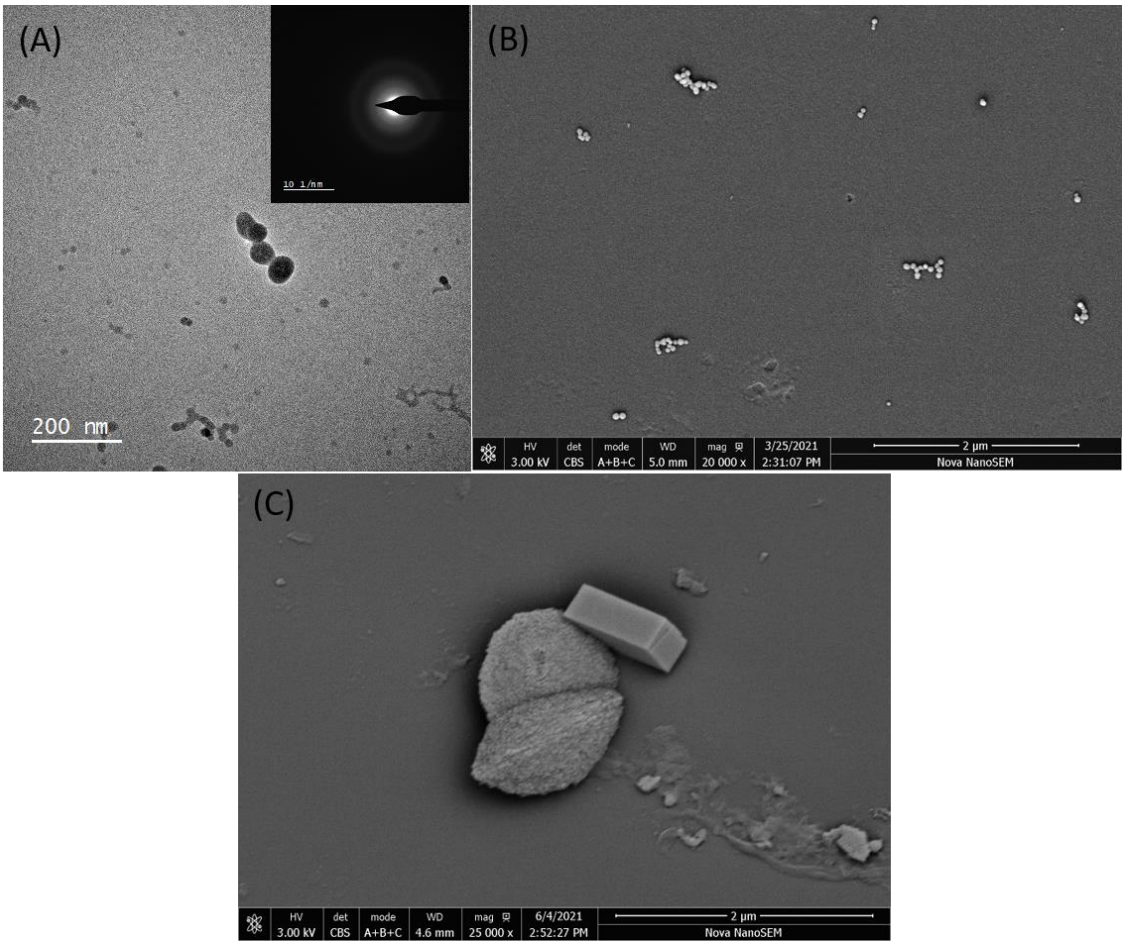

Figure 53 TEM images of precipitates formed in bulk solution at 1.0 mM concentration showing: (A) spherical ACC particles after 5 min of reaction, the diffuse ring in the selected area electron diffraction (SAED) confirms the amorphous nature of the particles; (B) SEM image of ACC particles taken from the same sample at lower magnification, and (C) showing the formation of vaterite and calcite after 5 minutes.

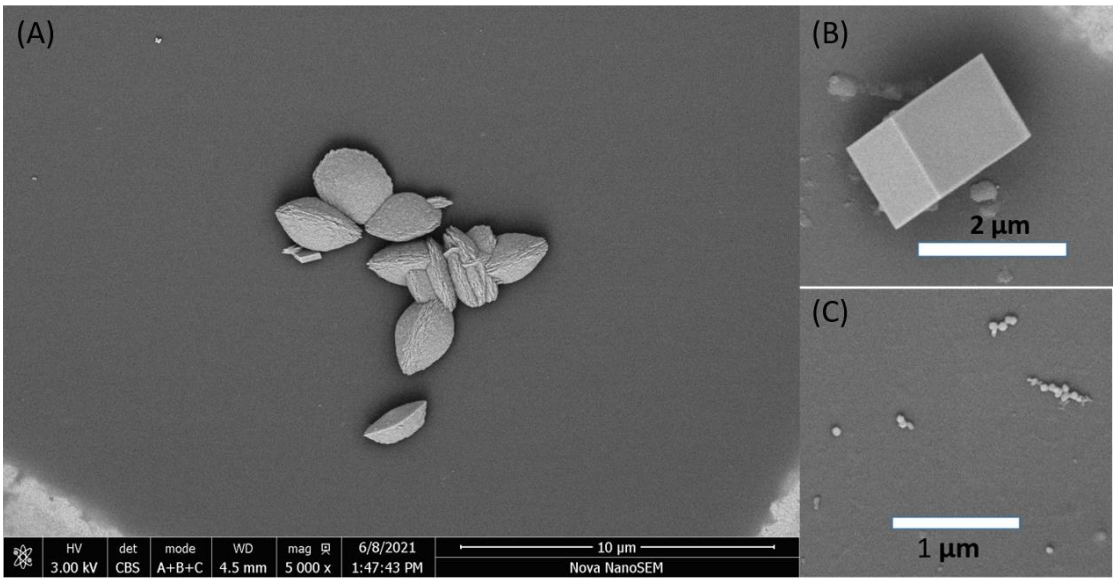

Figure 54 SEM images of particles formed in bulk $CaCO_3$ solution at a concentration of 1.0 mM after 10 min. The precipitates were: A) vaterite, (B) calcite and (C) ACC particles.

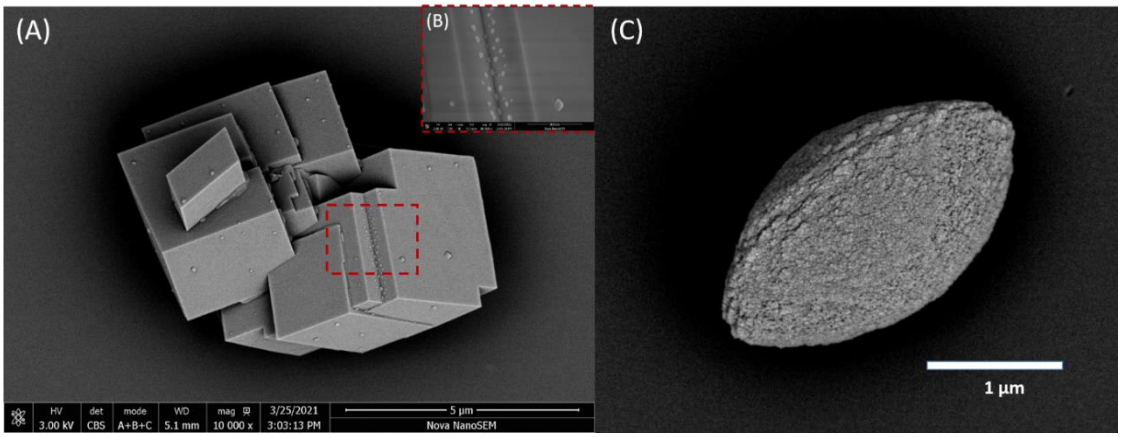

Figure 55 Different morphologies of $CaCO_3$ formed in bulk $CaCO_3$ solution at a concentration of 1.0 mM: (A) SEM image of aggregated calcite particles obtained after 15 min; (B) inset, a higher magnification image of the region marked by the dotted square in (A) showing ACC particles; and (C) a single crystal of vaterite after 15 min of reaction.

4.3.3 Characterisation of 2.5 mM $CaCO_3$ solutions using TEM and SEM

Increasing the final molar concentration to 2.5 mM, a mixture of ACC particles and calcite can be observed after only 15 seconds (Figure 56 A and B). After 5 and 10 minutes of the reaction, ACC particles, vaterite and calcite are observed (Figures 57 and 58). SEM analysis showed that the proportion of microsized

calcite and vaterite increased from 5 minutes to 10 minutes. The microscopic observations revealed the presence of calcite and vaterite together with continued presence of ACC particles after 20 minutes at the concentration of 2.5 mM with their corresponding diffraction patterns shown (Figure 59).

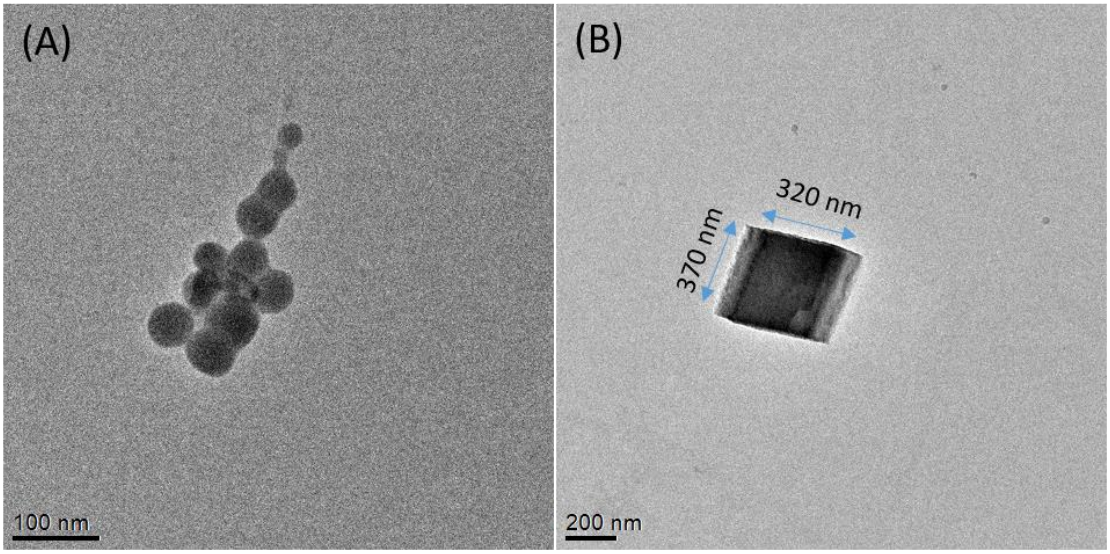

Figure 56 TEM images of $CaCO_3$ obtained from 2.5 mM final concentration solutions after 15 seconds of reaction time: both (A) spherical ACC particles and (B) calcite particles are observed.

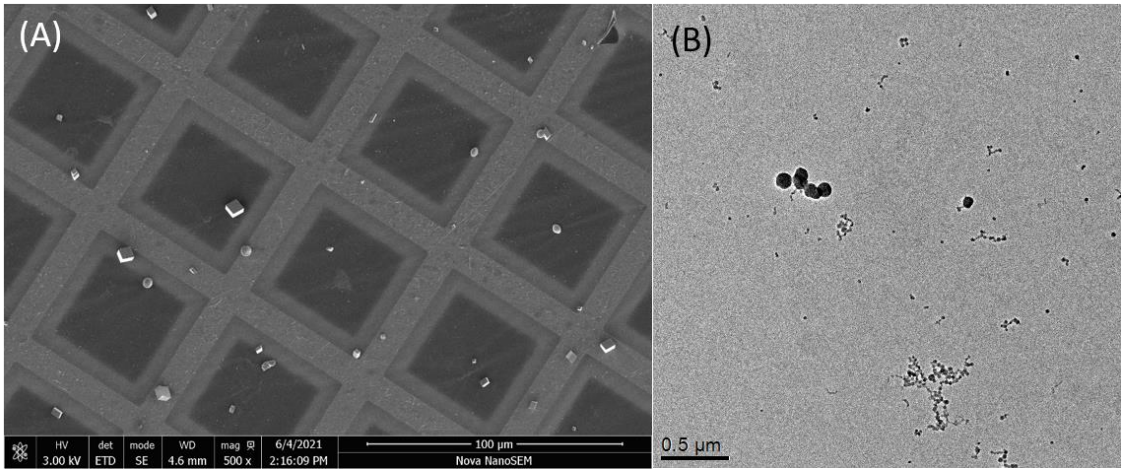

Figure 57 (A) a SEM image of $CaCO_3$ particles from a 2.5 mM final concentration after 5 minutes of reaction showing both calcite and vaterite. (B) a TEM image shows ACC particles are still present after 5 minutes.

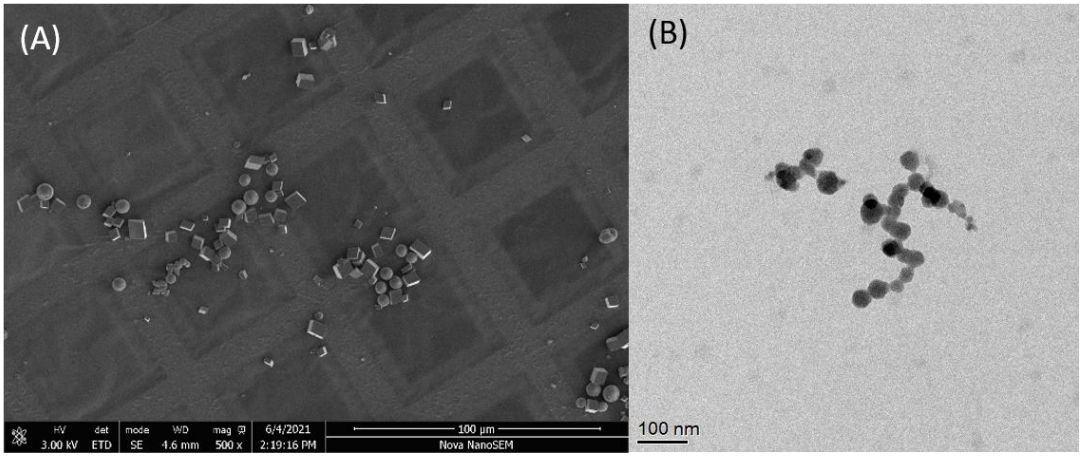

Figure 58 (A) SEM image of calcite and vaterite crystals formed from a 2.5 mM final concentration after 10 minutes of reaction and (B) a TEM image confirms the presence of ACC particles after 10 minutes.

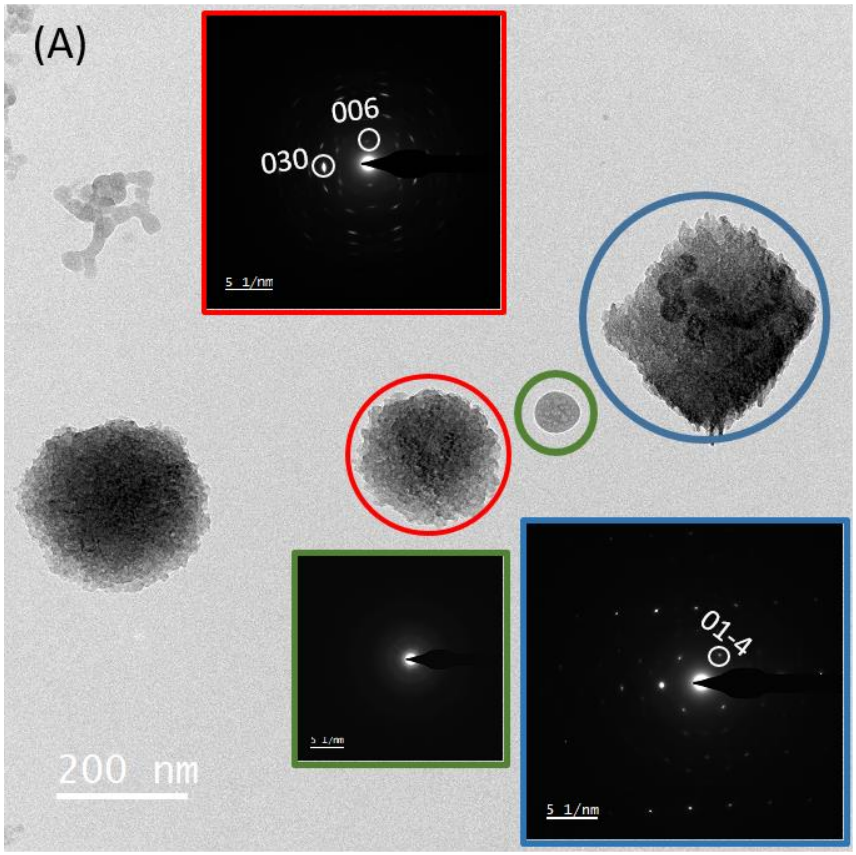

Figure 59 TEM observation of $CaCO_3$ precipitates from a 2.5 mM final concentration after 20 minutes reaction time, indicating the presence of ACC particles (green circle), vaterite (red circle) and calcite (blue circle) with their corresponding electron diffraction patterns (SAED) inset in the corresponding coloured boxes.

4.3.4 Characterisation of 4.5 mM $CaCO_3$ solutions using TEM and SEM

At the highest concentration of 4.5 mM, after only 20 seconds of the crystallisation reaction, large calcite particles on the order of ~ 2.5 μm were observed using TEM (Figure 60 A). Managing sample preparation within shorter timescales, specifically less than 20 seconds, poses significant challenges. Therefore, 20 seconds was chosen as the earliest feasible time point, as any earlier timeframe was not physically achievable within the experimental parameters. By comparison, calcite particles formed at a concentration of 2.5 mM were significantly smaller (~ 400 nm, see Figure 56 B) suggesting that a higher concentration leads to the faster formation of larger crystals. Additionally, the presence of clusters of ACC particles are a distinguishing feature of $CaCO_3$ solutions at 4.5 mM where ACC particles formed a network, rather than being individually present on the support film (Figure 60 B and 61 A). At a longer reaction time of 15 minutes, a variety of $CaCO_3$ morphologies including both individual ACC particles and clusters of ACC particles as well as rhombohedral calcite and spheroid-like vaterite crystals are observed (Figure 61 A-B).

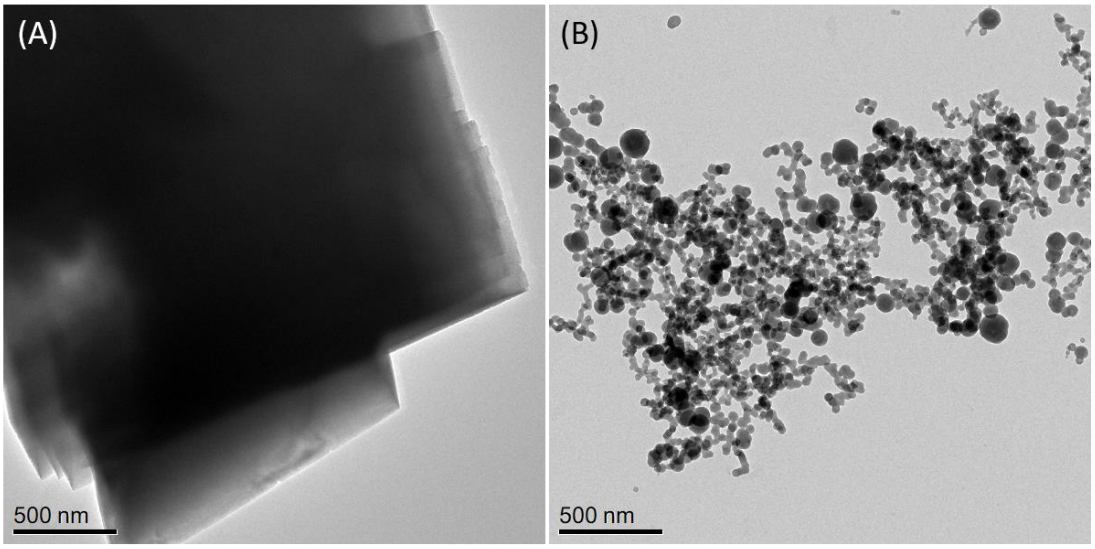

Figure 60 TEM images of $CaCO_3$ precipitates formed at concentration of 4.5 mM in bulk solution after 20 seconds showing: (A) aggregated calcite crystals, and (B) a network of ACC particles.

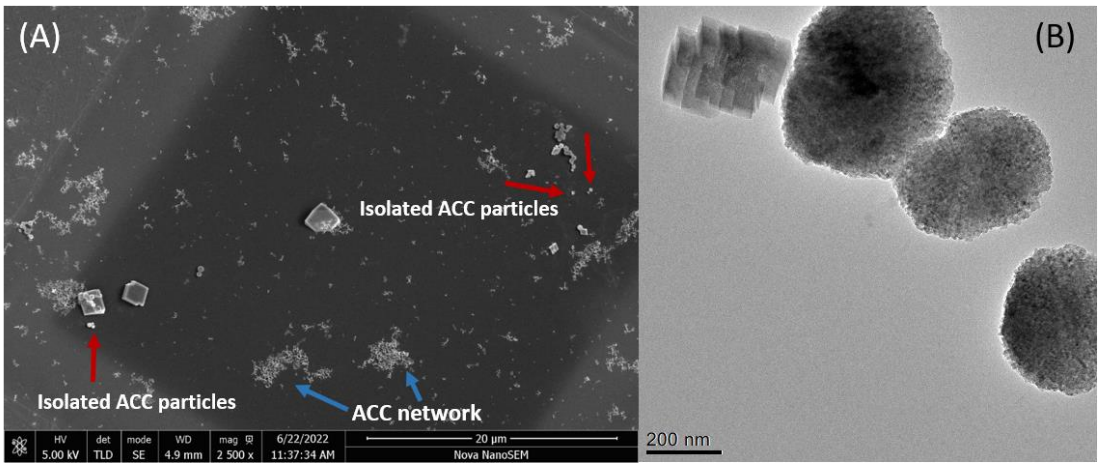

Figure 61 $CaCO_3$ precipitates formed at concentration of 4.5 mM in bulk solution after 15 minutes: (A) SEM image showing a mixture of isolated ACC particles, ACC clusters and calcite, and (B) TEM image at higher magnification showing the presence of vaterite along with aggregated calcite particles.

Table 2 provides an overall summary of the morphologies and polymorphs of $CaCO_3$ particles that formed in bulk solution at the various concentrations (0.5, 1.0, 2.5 and 4.5 mM) and time points (15 s to 30 min) using the quenching and drying sample preparation method.

Table 2: Morphologies of $CaCO_3$ precipitates at different concentrations and reaction times.

	15 – 20 sec	5 min	10 min	15 min	20 min	30 min
0.5 mM	No experiment	Diffuse regions of higher contrast	No experiment	No experiment	ACC, diffuse regions of higher contrast	ACC, diffuse regions of higher contrast, vaterite and calcite
1.0 mM	No experiment	ACC, vaterite and calcite	ACC, vaterite and calcite	ACC, vaterite and calcite	No experiment	No experiment
2.5 mM	ACC and calcite	ACC, vaterite and calcite	ACC, vaterite and calcite	No experiment	ACC, vaterite and calcite	No experiment
4.5 mM	ACC and calcite	No experiment	No experiment	ACC, ACC clusters, vaterite and calcite	No experiment	No experiment

4.4 Discussion

As shown from the SEM and TEM images, at the lowest concentration of $CaCO_3$ (0.5 mM) in the bulk solution, only a diffuse region of higher contrast was observed after 5 minutes of the reaction (Figure 48 A-D). Longer reaction times of 20 and 30 minutes led to the formation of isolated ACC particles (Figure 50 A and B and Figure 52 A) along with the persistence of diffuse regions of higher contrast (Figures 49 A and 51 A). SAED and EDX techniques confirmed the amorphous nature of the regions as well as the presence of calcium, carbon and oxygen as shown in Figure 48 E and F, 49 A and B and 51 A and B (the carbon signal from the grid and the oxygen from the air will consistently be present). The presence of these highly disordered diffuse structures could be attributed to the remains of a dense liquid-like structure as proposed by Faatz et.al, who explained the formation of ACC particles by the liquid-liquid phase segregation in $CaCO_3$ solutions (Faatz et al., 2004; Smeets et al., 2017; Ramnarain et al., 2022).

According to the nonclassical theory proposed by Gebauer, phase separation takes place in the solution through processes such as liquid-liquid binodal demixing and/or spinodal decomposition. This leads to the formation of dense liquid nano-droplets by creating interfaces and altering the chemical speciation. At this point nano-droplets undergo progressive dehydration and aggregate to create larger nano-droplets where solid ACC particles are formed by coalescence of individual nano-droplets into a continuous phase (Gebauer et al., 2014). ACC particles are identified as a post nucleation-stage precursor phase in $CaCO_3$ which ultimately crystallises (Gebauer et al., 2008). Wang (Wang et al., 2017) studied an identical concentration of 0.5 mM in bulk solution. However, interestingly, no evidence for the presence of ACC particles and crystals were found after 24 hours. The reason for the distinct difference in the results of our study in comparison to Wang's, could be due to the treatment of TEM grids. All the TEM grids that were used in this study were plasma cleaned for 20 seconds to increase the hydrophilicity of the support film, therefore more particles can adhere to the surface of the grids for analysis.

At a concentration of 1.0 mM, ACC particles were detected after 5 minutes of the reaction, which is much earlier than the formation of ACC particles at the

concentration of 0.5 mM, where ACC formed after 20 minutes of the reaction. However, crystalline structures were undetectable at this time point. Wang et.al (2015) also studied the precipitation of $CaCO_3$ at a concentration of 1.0 mM and showed that ACC particles could be detected occasionally in bulk solution, in 3 out of 10 experiments. However, in our study, the presence of ACC particles was consistent in all the samples, apart from the concentration of 0.5 M after 5 minutes. As the supersaturation level increased, from a concentration of 0.5 mM to 1.0 mM, the formation of crystalline structures occurred at shorter reaction times. At the concentration of 1.0 mM, the formation of spindle-like vaterite and rhombohedral calcite was first detected after 5 minutes of the crystallization reaction, whereas at the concentration of 0.5 mM, crystalline structures of vaterite and calcite were detected after 30 minutes.

Finally, at higher supersaturation levels and concentrations of 2.5 mM and 4.5 mM, TEM observations revealed that crystals of $CaCO_3$ have well-defined crystalline morphologies (Cauliflower vaterite and rhombohedral calcite) which were formed almost immediately and grew over time, together with the continued presence of some isolated ACC particles and clusters (Zhou et al., 2010). The presence of ACC particles is in good agreement with Wang's study who detected ACC particles after 15 seconds at 2.5 mM in bulk, however there was no evidence for the presence of calcite at this time point in their study.

The larger number of $CaCO_3$ at higher at higher supersaturation levels can be explained by the increased nucleation rate. The results demonstrate that by reducing the supersaturation level at early times, diffuse regions of higher contrast form, leading to longer reaction times for the formation of crystalline structures due to the lower driving force for crystallization. For example, at a concentration of 0.5 mM, the formation of calcite crystals was observed after 30 minutes, whereas a concentration of 4.5 mM resulted in the formation of micron-sized calcite after only 20 seconds.

Microscopic observations show variations in the magnitudes of the diffuse regions of higher contrast. This variability could be attributed to the size differences of the ACC particles. ACC particle sizes range from as small as 5 nm to as large as 350 nm, and these structures of diffuse regions of higher

contrast are proposed to be precursors of possible dense liquid, providing an explanation for the different sizes observed.

4.5 Investigating the effect of sample preparation on the observed crystallisation of $CaCO_3$

In the previous section, samples were prepared by chemically quenching the aqueous crystallisation process via immersion in ethanol at a given time point. However, the stabilising effect of alcohol has been well documented in the literature. Alcohol is thought to stabilise intermediate phases in water-ethanol mixtures by lowering the water activity which consequently prevents the formation of the most thermodynamically stable phase (Sand et al., 2012) (Manoli and Dalas, 2000) (Sand et al., 2012). Researchers (Online, Chen, Co, Antonietti, & Yu, 2013) have investigated the synthesis of ACC particles in a mixture of alcohol and water and showed that stable monodispersed ACC nanoparticles can be produced in an ethanol-rich aqueous phase. The presence of an ACC network at higher supersaturation levels (25 mM) were observed by Walker et al. who investigated the formation of aragonite in an alcohol-water system using cryo-TEM. However, the role of alcohol, in the transformation of ACC to aragonite has not received fundamental attention (Jessica M Walker et al., 2017).

The overall aim of this study is to understand the early stages of crystallisation of $CaCO_3$ in its native state. As an ethanol-quenching technique was used to halt the crystallisation reaction on the TEM grids, it is important to determine whether ethanol has any effect on the morphologies or types of $CaCO_3$ precipitates formed. Therefore, the influence of different sample preparation techniques, in the presence and absence of ethanol, on the observed precipitation of $CaCO_3$ will be investigated.

A range of different sample preparation methods including air-drying, vacuum filtering, chemical quenching (Wang et al., 2017), and plunge freezing-vacuum drying as well as plunge freezing and direct examination in cryo-TEM, were investigated and compared. For this purpose, equal quantities of equimolar aqueous solutions of 9 mM $CaCl_2$ and 9 mM Na_2CO_3 were directly mixed

leading to a final concentration of 4.5 mM $CaCO_3$ and left for set times of 5, 15 and 40 min before preparing samples for microscopic analysis (both SEM and TEM). Additionally, the restricted particle count observed in each dataset is attributed to the low concentration of the solution.

Drop casting is one of the most common methods used to prepare samples for SEM and TEM analysis. This technique involves the formation of a thin layer of a solution on a TEM grid followed by blotting and drying (M. Ilett et al., 2020) (Michen et al., 2015). Both simple air drying and vacuum filtration techniques can be used to dry the samples on TEM grids at ambient temperature. For the latter technique however, a vacuum is used to accelerate the drying process. One drawback of both these techniques is that the solution supersaturation level increases during the drying process which may potentially cause ACC and different polymorphs to precipitate at earlier times. Furthermore, the drop-casting and drying technique may result in the formation of nanoparticle aggregates as the liquid meniscus recedes which makes it challenging to identify the 'true' aggregates from the aggregates that are produced ('formed' aggregates) during sample preparation (Dieckmann et al., 2009).

Chemical quenching can also be used to prepare samples for microscopic analysis. However, as mentioned above, it has been reported that the addition of ethanol can stabilise intermediate phases of $CaCO_3$. It has also been suggested that this technique may influence the precipitation pathways of $CaCO_3$, i.e., classical versus non-classical routes, and hence the resultant precipitate morphology (Sand et al., 2012).

In addition to the aforementioned preparation methods, plunge freezing (preceded by blotting) of the solution in liquid ethane, followed by vacuum drying/sublimation of the vitreous ice, was also employed in this study. It has been demonstrated that samples prepared using this approach can maintain their original state meaning nanoparticle agglomerates can retain their native state (Hondow et al., 2012).

Finally, plunge freezing (preceded by blotting) the solution in liquid ethane followed by full examination by cryo-TEM allows imaging of the solution in close to its native state (Mccomb et al., 2019). Here the sample is examined in a thin layer of vitreous ice with the sample held at liquid nitrogen temperatures.

The following section aims to address the limitations of each of the above-mentioned sample preparation methods and so assess the most appropriate technique to better characterise the native state of the crystallisation process. It presents a comparative study of the different electron microscopy sample preparation methods benchmarked against full cryo-TEM.

For the air-dried samples at ambient temperature, after 5 minutes of reaction time, TEM micrographs show the presence of spherical ACC particles with diameters ranging between ~ 35-350 nm (Figure 62 A) as well as hexagonal vaterite and rhombohedral calcite crystals ~ 1-2 µm (Figure 62 B). After 15 minutes, it can be seen from SEM images that, larger ACC particles of between ~ 105-520 nm were evident (Figure 62 C) with the continued presence of vaterite and calcite which grow over time (Figure 62 D). After 40 minutes, vaterite and calcite were further aggregated into larger particles ~ 5-20 µm. However, no evidence was found for the presence of ACC particles suggesting all ACC particles had transformed to crystalline structures (Figure 62 E-F). Table 3 demonstrates the size range of ACC particles that were observed by the air-drying technique as a function of reaction time. The size distributions of ACC particles are shown as a box and whisker plot in Figure 63. This diagram is based on the minimum (lower whisker), the first quartile (bottom edge), the median (centre line), the third quartile (upper edge) and the maximum (upper whisker) (Köhnke et al., 2016).

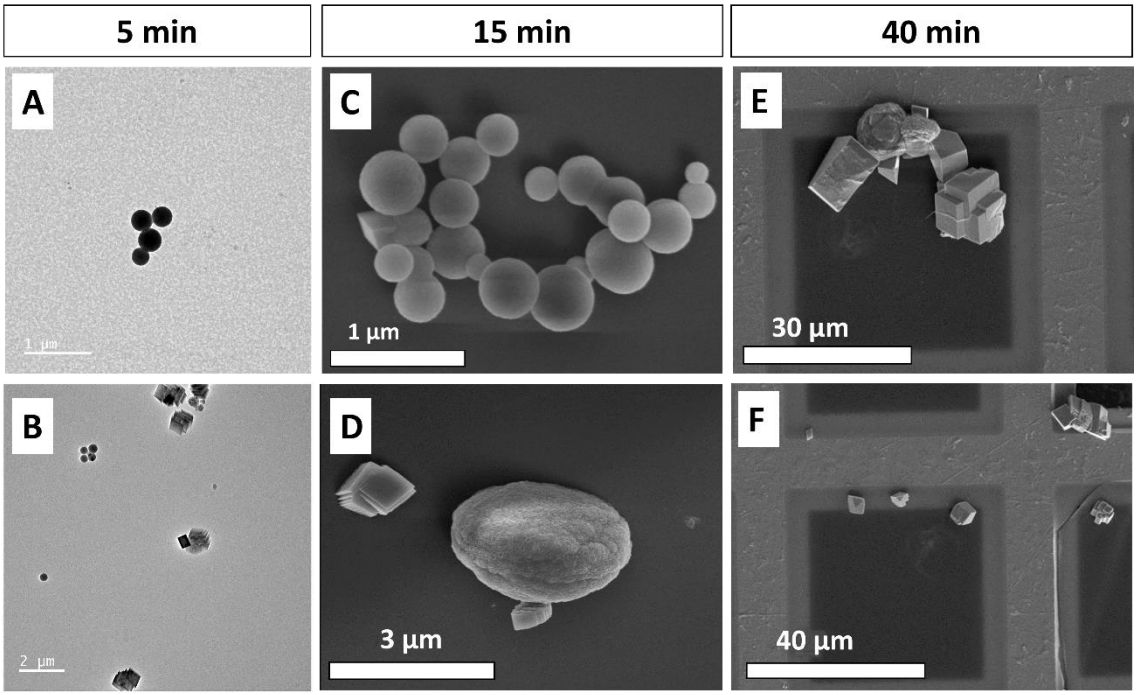

Figure 62 Precipitates formed by the air-drying method in 4.5 mM bulk solution. (A-B) are TEM images and (C-F) are SEM images. Precipitates were: after 5 minutes (A) ACC particles and (B) vaterite and calcite; after 15 minutes (C) ACC particles and (D) vaterite and calcite; and after 40 minutes (E) calcite and (F) calcite and vaterite.

Table 3: Size distribution of ACC particles of SEM and TEM images (measured from ~ 30 particles for each) prepared by the air-drying for various crystallisation times.

Sample preparation Method	Air-dried		
Time (min)	5	15	40
ACC particle size Diameter (nm)	35-350	105-520	No ACC

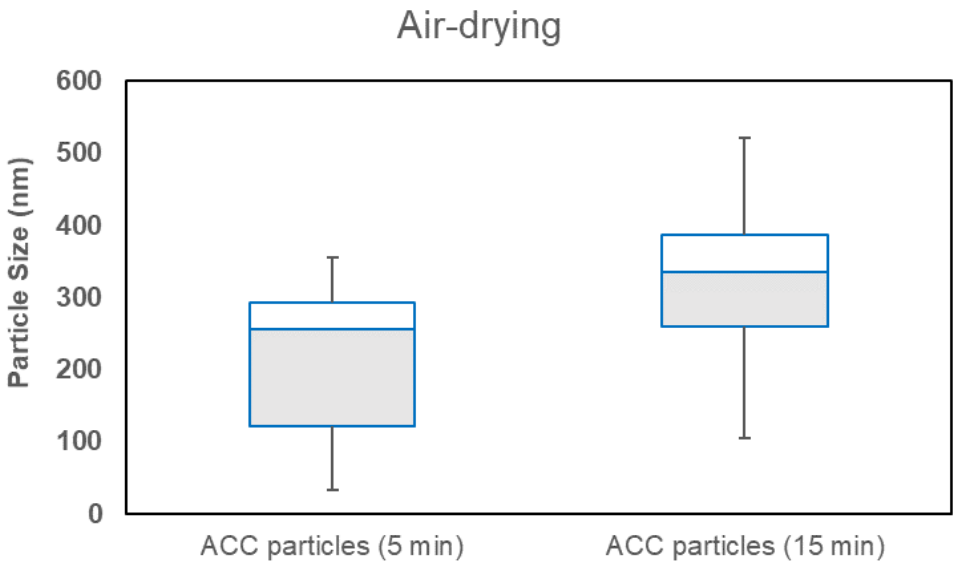

Figure 63 Box and whisker plots of ACC particle produced by air-drying at different times.

For the vacuum filtration technique, after 5 minutes of reaction time, ACC particles with diameters ranging between ~ 70- 540 nm and calcite particles ranging between 450-750 nm were detected (Figure 64 A-B). The precipitates observed after 15 minutes, were ACC (~ 100- 600 nm in size), vaterite and calcite with a size range of 700 nm - 10 µm (Figure 64 C-D). After 40 minutes only calcite and vaterite (~ 700 nm-12 µm) were observed (Figure 64 E-F). For the vacuum filtered samples, the smallest and the largest ACC particle sizes during the course of 5, 15 and 40 minutes reaction time are listed in Table 4. A box and whisker plot in Figure 65 demonstrates the size distribution of the ACC particles.

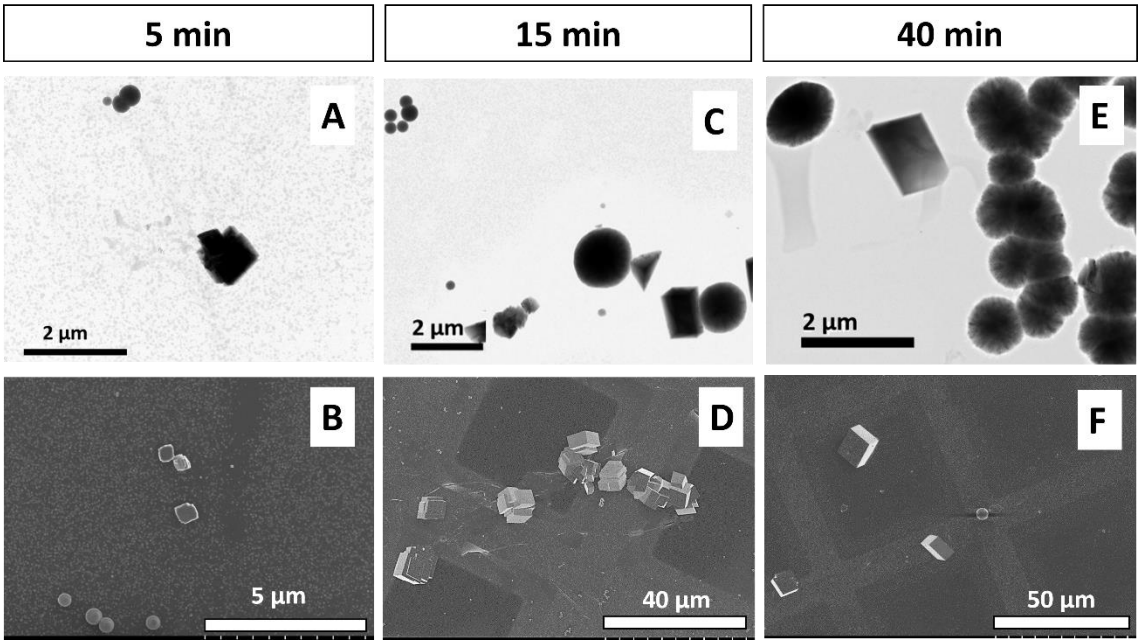

Figure 64 TEM images of $CaCO_3$ prepared by vacuum filtration techniques. Particles were: (A) ACC and calcite after 5 min, (B) ACC, vaterite and calcite after 15 min and (C) vaterite and calcite after 40 min.

Table 4: Size distribution of ACC particles measured from SEM and TEM images of ~ 40 particles for each time point) prepared by the vacuum filtrations at various crystallisation times.

Sample preparation Method	Vacuum-dried filtration		
Time (min)	5	15	40
ACC particle size diameter (nm)	70-540	100-600	No ACC

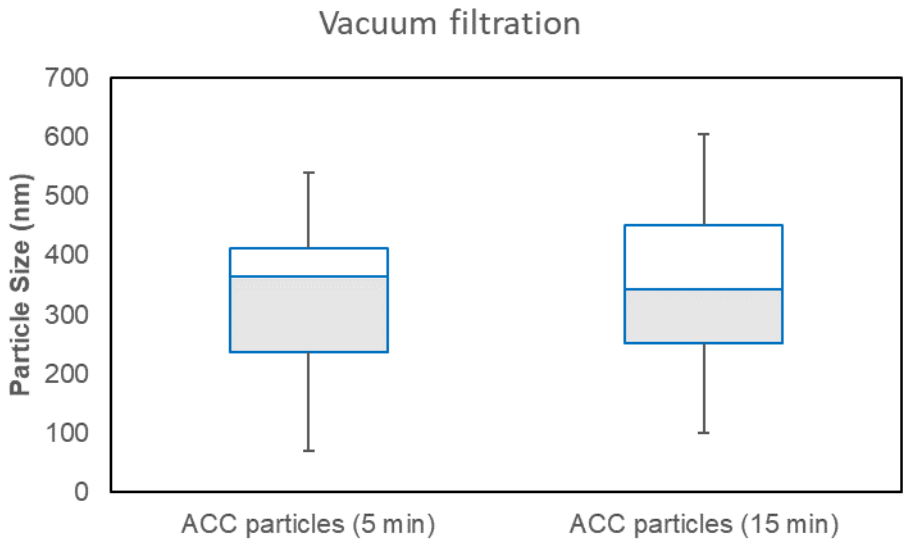

Figure 65 Box and whisker plots of ACC particle produced by vacuum filtration at different times. From measurement of 40 particles for each time point.

For the samples prepared by ethanol-quenching, two different morphologies of amorphous particles were observed: individual ACC particles (yellow arrows) and networks of ACC (white arrows), see Figure 66. Interestingly only ethanol quenching led to the formation of these extended ACC networks on the TEM grid. After 5 minutes of reaction, (Figure 66 A) a network of small ACC particles (2-60 nm) accompanied by isolated larger ACC particles with a size range of 50-500 nm were observed. TEM analysis revealed the presence of aggregated calcite after 5 minutes of reaction (Figure 66 A); the corresponding diffraction pattern identifies the material as calcite (Figure 66 B). Microscopic observation showed that the dimensions of the individual ACC particles (115-455 nm) and clusters of ACC particles (5-110 nm) grew after 15 minutes of reaction alongside an increased population of vaterite and calcite (Figure 66 C and D). Similar to the samples produced by both the drying techniques, no ACC particles were detected after 40 minutes; only aggregated vaterite and calcite were identified (Figure 66 E and F). The size range of the networks and individual ACC particles produced by the ethanol quenching method are summarised in Table 5. A detailed size distribution of the two different types of ACC particles is summarised in the box and whisker plot shown in Figure 67.

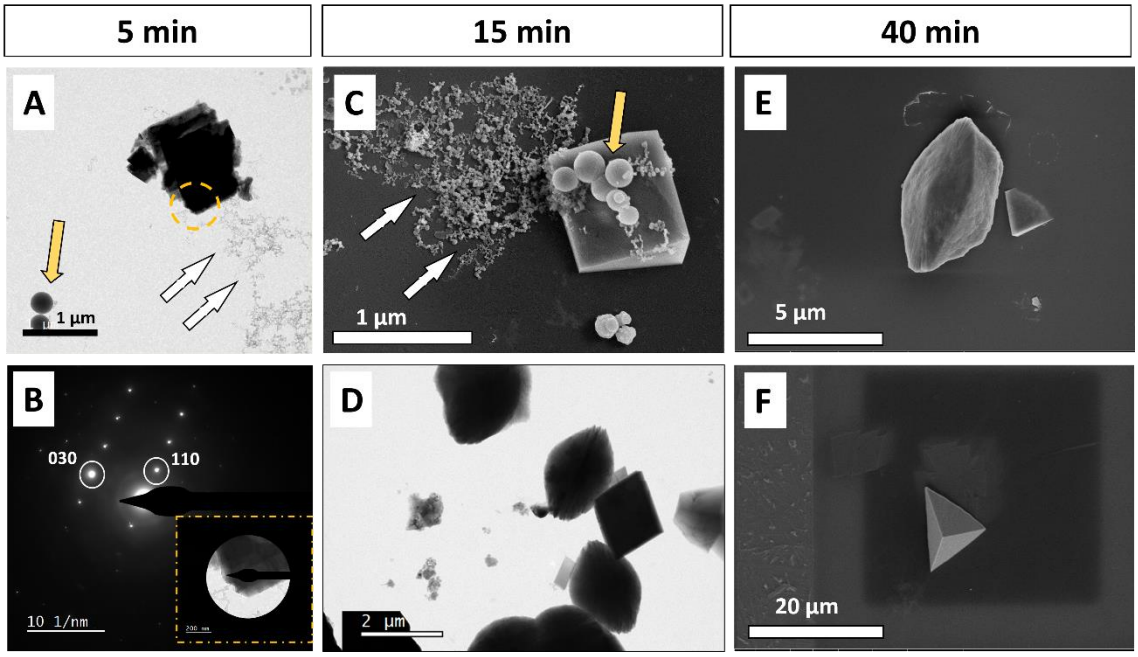

Figure 66 Precipitates formed in bulk solution by chemical quenching in ethanol showing: (A) spherical isolated ACC particles and calcite after 5 minutes of reaction; (B) the corresponding diffraction pattern identifies the material as calcite. (C) a large network of ACC clusters, individual ACC particles, as well as vaterite and calcite after 15 minutes; and (E and F) single crystals of vaterite and calcite after 40 minutes.

Table 5: Size distribution of ACC particles (~ 30 particles for each time point) prepared by ethanol-quenching technique at different crystallisation times.

Sample preparation Method	Ethanol-quenched		
Time (min)	5	15	40
Individual ACC particles size diameter (nm)	50-500	115-455	No ACC
Individual ACC particles size diameter (nm) within the network	2-60	5-110	No ACC

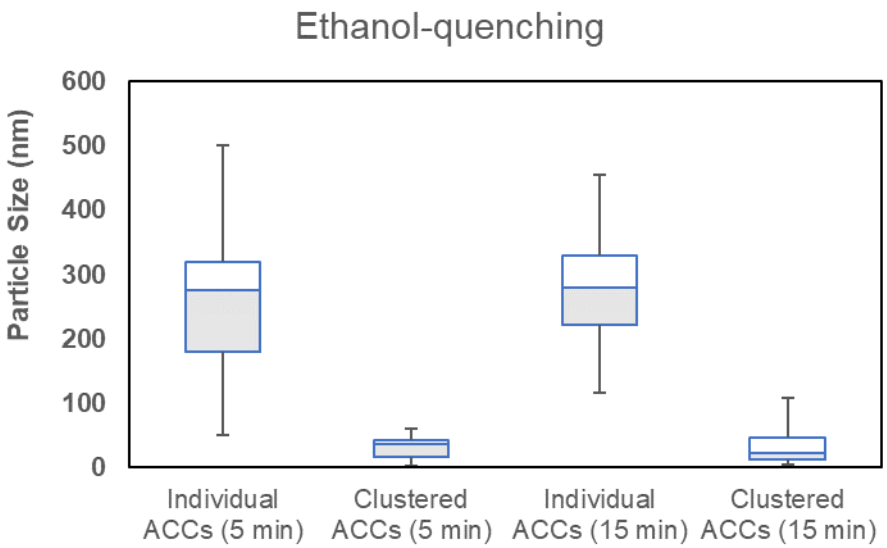

Figure 67 Box and whisker plot of ACC particles produced by the ethanol-quenching method.

For the samples prepared via the plunge freezing vacuum-drying technique, after 5 -15 minutes the samples contained only ACC particles. Extending the reaction time from 5 to 15 min, increased the size range of ACC particles from 25-525 nm (Figure 68 A) to 180-615 nm (Figure 68 B) respectively, although no crystalline structures could be clearly identified. However, after 40 minutes, SEM micrographs showed ACC particles in the size range 230-545 nm together with a change in morphology on the surface of the ACC particles (yellow arrows in Figure 68 C), perhaps suggesting that a phase transformation from an amorphous ACC structure to a crystalline structure was taking place. That said there was no evidence for a well-defined morphology indicative of a particular $CaCO_3$ polymorph.

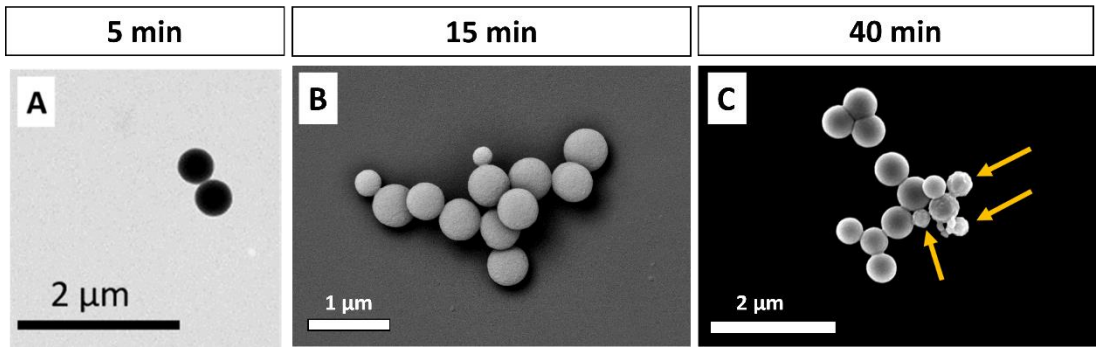

Figure 68 TEM and SEM images of samples prepared by the plunge-freezing vacuum drying technique. (A) shows the formation of small ACC particles (25-525 nm) after 5 min. (B) shows the presence of ACC particles (180-615 nm) after 15 min of reaction but no crystals were detected. (C) After 40 min ACC particles (230-545 nm in size) showing some possible emergent crystalline structure or evidence of dissolution (blue arrows).

During the plunge freezing process, the precipitation of NaCl salts was observed at the concentration of 4.5 mM after 40 minutes of crystallization, as shown in the SEM image in Figure 69. The formation of NaCl salts was also observed at the concentration of 1 mM after 1 minute of the reaction, which was confirmed by the diffraction pattern Figure 70.

In general, samples that are plunge-frozen or vacuum-sublimed often exhibit indications of Eutectic ridges (Wergin and Erbe, 1992). These eutectic ridges indicate the presence of dissolved solutes that have undergone partitioning during the freezing process. These ridges occur when dissolved solutes, which have eutectic points in their solute-water phase diagrams (such as sodium chloride, sodium sulfate, calcium chloride, and sodium carbonate), undergo a partitioning process into ice and solute hydrates during either the slower vacuum sublimation step or the faster initial freezing process (Wergin and Erbe, 1992). This partitioning may be influenced by the thickness of the ice, with thicker regions at the edges of the TEM grid presumably freezing and subliming more slowly. This solute partitioning can greatly complicate the observation of species that have actually crystallised in the original solution (Wergin and Erbe, 1992).

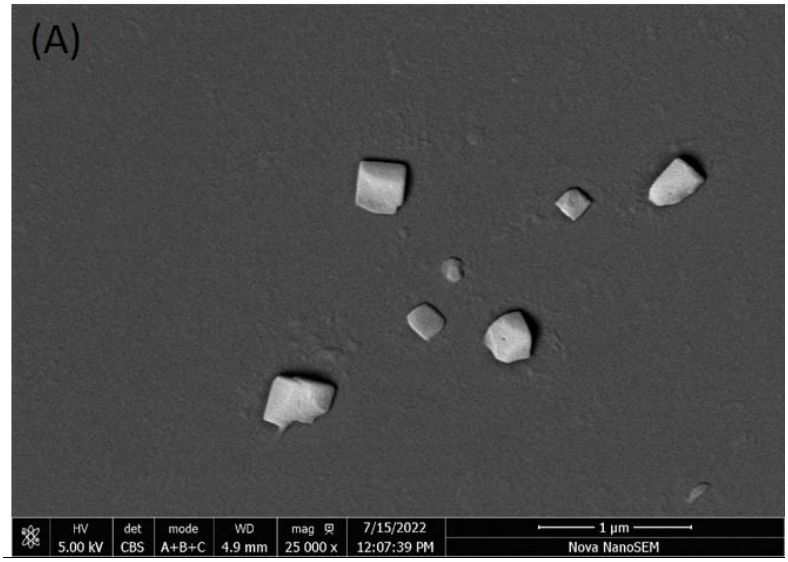

Figure 69 SEM image of precipitation of NaCl salts in the plunge-freezing vacuum drying of 4.5 mM $CaCO_3$ samples. (A) After 40 minutes of reaction time.

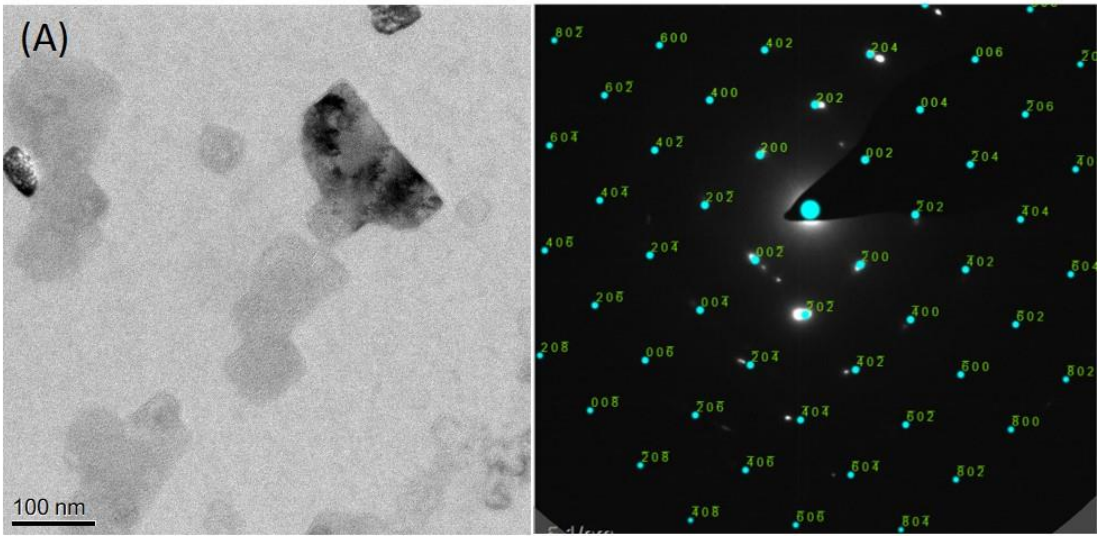

Figure 70 A TEM image (A) and its corresponding diffraction pattern (B) showing the formation of NaCl salt at the concentration of 1 mM after 1 min using plunge freezing vacuum dries technique.

The size range of the ACC particles produced by the plunge freezing vacuum drying method are summarised in Table 6. A box and whisker plot of the size distribution of ACC particles is shown in Figure 71.

Table 6: Size distribution of ACC particles (~ 30 particles for each time point) prepared by Plunge-frozen vacuum dried technique at various crystallisation times.

Sample preparation Method	Plunge frozen vacuum dried		
Time (min)	5	15	40
ACC particle size diameter (nm)	25-525	180-615	230-545

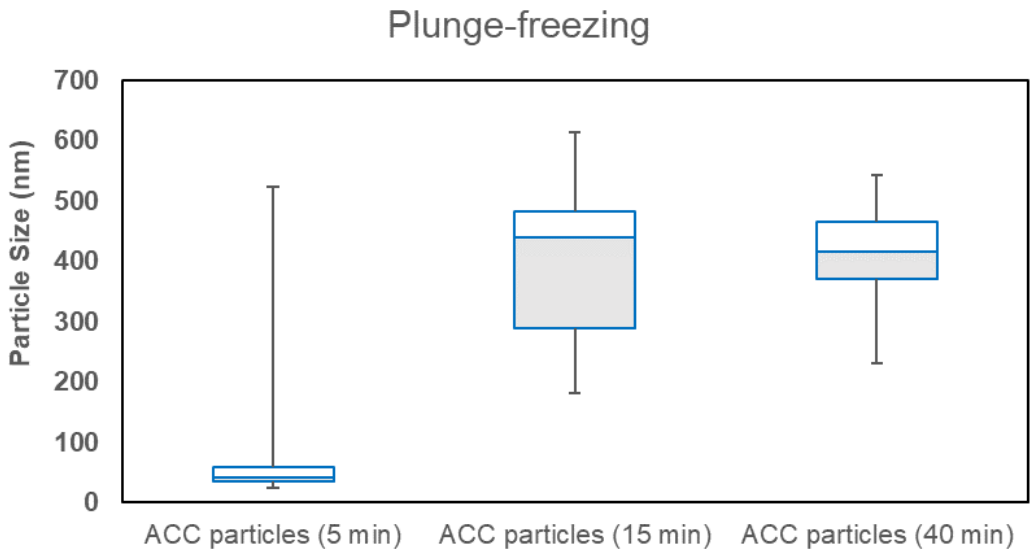

Figure 71 Box and whisker plots of ACC particle size versus time produced by plunge-freezing method (30 particles).

A cryo-TEM study was then carried out to investigate the evolution of morphology and structure of the $CaCO_3$ formed in the solution state. After a crystallisation time of 5 minutes, cryo-TEM images (Figure 72 A) showed the presence of nano-sized spherical ACC particles, with a size range 80-625 nm, together with micron-sized (~3 μm) diffuse regions of higher contrast than the surrounding vitreous ice. SAED patterns of the diffuse regions confirmed that they were amorphous. After 40 minutes (Figure 72 B), spherical ACC particles further aggregated into larger clusters with a size range of between 150-600

nm. In addition, the emergence of calcite crystals with faceted edges was observed which was confirmed with SAED.

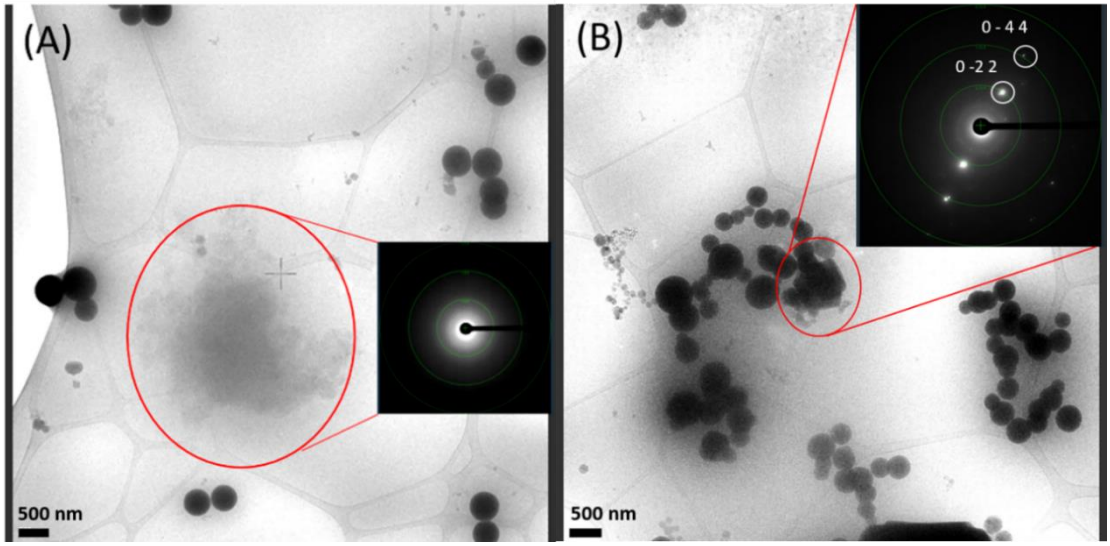

Figure 72 Cryo-TEM images of a 4.5 mM $CaCO_3$ solution indicating: (A) the presence of ACC particles as well as a dense region of higher contrast after 5 minutes of crystallisation reaction; inset: the selected area electron diffraction pattern of the dense region confirming its amorphous nature. (B) shows an increased population of ACC particles together with emergence of calcite after 40 minutes of reaction; inset: SAED pattern confirming the presence of calcite.

The size range of the ACC particles as a function of reaction time as observed by cryo-TEM are summarised in Table 7. A box and whisker plot of the size distribution of ACC particles is shown in Figure 73.

Table 7: Size distribution of ACC particles (measured from ~ 50 particles for each time point) observed by full cryo-TEM at various crystallisation times.

Sample preparation Method	Cryo-EM study		
Time (min)	5	15	40
ACC particles size diameter (nm)	80-625	140-540	150-600

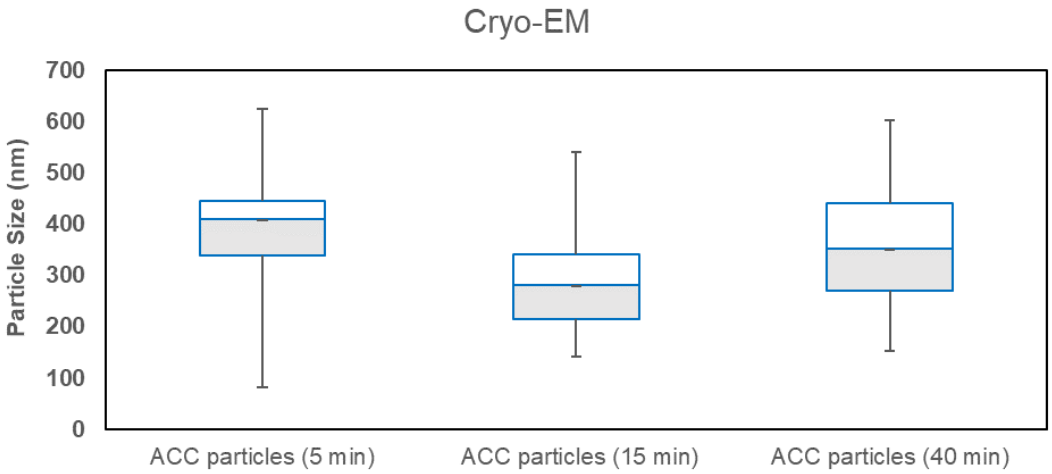

Figure 73 Box and whisker plots of ACC particle size versus time produced by ethanol-quenching method (50 particles per time point).

4.5.6 Benchmarking the Results against full Cryo-TEM

Reviewing the SEM and TEM results, both air-drying and vacuum filtration techniques resulted in morphologically similar $CaCO_3$ particles. ACC particles were only observed within the first 15 minutes and vaterite and calcite were observed at all-time points. Both these methods will lead to an increase in supersaturation levels (the difference between the actual concentration and the solubility concentration), albeit at different rates, which could explain the observed behaviour. The absence of ACC particles after 40 minutes of reaction, in the two above-mentioned drying techniques, could be attributed to the increased level of supersaturation during the drying process, which consequently shortens the lifetime of ACC particles as the driving force for crystallisation becomes larger and larger.

Amongst the various sample preparation techniques, it was only the ethanol-quenching technique that resulted in the formation of ACC clusters that appeared as an extended network. One possible explanation could be due to the stabilizing effects of ethanol on $CaCO_3$ particles in mixed water-ethanol solutions (Sand et al., 2012; Chen et al., 2013). The air-drying method gave rise to the formation of vaterite and calcite at all-time points, whereas in samples prepared by vacuum filtration and ethanol quenching techniques, calcite and vaterite crystals only coexisted at 15 and 40 minutes. Conversely, in the plunge freezing vacuum sublimation method, such drastic increases in supersaturation

levels should be diminished, potentially explaining why only ACC particles were observed after 5 and 15 minutes of reaction time with no clear evidence of crystalline polymorphs. Following 40 minutes of observation, ACC particles persisted whilst simultaneously showing an emerging rough surface, which could be indicative of the potential transformation of ACC to crystalline polymorphs or dissolution. Nielsen et al. performed in situ TEM to study the nucleation of $CaCO_3$ where he proposed two different dissolution mechanism for ACC particles: 1) Shrinking and disappearance of ACC particles, and 2) gradual roughening and pitting of ACC particles until they disappeared completely (Michael H.Nielsen, Shaaul Aloni, 2014).

The full cryo-TEM preparation and study suggested the formation of disordered diffuse structures which could be evidence of a dense liquid-like structure embedded within the vitrified solution which is associated with the subsequent precipitation of ACC particles. The dense liquid-like structure was not exclusively observed in the cryo-TEM study but was also visible at a very low concentration of 0.5 mM. Smeets et al. (2017) conducted a cryo-TEM study on diluted $CaCO_3$ solutions and observed low density objects that were proposed to be vitrified droplets of a dense liquid phase (DLP), as they exhibit a high degree of hydration and contained a high amount of calcium. This DLP is formed from the solution through a liquid-liquid phase separation process (Smeets et al., 2017).

4.6 Conclusion

The study of the crystallisation of $CaCO_3$ showed that the morphology and particle size of $CaCO_3$ polymorphs that form differ dramatically both as a function of the different final molar concentration (0.5, 1.0, 2.5 and 4.5 mM) and as a function of different reaction times (ranging between 15 s and 30 minutes). Both supersaturation level and reaction time can influence the size of the particles. An increased reaction time resulted in the formation of larger particles, which is accompanied by the disappearance of nano-sized particles.

The second section of this study focused on the effect of different sample preparation techniques on the observed crystallisation of $CaCO_3$. The microscopic observations suggested that the sample preparation technique can

significantly influence the formed precipitates of $CaCO_3$. Air-drying and vacuum filtration techniques do not reflect the native state of the samples due to the increased supersaturation levels created during the drying stage. This results in a greater driving force for crystallisation and leads to fast $CaCO_3$ precipitation as crystalline polymorphs. In addition, the use of ethanol in the quenching technique resulted in the formation of both a significant network of ACC and individual ACC particles. This finding suggests that occurrence of the ACC network can be an artefact caused by the addition of ethanol to the solution. In comparison samples prepared via plunge freezing and vacuum drying showed only ACC particles and equally samples observed by full cryo-TEM revealed a significant population of ACC particles along with the emergence of a few crystalline structures after 5 minutes of the reaction. Consequently, it can be concluded that despite drying and ethanol quenching often being used in crystallisation studies, this technique may not always be a true representation of the native state of a sample and ultimately cryo-TEM should be used wherever possible to try and eliminate any sample preparation artefacts. Therefore, in the next chapter cryo-TEM has been used to study the transformation process of $CaCO_3$ in more detail.

Chapter 5 Results

5.1 In-situ study of $CaCO_3$ formed from equimolar aqueous solutions of $CaCl_2$ to Na_2CO_3 in real time.

In the previous chapter, a diffuse region of higher contrast was observed in TEM images at a $CaCO_3$ concentration of 0.5 mM, which was proposed to be a dense liquid-like structure formed prior to nucleation. Here, TEM sample preparation involved the use of ethanol to quench the reaction followed by simple drying. However subsequently this was found to have a direct effect on the morphology of $CaCO_3$ precipitates, as well as changing the supersaturation of the solution during drying. Hence, in order to conduct further examination and to determine whether the observation of a dense liquid-like structure is representative of the native-state of the crystallising solution and not a result of the presence of ethanol, cryo-TEM imaging of the $CaCO_3$ solutions within their frozen, hydrated state was performed. For this study, two final concentrations of $CaCO_3$ (4.5 and 0.5 mM), containing equal molar ratios of $CaCl_2$ and Na_2CO_3 were selected and monitored at different time points.

In order to confirm the nature of the nano and micro- sized structures, a combination of different techniques has been implemented. Electron diffraction analysis was used to identify whether the particles were amorphous or crystalline. In addition, cryo-scanning transmission electron microscopy (STEM) imaging and EDX mapping was employed for elemental mapping within the frozen hydrated sample. Cryo-STEM offers an advantage over conventional TEM by reducing the damage rate of vitreous ice (Ilett, 2020). Finally, to gain insight into the mechanism by which $CaCO_3$ precipitates form, in-situ crystallisation processes of a 4.5 mM $CaCO_3$ solution were visualised in real time using liquid cell (LC)-TEM.

It has been proposed that the precipitation of $CaCO_3$ involves a transitional stage called liquid- liquid phase separation (LLPS) (Driessche et al., 2017). Phase separation occurs, when a supersaturated solution spontaneously splits into two liquid phases upon bimodal demixing, with one phase containing a high concentration of solute while the other phase contains a low concentration of solute. In this case, the system becomes metastable, and phase separation can

take place. Crossing the binodal line leads to the formation of a dense liquid phase (DLP) (Gebauer et al., 2014; Wallace et al., 2013). In a cryo-TEM study conducted by Smeets et al. on dilute $CaCO_3$ solutions (5 mM), low-density spherical objects with a diameter of approximately 200 and 400 nm were observed, which were attributed to the presence of vitrified DLPs. The authors noted that the image contrast observed for this system was much lower than expected for ACC particles of comparable size, suggesting that the round objects were a low-density phase and had a high level of hydration. The amorphous nature of the observed particles was also confirmed by electron diffraction (Smeets et al., 2017).

In our work, the diffuse regions with higher contrast were mostly observed at the lowest concentration (0.5 mM). These regions exhibited lower contrast relative to ACC particles and, based on electron diffraction pattern analysis, were determined to have an amorphous nature. Therefore, the appearance of these diffuse regions of higher contrast could be explained by the formation of a dense liquid amorphous precursor phase resulting from the liquid-liquid phase separation.

5.2 Materials and methods

5.2.1 Sample preparation for cryogenic transmission electron microscopy

Supersaturated solutions containing 4.5 and 0.5 mM $CaCO_3$ were prepared through equimolar mixing of $CaCl_2$ and Na_2CO_3 (full details can be found in section 3.3.1.2 (sample preparation for Cryo-TEM study).

5.3 Results

5.3.1 Cryo-TEM study of $CaCO_3$ at a concentration of 4.5 mM after 5 minutes of the reaction

Continuing the discussion from the cryo-TEM results presented towards the end of chapter 4 (section 4.5.5), after 5 minutes of crystallisation reaction, cryo-TEM images of the 4.5 mM $CaCO_3$ solution revealed the presence of diffuse regions of higher contrast (relative to the background vitreous ice) with a diameter of ~3 µm (Figure 74 A). This diffuse region was identified as amorphous via selected

area electron diffraction (SAED) (inset). The thickness and density of the specimen will affect the image contrast. In thicker samples or regions with higher density, the image will appear darker. The Beer-Lambert law serves as a conceptual framework to understand how material density and sample thickness influence mass-thickness image contrast, I, in TEM. The given expression can be written as Eq.22:

$$I = I_0.exp\ (-S.\rho.t) \qquad (22)$$

Here I_0 represents the incident intensity, ρ denotes the sample density, S represents the effective total electron scattering cross section per unit mass of material, and t represents the sample thickness. We assume that the last two quantities are equal for both the diffuse region and the surrounding background (Mayerhöfer et al., 2020). Measurement of the intensity difference (the Gray value) between the diffuse region and the surrounding vitreous ice (Figure 74 B) would suggest that the density of the diffuse region is approximately 10% greater than the density of the background ice (which is 0.94 g/cm^3 for low density amorphous ice) (Yan et al., 2015).

In addition to higher contrast, diffuse regions, cryo-TEM imaging revealed the presence of various other structures. These included a network of loosely packed 2-10 nm sized particles which could be remnants of a DLP that has undergone dehydration (Figure 75 A-B). Additionally, much larger spherical ACC particles with diameters of approximately 60-480 nm were observed (Figures 74-78). Figure 74 A (top left) shows a large, isolated ACC particle that has formed within a surrounding region of higher contrast. These ACC particles were found to be distributed as a single particle or assembled in small groups (Figure 74-78). The ACC particles were subjected to STEM-EDX mapping (Figure 77 A-D) and revealed the presence of calcium and carbon. Meanwhile, Figure 78 A-B shows the emergence of calcite crystals from the larger ACC particles and the diffraction pattern associated with it confirms the existence of the (0 -2 2) calcite planes.

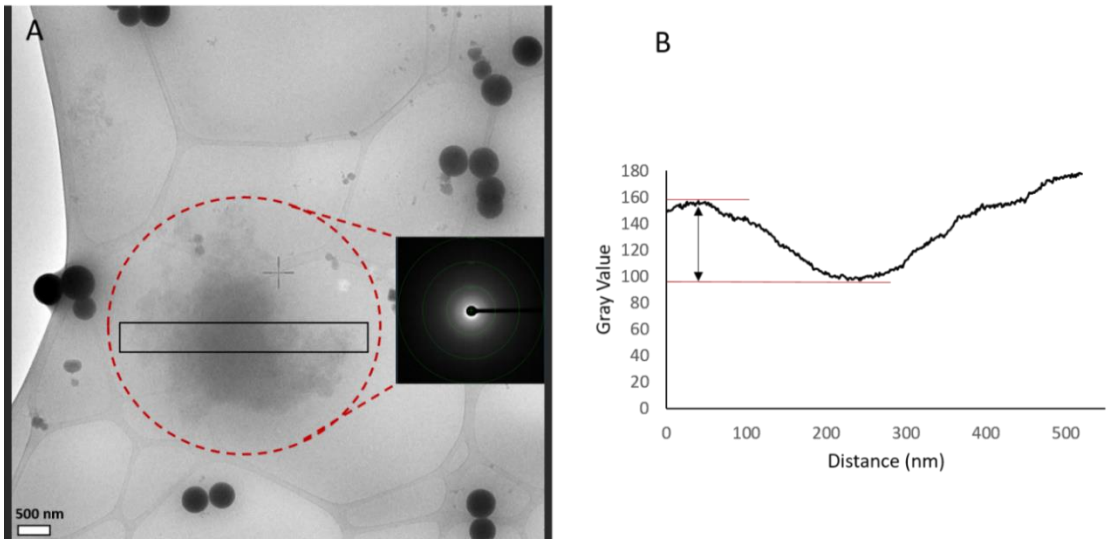

Figure 74. Cryo-TEM images of a 4.5 mM CaCO3 solution after 5 minutes of crystallisation reaction indicating: (A) the presence of ACC particles as well as a dense region of higher contrast; inset: the SAED pattern of the dense region confirming its amorphous nature. (B) Intensity line profile across the area of higher contrast and the surrounding ice (shown in the black box).

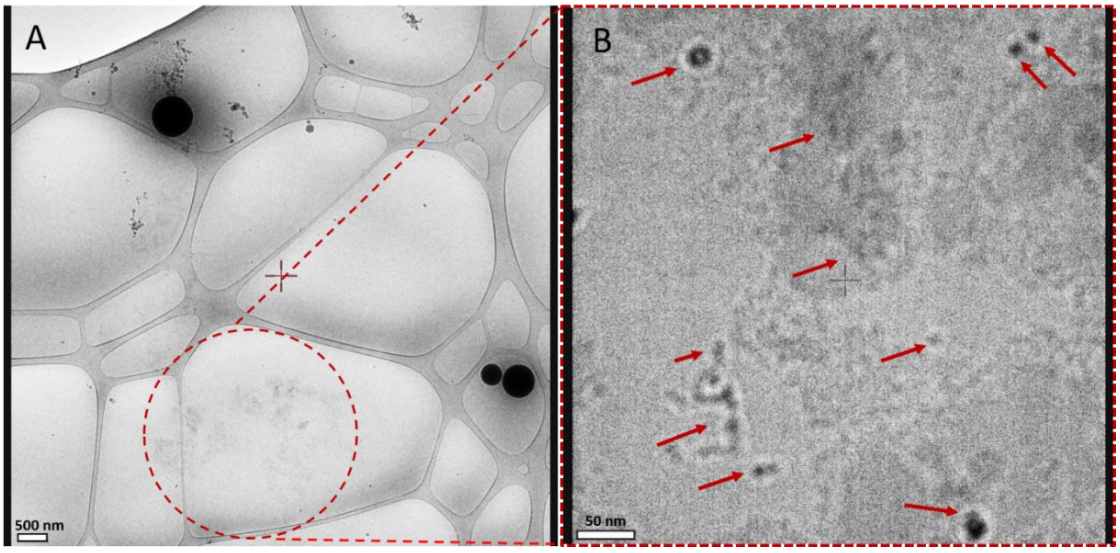

Figure 75. Cryo-EM observation of 4.5 mM $CaCO_3$ particles formed on the support film, showing (A) spherical ACC particles along with loosely packed nano particles (dashed red circle). (B) A higher resolution image from the dashed area in image (A) showing individual nanoclusters with size range of ~ 2-10 nm after 5 minutes (shown by red arrows).

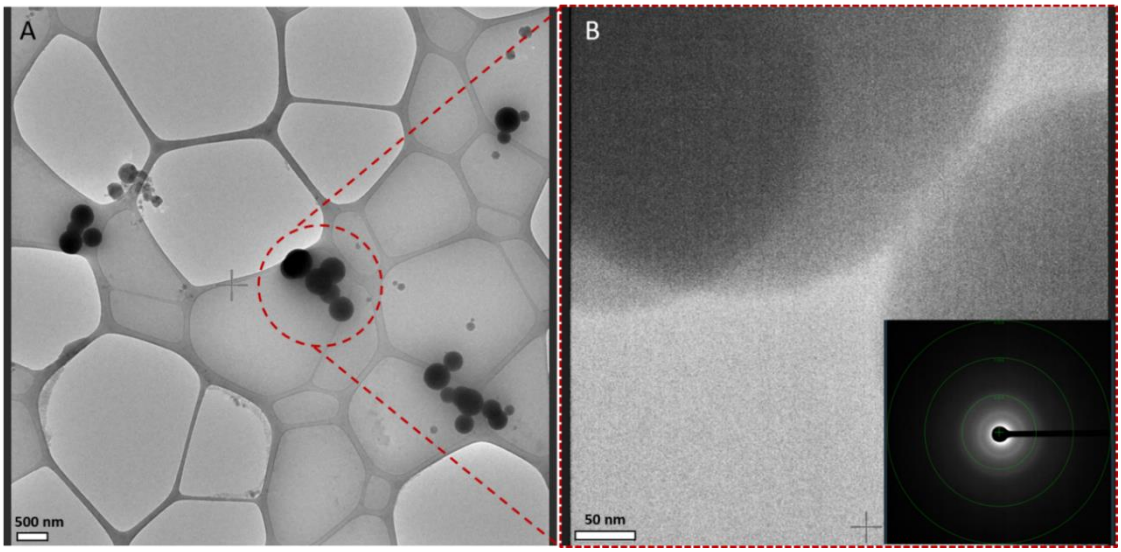

Figure 76. Cryo-TEM images of the $CaCO_3$ precipitates formed at the concentration of 4.5 mM after 5 minutes of the reaction: (A) showing spherical ACC particles. (B) High resolution image of the area in the dashed circle in (A). The inset in B is corresponding to the SAED pattern confirming that the particles are of an amorphous nature.

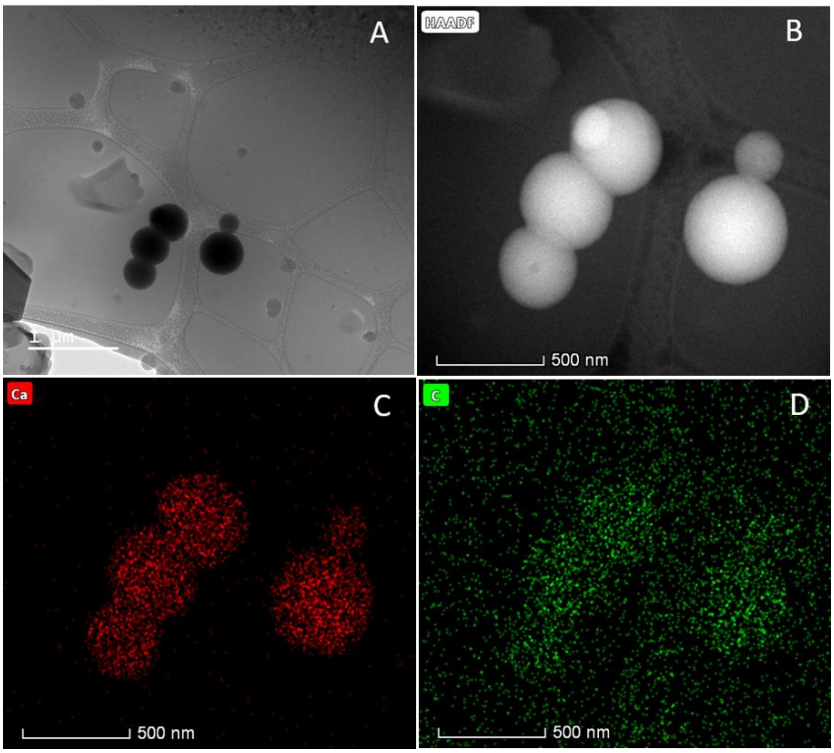

Figure 77. Cryo-TEM image of (A) ACC particles formed at a concentration of 4.5 mM after 5 minutes of the crystallisation reaction. In (B), a HAADF STEM image of the same ACC particles observed in image (A) is presented along with corresponding STEM/EDX maps: (C) demonstrates the presence of calcium in the ACC particles, and in (D) the presence of carbon is confirmed from both the sample and the lacy carbon grid.

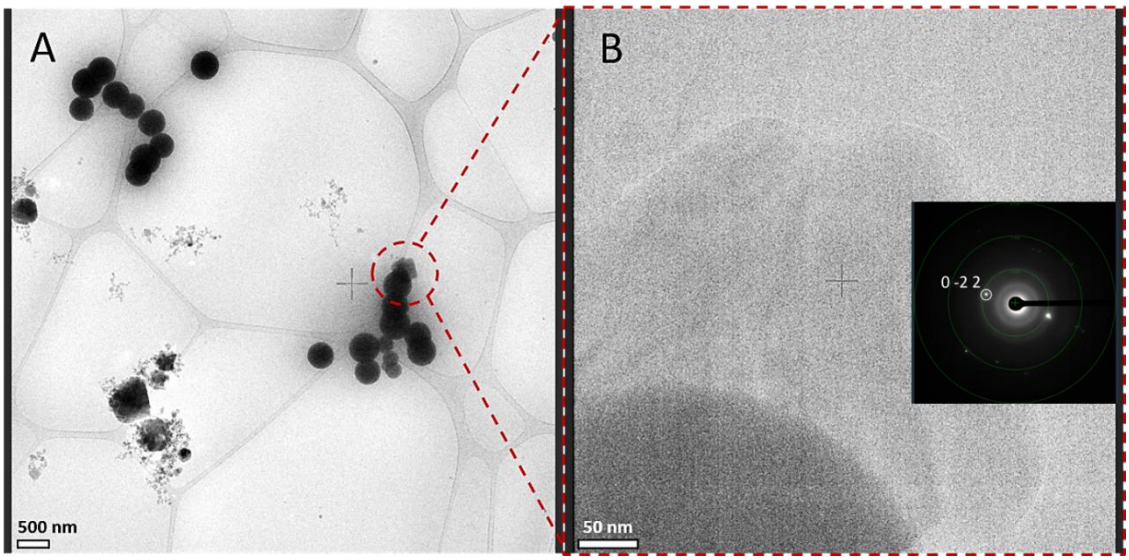

Figure 78. (A) Cryo-TEM observation of $CaCO_3$ particles at the concentration of 4.5 mM after 5 minutes showing spherical ACC particles as well as the emergence of calcite from ACC. (B) a higher magnification image of the region marked by the dashed circle in (A) with the corresponding SAED pattern which is labelled with (0 -2 2) crystal plane of calcite.

5.3.2 Cryo-TEM study of $CaCO_3$ at a concentration of 4.5 mM after 40 minutes of the reaction

In addition to the 5 minutes reaction time, the process of $CaCO_3$ crystallisation at a concentration of 4.5 mM was monitored after 40 minutes. Cryo-TEM observation revealed a large increase in the population of spherical ACC particles (ranging from 140 to 590 nm) in comparision to 5 minutes. The particles appeared denser and had started to form large aggregated networks as depicted in Figure 79 A. The corresponding SAED pattern confirms the amorphous nature of the ACC particles (Figure 79 B). Also, the formation of a faceted calcite crystal from ACC was observed after 40 minutes (Figure 80 A), however this was not prevalent in terms of abundance. The associated diffraction pattern confirms the presence of calcite, which spots corresponding to d-spacings of 2.08 Å and 1.06 Å which index to the (-2 2 2) and (-4 4 4) lattice planes of calcite respectively (Figure 80 B).

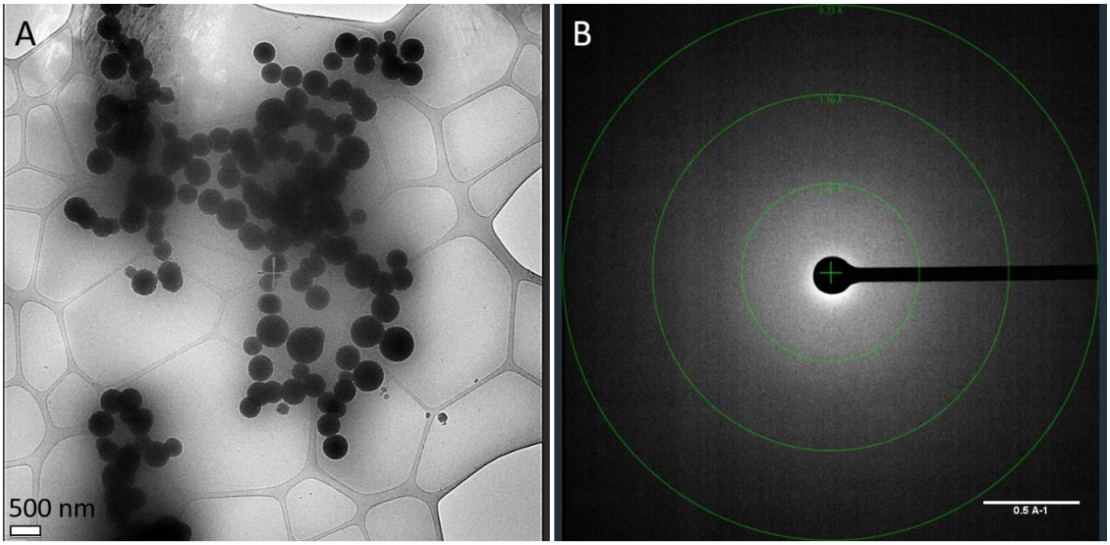

Figure 79. (A) Cryo-TEM image of $CaCO_3$ precipitates at the concentration of 4.5 mM confirming existence of ACC particles after 40 minutes with the corresponding amorphous diffraction pattern shown in (B).

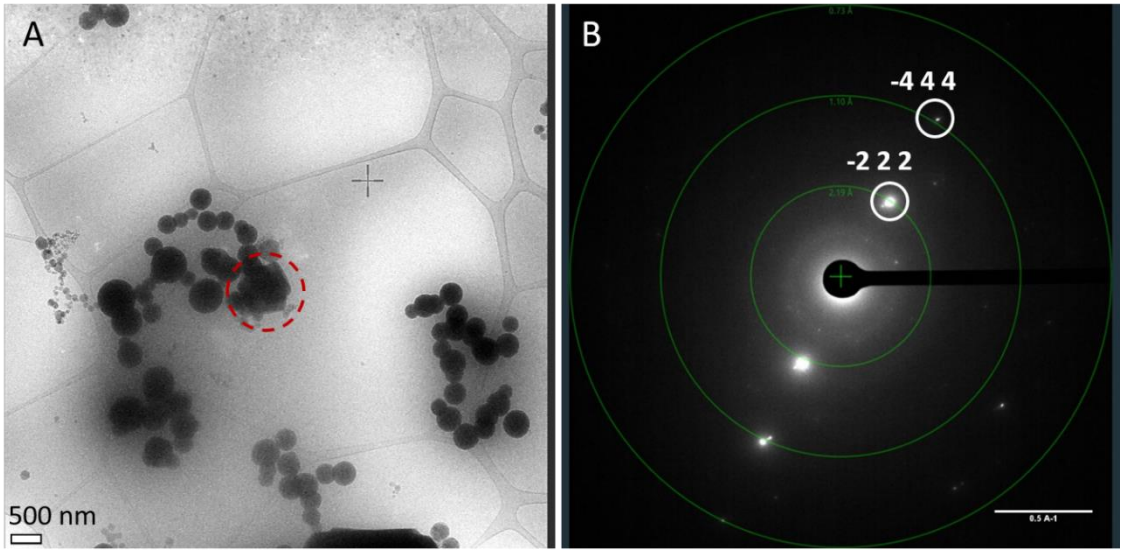

Figure 80. (A) Cryo-TEM image of 4.5 mM CaCO3 after 40 minutes showing the emergence of a calcite crystal from ACC particles along with (B) the corresponding SAED from the red-dashed circle in (A) indexed to the (-2 2 2) and (-4 4 4) crystal planes of calcite.

5.3.3 Cryo-TEM study of $CaCO_3$ at a concentration of 0.5 mM after 20 minutes of the crystallisation reaction

In the previous chapter, using the chemical quenching and simple drying sample preparation method for TEM, it was observed that a $CaCO_3$ concentration of 0.5 mM resulted in the observation of diffuse regions with

greater contrast after 5, 20 and 30 minutes of the crystallisation reaction (Chapter 4). Similar features were also observed at a concentration of 4.5 mM using cryo-TEM (Figure 74 A and 75 B). Therefore, further investigations were conducted to determine whether the formation of the diffuse regions of higher contrast would be observed at the lowest supersaturation levels – a concentration of 0.5 mM. After conducting a full cryo-TEM study, it was found that a network of loosely packed nanoparticles with a size range of 2-5 nm was observed after 20 minutes of the reaction, as presented in Figure 81 A (indicated by the red arrows). The right hand side of the cluster suggests that nanoparticles were more tightly packed at one end. The corresponding diffraction pattern confirms that these particles were amorphous (Figure 81 B). At the same time point (20 min), a different feature with a dimension of approximately 1.5 µm was also observed which showed a sharp edge with a vertex of 78 degrees at one end. According to Kimura et al. (2022), an angle of 78 º corresponds to the angle between two neighbouring faces (104) of the calcite structure, as shown in Figure 82 A (Teng et al., 1998). The corresponding electron diffraction pattern which is taken down the <031> direction reveals the (-2 -2 6) and (1 -2 6) planes of calcite (Figure 82 B). No formation of spherical ACC particles was observed at this stage.

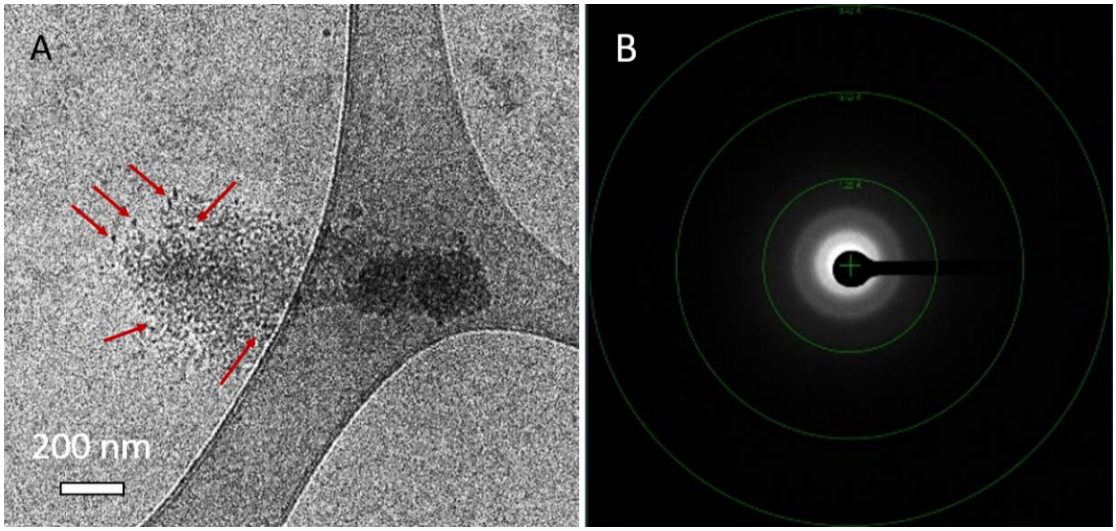

Figure 81. (A) Cryo-TEM observation of $CaCO_3$ precipitates at a concentration of 0.5 mM after a time period of 20 minutes showing loosely packed particles with a size range of 2-5 nm (red arrows) which are more tightly packed and denser at the right hand end of the cluster. (B) The associated diffraction pattern verifies the amorphous nature of the object.

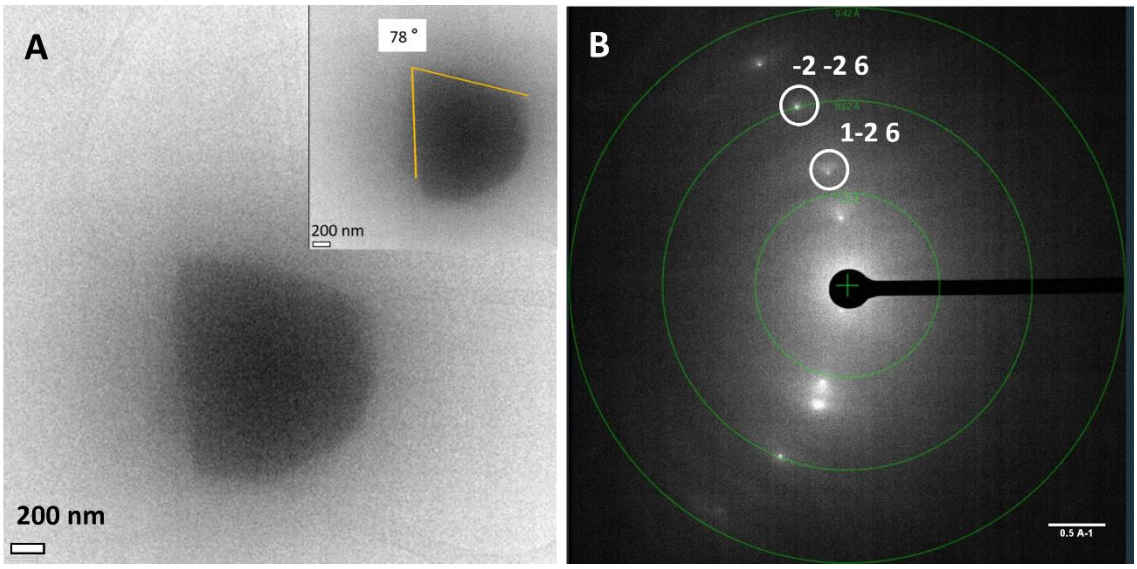

Figure 82. (A) Cryo-TEM image of 0.5 mM $CaCO_3$ after a time period of 20 minutes indicating the formation of calcite crystal. The inset ishows an angle of 78 °, corresponding to the angle of two neighbouring faces of the calcite (104) structure. The corresponding electron diffraction pattern from <031> direction corresponds to the (-2 -2 6) and (1 -2 6) planes of calcite.

5.3.4 Cryo-TEM study of $CaCO_3$ at the concentration of 0.5 mM after 45 minutes of the crystallisation reaction

At longer reaction time (45 minutes), in-situ cryo-TEM analysis also revealed the formation of diffuse regions of higher contrast with dimensions of approximately 2.5 µm, as presented in Figures 83 A and 84 A. The high-resolution image from Figure 83 A shows that the diffuse region of higher contrast consists of individual nanoparticles with an average diameter of 2-7 nm (the red arrows in Figure 83 B point out the individual nanoparticles). The associated diffraction patterns verify the amorphous nature of this feature. The black boxes in both Figure 83 A and 84 A are line scans through the diffuse region and the background vitreous ice, which indirectly measures the density difference between these areas from the change in mass-thickness contrast. The Gray value differences indicate that the diffuse regions of higher contrast are 30% and 20% denser than the background ice in Figure 83 A and 84 A respectively. In addition, at this time point, no evidence was found for the formation of ACC particles or crystals.

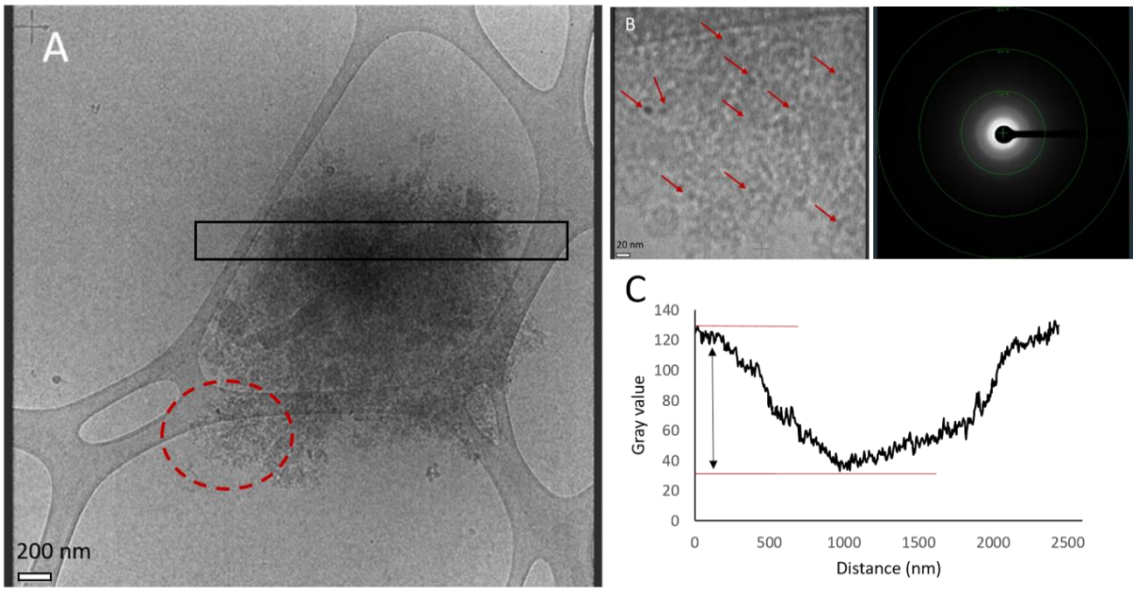

Figure 83. (A) Cryo-TEM Image of 0.5 mM $CaCO_3$ after 40 minutes reaction time where a diffuse region of higher contrast is visible. (B) A high-resolution cryo-TEM image of the dashed circle taken from image (A) shows nanoclusters with a size range of 2-7 nm (shown by the red arrows), with the corresponding diffraction pattern indicating that the particles are amorphous. (C) The Gray value line-scan across the black boxed area in (A) shows the intensity difference between the background ice and the diffuse region of higher contrast.

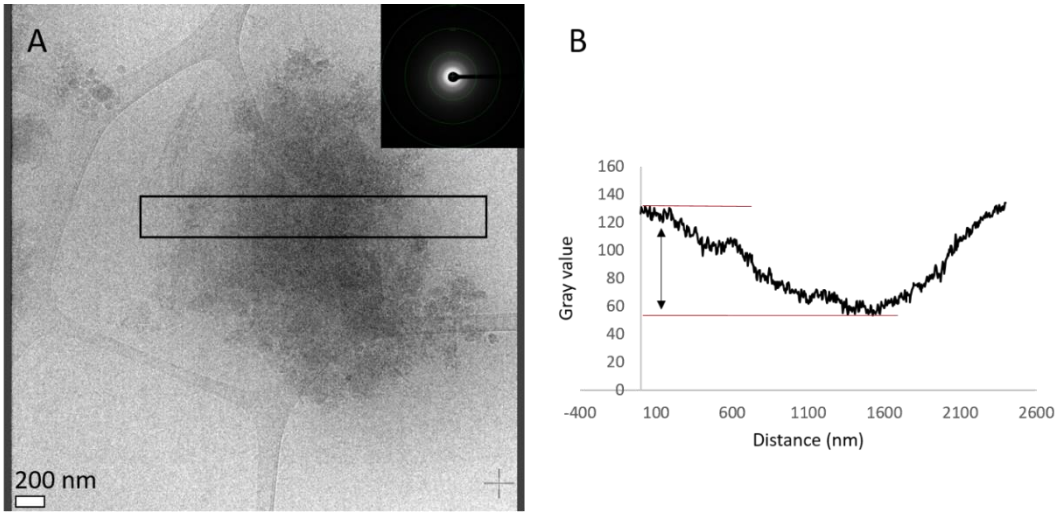

Figure 84. Cryo-TEM Image of 0.5 mM $CaCO_3$ after 40 minutes of the reaction reveals an amorphous diffuse region of higher contrast similar to that in Figure 83, but from a different area of the same grid to confirm the consistency of this structure. (B) Shows an intensity line scan (black box in (A)) through the diffuse region of higher contrast and the background ice.

5.4 Discussion of Cryo-TEM results

Cryo-TEM study was used to investigate the early-stages of the morphological and structural development of $CaCO_3$ precipitates formed in bulk solution. Cryo-TEM analysis of both the 4.5 mM and 0.5 mM supersaturated solutions of $CaCO_3$ revealed the structures and processes that contribute to the formation of $CaCO_3$, as follows:

1) Dense liquid phase regions evident as diffuse regions of higher contrast with dimensions of a few micrometres (Figures 74, 83 and 84),

2) Individual nano clusters with a diameter of 2-10 nm within the diffuse regions of higher contrast (Figures 75, 81 and 83),

3) Individual and aggregated spherical ACC particles (Figures 74-80);

4) Transition of ACC particles into calcite crystals (Figure 78 and 80); and

5) The emergence of calcite directly from the solution or through ACC (Figure 82).

The subsequent paragraphs will elaborate on each of the aforementioned structures in a sequential manner.

5.4.1 Dense Liquid Phase

At a concentration of 0.5 mM, after 20 and 45 minutes of the reaction, diffuse areas of higher contrast (~ 2-3 μm in diameter) were the most dominant features in Cryo-TEM images (as seen in Figures 81, 83 and 84). However, at a concentration of 4.5 mM, this feature was only observed once after 5 minutes of the reaction (as shown in Figure 74). The reason for the occurrence of diffuse regions of higher contrast at the lower concentration (0.5 mM) could be attributed to a reduced driving force at very low supersaturations. In fact, as the thermodynamic force decreases at lower supersaturation, the rate of precipitation slows down, therefore, the early stages become more visible. The diffuse regions of higher contrast were irregular in shape and were much larger and had a lower contrast than observed individual ACC particles. It is possible that the diffuse regions of higher contrast are precursor phases to ACC formation, such as dense liquid phases (DLP) which contain a significant concentration of calcium and carbonate ions and are highly hydrated (Avaro et

al., 2020). Furthermore, high resolution images of the diffuse regions of higher contrast reveals that these features contain individual and aggregated nanoclusters with a size range of 2-7 nm which were verified to be amorphous (as depicted in Figures 81 and 83).The nanoparticles were found to be loosely packed within these regions.The findings of our study are in agreement with those of Ramnarain et al. (2022), who used LC-TEM to visualize the process of transformation of dense liquid droplets through bimodal separation into nanoparticles of hydrated ACC. However, the presence of these droplets reported after 5 minutes of the reaction, which coalesced over time (15 minutes) and formed microdroplets of several micrometres in size. These microdroplets then transformed into nanoparticles of hydrated ACC (Ramnarain et al., 2022). Interestingly, Zou et al., (2017). have derived a phase diagram for $CaCO_3$ solutions as a function of concentration and temperature via SEM analysis of the observed size of ACC particles formed during the fast mixing of calcium chloride and sodium carbonate solutions (Zou et al., 2017). Applying established theories of phase separation, they predicted that the room temperature solution is unstable beyond a concentration of 3–4 mM of calcium and carbonate ions and will spontaneously precipitate ACC via spinodal decomposition. Below this spinodal limit, but above the solubility limit, they predict that the fluid mixture is metastable and can phase separate into a liquid rich in solvent and a liquid rich in solute (i.e. a dense liquid phase); at longer times, this dense liquid phase can potentially form a crystalline nucleus of composition close to the final one via thermal fluctuations and, if larger than the critical nucleus size, it can grow leading to a crystalline polymorph such as vaterite or calcite. This derived phase diagram fits well with our current cryo-TEM observations, in that at a concentration of 4.5 mM, we are above the spinodal line and observe the presence of both a dense liquid phase and ACC particles. At a lower supersaturation of 0.5 mM, we are in the metastable region and here we observe only the presence of a DLP which is significantly denser (approximately 20–30% denser than the surrounding vitreous ice based on a Beer–Lambert type analysis of cryo-TEM micrographs) than the DLP observed above the spinodal line, with no evidence for the formation of ACC particles at this lower supersaturation level. Smeets et al. (2017) employed cryo-TEM to investigate the morphological and structural changes during the precipitation of

$CaCO_3$ at a concentration of 1 mM.The study revealed the presence of spherical amorphous objects with sizes ranging from 200–400 nm. These entities exhibited a lower mass contrast when compared to ACC particles (the mass contrast was determined using the Beer-Lambert law). The observed objects were suggested to be droplets of a DLP embeded in vitrified ice, which subsequently transformed into vaterite without the formation of ACC. Although, our concentration and the characterisation method were very similar, the morphology of their observed DLP differed from our observations and they demonstrated the formation of vaterite through the DLP (Smeets et al., 2017).

5.4.2 Individual nano clusters with a diameter of 2-10 nm

A network of loosely packed structures containing individual nanoclusters in the size range of 2-10 nm (Du and Amstad., 2020; Sebastiani et al., 2017; Smeets et al., 2017) (Su et al., 2021) was also observed at a concentration of 4.5 mM after 5 minutes of the reaction (Figure 75). Additionally, after 40 minutes of the reaction time, these clusters were observed within the diffuse region of higher contrast (Figure 81 and 83). As discussed previously, this structure could be attributed to dehydration of DLPs into nanoparticles of hydrated ACC (Ramnarain et al., 2022b). The particles that underwent dehydration can then self-assemble to form ACC particles or dissolve into ions and then recrystallise.

5.4.3 Individual and aggregated spherical ACC particles

At the concentration of 4.5 mM, the number of ACC particles increased progressively over time (from 5-40 minutes), with a tendency towards assembly and formation of more densely packed ACC particles. The dimensions of the particles increased over time, from an initial range of 60-480 nm to a larger range of 140-590 nm (Figures 74-80). Conversely, no spherical ACC particles were observed at the concentration of 0.5 mM. The absence of ACC at the lowest concentration, could be explained by the fact that a reduced concentration of solutes in the solution results in a weaker driving force for nucleation and crystal formation. From a kinetic point of view, lower supersaturation results in a decreased rate of nucleation and growth of ACC particles (Vedantam and Ranade, 2013).

5.4.4 Direct transfomation of ACC particles into calcite crystal

In Figure 78, a distinct morphology with sharp edges which can be associated with crystalline structures was observed after 5 minutes in the immediate region of ACC particles. The diffraction pattern further confirmed the phase as calcite. After 40 minutues (Figure 80), calcite particles were observed which had doubled in size compared to the 5 minutes reaction results. Additionally, the diffraction pattern indicated the presence of calcite, providing evidence for the formation of calcite crystals from ACC particles at both 5 and 40 minutes of the reaction. Nielsen et al. studied the early stages of crystallization of $CaCO_3$ and its nucleation pathway using in-situ TEM. Multiple pathways in the formation of $CaCO_3$ were observed, including the direct nucleation and growth of ACC and vaterite, the direct transformation of ACC into crystalline phases such as aragonite and vaterite, and the simultaneous nucleation and growth of calcite crystals directly from the solution. However, the transformation of ACC to calcite was not observed (Michael H.Nielsen, Shaaul Aloni, 2014).

5.4.5 Emergence of calcite from the solution or trough ACC?

Finally, cryo-TEM imaging captured the emergence of rhombohedral calcite (Figure 82 A) with a diameter of approximately 1.5 μm from the solution after 20 minutes of the reaction, at a concentration of 0.5 mM. A sharp edge, which is a characteristic of calcite, was also observed on one side of the crystal, while the other part was not fully formed. The face angle was measured to be ca. 78 degrees, which corresponds to a typical angle observed in calcite crystals (Kimura, 2022). Additionally, the corresponding diffraction pattern indexed to the planes of a calcite crystal. The formation mechanism of calcite remains unclear in this case, as it is uncertain whether it occurs directly from the solution or through ACC particles. The formation of calcite could occur from the ACC particles that are either stacked on top of each other or aggregated. However, the image quality is not sufficient to provide a clear visualization or confirmation of this process.

There are differing theories regarding whether $CaCO_3$ nucleation occurs through CNT or through the pre-nucleation cluster (PNC) pathway Nielsen et al., (2014). Avaro et al. (2020) introduced a quantitative approach that indicated that transformation of ACC through the dehydration of the liquid precursors can

be explained by the non-classical mechanism rather than by classical theory (Avaro et al., 2020). Ramnarain et al. (2022) also observed the birth and evolution of microdroplets of $CaCO_3$ using LCTEM through nonclassical pathways (Ramnarain et al., 2022).

5.5 Conclusions from Cryo-TEM study

In this cryo-TEM study, diffuse regions of higher contrast were observed at short times and at low supersaturation. Based on the existing literature, these regions could represent early-stage products originating from potential DLP regions which later dehydrate and solidify to ACC particles or may even directly transform into crystalline structures.

Our results suggest that that the precipitation of $CaCO_3$ potentially follows a multi-step process shown schematically in Figure 85. This includes the formation of dense liquid phases that undergo dehydration. Within the DLP structure, individual amorphous nano clusters with diameters ranging from 2 to 10 nm are observed, which subsequently are replaced with either individual or aggregated spherical ACC particles. The ACC particles then replaced by calcite.

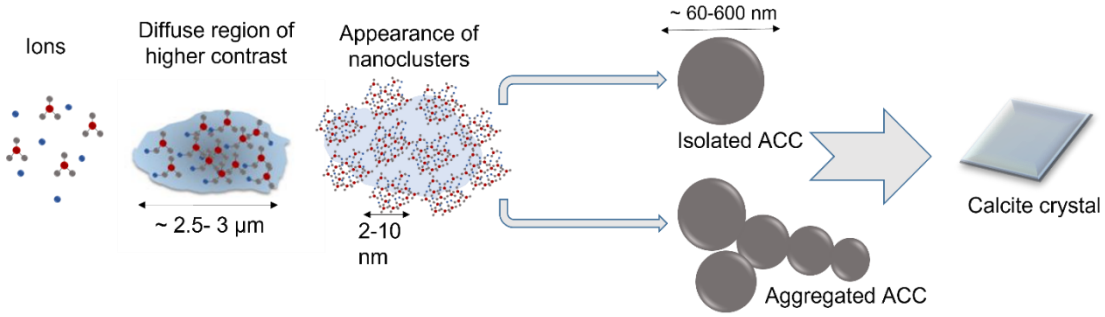

Figure 85. Proposed pathway of precipitation of $CaCO_3$ through non classical pathway.

5.6 Transformation process of 4.5 mM $CaCO_3$ through real-time liquid cell TEM

Cryo-TEM captures a momentary snapshot of the processes occurring in a crystallising solution. In principle LC-TEM can view these processes in real time although the technique suffers from the issues mentioned in Chapter 3 section

3.1.6, including the effects of the electron beam on the chemistry of the solution, as well as confinement effects and potentially non-uniform flow and mixing of solutions. Furthermore, capturing the actual moment of nucleation remains a challenge because the direct mixing of the $CaCO_3$ solution take place before the observation window. Therefore nucleation could occur prior to the observable area. However LC-TEM studies of the crystallisation of calcium carbonate were investigated and are detailed below.

5.6.1 Sample preparation

Stock solutions of equimolar amounts of $CaCl_2$ and Na_2CO_3 were prepared for real time observation of the $CaCO_3$ crystallisation process (full details in section 3.1.3).

5.7 Results

In situ observation of the formation of $CaCO_3$ at a concentration of 4.5 mM revealed the presence of four distinct particles with diameters of approximately 1 μm from various parts of the window 30 minutes after initiating the liquid flow, as depicted in Figure 86 A-D. This experiment was conducted 5 times, but in only one experiment was precipitation observed within the field of view and vaterite was only observed once. Based on the morphology and size of these particles (from previous cryo-TEM observations, and those using dried samples, ACC particle sizes do not exceed 600 nm hence these particles should not be ACC), it can be inferred that all four formed particles shown in Figure 86 are vaterite. In order to ensure that the observed phenomena were not a result of the beam, as soon as $CaCO_3$ solution was flown through the inlets, the beam was blanked and then unblanked after 30 minutes of the reaction. EDX analysis were carried out to identify the elemental composition of the particles. However, the particle underwent dissolution event when subjected to irradiation by a focused electron beam. The dissolution occurred so rapidly that after one minute of irradiation, the particle showed a significant reduction in size until it nearly disappeared (Figure 87 A-C).

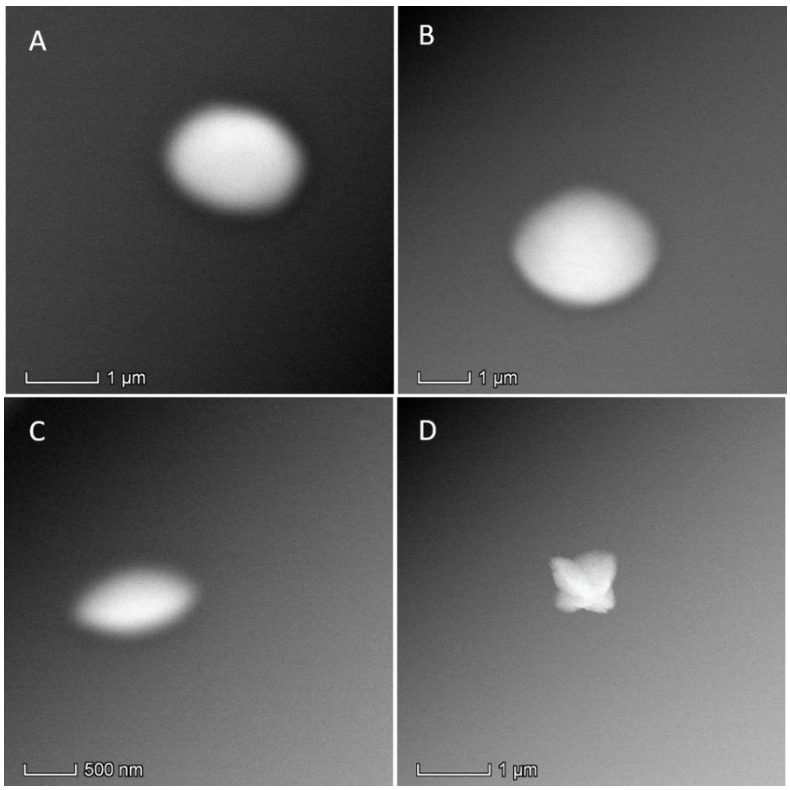

Figure 86 HAADF STEM images of 4.5 mM $CaCO_3$ (equal ratio of Ca^{2+}: CO_3^{2-}) after 30 minutes of mixing the solutions in real- time (A-D) showed that the precipitates were vaterite. Vaterite was only observed once out of 5 repeat experiments.

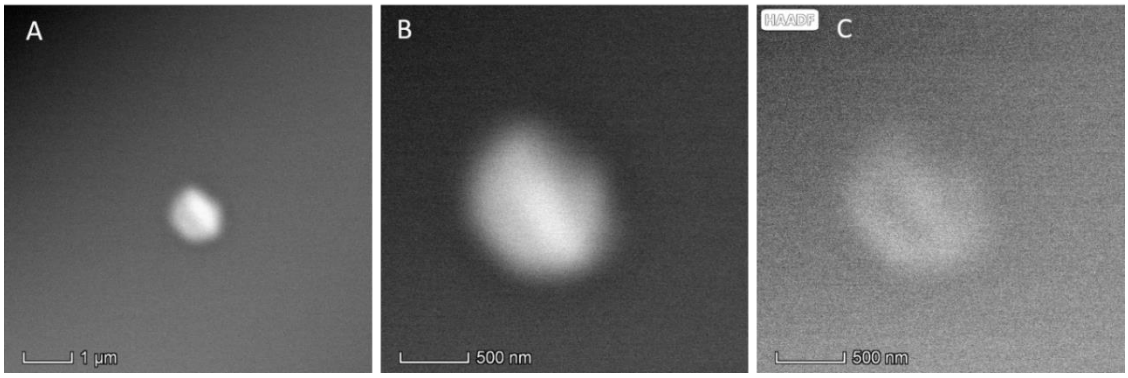

Figure 87 LC-TEM study of 4.5 mM $CaCO_3$ showing the disappearance of a particle 1 min after EDX was conducted.

5.7.1 The effect of pH variation on the formation of $CaCO_3$ using PHREEQC modelling programme.

The impact of pH variation on the precipitation of $CaCO_3$ was investigated using the PHREEQC thermodynamic modelling software (Mosley et al., 2015). The software was employed to predict ion speciation and calculate the pH of water

under thermodynamic equilibrium (Luke M Mosley et al., 2015). The experimental data values, with a molar concentration of 4.5 mM, was used as input for the simulations. To conduct preliminary studies, a mixture of identical molar ratios of 20 mL of 9 mM $CaCl_2$ and 20 mL of 9 mM Na_2CO_3 was modelled at room temperature, resulting in a final concentration of 4.5 mM $CaCO_3$. Figure 88 shows the formation of different species of $CaCO_3$ as the pH of the system changes according to PHREEQC calculations. The results show that all $CaCO_3$ solid phases will undergo precipitation when the pH of the system surpasses 7 and the SI > 0 and also demonstrate a clear correlation between the pH value of the system and the saturation index (SI), whereby a decrease in pH (< 7) leads to a negative SI (i.e., dissolution) for all species. The molality of $CaCO_3$ aqueous phase containing Ca^{2+} and CO_3^{2-} ions was plotted against pH values as shown in Figure 89. The results demonstrate the carbonate-bicarbonate equilibrium and indicate that at very low pH values, dissolved CO_2 is the dominant species and the amount of Ca^{2+} ions present in the solution remains constant below pH 6.

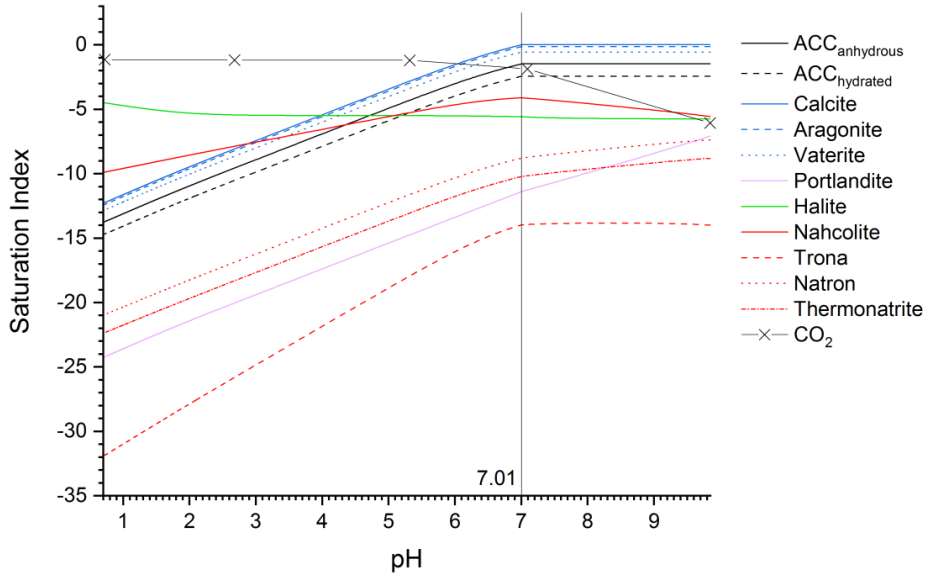

Figure 88 Saturation index of all possible solid phases of $CaCO_3$ as a function of pH.

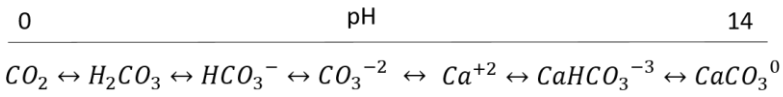

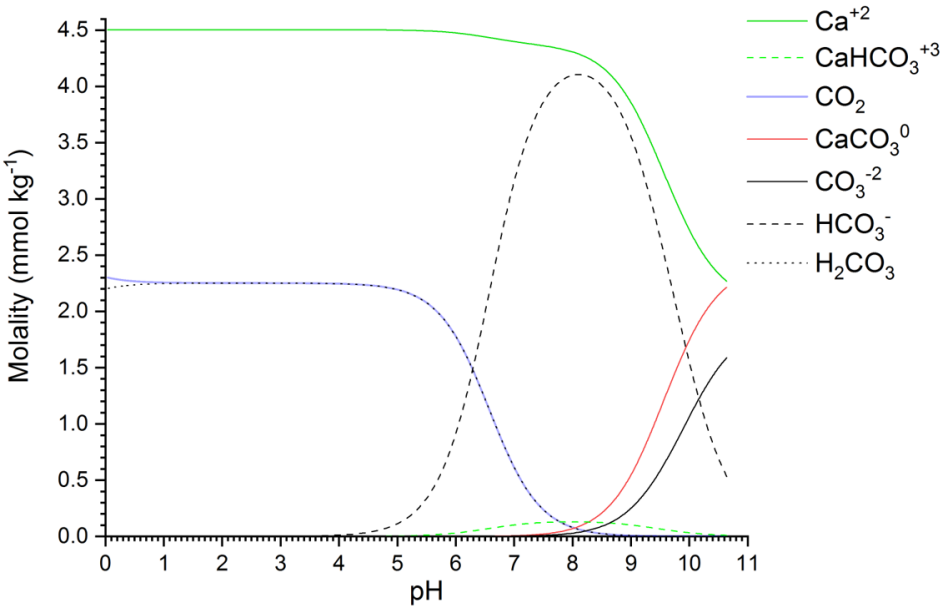

Figure 89 Effect of pH on the formation of various species of $CaCO_3$ in the solution.

5.7.2 The effect of confinement on the crystallisation of 4.5 mM $CaCO_3$

An investigation of precipitation in confinement (200 nm spacer) was carried out via ex-situ studies with the LC-TEM chip. A $CaCO_3$ solution with a supersaturation of 4.5 mM was prepared by flowing equal quantities of equimolar aqueous solution of 9 mM Na_2CO_3 and 9 mM $CaCl_2$ through the inlets of liquid cell holder at a flow rate of 0.5 ml/min. The flow was stopped after a specific time point and experiment was terminated after different time periods (15 minutes, 1 and 3 hours), by separating the surfaces of the chips. For the 15 minutes time point, air was pushed into the inlets of LC chips. However, for the 1 hour and 3 hour time points, ethanol was used to quench the reaction. The chips were then imaged using SEM. SEM images of LC chips showing where the crystallization of $CaCO_3$ occurred are presented in Figure 90 (A-C). Figure 90 A shows a low magnification image of the upper and lower LC chips. Higher magnification images in Figures 90 B and 90 C, show the windowed region where the crystallization process is examined in the TEM, indicated by black and white arrows, respectively.

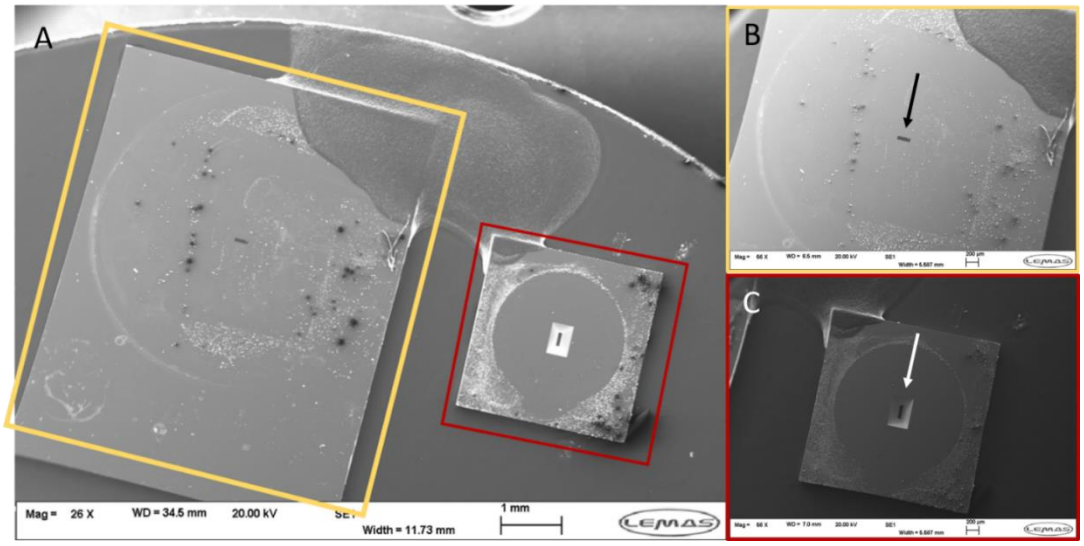

Figure 90 (A) SEM images illustrating the separated liquid cell chips where crystallisation reaction occurred. (B and C) display the upper and lower chips respectively. The black and white arrows show the confined area of the window.

In Figure 91 A, the low-magnification SEM images of the 15-minute sample show the distribution of $CaCO_3$ precipitates within the LC chips. To stop the reaction, air was blown into the inlets of LC chips at the end of the experiment. Nevertheless, when the chips were separated, it was noted that the window had shattered during opening. It is evident that more particles tend to form towards the non-confined regions located outside the viewing window. Conversely, fewer particles are observed towards the confined area, which could be due to its limited space, poor mixing resulting in changing concentration, or the creation of diffusion-limited growth. Confinement can affect the nucleation and growth of mineral phases in nanometre scale-pore spaces. Experimental evidence has shown that the nucleation pathways, selection of polymorphs, and morphologies of crystals are all influenced by the geometry of the confined spaces in which crystallization takes place. Additionally, it has been observed that confinement creates a thermodynamic barrier that controls the transformation rate, thereby playing a significant role on the dynamics of particles (Cavanaugh et al., 2019). The SEM image shown in Figure 91 B is a higher magnification view of the region within the red square in Figure 91 A. Figure 91 C is an even higher magnification SEM image of the white dashed square in Figure 91 B, which shows the formation of hexagonal vaterite and

rhombohedral calcite. Figure 91 D illustrates that EDX mapping identifying the presence of calcium, oxygen, and carbon.

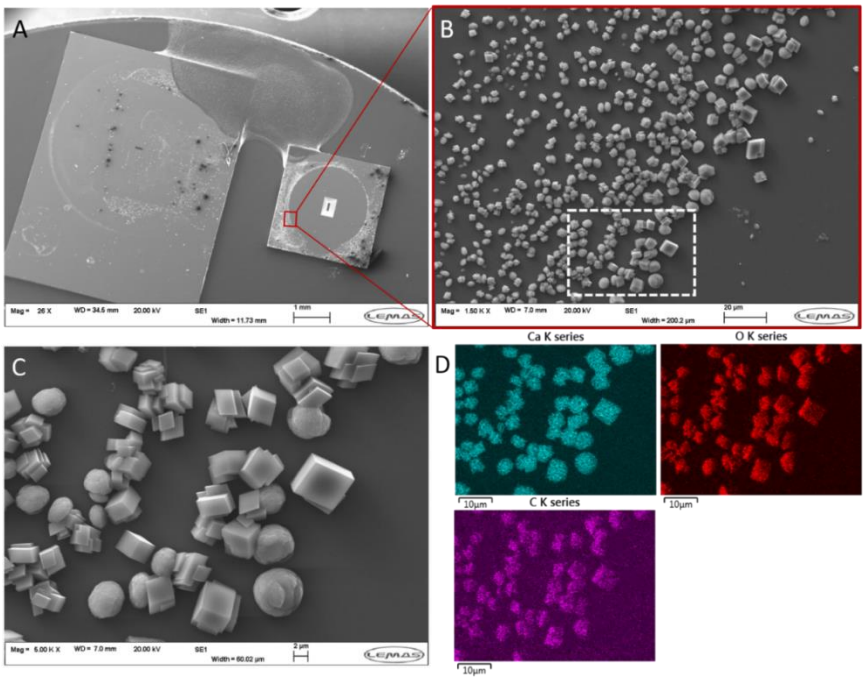

Figure 91. SEM images of separated LC chips at 4.5 mM concentration after 15 minutes of the reaction. (A) Displays low-magnification images of the chips, while (B) shows a higher magnification view of the region within the red square in A. (C) Presents a higher magnification SEM image of the white dashed square in B, and D depicts the SEM/EDX elemental mapping of the elements identified in C. Notably, no ethanol was used in this experiment.

For the crystallisation reaction after 1 hour, significantly fewer particles were present when compared to the sample taken at 15 minutes (as shown in Figure 92). The decrease in the number of particles observed is attributed to the use of ethanol to halt the crystallization reaction. Figure 92 A presents a low-magnification image of the LC chips, while Figure 92 B provides a higher magnification view of the confined window area, as indicated by the yellow arrows. Figure 92 C (a higher magnification image of blue dashed square in Figure 92 A) highlights a large number of particles formed in the unconfined area, with morphologies consistent with vaterite and calcite. However, in Figure 92 D (an enlargement of the red dashed square from Figure 92 B) reveals only a few aggregates of particles formed within the confined window region. These particles do not exhibit a distinct morphology similar to that of spherical ACC particles or crystalline forms of $CaCO_3$ such as calcite and vaterite. These

findings confirm that confinement can affect the morphology and size of particles. These results are comparable to those of our earlier study (section 4.3.4), which showed that after 20 seconds of the reaction, micro-sized calcite had already formed in bulk solution.

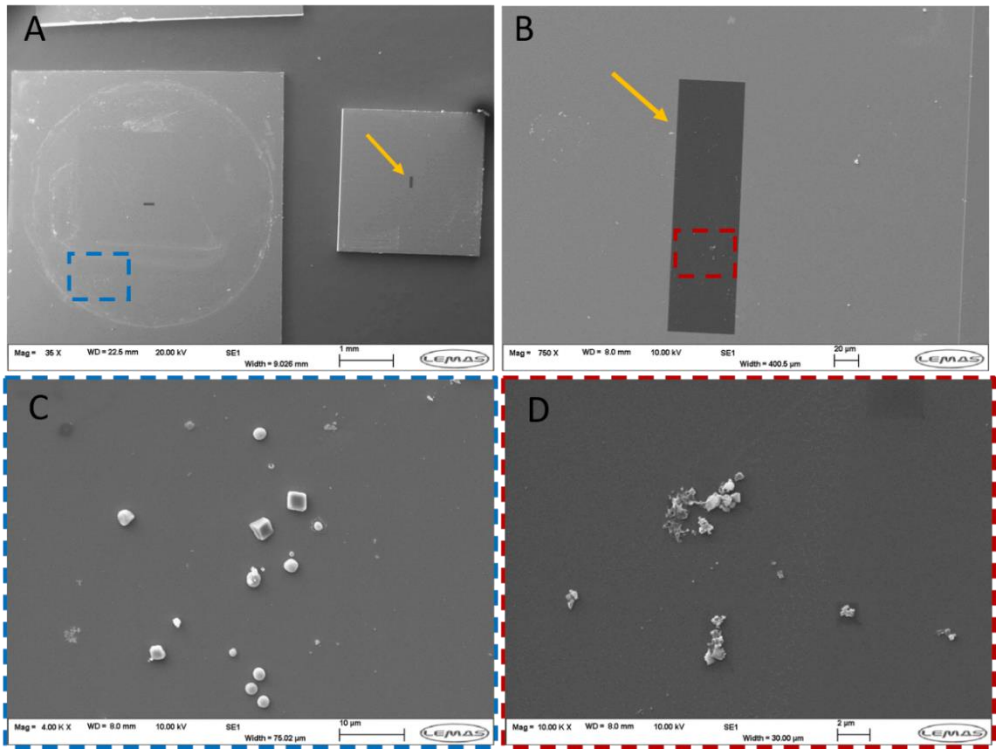

Figure 92. SEM images of particles formed in the confined space of liquid cell chip at a concentration of 4.5 mM after 1 hour. Here ethanol was used to stop the reaction.

At a solution concentration of 4.5 mM and a precipitation time of 3 hours, it is evident from the SEM image in Figure 93 A that the window had fractured during the process of separating the chips. Figure 93 B shows a higher magnification view of Figure 93 A at the position of the yellow arrow. Figure 93 C is an enlargement of the red dashed square in Figure 93 B and reveals that the precipitates were ACC particles, with a typical spherical shape. Figure 93 D is an enlargement of the blue dashed circle in Figure 93 B where the precipitates were identified as rhombohedral calcite. Micron-sized aggregated calcite particles were also observed outside the confined region, as shown in the Figure 93 E.

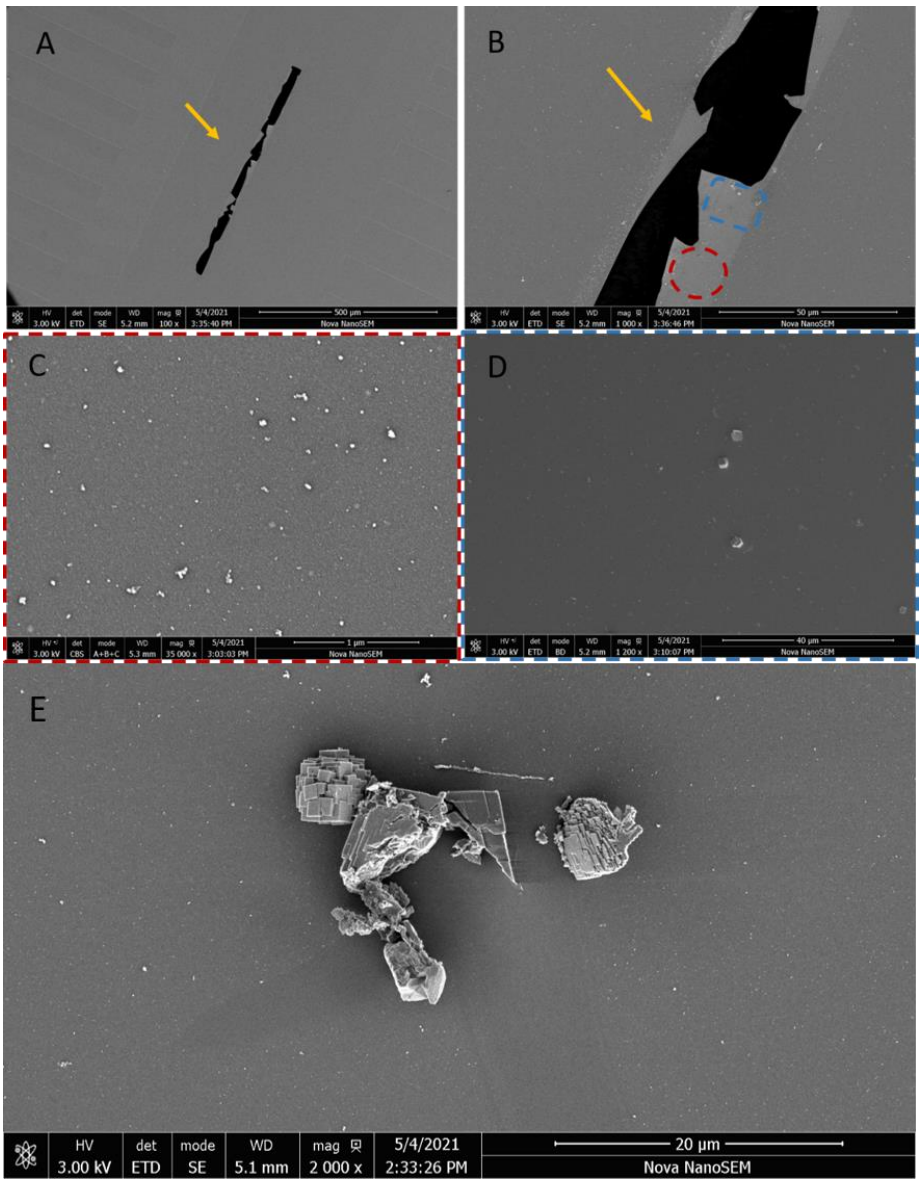

Figure 93 SEM images of particles formed in a confined space of liquid cell holder at the concentration of 4.5 mM after 3 hours. Ethanol was used to stop the reaction.

5.8 Discussion of liquid cell TEM results

The advanced technique of LC-TEM enables dynamic observation of particles. In this study, LC-TEM chips have been utilised as a controlled area of confinement to explore the crystallisation of $CaCO_3$. However, capturing the actual moment of nucleation remains a challenge because the direct mixing of the $CaCO_3$ solution takes place well beyond the observation window. Therefore, nucleation occurs prior to the solution entering the observable area. The spherical-shaped particle that was observed after 30 minutes of the reaction is a

post-nucleation product (Figure 86). Therefore, it is highly probable that the nucleation event occurred very early on at the initial point of fluid mixing. When imaging liquids within an electron microscope, it is essential to consider various factors that may affect the observations. These factors include the influence of the confined area, which is evident in all the specimens, as a considerable number of particles are observed to be formed outside the window chips. This is in contrast to the window (the confined region), where a lower number of particles are observed, as depicted in Figures 91-93. The confinement can have an impact on both the thermodynamics and kinetics of nucleation and crystal growth (Meldrum and O'Shaughnessy, 2020b) (section 2.4.6). Another important factor is the effect of electron beam on the crystallisation process of $CaCO_3$. Schneider et al., (2014) investigated the impact of irradiating electron on the aqueous medium within the liquid cell. They demonstrated that exposing both neutral and alkaline solutions to a beam of electrons with a dose rate of $>10^5$ Gy/s causes a substantial impact through the radiolysis of water, which can alter the solution's chemistry by changing the pH of the system (Schneider et al., 2014). If the pH of the solution is decreased, the increased activity of hydrogen ions causes CO_3^{-2} ions to react with H^+ ions, producing bicarbonate ions, carbonic acid, and carbon dioxide. This reduction in the number of CO_3^{-2} ions present in the solution hinders the formation of $CaCO_3$ and actually causes any carbonate species to dissolve (see Figure 89). Therefore, it can be concluded that LC-TEM can directly affect the crystallization process because the electron beam can reduce the pH of water, and $CaCO_3$ cannot precipitate at low pH.

5.9 Conclusions from LC-TEM Study

The study of $CaCO_3$ crystallization using LC-TEM demonstrates that the decrease in pH within LC-TEM chip caused by the radiolysis of water by the electron beam results in the dissolution of $CaCO_3$, even at relatively low electron flux. The substantial number of particles that were observed outside the window of the chips, in comparison to the confined region where a lower particle count was observed, highlights the influence of the confined area on the bulk behaviour. This is presumably a combination of the confined volume and

the heterogeneous nature of the flow pattern through the LC-TEM chip. Hence overall it is unclear how representative and reproducible LC-TEM results are of the native state of crystallising solutions suggesting that cryo-TEM provides a more faithful analysis. One advantage of Cryo-TEM technique is that multiple analysis, e.g., EDX and electron diffraction, can be carried out on the same sample in a fixed state which minimises the effects of radiolysis and pH change.

Chapter 6 Results

6.1 $CaCO_3$ polymorph selection during crystallisation process

In the previous chapters, it has been demonstrated that an equimolar ratio of Ca^{2+} to CO_3^{2-}, under normal room temperature conditions and without the presence of additives, typically results in the transformation of ACC into polycrystalline structures such as cauliflower vaterite, and rhombohedral calcite. However, aragonite was not observed under these conditions (chapters 4 and 5).

Calcite, the thermodynamically stable polymorph of $CaCO_3$, typically forms under low supersaturation conditions during $CaCO_3$ crystallization. However, the precipitation of kinetically favoured polymorphs such as ACC, ikaite, vaterite, or aragonite can be achieved by increasing the supersaturation level, adjusting the crystallization temperature, or introducing specific additives (Jessica M. Walker et al., 2017). ACC is known to undergo transformations into both calcite and aragonite during bio- mineralization, however there are limited instances of ACC transforming into aragonite in synthetic aqueous systems. Biologically produced ACC incorporates magnesium ions and organic molecules, which serve to prolong its lifetime and significantly influence the resulting crystal polymorph which is ultimately formed (Zhang et al., 2022).Therefore, the objective of this chapter is to concentrate on the early stages of polymorph selection, particularly the process of aragonite formation over calcite in synthetic aqueous systems.

Magnesium ions are recognized as the most influential additive for aragonite synthesis (Park et al., 2008; Clark et al., 2022). Additionally, there is evidence showing that solutions containing alcohol, confined systems, other additives (SO_4^{2-}, PO_4^{2-} Poly acrylic acid (PAA)) (Zou et al., 2018) (Clark et al., 2022), or elevated temperatures can be utilized to fine-tune or control the crystallization process (Zhang et al., 2022).

In this chapter, my focus is to gain understanding of the early stages of aragonite crystallization using SEM, TEM, and Cryo-TEM. For this purpose, three different systems were investigated to examine polymorph selection under

room temperature conditions. Firstly, the well-known effect of $Mg^{2+,}$ which encourages aragonite formation, was initially utilized. In addition, the chemistry of solution was investigated by employing an excessive quantity of either (a) carbonate ions and, in a separate experiment, (b) calcium ions.

6.2 Methodology

6.2.1 Sample preparation of the Mg^{2+} rich system

The precipitation of $CaCO_3$ was carried out in the presence of $[Mg^{2+}]$: $[Ca^{2+}]$ ratio maintained at 4:1, to promote the formation of aragonite using the Ammonium diffusion method (ADM) (Ihli et al., 2013). The presence of amorphous and crystalline structure of $CaCO_3$ polymorphs, were analysed using a SEM and TEM (full details can be found in section 3.3.3).

6.3 Results

6.3.1 Precipitation of $CaCO_3$ in the presence of Mg^{2+} using ADM

SEM observations at lower magnification revealed a substantial network of precipitates that appeared as desert rose-like structures, with individual sizes of approximately ~1.5 µm after 30 minutes of the reaction. These precipitates were aggregated into a network of ~10 µm on the silicon wafer, as shown in Figure 94 A. Subsequently, a TEM study was conducted to visualize the precipitates at a higher magnification. A network of nano-sized spherical particles ranging in size from 30 to 70 nm was observed on a gold Quantifoil grid. The presence of calcium and magnesium elements in this structure was confirmed by EDX analysis. However, the ratio of magnesium to calcium is quite low at 1:5 (inset from the Figure 94 B). Moreover, the amorphous nature of these particles is verified by SAED analysis, suggesting that they are ACC particles with incorporation of Mg^{2+}, as illustrated in inset of Figure 94 B. Figure 95 A illustrates the structure of desert rose-like particles after 1 hour of the reaction, which contain magnesium as confirmed by the inset EDX analysis. Figure 95 B is an EDX map of the desert rose-like structure, which shows the incorporation of both Mg^{2+} and Ca^{2+} within the particles. After 3 hours of the reaction, the formation of spherical particles ranging in size from 300 nm to 2 µm, as well as spindle-shaped aragonite with a size range of 200-470 nm was observed, as

shown in Figure 96 A-B. EDX analysis confirmed the presence of both magnesium and calcium within the structure of spherical particles Figure 96 B. There is no evidence for the presence of desert rose-like morphology after 3 hours. A TEM study was also conducted to further study the precipitates that formed on the Quantifoil grids by performing SAED on the particles to determine whether they were amorphous or crystalline. Only spherical particles with an amorphous nature were captured using TEM as shown in Figure 97 A-C. This experiment was done only once.

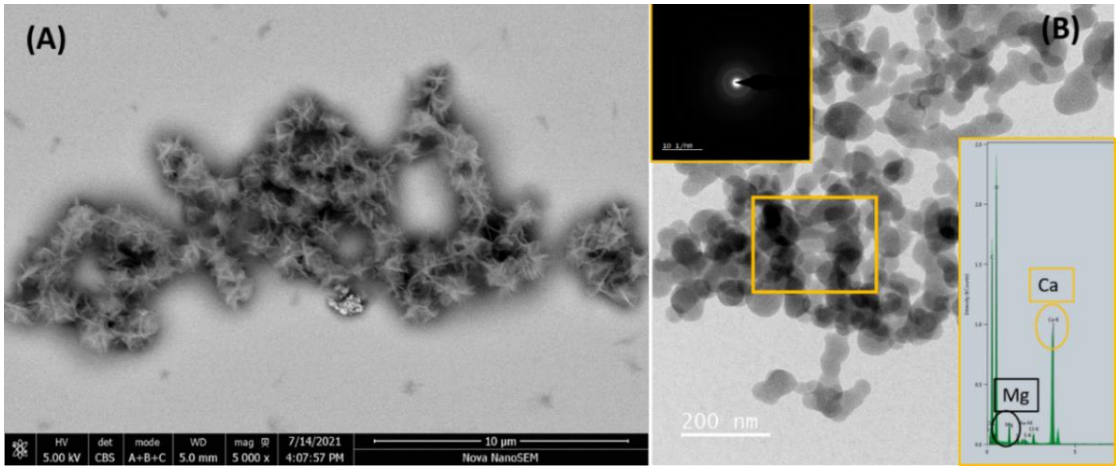

Figure 94 (A) SEM image of the precipitates formed at a concentration of 400 mM MgCl2 and 100 mM CaCl2 after 30 minutes of the reaction under ambient conditions. (B) The TEM image reveals the presence of nano-sized amorphous particles on quantifoil grid. The corresponding diffraction analysis confirms the amorphous nature of the particles, and the EDX spectrum indicates the presence of both calcium and magnesium elements.

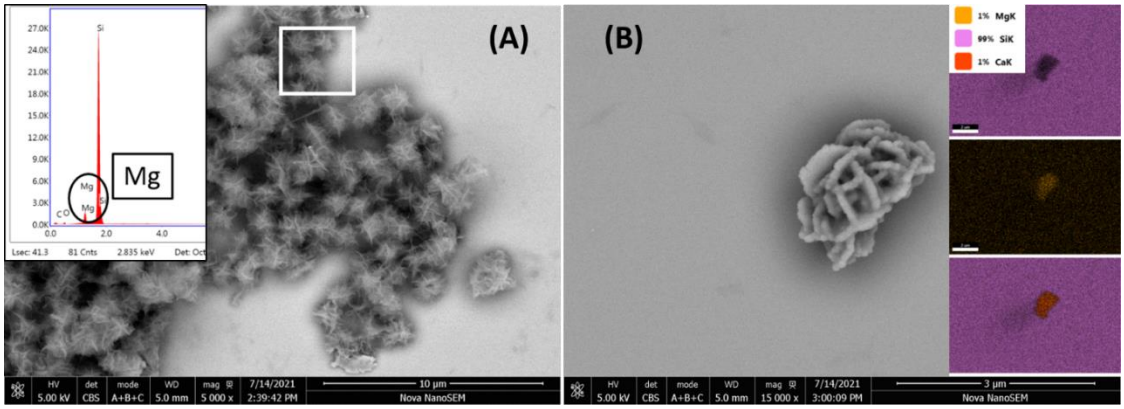

Figure 95 SEM image of precipitates formed at a concentration of 400 mM $MgCl_2$ and 100 mM $CaCl_2$ after 1 hour of the reaction under ambient conditions. The corresponding EDX spectrum confirms the presence of both calcium and magnesium. (B) A SEM image of the same grid at a higher magnification reveals the presence of desert rose particle, which also contains both magnesium and calcium within their structure.

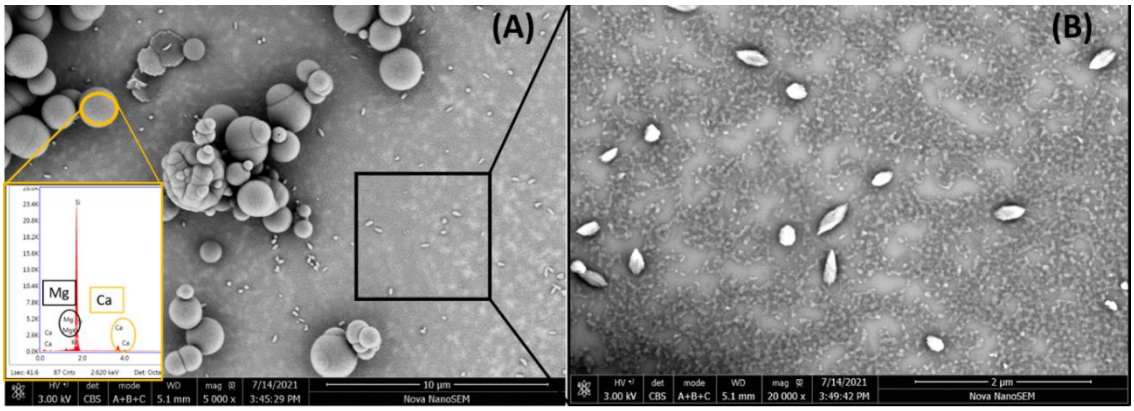

Figure 96 SEM image of the precipitates formed at a concentration of 400 mM MgCl2 and 100 mM CaCl2 after 3 hours of the reaction under ambient conditions. (A) Shows spherical particles with a size range of 300 nm to 2 µm were observed. The EDX spectrum confirms the presence of both calcium and magnesium within this structure. (B) A SEM image of the selected region in A indicates the existence of aragonite particles.

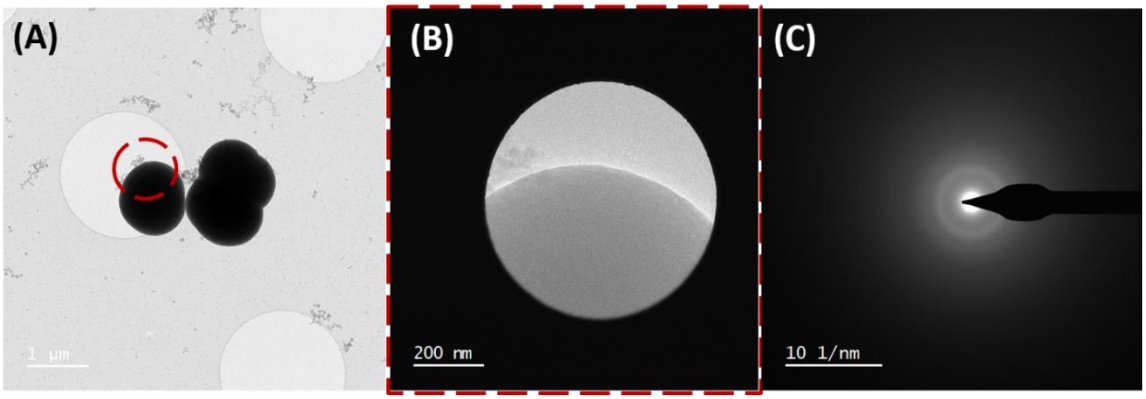

Figure 97 TEM image of spherical particles precipitated after 3 hours of the reaction in a 400 mM $MgCl_2$ and 100 mM $CaCl_2$ solution. (B-C) SAED analysis indicates that the particles are amorphous.

6.4 Discussion

The study involving the inclusion of Mg^{2+} in the $CaCO_3$ crystallisation process revealed the formation of aragonite after 3 hours of the reaction (Figure 96 B). Interestingly, in the early stages of the reaction, at around 30 minutes, spherical amorphous particles formed, as confirmed by diffraction analysis. EDX indicated the presence of both Mg and Ca, incorporated into the structure of these spherical particles (Figure 94 A). It can be assumed that these particles are ACC particles that contain Mg^{2+} in their structure since the ratio of Ca^{2+} to Mg^{2+} is four times higher. Molnar et al. (2023) studied the formation of $CaCO_3$ in the presence of Mg^{2+} at the Mg^{2+}: Ca^{2+} ratio of 4:1 after 30 minutes, and they reported Mg^{2+} incorporation into ACC particles. They identified two different populations of ACC that contained varying amounts of Mg^{2+} in their structure (Molnár et al., 2023). After 1 hour of the reaction the desert rose-like morphology of the ACC has replaced by spherical-shaped particles (Figure 96 A). However, no formation of vaterite or calcite was observed.

A widely recognized fact is that an elevated dissolved Mg^{2+}: Ca^{2+} ratio, specifically greater than 4, promotes the creation of aragonite (Molnár et al., 2023). It is assumed that Mg^{2+} ions lead to an increase in the surface free energy of calcite, while Mg^{2+} has no effect on altering the free surface energy of aragonite. As a result, aragonite is expected to initiate nucleation first (Boon et al., 2020). Sun and et al. (2015) reported that inclusion of Mg^{2+} into calcite is

more than 4 times energetically favourable compared to its incorporation into aragonite (Sun et al., 2015). In aragonite, the divalent cation is coordinated by oxygen in a ninefold manner, whereas in calcite, it is coordinated by oxygen in a sixfold manner. As a result, the energy penalty associated with the substitution of Mg^{2+} for Ca^{2+} is significantly higher in the aragonite structure. Additionally, it is extremely rare to observe Mg^{2+} being coordinated in a ninefold manner in crystals (Sun et al., 2015a). Boon et al. (2020) investigated the role of Mg^{2+} in $CaCO_3$ solution where they showed that incorporation of Mg^{2+} into calcite is more energetically favourable than into aragonite. Mg^{2+} is a strong growth inhibitor of calcite that causes notable morphological changes compared to what is anticipated in pure water, whereas the aragonite morphology remains unaffected (Boon et al., 2020; Zhang et al., 2022).

6.5 Study on polymorph selection of $CaCO_3$ in both carbonate-rich and calcium-rich systems

In this study, the effect of a significant excess of carbonate ions compared to calcium ions was investigated. In addition, an excess amount of calcium was used to compare with the results from the carbonate rich system.

6.5.1 Sample Preparation of carbonate-rich solution

Preliminary studies were carried out on the effect of different molar ratios of reactants ($CaCl_2$:Na_2CO_3, 1:200) on the crystallisation of $CaCO_3$ (full details in section 3.2.1).

6.5.2 Preparation of carbonate rich samples for Cryo-TEM study:

In chapter 4 where equimolar ratios of calcium and carbonate ions were used, it was found that ethanol quenching has an impact on the formed products. It was observed that ethanol had a stabilising effect, leading to the formation of a network of small ACC particles joined in a chain-like structure. This phenomenon was further supported by the literature, specifically the study by Walker et al. (2017), which reported a preference for aragonite formation over calcite in the presence of 50% ethanol relative to water (Jessica M. Walker et al., 2017) . Consequently, Cryo-TEM was employed to investigate the solution in its natural state without the presence of ethanol. $CaCl_2$ and Na_2CO_3 solutions

were prepared at concentration of 1 mM and 200 mM respectively mM (full details in section 3.2.2).

6.5.3 Sample preparation of calcium-rich solutions

For comparison with the carbonate-rich system, supersaturated solutions of $CaCO_3$ were prepared at final concentrations of 100: 0.5 Ca^{2+}: CO_3^{2-} mM (full details in section 3.2.3).

6.6 Results

6.6.1 TEM and SEM analysis of carbonate-rich sample formation prior to method improvement in sample preparation

In TEM observation of a carbonate-rich solution containing $CaCl_2$:Na_2CO_3 in a 1:200 ratio, only aragonite formation was observed while there was no evidence of the spherical ACC, vaterite or calcite. After 10 and 20 minutes, no distinct morphology of $CaCO_3$ particles was observed as shown in Figure 98 A and B. The formation of particles with various sizes was observed, but due to the high carbonate content in the solution, it was difficult to distinguish $CaCO_3$ particles from other salts such as excess sodium carbonate which had dried on the grid. EDX analysis was conducted to determine the elements present in the dried sample. As shown in Figure 98 C, a prominent sodium peak is observed, while a smaller calcium peak is also present. At a longer time point of 30 minutes, the emergence of needle-like or sheaf-shaped aragonite is detected, exhibiting an average particle size of approximately 10 µm, as depicted in Figure 99 A-B. EDX analysis reveals a prominent calcium peak, suggesting the formation of aragonite. However, a substantial sodium peak is still present from the excess amount of sodium carbonate (inset in Figure 99 B). Electron diffraction analysis was conducted and confirmed the presence of (102) and (002) peaks, as shown in Figure 99 C. The pH value of the carbonate-rich system was measured and was 10.81 after a reaction time of 30 minutes. After 45 minutes of the reaction, a significant number of needle-like crystals were observed by TEM (Figure 100 A-C). Aragonite, characterized by its orthorhombic crystal structure, forms as clustered needle-like structures that grow along the crystallographic c-axis (Dey et al., 2010). The crystallinity of these crystals was confirmed through electron diffraction analysis. Indexing of the diffraction arcs to the (021) aragonite plane

provided conclusive evidence of the aragonite crystal structure with the presence of arcs indicating potential alignment of the needle-shaped crystallites (Figure 100 C). Since the excessive amount of salt hinders a thorough investigation of the system, it is necessary to improve the system to eliminate the excess salts and create a clearer environment suitable for studying the early stages of aragonite crystallization.

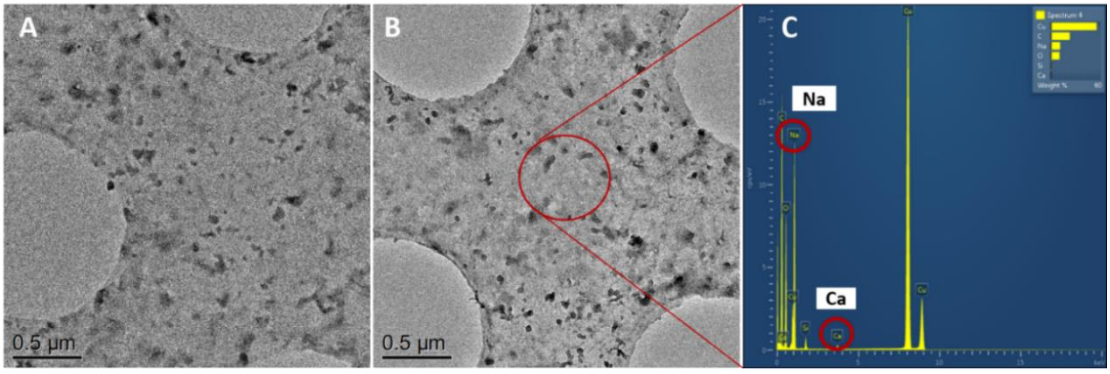

Figure 98 TEM images of the carbonate-rich sample ($CaCl_2$:Na_2CO_3, 1:200) before improvement of the sample preparation method. (A) Particles formed on the TEM grid after 10 minutes, (B) particles formed after 20 minutes of the reaction, and (C) EDX spectrum of the area indicated by the red circle in B.

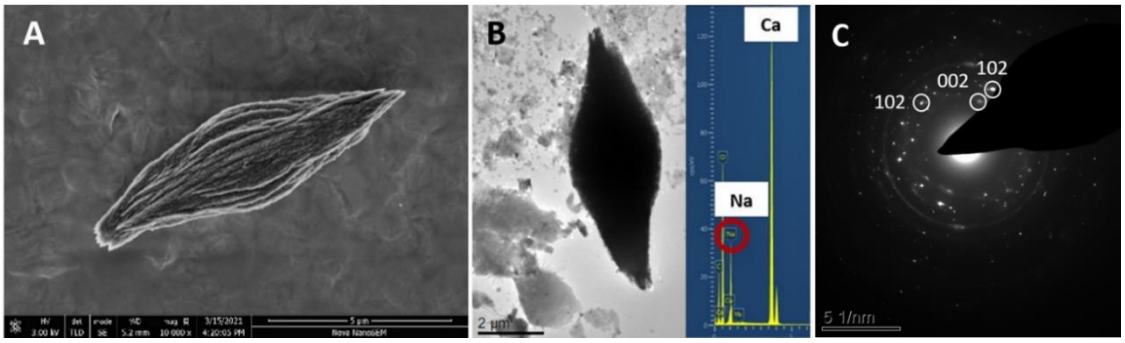

Figure 99 (A) SEM image and (B) TEM image of aragonite after 30 minutes of the reaction, along with the corresponding EDX spectrum. (C) Electron diffraction analysis confirmed the presence of (102) and (002) peaks.

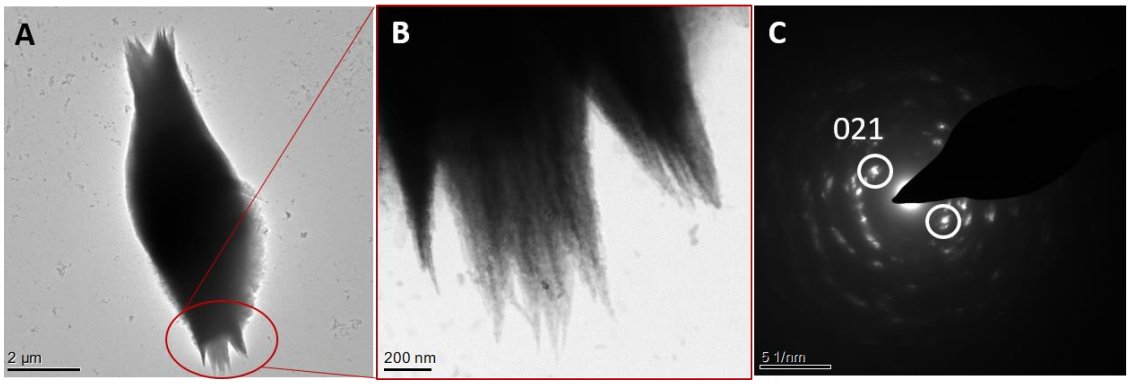

Figure 100 (A) TEM image of a micron-sized aragonite needle-like structure formed after 45 minutes of the reaction. (B) Higher magnification of the region indicated by the red circle in A. (C) Selected area electron diffraction (SAED) pattern from the area in B, indexed to the prominent 021 planes of aragonite.

6.6.2 TEM analysis of carbonate-rich sample formation after improvement of the sample preparation method (centrifuged with a mixture of water and ethanol)

In section 6.6.1, the excessive amount of sodium carbonate hindered the study of the early stages of aragonite formation. To overcome this challenge, the sample was centrifuged to concentrate the product. Subsequently, a mixture of 50% ethanol and 50% water was utilized to effectively remove all traces of carbonate salt and chemically quench the reaction. This allowed for the investigation of earlier time points, specifically at 20 and 25 minutes prior to the formation of fully formed aragonite. The TEM image in Figure 101 A shows the formation of nano-sized particles, which were confirmed to be amorphous by electron diffraction. The presence of a Ca peak and the absence of a Na peak in the EDX spectrum confirm that the excess sodium carbonate salt was dissolved by water and ethanol mixture, resulting in the formation of a clear solution (Figure 101 B). After a reaction time of 25 minutes formation of aragonite with a characteristic needle-like morphology was observed, as depicted in Figure 102 A-B.

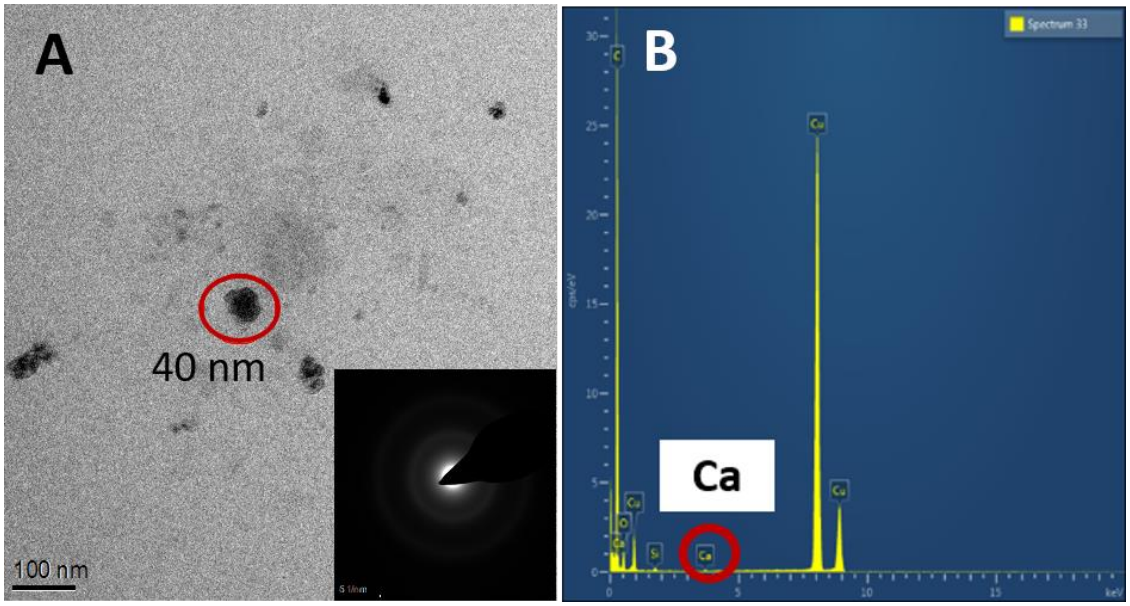

Figure 101 TEM image of a carbonate-rich sample centrifuged with a 50% water: 50% ethanol solution. (A) Formation of $CaCO_3$ after 20 minutes, with the corresponding diffraction pattern indicating the amorphous nature of the particle circled in red. (B) EDX spectrum taken from the red-circled area in A, confirming the presence of Ca but no trace of Na.

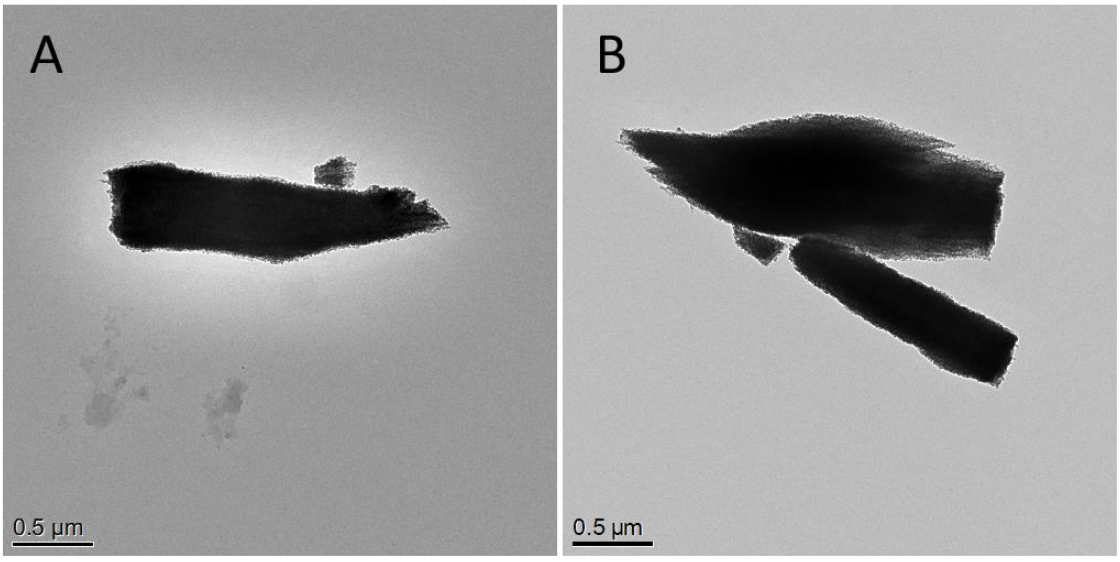

Figure 102 TEM images of carbonate-rich samples centrifuged with 50% water: 50% ethanol after 25 minutes reaction clearly show the formation of an aragonite morphology.

6.6.3 Cryo-TEM analysis of carbonate-rich samples

A cryo-TEM study was conducted to investigate the formation of aragonite at a molar ratio of $CaCl_2$:Na_2CO_3 of 1:200. The study aimed to directly visualize the

initial stages of crystal formation within the vitreous ice. Three different time points of 20, 25, and 30 minutes were selected for analysis. The sample was centrifuged, and no water and ethanol mixture were used to remove the excess sodium carbonate salt from the system since the salt was already dissolved within the vitreous ice.

Cryo-TEM revealed "rugby ball" shaped clusters of proto-aragonite with a dimension of 1.5 µm after 20 minutes of the crystallisation reaction. These exhibited a dense core surrounded by a less dense outer layer (indicated by the red arrows) consisting of aligned clusters of nanowires (Figure 103 A). Figure 103 B provides a higher magnification of the left tail of the particle shown in Figure 103 A, revealing that the nanowires comprised particles of sizes ranging from 2 to 3 nm arranged in linear chains. At the same time point of 20 minutes, the presence of elongated, dense nano-sized particles aligned linearly, with a size range of approximately 30 nm in length and 5 nm in width, was observed (highlighted by the red circles in Figure 104 A and B). No spherical ACC, vaterite and calcite crystals were observed (note the spherical particles in the background were confirmed to be ice crystals (yellow arrows)). Figure 105 A-B show the presence of aligned elongated nanowires after 25 and 30 minutes of the crystallization reaction respectively. In order to confirm that these structures were proto-aragonite, STEM/EDX mapping was conducted on the vitrified sample. As shown in Figure 106 (A-F), the bright regions in the STEM ADF image (Figure 106 B and D) indicates the presence of higher average atomic in the particle and STEM/EDX maps show the presence of calcium (and to some extent carbon) within the particle.

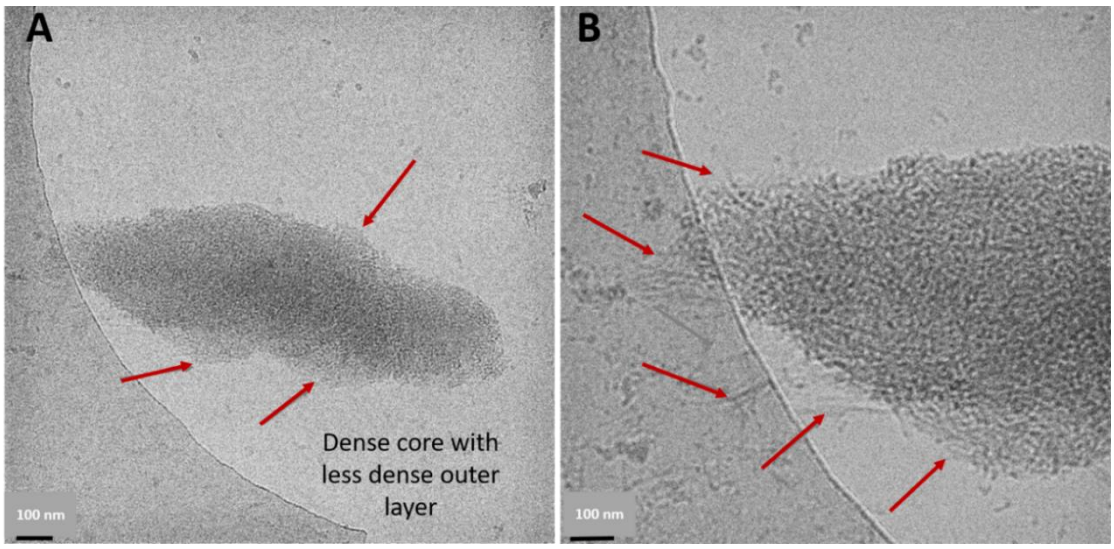

Figure 103 Cryo-TEM images of the emergent aragonite structure with dimension of 1.5 µm after 20 minutes, revealing an emergent fibrous structure in image (A). Image (B) provides a higher magnification of the left tail of the particle depicted in A, highlighting particles with sizes ranging from 2 to 3 nm.

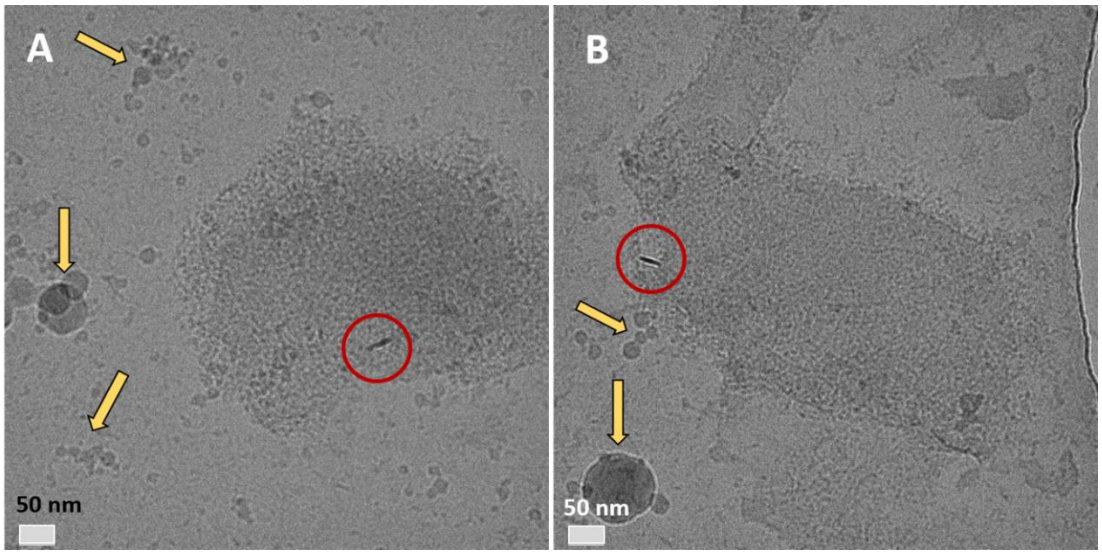

Figure 104 Cryo-TEM images of the fibrous structure from different areas of the TEM grid captured after 20 minutes of the reaction A-B. The red circles indicate elongated small clusters with a length of approximately 30 nm and a width of 5 nm. Yellow arrows indicate the presence of ice crystals.

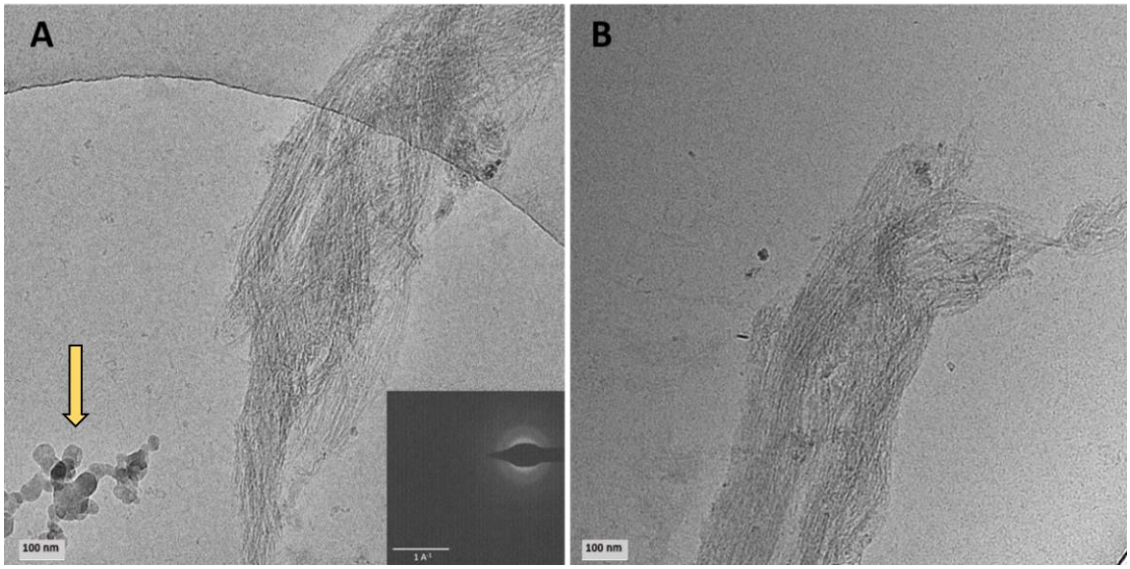

Figure 105 Cryo-TEM study of the carbonate-rich system reveals the formation of elongated fibrous structure of aragonite after (A) 25 and (B) 30 minutes. The yellow arrow indicates the presence of ice crystals.

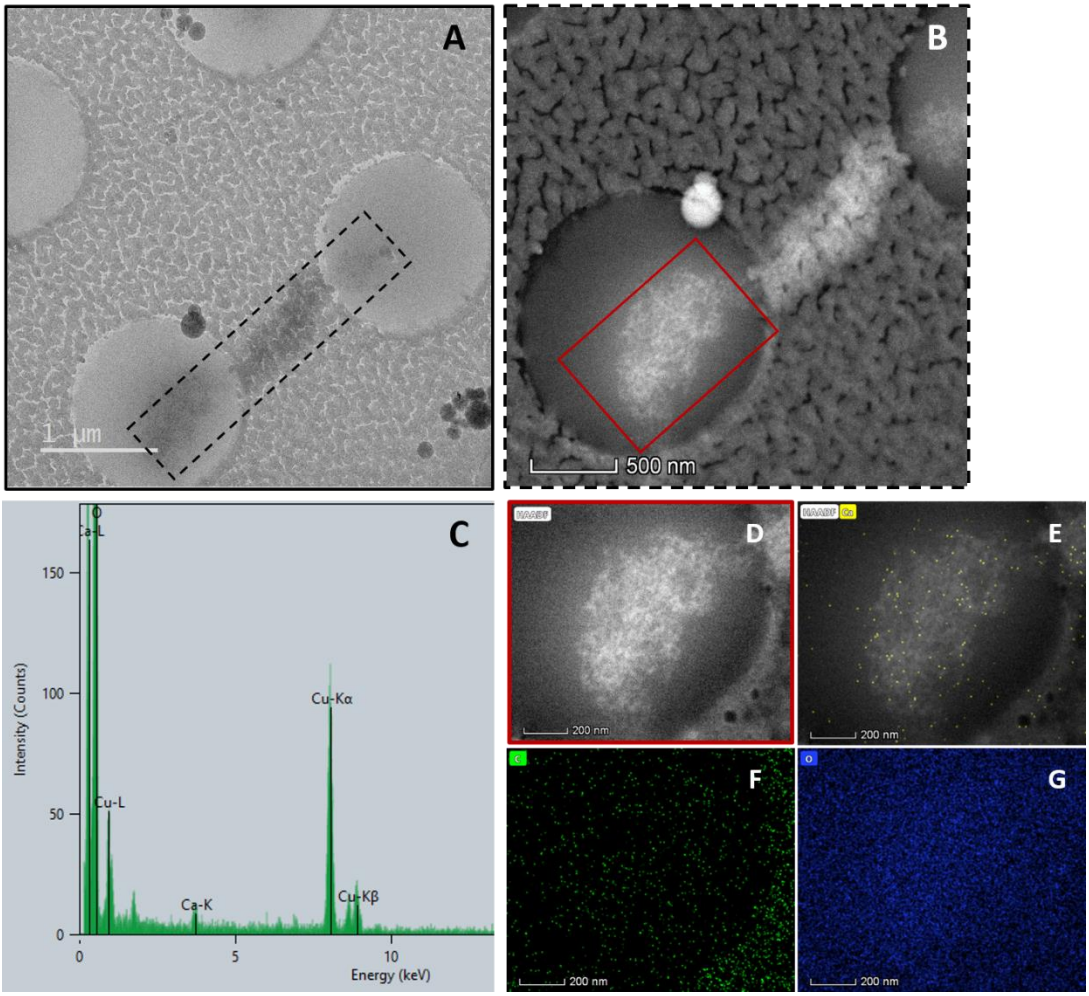

Figure 106 Cryo-TEM image of the carbonate-rich sample ($CaCl_2$:Na_2CO_3, 1:200). (B) Annular Dark Field STEM image showing atomic number contrast, where the bright regions indicate higher atomic number materials. (C) EDX spectrum confirming calcium, carbon, and oxygen signals. Cupper signal is from the TEM grid. (D-G) STEM-EDX mapping displays the elemental composition of the region in image C, including (D) calcium, (E) carbon, and (F) oxygen.

6.6.4 TEM Analysis of calcium-rich solutions

For completeness, the effects of inequivalent proportions of $CaCl_2$:Na_2CO_3, in a calcium rich ratio 200:1, on the morphology and particle size of $CaCO_3$ solutions were studied after 20 minutes of the crystallisation reaction using TEM. In contrast to the carbonate-rich system, here the formation of rhombohedral calcite and spindle-like vaterite was observed as illustrated in Figure 107 A-B. The SAED pattern exhibited sets of diffraction spots, with d-spacing of 2.10 A° and 1.67 A° corresponding to the (030) and (226) planes of hexagonal vaterite,

indicating that the spindle-like morphology consists of vaterite crystals (Figure 107 C).

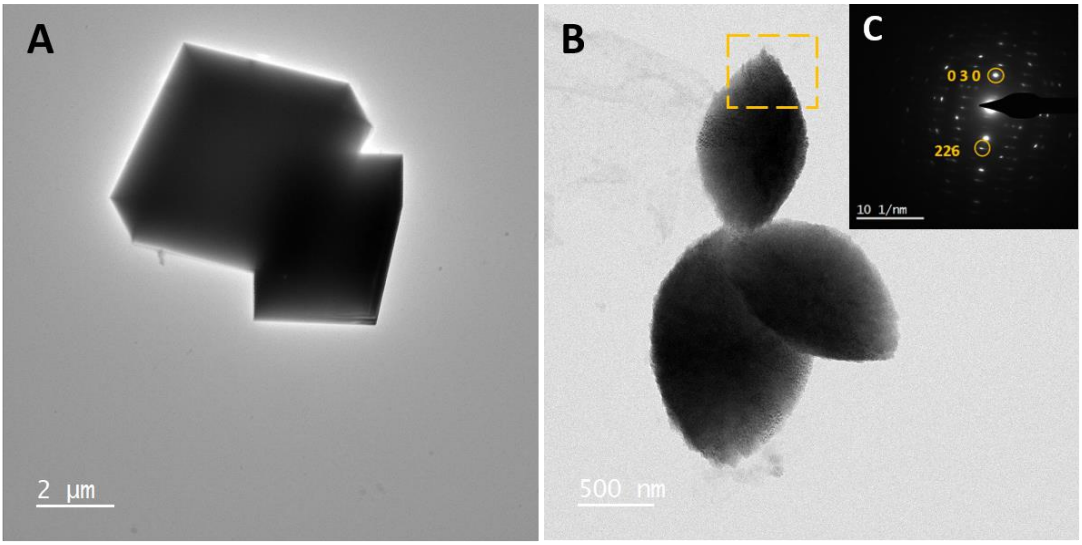

Figure 107 TEM images of the calcium-rich sample ($CaCl_2$:Na_2CO_3, 200:1) showing the formation of (A) rhombohedra calcite and (B) spindle-like vaterite after 20 minutes of the reaction. (C) The SAED pattern was obtained from the boxed area in B, which can be indexed to the (030) and (226) planes of hexagonal vaterite.

6.6.5 The effect of pH changes as a function of molar ratio using PHREEQC modelling programme

The PHREEQC modelling program was employed to track the change in the solution as $CaCl_2$ is added to a Na_2CO_3 solution, and vice-versa. A 40 mL solution was set up with 4.5 mM of $CaCl_2$, and the REACTION function was used to add Na_2CO_3 to the solution until the molar quantity of CO_3^2 ions became twice the molar quantity of the original Ca^{+2} ions. The quantity of Ca^{+2} and CO_3^2 ions were tracked during the reaction. This was repeated by adding $CaCl_2$ to a solution containing 4.5 mM Na_2CO_3.

The pH value of the system decreases as the quantity of Ca^{2+} increases (Figure 108). Conversely, an excess amount of CO_3^{-2} leads to an increase in pH value of the system (Figure 109). Potentially this may affect polymorph selection and formation. We note that the Saturation Indices for the different polymorphs tend to converge at low [Ca^{2+}]: [CO_3^{2-}] and [CO_3^{2-}]: [Ca^{2+}] ratios indicating that the differences in stability become small.

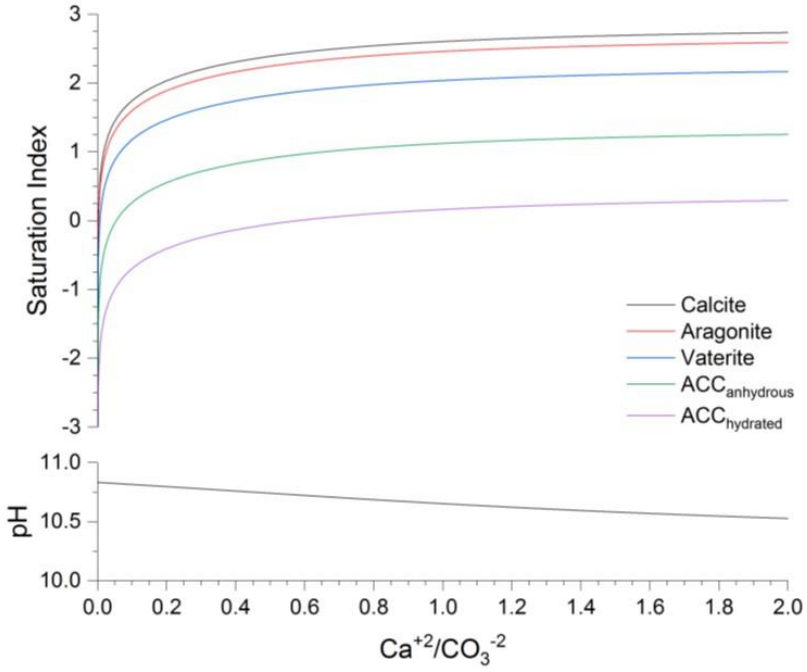

Figure 108 Variation in the saturation index of solid calcium carbonate phases with increasing $[Ca^{2+}]$: $[CO_3^{2-}]$ ratio from 0 to 2, accompanied by the corresponding Saturation Indices and also pH. Obtained from MSc report of Dario Fernandez.

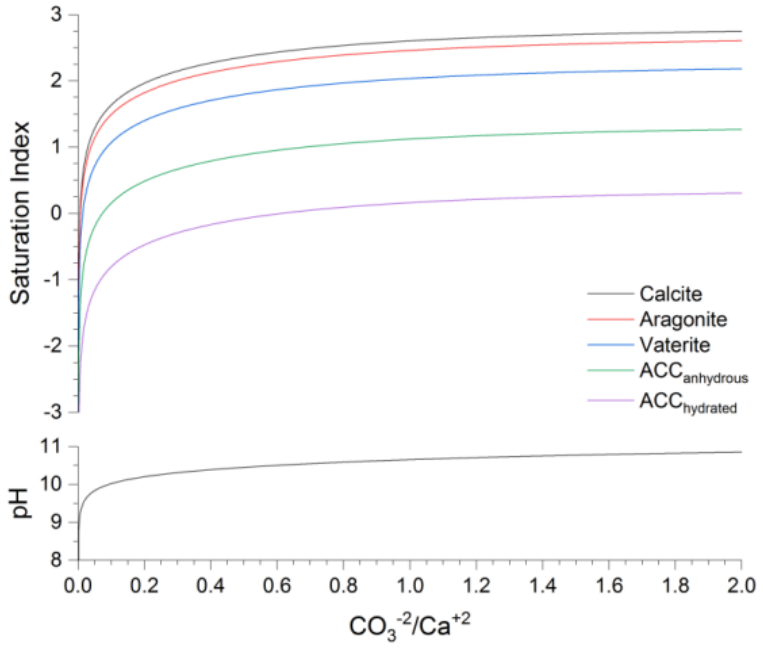

Figure 109 Variation in the saturation index of solid calcium carbonate phases with increasing $[CO_3^{2-}]$: $[Ca^{2+}]$ ratio from 0 to 2, accompanied by the corresponding Saturation Indices and pH. Obtained from MSc report of Dario Fernandez.

6.7 Discussion

In chapter 4, the crystallisation of $CaCO_3$ solutions (0.5, 1.0, 2.5 and 4.5 mM) containing equimolar ratios of $CaCl_2$ and Na_2CO_3 resulted in a variety of $CaCO_3$ particles including ACC particles, spheroidally shaped vaterite (Zhou et al., 2010) and rhombohedral calcite, and no evidence was found for the presence of aragonite. However, in the presence of Mg^{2+} at a ratio of 4 times to Ca^{2+}, aragonite formation occurred after 3 hours (see section 6.3). Additionally varying the solution stoichiometry at room temperature in the absence of any additive (see section 6.5), showed that high $[CO_3^{2-}]/ [Ca^{2+}]$ ratios (i.e., $CaCl_2$:Na_2CO_3 1:200) can yield pure, monodispersed populations of needle-like aragonite crystals. The morphologies of the observed crystals consisted of elongated needles, approximately consistent with those of aragonite previously reported by others (Cefalas et al., 2008)). Analysis of the *d*-spacing observed in the electron diffraction pattern revealed inter-planar distances of 3.20 Å, corresponding to the (021) planes of aragonite, (Zhou and Yao, 2014; Zeng et al., 2018).

When samples were prepared by chemical quenching and drying, TEM conclusively showed the formation of aragonite after 30 minutes of the reaction at a molar ratio of $CaCl_2$:Na_2CO_3 of 1:200, as shown in Figure 99. After 45 minutes of the reaction, fully formed aragonite with a size of approximately 9.5 µm was observed. SAED revealed prominent planes of aragonite with a d-spacing value of 3.27 Å corresponding to the (021) crystallographic plane (Figure 100).

However, chapter 4 has shown the influence of sample preparation on the results of crystallisation experiments and consequently, a cryo-TEM study was initiated at time points of 20, 25 and 30 minutes in order to examine the early stages of aragonite crystallization in its frozen native state. After 20 minutes, loosely packed fibrous nanoparticles with a size of 3 nm were observed (Figure 103), which further arranged into a linear structure after 25 and 30 minutes (Figure 105). This suggests that the fibrous particles may undergo dehydration, resulting in the alignment and aggregation of small, spherical pre-cursor particles into chain-like and elongated fibres. Walker et al. (Jessica M. Walker et al., 2017) have reported a similar mechanism for aragonite formed in water:

ethanol mixtures, stating that the formation of aragonite involves a solid-state transformation from ACC to a crystalline structure via a non-classical route. In their observations, they found the coexistence of amorphous and crystalline structures within the needle of the same aragonite sample.

In general, the least stable polymorphs are expected to precipitate first from a supersaturated solution, subsequently to be replaced by more stable phases (De Yoreo, 2022). Ostwald rule of stage suggests that less stable polymorphs tend to crystallize first. According to this rule, in a system with multiple metastable phases, a sequential progression occurs as it transitions from the nearest thermodynamic state to the most stable phase (Cardew, 2023; Du & Amstad, 2020; Smeets et al., 2017). However, for a number of materials the crystallisation of the stable phase can be replaced by the formation of a less metastable phase. This can be carried out by modifying the chemistry of the solution thereby influencing the surface energy at the solvent-crystal interface which consequently decreases the nucleation barrier of the metastable phase (Sun et al., 2015b). It has been demonstrated in a large number of experiments in the literature that aragonite is preferentially formed in hot solutions (60°C to 80 °C), as compared with its more stable counterpart (calcite) (Sawada, 1997) (Gopi et al., 2013). This can be explained by the higher crystallisation rate of aragonite than calcite at high temperature. According to the findings by Ma et al. (2010), an increase in temperature was correlated with a reduction in the Gibbs free energy linked to the phase transition reaction from aragonite to calcite. The highest nucleation rate of aragonite was observed at temperatures exceeding 50°C. By considering the thermodynamic and kinetic properties of polymorphs, it can be inferred that aragonite undergo kinetic control at varying temperatures (Ma et al., 2010). Interestingly, in this study, the formation of aragonite occurred at room temperature, for the specific case of a very carbonate-rich solution ratio of 1:200 Ca^{2+} to CO_3^{2-} (mM). A possible reason for the formation of aragonite at ambient temperature can be attributed to the change in the chemistry of the solution (a remarkably higher ratio of carbonate anions to divalent calcium cations). Aragonite has an increased (nine-fold) coordination of oxygen (from the carbonate anions) ((Some of the links are bidentate (two oxygens from the same carbonate group) and some mono-dentate (only one oxygen))

surrounding the calcium cations, relative to six-fold coordination in calcite (Lippmann, 2012). Potentially this could affect the surface energy of a crystal nucleus in the carbonate-rich medium leading to an increased nucleation rate of aragonite.

A further possible reason for the formation of aragonite under carbonate-rich conditions, could be due to the change in pH value of the system which is expected to become more alkaline under carbonate-rich conditions. The pH value of the carbonate-rich system was measured after 30 minutes, and it was recorded as 10.81. Dario Fernandez also investigated the impacts of changes in the molar ratio of calcium to carbonate ions on pH using PHREEQC, where he demonstrated that as the ratio of $[CO_3^{2-}]$/ $[Ca^{2+}]$ increased, the pH value of the system also increased.

Gebauer et al., (2008) has reported the pH dependency of prenucleation clusters leading to the precipitation of two distinct ACC phases. One phase, noted as ACC I or proto-calcite, forms within clusters with stronger bindings pH levels ranging from 9.00 to 9.50. Conversely, a less stable phase referred to as ACC II or proto-vaterite emerges within clusters with weaker bindings at pH values ranging from 9.75 to 10.0 (Gebauer et al., 2008). Potentially, an even higher pH may favour a proto-aragonite ACC phase as observed here. Conversely a calcium-rich system (relative to carbonate), where we would predict a lowering of pH, resulted in the formation of vaterite and calcite. Therefore, the relationship between aragonite's abundance and the pH value of the solution should be investigated in the future.

6.8 Conclusion

The spontaneous formation of metastable aragonite from an additive-free solution at room temperature is a remarkably infrequent phenomenon (Zhang et al., 2022). However, we have shown that the chemistry of the solution plays a crucial role in determining the polymorphs.

This study demonstrates that a considerably higher molar ratio of Na_2CO_3 to $CaCl_2$ gave rise to the formation of aragonite in the solution at 25º C, despite the fact that aragonite is an abundant polymorph only at temperatures between 60°C to 80°C. Interestingly, the emergent aragonite structure is not confined to

a carbonate-rich reactant system but is also observed in the presence of magnesium using ADM. Additionally, microscopic observation showed that an excess amount of $CaCl_2$ over Na_2CO_3 gave rise to the formation of calcite and vaterite, while no aragonite formation was observed.

Chapter 7 Conclusion and future work

The overall aim of this research was to investigate the use of both conventional and advanced electron microscopy methods (e.g., SEM, TEM, Cryo-TEM, and LC-TEM) as spatially resolved and time-resolved tools for gaining an in-depth understanding of the early stages of crystallisation processes, in particular $CaCO_3$ crystallisation.

In chapter 4, it was observed that the morphology and size of $CaCO_3$ polymorphs can vary significantly based on the final molar concentrations of reactants (0.5, 1.0, 2.5, and 4.5 mM) and the different reaction times (ranging between 15 s and 30 minutes). Both supersaturation levels and reaction times can impact the particle size, with longer reaction times leading to larger particles and the disappearance of nano-sized particles. At the lowest concentration of 0.5 mM, diffuse regions of higher contrast were observed after 5 minutes, with little evidence for the formation of ACC particles or any crystals. These could have been indicative of a dense liquid phase occurring prior to nucleation. However, at the highest concentration of 4.5 mM, micron-sized calcite crystals were observed after only 20 seconds of the reaction. This demonstrates that at the lowest concentration, the decreased driving force results in a significantly reduced reaction rate for crystallisation. Such low supersaturation conditions may favour study of the very early stages of the crystallisation process in that it provides slower nucleation.

However, following these initial scoping studies, subsequent investigations focused on evaluating the influence of a variety of commonly employed electron microscopy sample preparation methods for the study of $CaCO_3$ crystallisation. The microscopy observations revealed that methods such as air-drying and vacuum filtration fail to represent the native state of the samples due to increased supersaturation levels present during the drying stage, irrespective of the speed of the drying process. Consequently, this results in accelerated $CaCO_3$ precipitation as crystalline polymorphs. Moreover, the use of ethanol in the quenching process resulted in the formation of a notable network of nanometre-sized ACC particles along with larger individual ACC particles, suggesting that the ACC network might be an artefact caused by ethanol

addition. In contrast, samples prepared using plunge freezing and vacuum sublimation exhibited only ACC particles, with cryo-TEM observations displaying a substantial population of ACC particles and a few crystalline structures after 5 minutes of the reaction. Thus, while drying and ethanol quenching are common in crystallization studies, they might not always accurately represent the native state of a sample. Therefore, the general use of cryo-TEM is advocated to mitigate any potential sample preparation artefacts.

After identifying the most effective characterization method for studying the crystallization of $CaCO_3$, a full cryo-TEM study was conducted in Chapter 5. During the dry TEM study in Chapter 4, the lowest concentration of $CaCO_3$ (0.5 mM) exhibited a diffuse area at the very early stages. As the dry TEM technique has been shown to be unrepresentative of the native state of the sample, a cryo-TEM study was conducted at both the lowest (0.5 mM) and highest (4.5 mM) concentrations to determine whether the diffuse region was an artefact or naturally appeared in that manner during the early stages of the crystallisation process. In the cryo-TEM analysis, diffuse regions with increased contrast were again observed but only very occasionally at the concentration of 4.5 mM, and only after 5 minutes of the reaction. Here, mostly ACC particles were observed, with the appearance of calcite crystals emerging from the ACC. In contrast, at the lowest supersaturation of 0.5 mM, only diffuse regions of higher contrast were observed, and even after 40 minutes, no formation of ACC or crystals was detected.

According to existing literature, these diffuse regions may indicate early-stage products originating from potential dense liquid phases (DLP) arising from a liquid-liquid phase separation process. These DLP regions then later dehydrate and nucleate ACC particles or directly transform into crystalline structures. Thus, the findings potentially suggest that the precipitation of $CaCO_3$ follows a multi-step process involving the initial; formation of dense liquid phases containing 2-10 nm nano clusters, which subsequently dehydrate and transform into ACC particles, eventually undergoing further conversion into calcite.

In this research, additionally the use of liquid cell (LC) TEM for the direct visualisation of crystallisation was investigated. Here the effect of confinement within the LCTEM chip was initially investigated. As confinement (and also

incomplete mixing within the chip) is known to slow down the precipitation rate, the highest concentration of $CaCO_3$, 4.5 mM, was used. Two sets of experiments were conducted: firstly, an LCTEM holder was utilized to conduct crystallization on the chip viewing window, and then the chips were separated and taken to the SEM and compared with dry TEM observations at the same concentration. It was observed that in the confined area, fewer particles formed after 30 minutes, whereas outside the confined area, crystals of calcite and vaterite exhibited well-defined morphology. Secondly, direct examination of 4.5 mM crystallising solutions in real-time was studied, and after five experiments, only once was it possible to detect particles within a certain size range, which could be attributed to vaterite in terms of their morphology and size. Furthermore, PHREEQC chemical speciation modelling studies were conducted to study the effect of pH on the precipitation of $CaCO_3$. This highlighted that electron beam radiolysis of the aqueous solution can reduce the pH, subsequently halting the formation of $CaCO_3$. It was concluded that the effects of both confinement and the chemical changes associated with the radiolysis of water significantly limit the application of LCTEM to the direct study of crystallisation processes.

Finally, in the last chapter 6, the effects of Mg^{2+} and also changes in the solution chemistry were investigated in terms of the selection of the ultimate crystalline polymorph formed. The formation of aragonite over calcite at room temperature has only been observed in the presence of Mg^{2+},(Molnár et al., 2023) in the presence of ethanol-rich solvents (Jessica M. Walker et al., 2017) and also in confined areas (Zeng et al., 2018).. In this study it was confirmed using cryoTEM that maintaining a ratio of $[Mg^{2+}]$: $[Ca^{2+}]$ ions at 4:1, promoted the formation of aragonite after 3 hours at room temperature. However, in our study, a substantial excess of carbonate, i.e., a ratio of $[CO_3^{2-}]$/ $[Ca^{2+}]$ of 200:1, also facilitated the formation of aragonite at room temperature, which is highly unusual. PHREEQC chemical speciation modelling demonstrated that as the ratio of $[CO_3^{2-}]$/ $[Ca^{2+}]$ increased, the pH value of the system also increased which may have some bearing on this process.

In our investigation, an emergent aragonite structure appeared in the presence of Mg^{2+} as well as in a carbonate-rich system. This phenomenon aligns with

findings by Walker et al, (2017), who observed the formation of aragonite in an ethanol environment using Cryo-TEM (Jessica M. Walker et al., 2017). However, they reported ACCs with a size range of 60 nm, going up to 300 nm, while our particles range from 2 to 3 nm. The underlying mechanism involves the self-organization of fibrous amorphous particles into a linear structure, resulting in the alignment and aggregation of small, spherical precursor particles into chain-like and elongated fibres. Subsequently these fibres self-organized into aragonite sheaves (Figure 110).

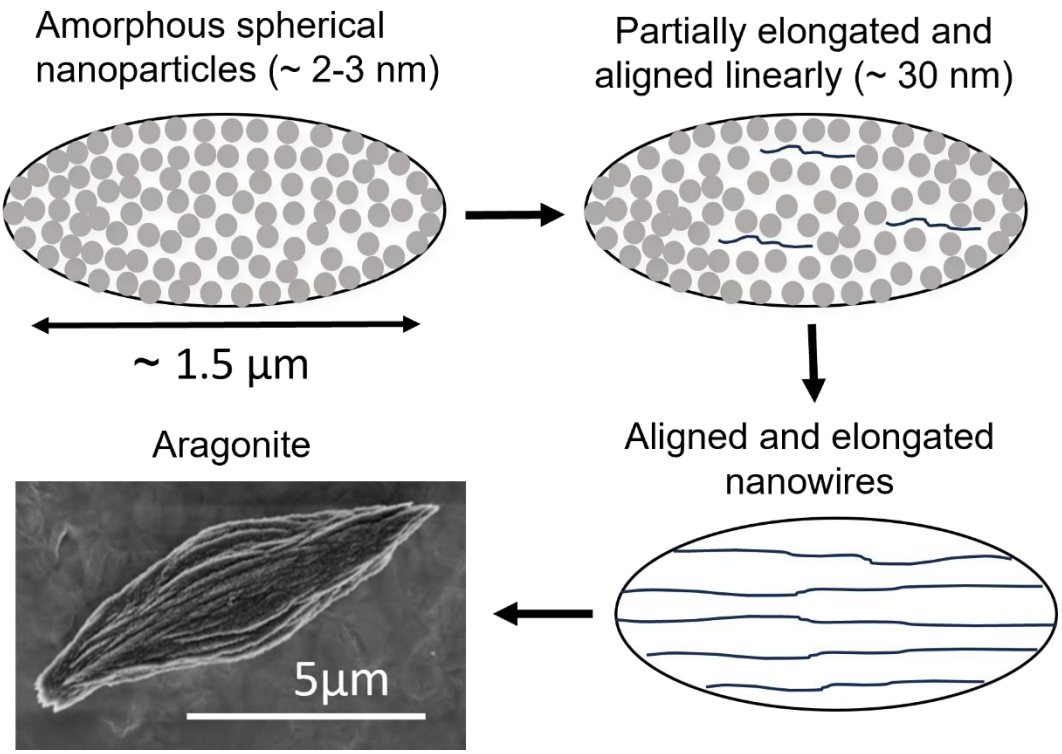

Figure 110 Mechanism depicting the formation of aragonite in a carbonate-rich system. Initially, small amorphous nano clusters form, organizing into a linear structure of nano wires, ultimately leading to the creation of aragonite.

7.1 Future work

Finally, to expand upon the findings outlined in this thesis, several additional studies are suggested:

Use Cryo-TEM techniques to study the morphological properties of $CaCO_3$ crystallisation at concentration levels of 2.5- and 1.0-mM.

Cryo-TEM studies of $CaCO_3$ at 4.5 mM after 5 and 40 minutes of reaction time and at 0.5 mM after 20 and 40 minutes have been conducted. To fill the gaps and compare the findings with the results obtained from Cryo-TEM under the same conditions, concentrations of 1.0 and 2.0 mM should also be studied to better understand the early stages of $CaCO_3$ formation.

Investigate the formation of aragonite in a carbonate rich system ($CaCl_2$:Na_2CO_3 1:200) at different pH values using Cryo-TEM:

It has been demonstrated that the formation of aragonite was induced by significantly carbonate-rich conditions at a ratio of 200:1 Na_2CO_3/$CaCl_2$. One possible reason for this could be the alteration in the system's pH value and increased alkalinity. Consequently, the association between the abundance of aragonite and the solution's pH value requires investigation achieved by adding a pH buffer solution to the system.

Cryo-TEM studies at earlier timescales using mixing/spraying technique for grid preparation:

Investigating earlier timescales (1 second) at higher supersaturation levels (>4.5 mM) could potentially indicate whether the current findings are more widely applicable. New methods for cryo-TEM sample preparation involving rapid mixing and spraying solutions onto cold TEM grids allows freezing within millisecond time frames (>10 ms), providing great time resolution (Klebl et al., 2020).

Further investigate use of in-situ Liquid cell TEM techniques to characterise directly the morphologies and crystalline structure of $CaCO_3$ formed in solutions:

Use low electron dose techniques and calibrate pH changes as a function of electron dose (using standards that have undergone well-defined dissolution or aggregation reactions at known pH values (e.g., CeO_2 nanoparticles dissolve below pH 5, and ZnO below pH 6)) to better define the conditions within the LCTEM chip during reactions. This also includes the use of much lower flow rates than employed in this work so as to promote diffusive mixing of reactant solutions. Potential experiments include:

i. The study of the transformation of ACC particles, pre-loaded into the LCTEM chip, into calcite crystals to understand and visualise transformation of amorphous nano particles to crystalline structures.
ii. Conduct controlled LCTEM studies at higher supersaturations (e.g. > 10 mM) in order to explore and better understand the nucleation step (Michael H.Nielsen, Shaaul Aloni, 2014).
iii. Study the formation of aragonite in carbonate-rich conditions using controlled LC-TEM studies and investigate whether the formation of aragonite is via direct nucleation from the solution or via ACC to aragonite by dissolution/re-precipitation reaction.

LCTEM studies should be benchmarked against ex-situ studies (e.g. cryoTEM) which would allow for the effect of restricted mobility of solution species to be investigated when in confinement within the LCTEM chip.

Appendix A – Additions to the PHREEQC Database

Below are all the aqueous species and solid phases added to the PHREEQC database, as formatted in the database itself. The references from where the data was taken are included below each entry.

```
SOLUTION_SPECIES
Ca+2 + H2O = CaOH+ + H+
log_k -12.78
#Wateq4f
2H+ + CO3-2 = H2CO3
log_k 16.681
#Wateq4f
HCO3- + H+ = H2CO3
log_k 6.351
delta_h -2.247 kcal
-analytical_expression 356.3094 0.0609196 -21834.37 -126.8339 1684915
0
#Wateq4f
PHASES
Vaterite
CaCO3 = CO3-2 + Ca+2
log_k -7.913
-analytical_expression -172.1295 -0.077993 3074.688 71.595 0 0
#PLUMMER, L. N. & BUSENBERG, E. 1982.
ACChyd
CaCO3 = CO3-2 + Ca+2
log_k -6.04
delta_h -52.02 kJ
#(Radha et al., 2010, Forbes et al., 2011, Rodriguez-Navarro et al.,
2014, Cuesta Mayorga et al., 2019)
ACCan
CaCO3 = CO3-2 + Ca+2
log_k -7
delta_h -43.45 kJ
#(Radha et al., 2010, Forbes et al., 2011, Rodriguez-Navarro et al.,
2014, Carino et al., 2017)
Portlandite
Ca(OH)2 + 2H+ = Ca+2 + 2H2O
log_k 22.8
delta_h -31 kcal
#Wateq4f
Halite
NaCl = Cl- + Na+
log_k 1.582
delta_h 0.918 kcal
#Wateq4f 57
```

```
Nahcolite
NaHCO3 = HCO3- + Na+
log_k -0.548
delta_h 3.72 kcal
#Wateq4f
Trona
NaHCO3:Na2CO3:2H2O = CO3-2 + 2H2O + HCO3- + 3Na+
log_k -0.795
delta_h -18 kcal
#Wateq4f
Natron
Na2CO3:10H2O = CO3-2 + 10H2O + 2Na+
log_k -1.311
delta_h 15.745 kcal
#Wateq4f
Thermonatrite
Na2CO3:H2O = CO3-2 + H2O + 2Na+
log_k 0.125
delta_h -2.802 kcal
#Wateq4f 58
```

Appendix B – Examples of PHREEQC Setups

The following is the main body of the code used for the titration experiments, with all solid phases being allowed to precipitate using the EQUILIBRIUM_PHASES function.

```
EQUILIBRIUM_PHASES 1
ACCan 0 0
ACChyd 0 0
Aragonite 0 0
Calcite 0 0
Vaterite 0 0
Portlandite 0 0
Halite 0 0
Nahcolite 0 0
Trona 0 0
Natron 0 0
Thermonatrite 0 0
CO2(g) 0 0
O2(g) 0 0
H2(g) 0 0
SOLUTION 1
temp 25
pH 7 charge
pe 4
redox pe
units mmol/l
density 1
C(4) 4.5
Ca 4.5
Cl 9
Na 9
-water 0.04 # kg
INCREMENTAL_REACTIONS True
REACTION 1
HCl 1
10 millimoles in 10000 steps
#Continued next page 59
```

```
SELECTED_OUTPUT 1
-file Equilibrium Phases v2.6.sel
-reset false
-simulation true
-pH true
-pe true
-reaction true
-temperature true
-totals C(4) Ca Cl Na
-molalities Ca+2 CaCO3 CaHCO3+ CaOH+
H2CO3 HCO3- CO3-2 Na+
NaCO3- NaHCO3 NaOH Cl-
CO2 H+ H2 OH-
O2 H2O
-activities Ca+2 CaCO3 CaHCO3+ CaOH+
H2CO3 HCO3- CO3-2 Na+
NaCO3- NaHCO3 NaOH Cl-
CO2 H+ H2 OH-
O2 H2O
-equilibrium_phases ACCan ACChyd Calcite Aragonite
Vaterite Portlandite Halite Nahcolite
Trona Natron Thermonatrite CO2
O2 H2
-saturation_indices ACCan ACChyd Calcite Aragonite
Vaterite Portlandite Halite Nahcolite
Trona Natron Thermonatrite CO2
O2 H2
```

References

Abbe, E. (1881). VII.-On the Estimation of Aperture in the Microscope. Journal of the Royal Microscopical Society, 1(3), 388–423. https://doi.org/10.1111/j.1365-2818.1881.tb05909.x

Addadi, L., Raz, S., & Weiner, S. (2003). Taking advantage of disorder: Amorphous calcium carbonate and its roles in biomineralization. Advanced Materials, 15(12), 959–970. https://doi.org/10.1002/adma.200300381

Antony, A., How, J., Gray, S., Childress, A. E., Le-clech, P., & Leslie, G. (2011). Scale formation and control in high pressure membrane water treatment systems: A review. Journal of Membrane Science, 383(1–2), 1–16. https://doi.org/10.1016/j.memsci.2011.08.054

Al Nasser, W. N., Shah, U. V., Nikiforou, K., Petrou, P., & Heng, J. Y. Y. (2016). Effect of silica nanoparticles to prevent calcium carbonate scaling using an in situ turbidimeter. Chemical Engineering Research and Design, 110, 98-107. http://dx.doi.org/10.1016/j.cherd.2015.12.006

Avaro, J. T., Wolf, S. L. P., Hauser, K., & Gebauer, D. (2020). Stable Prenucleation Calcium Carbonate Clusters Define Liquid–Liquid Phase Separation. Angewandte Chemie - International Edition, 59(15), 6155–6159. https://doi.org/10.1002/anie.201915350

Aydinol, M. K., Mantese, J. V, & Alpay, S. P. (2007). A comparative ab initio study of the ferroelectric behaviour in KNO 3 and CaCO 3. Journal of Physics: Condensed Matter, Volume 19, Number 49. https://doi.org/10.1088/0953-8984/19/49/496210

Boon, M., Rickard, W. D. A., Rohl, A. L., & Jones, F. (2020). Stabilization of Aragonite: Role of Mg2+and Other Impurity Ions. Crystal Growth and Design, 20(8), 5006–5017. https://doi.org/10.1021/acs.cgd.0c00152

Borisov, S. V., Magarill, S. A., & Pervukhina, N. V. (2021). Crystallographic analysis of three modifications of CaCO3: calcite, aragonite, vaterite. Journal of Structural Chemistry, 62(7), 1027–1037. https://doi.org/10.1134/S0022476621070064

Bresme, F., & Cámara, L. G. (2006). Computer simulation studies of Crystallization under confinement conditions. Journal of Chemical Geology, 230, 197–206. https://doi.org/10.1016/j.chemgeo.2006.02.025

Browning, N. D., Sciences, P., & Abellan, S. (2014). Factors influencing quantitative liquid transmission electron microscopy. Chem. Commun., 2014, 50, 4873 https://doi.org/10.1039/c3cc48479c

Brydson, R., Brown, A., Benning, L. G., & Livi, K. (2014). Analytical transmission electron microscopy. In Spectroscopic Methods in Mineralogy and Materials Sciences. Published by De Gruyter (Vol. 78, pp. 219–269). https://doi.org/10.2138/rmg.2014.78.6

Caër, S. Le. (2011). Water radiolysis: Influence of oxide surfaces on H2 production under ionizing radiation. Water (Switzerland), 3(1), 235–253. https://doi.org/10.3390/w3010235

Cantaert, B., Beniash, E., & Meldrum, F. C. (2013). Nanoscale Confinement Controls the Crystallization of Calcium Phosphate: Relevance to Bone Formation. Chemistry a European Journal, 19(44), 14918–14924. https://doi.org/10.1002/chem.201302835

Cao, L., Caldeira, K., & Jain, A. K. (2007). Effects of carbon dioxide and climate change on ocean acidification and carbonate mineral saturation. Geophysical Research Letter 34(5). https://doi.org/10.1029/2006GL028605

Cardew, P. T. (2023). Ostwald Rule of Stages─Myth or Reality? Crystal Growth and Design, 23(6), 3958–3969. https://doi.org/10.1021/acs.cgd.2c00141

Cartwright, J. H. E., Checa, A. G., Gale, J. D., Gebauer, D., & Sainz-díaz, C. I. (2012). Calcium Carbonate Polyamorphism and Its Role in Biomineralization: How Many Amorphous Calcium Carbonates Are There ? Angewandte Chemie, 51(48), 11960–11970. https://doi.org/10.1002/anie.201203125

Cavanaugh, J., Whittaker, M. L., & Joester, D. (2019). Crystallization kinetics of amorphous calcium carbonate in confinement. Chemical Science, 10(19), 5039–5043. https://doi.org/10.1039/c8sc05634j

Cefalas, A., Hellenic, N., & Kobe, S. (2008). Nanocrystallization of CaCO (3) at solid / liquid interfaces in magnetic field : A quantum approach. Applied Surface Science 254 (2008) 6715–6724. https://doi.org/10.1016/j.apsusc.2008.04.056

Chen, S., Co, H., Antonietti, M., & Yu, S. (2013). Ethanol assisted synthesis of pure and stable amorphous calcium carbonate nanoparticles. Chem. Commun., 49, 9564–9566. https://doi.org/10.1039/c3cc45427d

Chen, S., & Wang, L. (2019). Dissociation path competition of radiolysis ionization-induced molecule damage under electron beam illumination. Chemical Science., 10, 10706–10715. https://doi.org/10.1039/c9sc04100a

Christy, A. G. (2017). A Review of the Structures of Vaterite: The Impossible , the Possible , and the Likely. Crystal Growth and Design.,17, 3567−3578. https://doi.org/10.1021/acs.cgd.7b00481

Clark, S. M., Grigorova, V., Colas, B., Darwish, T. A., Wood, K., Neuefeind, J., & Jacob, D. E. (2022). The Kinetics of Aragonite Formation from Solution via Amorphous Calcium Carbonate. Nanomaterials, 12(23), 1–13. https://doi.org/10.3390/nano12234151

Cölfen, H., & Mann, S. (2003). Higher-order organization by mesoscale self-assembly and transformation of hybrid nanostructures. Angewandte Chemie - International Edition, 42(21), 2350–2365. https://doi.org/10.1002/anie.200200562

Coto, B., Martos, C., Peña, J. L., Rodríguez, R., & Pastor, G. (2012). Effects in the solubility of CaCO3: Experimental study and model description. Fluid Phase Equilibria, 324, 1–7. https://doi.org/10.1016/j.fluid.2012.03.020

Dae, K. S., Chang, J. H., Koo, K., Park, J., Kim, J. S., & Yuk, J. M. (2020). Real-Time Observation of CaCO3 Mineralization in Highly Supersaturated Graphene Liquid Cells. ACS Omega, 5(24), 14619–14624. https://doi.org/10.1021/acsomega.0c01300

De Yoreo, J. J. (2022). Casting a bright light on Ostwald's rule of stages. Proceedings of the National Academy of Sciences of the United States of America, 119(7), 10–12. https://doi.org/10.1073/pnas.2121661119.

De Yoreo, J. J., Gilbert, P. U. P. A., Sommerdijk, N. A. J. M., Penn, R. L., Whitelam, S., Joester, D., Zhang, H., Rimer, J. D., Navrotsky, A., Banfield, J. F., Wallace, A. F., Michel, F. M., Meldrum, F. C., Cölfen, H., & Dove, P. M. (2015). Crystallization by particle attachment in synthetic, biogenic, and geologic environments. In Science (Vol. 349, Issue 6247) aaa6760-9. American Association for the Advancement of Science. https://dx.doi.org/10.1126/science.aaa6760.

De Yoreo, J., N. A. J. M., S. (2016). Investigating materials formation with liquid-phase and cryogenic TEM. Nature Review Materials, 1, 16035. https://doi.org/10.1038/natrevmats.2016.35

De Yoreo, J. J., & Vekilov, P. G. (2003). Principles of crystal nucleation and growth. Reviews in Mineralogy and Geochemistry, 54(1), 57–93. https://doi.org/10.2113/0540057

Demichelis, R., Raiteri, P., Gale, J. D., Quigley, D., & Gebauer, D. (2011). Stable prenucleation mineral clusters are liquid-like ionic polymers. Nature Communications, 2(1), 590. https://doi.org/10.1038/ncomms1604

Devau, N., Lach, A., Lassin, A., Andre, L., Beuvier, T., & Gibaud, A. (2018). Dynamics of calcium carbonate formation: Geochemical modeling of a two-step mechanism. Geochimica et Cosmochimica Acta, 240, 236–254. https://doi.org/10.1016/j.gca.2018.08.033.

Dey, A., De With, G., & Sommerdijk, N. A. J. M. (2010). In situ techniques in biomimetic mineralization studies of calcium carbonate. Chemical Society Reviews, 39(2), 397–409. https://doi.org/10.1039/b811842f

Dhami, N. K., Reddy, M. S., & Mukherjee, M. S. (2013). Biomineralization of calcium carbonates and their engineered applications: A review. Frontiers in Microbiology, 29(4), 314. https://doi.org/10.3389/fmicb.2013.00314

Dieckmann, Y., Cölfen, H., Hofmann, H., & Petri-Fink, A. (2009). Particle size distribution measurements of manganese doped ZnS nanoparticles. Analytical Chemistry, 81(10), 3889–3895. https://doi.org/10.1021/ac900043y

Driessche, A. E. S. Van, Stawski, T. M., & Benning, L. G. (2017). New Perspectives on Mineral Nucleation and Growth: From Solution Precursors to Solid Materials. Schematic Scholar, 12, 227–256. https://doi.org/10.1007/978-3-319-45669-0

Driessche, A. E. S. Van, Stawski, T. M., & Kellermeier, M. (2019). Calcium sulfate precipitation pathways in natural and engineered environments. Chemical Geology, 530(July), 119274. https://doi.org/10.1016/j.chemgeo.2019.119274

Du, H., & Amstad, E. (2020). Water: How Does It Influence the CaCO3 Formation? Angewandte Chemie - International Edition, 59(5), 1798–1816. https://doi.org/10.1002/anie.201903662

Faatz, M., Gröhn, F., & Wegner, G. (2004). Amorphous calcium carbonate: Synthesis and potential intermediate in biomineralization. Advanced Materials, 16(12), 996–1000. https://doi.org/10.1002/adma.200306565

Feder, J., Russell, K. C., Lothe, J., & Pound, G. M. (1966). Homogeneous nucleation and growth of droplets in vapours. Advances in Physics, 15(57), 111–178. https://doi.org/10.1080/00018736600101264

Florence, A. T., & Attwood, D. (2015). Physicochemical principles of pharmacy: In manufacture, formulation and clinical use. Pharmaceutical press. 39(5), 178. http://dx.doi.org/10.18773/ austprescr.2016.065

Friedman, A., Ross, D.S. (2003). Crystal Growth — Ostwald Ripening. In: Mathematical Models in Photographic Science. Mathematics in Industry,

Springer, Berlin, Heidelberg. vol 3, 12–26. https://doi.org/10.1007/978-3-642-55755-2_4

Gebauer, D. Völkel, A. Cölfen, H. (2008). Stable Prenucleation Calcium Carbonate Clusters. Science 322(5909), 1819–1823. DOI: 10.1126/science.1164271

Gebauer, D., Raiteri, P., Gale, J. D., & Cölfen, H. (2018). On Classical and Non-Classical Views on Nucleation. American Journal of Science, 318(9), 969–988. https://doi.org/10.2475/09.2018.05

Gebauer, D., & Cölfen, H. (2011). Prenucleation clusters and non-classical nucleation. Nano Today, 6(6), 564–584. https://doi.org/10.1016/j.nantod.2011.10.005

Gebauer, D., Gunawidjaja, P. N., Ko, J. Y. P., Bacsik, Z., Aziz, B., Liu, L., Hu, Y., Bergström, L., Tai, C., Sham, T., Edøn, M., & Hedin, N. (2010). Proto-Calcite and Proto-Vaterite in Amorphous Calcium Carbonates. Angewandte Chemie International Edition, 49(47), 8889–8891. https://doi.org/10.1002/anie.201003220

Gebauer, D., Kellermeier, M., Gale, J. D., Bergström, L., & Cölfen, H. (2014). Pre-nucleation clusters as solute precursors in crystallisation. Chemical Society Reviews, 43(7), 2348–2371. https://doi.org/10.1039/c3cs60451a

Giulietti, M., Seckler, M. M., Derenzo, S., Ré, M. I., & Cekinski, E. (2001). Industrial crystallization and precipitation from solutions: State of the technique. Brazilian Journal of Chemical Engineering, 18(4), 423–440. https://doi.org/10.1590/S0104-66322001000400007

Goodhew, P.J., Humphreys, J., & Humphreys, J. (2000). Electron Microscopy and Analysis (3rd ed.). CRC Press, 254. https://doi.org/10.1201/9781482289343

Gopi, S., Subramanian, V. K., & Palanisamy, K. (2013). Aragonite-calcite-vaterite: A temperature influenced sequential polymorphic transformation of CaCO3 in the presence of DTPA. Materials Research Bulletin, 48(5), 1906–1912. https://doi.org/10.1016/j.materresbull.2013.01.048

Grassucci, R. A., Taylor, D. J., & Frank, J. (2007). Preparation of macromolecular complexes for cryo-electron microscopy. Nature Protocols, 2(12), 3239–3246. https://doi.org/10.1038/nprot.2007.452

Gu, H., Li, G., Liu, C., Yuan, F., Han, F., & Zhang, L. (2017). Considerable knock-on displacement of metal atoms under a low energy electron beam. Scientific Reports, 7, 184. https://doi.org/10.1038/s41598-017-00251-3

Hands-portman, I., & Bakker, S. E. (2022). Customising the plunge-freezing workflow for challenging conditions. The Royal Society of Chemistry, 240, 44–54. https://doi.org/10.1039/d2fd00060a

Hondow, N., Brydson, R., Wang, P., Holton, M. D., Brown, M. R., Rees, P., Summers, H. D., & Brown, A. (2012). Quantitative characterization of nanoparticle agglomeration within biological media. Journal of Nanoparticle Research, 14(7), 977. https://doi.org/10.1007/s11051-012-0977-3

Hong, S., Moon, S., Cho, J., Park, A. H. A., & Park, Y. (2022). Effects of Mg ions on the structural transformation of calcium carbonate and their implication for the tailor-synthesized carbon mineralization process. Journal of CO2 Utilization, 60(April), 101999. https://doi.org/10.1016/j.jcou.2022.101999

Hooley, R.W.M. (2019). Low-Dose STEM Characterisation of Nanoscale Calcium Carbonate Particles, PhD thesis, White Rose eTheses Online. EthosID: uk.bl. ethos.798004

Hooley, R., Brown, A., & Brydson, R. (2019). Factors affecting electron beam damage in calcite nanoparticles. Micron, 120, 25–34. https://doi.org/10.1016/j.micron.2019.01.011

Hu, Q., Nielsen, M. H., Freeman, C. L., Hamm, L. M., Tao, J., Lee, J. R. I., Han, T. Y. J., Becker, U., Harding, J. H., Dove, P. M., & De Yoreo, J. J. (2012). The thermodynamics of calcite nucleation at organic interfaces: Classical vs. non-classical pathways. Faraday Discussions, 159, 509–523. https://doi.org/10.1039/c2fd20124k

Hu, Y., Wolf-gladrow, D. A., & Nehrke, G. (2015). Effect of pH and Phosphate on Calcium Carbonate Polymorphs Precipitated at near-Freezing Temperature. Crystal Growth & Design, 15 (4), 1596-1601. https://doi.org/10.1021/cg500829p

Ihli, J., Bots, P., Kulak, A., Benning, L. G., & Meldrum, F. C. (2013). Elucidating mechanisms of diffusion-based calcium carbonate synthesis leads to controlled mesocrystal formation. Advanced Functional Materials, 23(15), 1965–1973. https://doi.org/10.1002/adfm.201201742

Ihli, J., Wong, W. C., Noel, E. H., Kim, Y. Y., Kulak, A. N., Christenson, H. K., Duer, M. J., & Meldrum, F. C. (2014). Dehydration and crystallization of amorphous calcium carbonate in solution and in air. Nature Communications, 5, 3169. https://doi.org/10.1038/ncomms4169

Ilett, M. A. (2020). Characterising nanoparticles in complex biological media. PhD thesis, University of Leeds. uk.bl. ethos.811221

Ilett, M., Brydson, R., Brown, A., & Hondow, N. (2019). Cryo-analytical STEM of frozen, aqueous dispersions of nanoparticles. Micron, 120, 35–42. https://doi.org/10.1016/j.micron.2019.01.013

Ilett, M., S'Ari, M., Freeman, H., Aslam, Z., Koniuch, N., Afzali, M., Cattle, J., Hooley, R., Roncal-Herrero, T., Collins, S. M., Hondow, N., Brown, A., & Brydson, R. (2020). Analysis of complex, beam-sensitive materials by transmission electron microscopy and associated techniques: TEM of Beam Sensitive Materials. Philosophical Transactions of the Royal Society A: Mathematical, Physical and Engineering Sciences, 378(2186), 20190601. https://doi.org/10.1098/rsta.2019.0601

Ilett, M., Wills, J., Rees, P., Sharma, S., Micklethwaite, S., Brown, A., Brydson, R., & Hondow, N. (2020). Application of automated electron microscopy imaging and machine learning to characterise and quantify nanoparticle dispersion in aqueous media. Journal of Microscopy, 279(3), 177–184. https://doi.org/10.1111/jmi.12853

Karpiński, P. H., & Bałdyga, J. (2019). Precipitation processes. Handbook of Industrial Crystallization, 216–265. https://doi.org/10.1017/9781139026949.008

Karthika, S., Radhakrishnan, T. K., & Kalaichelvi, P. (2016). A Review of Classical and Nonclassical Nucleation Theories. Crystal Growth & Design, 16 (11), 6663-6681. https://doi.org/10.1021/acs.cgd.6b00794

Kashchiev, D. (2000). Nucleation. Elsevier. ISBN 978-0-7506-4682-6. https://doi.org/10.1016/B978-0-7506-4682-6.X5000-8

Kellermeier, M., Gebauer, D., Melero-García, E., Drechsler, M., Talmon, Y., Kienle, L., Cölfen, H., García-Ruiz, J. M., & Kunz, W. (2012). Colloidal stabilization of calcium carbonate prenucleation clusters with silica. Advanced Functional Materials, 22(20), 4301–4311. https://doi.org/10.1002/adfm.201200953

Kelly, D. J., Clark, N., Zhou, M., Gebauer, D., Gorbachev, R. V., & Haigh, S. J. (2021). In Situ TEM Imaging of Solution-Phase Chemical Reactions Using 2D-Heterostructure Mixing Cells. Advanced Materials, 33(29), 2100668 (1 of 8). https://doi.org/10.1002/adma.202100668

Kim, D., Lee, B., Thomopoulos, S. et al. (2018). The role of confined collagen geometry in decreasing nucleation energy barriers to intrafibrillar mineralization. Nature Communications, 9, 962. https://doi.org/10.1038/s41467-018-03041-1

Kimura, Y., Katsuno, H., Yamazaki, T., (2022). Possible embryos and precursors of crystalline nuclei of calcium carbonate observed by liquid-cell transmission electron microscopy. Faraday Discussions, 235, 81–94. https://doi.org/10.1039/D1FD00125F

Klebl, D. P., Monteiro, D. C. F., Kontziampasis, D., Kopf, F., Sobott, F., White, H. D., Trebbin, M., & Muench, S. P. (2020). Sample deposition onto cryo-EM grids: From sprays to jets and back. Acta Crystallographica Section D: Structural Biology, 76, 340–349. https://doi.org/10.1107/S2059798320002958

Köhnke, Janea, Christian Fürst, Christoph Unterweger, Harald Rennhofer, Helga C. Lichtenegger, Jozef Keckes, Gerhard Emsenhuber, Arunjunai Raj Mahendran, Falk Liebner, and Wolfgang Gindl-Altmutter. (2016). Carbon Microparticles from Organosolv Lignin as Filler for Conducting Poly (Lactic Acid). Polymers 8, no. 6: 205. https://doi.org/10.3390/polym8060205

Kralj, D., Brečević, L. (1995). Dissolution kinetics and solubility of calcium carbonate monohydrate. Colloids and Surfaces A: Physicochemical and Engineering Aspects, 96(3), 287-293. https://doi.org/10.1016/0927-7757(94)03063-6

Liendo, F., Arduino, M., Deorsola, F. A., & Bensaid, S. (2022). Nucleation and growth kinetics of CaCO3 crystals in the presence of foreign monovalent ions. Journal of Crystal Growth, 578, 126406. https://doi.org/10.1016/j.jcrysgro.2021.126406

Lin, Kun-Lin. (2014). Phase Identification Using Series of Selected Area Diffraction Patterns and Energy Dispersive Spectrometry within TEM. Microscopy Research. 02(04) 57-66. https://doi.org/10.4236/mr.2014.24008

Lippmann, F. (2012). Sedimentary carbonate minerals (Vol. 6). Springer Science & Business Media.

Liu, M., Xu, L. and Lin, X. (1994), Heating effect of electron beam bombardment. Scanning, 16, 1-5. https://doi.org/10.1002/sca.4950160102

Loste, E., Wilson, R. M., Seshadri, R., & Meldrum, F. C. (2003). The role of magnesium in stabilising amorphous calcium carbonate and controlling calcite morphologies. Journal of Crystal Growth, 254(1–2), 206–218. https://doi.org/10.1016/S0022-0248(03)01153-9

Lu, P., Zhang, G., Apps, J., & Zhu, C. (2022). Comparison of thermodynamic data files for PHREEQC. Earth-Science Reviews, 225, 103888. https://doi.org/10.1016/j.earscirev.2021.103888

Ma, Y. F., Gao, Y. H., & Feng, Q. L. (2010). Effects of pH and temperature on CaCO3 crystallization in aqueous solution with water soluble matrix of pearls. Journal of Crystal Growth, 312(21), 3165–3170. https://doi.org/10.1016/j.jcrysgro.2010.07.053

Manoli, F., & Dalas, E. (2000). Spontaneous precipitation of calcium carbonate in the presence of ethanol, isopropanol and diethylene glycol. Journal of Crystal Growth, 218 (2-4), 359–364.https://doi.org/10.1016/S0022-0248(00)00560-1x

Marton, L. and Hutter, R.G.E, (1944). The Transmission Type of Electron Microscope and Its Optics. Proceedings of the IRE, 32(1) 3-12. doi:10.1109/JRPROC.1944.232733

Marqusee, J. A., & Ross, J. (1983). Kinetics of phase transitions: Theory of Ostwald ripening. The Journal of Chemical Physics, 79(1), 373–378. https://doi.org/10.1063/1.445532.

Mayerhöfer, T. G., Pahlow, S., & Popp, J. (2020). The Bouguer-Beer-Lambert Law: Shining Light on the Obscure. Chemphyschem : A European Journal of Chemical Physics and Physical Chemistry, 21(18), 2029–2046. https://doi.org/10.1002/cphc.202000464.

Mccomb, D. W., Lengyel, J., & Carter, C. B. (2019). Cryogenic transmission electron microscopy for materials research. MRS Bulletin, 44(12), 924–928. https://doi.org/10.1557/mrs.2019.283.

Mejri, W., Korchef, A., Tlili, M., & Ben Amor, M. (2014). Effects of temperature on precipitation kinetics and microstructure of calcium carbonate in the presence of magnesium and sulphate ions. Desalination and Water Treatment, 52(25–27), 4863–4870. https://doi.org/10.1080/19443994.2013.808813.

Meldrum, F. C., & Cölfen, H. (2008). Controlling mineral morphologies and structures in biological and synthetic systems. Chemical Reviews, 108(11), 4332–4432. https://doi.org/10.1021/cr8002856.

Meldrum, F. C., & O'Shaughnessy, C. (2020). Crystallization in Confinement. In Advanced Materials, 32(31). https://doi.org/10.1002/adma.202001068.

Michen, B., Geers, C., Vanhecke, D., Endes, C., Rothen-Rutishauser, B., Balog, S., & Petri-Fink, A. (2015). Avoiding drying-artifacts in transmission electron microscopy: Characterizing the size and colloidal state of nanoparticles. Scientific Reports, 5. https://doi.org/10.1038/srep09793

Jensen, E. (2012). Types of Imaging, Part 1: Electron Microscopy. The Anatomical Record, 295(5), 716–721. https://doi.org/10.1002/ar.22453

Molnár, Z., Dódony, I., & Pósfai, M. (2023). Transformation of amorphous calcium carbonate in the presence of magnesium, phosphate, and mineral surfaces. Geochimica et Cosmochimica Acta, 345, 90–101. https://doi.org/10.1016/j.gca.2023.01.028

Mosley, L. M., Daly, R., Palmer, D., Yeates, P., Dallimore, C., Biswas, T., & Simpson, S. L. (2015). Applied Geochemistry Predictive modelling of pH and dissolved metal concentrations and speciation following mixing of acid drainage with river water. Applied Geochemistry, 59, 1–10. https://doi.org/10.1016/j.apgeochem.2015.03.006.

Mourdikoudis, S., & Pallares, R. M. (2018). Characterization techniques for nanoparticles: comparison and complementarity upon studying. Nanoscale, 12871–12934. https://doi.org/10.1039/c8nr02278j

Mukkamala, S. B., Anson, C. E., & Powell, A. K. (2006). Modelling calcium carbonate biomineralisation processes. Journal of Inorganic Biochemistry, 100(5–6), 1128–1138. https://doi.org/10.1016/j.jinorgbio.2006.02.012.

Murata, K., & Wolf, M. (2018). Cryo-electron microscopy for structural analysis of dynamic biological. BBA - General Subjects, 1862(2), 324–334. https://doi.org/10.1016/j.bbagen.2017.07.020

Nahi, O., Kulak, A. N., Broad, A., Xu, Y., O'shaughnessy, C., Cayre, O. J., Day, S. J., Darkins, R., & Meldrum, F. C. (2021). Solvent-Mediated. Enhancement of Additive-Controlled Crystallization. Crystal Growth and Design, 21(12), 7104–7115. https://doi.org/10.1021/acs.cgd.1c01002

Nasser, W. N. Al, Shah, U. V, Nikiforou, K., Petrou, P., & Heng, J. Y. Y. (2016). Chemical Engineering Research and Design Effect of silica nanoparticles to prevent calcium carbonate scaling using an in situ turbidimetre. Chemical Engineering Research and Design, 110, 98–107. https://doi.org/10.1016/j.cherd.2015.12.006

Niederberger, M., & Cölfen, H. (2006). Oriented attachment and mesocrystals: Non-classical crystallization mechanisms based on nanoparticle assembly. Physical Chemistry Chemical Physics, 8(28), 3271–3287. https://doi.org/10.1039/b604589h

Nielsen, M. H., Aloni, S., De Yoreo, J. J. (2014). In situ TEM imaging of CaCO3 nucleation reveals coexistence of direct and indirect pathways. Science, 345(6201),1158-1162. DOI: 10.1126/science.1254051

Ogino, T., Suzuki, T., & Sawada, K. (1987). The formation and transformation mechanism of calcium carbonate in water. Geochimica et Cosmochimica Acta, 51 (10), 2757–2767. https://doi.org/10.1016/0016-7037(87)90155-4.

V. A., Chen, S., Co, H., Antonietti, M., & Yu, S. (2013). Ethanol assisted synthesis of pure and stable amorphous calcium carbonate nanoparticles. Chemical Communication, 49, 9564–9566. https://doi.org/10.1039/c3cc45427d

Park, W. K., Ko, S. J., Lee, S. W., Cho, K. H., Ahn, J. W., & Han, C. (2008). Effects of magnesium chloride and organic additives on the synthesis of aragonite precipitated calcium carbonate. Journal of Crystal Growth, 310(10), 2593–2601. https://doi.org/10.1016/j.jcrysgro.2008.01.023

Parkhurst, D. L., & Appelo, C. A. J. (1999). User's guide to PHREEQC (Version 2): A computer program for speciation, batch-reaction, one-dimensional transport, and inverse geochemical calculations. In Water-Resources Investigations Report. https://doi.org/10.3133/wri994259

Pennycook, S. J., Lupini, A. R., Varela, M., Borisevich, A., Peng, Y., Oxley, M. P., Van Benthem, K., & Chisholm, M. F. (2007). Scanning transmission electron microscopy for nanostructure characterization. In Scanning Microscopy for Nanotechnology: Techniques and Applications (pp. 152–191). Springer New York. https://doi.org/10.1007/978-0-387-39620-0_6

Peters, J. J. P., Mullarkey, T., Hedley, E., Müller, K. H., Porter, A., Mostaed, A., & Jones, L. (2023). Electron counting detectors in scanning transmission electron microscopy via hardware signal processing. Nature Communications, 14(1), 5184. https://doi.org/10.1038/s41467-023-40875-w

Pouget, E. M., Bomans, P. H. H., Dey, A., Frederik, P. M., With, G. De, & Sommerdijk, N. A. J. M. (2010). The Development of Morphology and Structure in Hexagonal Vaterite. Journal of the American Chemical Society, 20(15), 11560–11565. https://doi.org/10.1021/ja102439r

Radha, A. V, Forbes, T. Z., Killian, C. E., Gilbert, P. U. P. A., & Navrotsky, A. (2010). Transformation and crystallization energetics of synthetic and biogenic amorphous calcium carbonate. Proceedings of the National Academy of Sciences, 107 (38) 16438-16443. https://doi.org/10.1073/pnas.1009959107

Ramnarain, V., Georges, T., Ortiz Peña, N., Ihiawakrim, D., Longuinho, M., Bulou, H., Gervais, C., Sanchez, C., Azaïs, T., & Ersen, O. (2022a). Monitoring of CaCO3Nanoscale Structuration through Real-Time Liquid Phase Transmission Electron Microscopy and Hyperpolarized NMR. Journal of the American Chemical Society, 144(33), 15236–15251. https://doi.org/10.1021/jacs.2c05731

Rodriguez-Blanco, J. D., Shaw, S., & Benning, L. G. (2011). The kinetics and mechanisms of amorphous calcium carbonate (ACC) crystallization to calcite, via vaterite. Nanoscale, 3(1), 265–271. https://doi.org/10.1039/c0nr00589d

Rodríguez-Hornedo, N., Murphy, D. (1999). Significance of Controlling Crystallization Mechanisms and Kinetics in. Pharmaceutical Sciences, 88(7), 651–660. https://doi.org/10.1021/js980490h

Rodriguez-Navarro, C., Kudłacz, K., Cizer, Ö., & Ruiz-Agudo, E. (2015). Formation of amorphous calcium carbonate and its transformation into mesostructured calcite. CrystEngComm, 17, 58-72. https://doi.org/10.1039/C4CE01562B

Rohleder, J.; Kroker, E. (2001). Calcium Carbonate from the Cretaceous Period into the 21 century. Springer Basel AG. ISBN: 9783034882453, 3034882459

Rose, H., & Wan, W. (2005). Aberration correction in electron microscopy. Proceedings of the IEEE Particle Accelerator Conference, 44–48. https://doi.org/10.1109/PAC.2005.1590354

Ross, F. M. (2015). Opportunities and challenges in liquid cell electron microscopy. 9886. https://doi.org/10.1126/science.aaa9886

Sanciolo, P., Zou, L., Gray, S., Leslie, G., & Stevens, D. (2008). Accelerated seeded precipitation pre-treatment of municipal wastewater to reduce scaling. Chemosphere, 72(2), 243–249. https://doi.org/10.1016/j.chemosphere.2008.01.045

Sand, K. K., Makovicky, E., Benning, L. G., & Stipp, S. L. S. (2012). Crystallization of CaCO 3 in Water − Alcohol Mixtures: Spherulitic Growth, Polymorph Stabilization, and Morphology Change. Crystal Growth Design, 12(2), 842–853. https://doi.org/10.1021/cg2012342

Sawada, K. (1997). The mechanisms of crystallization and transformation of calcium carbonates. Pure and Applied Chemistry, 69(5), 921–928. https://doi.org/10.1351/pac199769050921

Schecher W. D; Mcavoy, D. C. (1992). MINEQL+: A software environment for chemical equilibrium modelling. Computers, Environment and Urban Systems, 16, (1) 65–76. https://doi.org/10.1016/0198-9715(92)90053-T.

Schmidt, M. P., Ilott, A. J., Phillips, B. L., & Reeder, R. J. (2014). Structural changes upon dehydration of amorphous calcium carbonate. Crystal Growth and Design, 14(3), 938–951. https://doi.org/10.1021/cg401073n

Schneider, N. M., Norton, M. M., Mendel, B. J., Grogan, J. M., Ross, F. M., & Bau, H. H. (2014). Electron − Water Interactions and Implications for Liquid Cell

Electron Microscopy. Physical Chemistry, 118(38), 22373-22382. https://doi.org/10.1021/jp507400n

Schultz, P. (1988). Cryo-electron microscopy of vitrified specimens. Quarterly Reviews of Biophysics, 21(2), 129–228. https://doi.org/10.1017/S0033583500004297

Scoutaris, N., Vithani, K., Slipper, I., Chowdhry, B., & Douroumis, D. (2014). SEM / EDX and confocal Raman microscopy as complementary tools for the characterization of pharmaceutical tablets. International Journal of Pharmaceutics, 470(1–2), 88–98. https://doi.org/10.1016/j.ijpharm.2014.05.007

Sebastiani, F., Wolf, S. L. P., Born, B., Luong, T. Q., Cölfen, H., Gebauer, D., & Havenith, M. (2017). Water Dynamics from THz Spectroscopy Reveal the Locus of a Liquid–Liquid Binodal Limit in Aqueous CaCO3 Solutions. Angewandte Chemie - International Edition, 56(2), 490–495. https://doi.org/10.1002/anie.201610554

Sigle, W. (2005). Analytical transmission electron microscopy. Annu. Rev. Mater. Res., 35, 239–314. https://doi.org/10.1146/annurev.matsci.35.102303.091623

Smeets, P. J. M., Finney, A. R., Habraken, W. J. E. M., Nudelman, F., & Friedrich, H. (2017). A classical view on nonclassical nucleation. Proc Natl Acad Sci U S A, 114(38), E7882-E7890. https://doi.org/10.1073/pnas.1700342114

Soldati, A. L., Jacob, D. E., Glatzel, P., Swarbrick, J. C., & Geck, J. (2016). Element substitution by living organisms: The case of manganese in mollusc shell aragonite. Scientific Reports, 6, 22514. https://doi.org/10.1038/srep22514

Stephens, C. J., Kim, Y. Y., Evans, S. D., Meldrum, F. C., & Christenson, H. K. (2011). Early stages of crystallization of calcium carbonate revealed in picoliter droplets. Journal of the American Chemical Society, 133(14), 5210–5213. https://doi.org/10.1021/ja200309m

Su, H., Bomans, P. H. H., Friedrich, H., Xu, Y., & Sommerdijk, N. (2021). Crystallization via Oriented Attachment of Nanoclusters with Short-Range Order in Solution. Journal of Physical Chemistry C, 125(1), 1143–1149. https://doi.org/10.1021/acs.jpcc.0c10323

Sulpis, O., Agrawal, P., Wolthers, M., Munhoven, G., Walker, M., & Middelburg, J. J. (2022). Aragonite dissolution protects calcite at the seafloor. Nature Communications, 13(1), 1104. https://doi.org/10.1038/s41467-022-28711-z

Sun, W., Jayaraman, S., Chen, W., Persson, K. A., & Ceder, G. (2015). Nucleation of metastable aragonite CaCO 3 in seawater. Proc Natl Acad Sci U S A, 112 (11) 3199-3204. https://doi.org/10.1073/pnas.1423898112

Takahashi, T. (2016). Bioassay of Components Eluted from Electric Arc Furnace Steel Slag Using Microalgae Chlorella. ISIJ International, 56(8),1497-1505 https://doi.org/10.2355/isijinternational.ISIJINT-2015-539

Tang, C. Y., & Yang, Z. (2017). Chapter 8 - Transmission Electron Microscopy (TEM). In N. Hilal, A. F. Ismail, T. Matsuura, & D. Oatley-Radcliffe (Eds.), Membrane Characterization (pp. 145–159). Elsevier. https://doi.org/https://doi.org/10.1016/B978-0-444-63776-5.00008-5

Teng, H. H., Dove, P. M., Orme, C. A., & De Yoreo, J. J. (1998). Thermodynamics of calcite growth: Baseline for understanding biomineral formation. Science, 282(5389), 724–727. https://doi.org/10.1126/science.282.5389.724

Terrones, M. Visualizing fullerene chemistry. Nature Chemistry, 2, 82–83. https://doi.org/10.1038/nchem.526

Thompson, R. F., Walker, M., Siebert, C. A., Muench, S. P., & Ranson, N. A. (2016). An introduction to sample preparation and imaging by cryo-electron microscopy for structural biology. Methods, 100(2016), 3–15. https://doi.org/10.1016/j.ymeth.2016.02.017.

Thompson, C. V, & Spaepen, F. (1983). Homogeneous crystal nucleation in binary metallic melts, Acta Metallurgica, 31(12) 2021-2027. https://doi.org/10.1016/0001-6160(83)90019-6

Ueckert, M., Wismeth, C., & Baumann, T. (2020). Crystallization of calcium carbonate in a large-scale push–pull heat storage test in the Upper Jurassic carbonate aquifer. Geothermal Energy, 8(1), 7. https://doi.org/10.1186/s40517-020-0160-5

Ural, N. (2021). The significance of scanning electron microscopy (SEM) analysis on the microstructure of improved clay: An overview. Open Geosciences, 13(1), 197–218. https://doi.org/10.1515/geo-2020-0145

Van Driessche, A. E. S., Kellermeier, M., Benning, L. G., & Gebauer, D. (2016). New perspectives on mineral nucleation and growth: from solution precursors to solid materials. Springer.

Vedantam, S., & Ranade, V. V. (2013). Crystallization: Key thermodynamic, kinetic, and hydrodynamic aspects. Sadhana - Academy Proceedings in Engineering Sciences, 38(6), 1287–1337. https://doi.org/10.1007/s12046-013-0195-4

Vidallon, M. L. P., Yu, F., & Teo, B. M. (2020). Controlling the Size and Polymorphism of Calcium Carbonate Hybrid Particles Using Natural Biopolymers. Crystal Growth and Design, 20(2), 645–652. https://doi.org/10.1021/acs.cgd.9b01057

Von Euw, S., Azaïs, T., Manichev, V., Laurent, G., Pehau-Arnaudet, G., Rivers, M., Murali, N., Kelly, D. J., & Falkowski, P. G. (2020). Solid-State Phase Transformation and Self-Assembly of Amorphous Nanoparticles into Higher-Order Mineral Structures. Journal of the American Chemical Society, 142(29), 12811–12825. https://doi.org/10.1021/jacs.0c05591

Walker, J. M., Marzec, B., & Nudelman, F. (2017a). Solid-State Transformation of Amorphous Calcium Carbonate to Aragonite Captured by CryoTEM. Angewandte Chemie - International Edition, 56(39), 11740–11743. https://doi.org/10.1002/anie.201703158

Wallace, A. F., Hedges, L. O., Fernandez-martinez, A., Raiteri, P., Gale, J. D., Waychunas, G. A., Whitelam, S., Banfield, J. F., & Yoreo, J. J. De. (2013). Supersaturated CaCO3 Solutions. Science, 692(August), 885–889.

Wang, Y., Zeng, M., Meldrum, F. C., & Christenson, H. K. (2017). Using confinement to study the crystallization pathway of calcium carbonate. Crystal Growth and Design, 17(12), 6787–6792. https://doi.org/10.1021/acs.cgd.7b01359

Ward, M.B., Hondow, N.S., Brown, A.P., & Drummond-Brydson, R.M. (2015). Nanocharacterisation: Electron Energy Loss Spectroscopy and Energy Dispersive X-ray Analysis. Royal Society of Chemistry, (pp. 108–157). https://doi.org/10.1039/9781782621867-00108

Weller, M., Weller, M. T., Overton, T., Rourke, J., Armstrong, F. (2014). 7th ed. Inorganic Chemistry. United Kingdom: Oxford University Press.

Weng, P. F. (1995). Silica scale inhibition and colloidal silica dispersion for reverse osmosis systems, Desalination, 103(1–2), 59-67, https://doi.org/10.1016/0011-9164(95)00087-9

Wergin, W. P., & Erbe, E. F. (1992). Techniques for obtaining and observing complementary images with a low-temperature field emission SEM and subsequent comparison of the identical cells in freeze-etch replicas viewed with a TEM. Scanning, 14(1), 17–30. https://doi.org/10.1002/sca.4950140105

Williams, D. B., & Carter, C. B. (2009). The Transmission Electron Microscope. In Transmission Electron Microscopy (pp. 3–22). Springer US. https://doi.org/10.1007/978-0-387-76501-3_1

Xu, Y., & Sommerdijk, N. A. J. M. (2018). Aragonite formation in confinements: A step toward understanding polymorph control. Proceedings of the National Academy of Sciences of the United States of America, 115(34), 8469–8471. https://doi.org/10.1073/pnas.1811696115

Yan, R., Edwards, T. J., Pankratz, L. M., Kuhn, R. J., Lanman, J. K., Liu, J., & Jiang, W. (2015). Simultaneous determination of sample thickness, tilt, and electron mean free path using tomographic tilt images based on Beer-Lambert law. Journal of Structural Biology, 192(2), 287–296. https://doi.org/10.1016/j.jsb.2015.09.019

Yu, L., & Reutzel-Edens, S. M. (2003). Crystallization| Basic Principles. Encyclopedia of Food Sciences and Nutrition (Second Edition), Academic Press, 1697–1702. Academic Press. https://doi.org/https://doi.org/10.1016/B0-12-227055-X/00313-8

Zeng, M., Kim, Y., Anduix-canto, C., Frontera, C., Laundy, D., & Kapur, N. (2018). Confinement generates single-crystal aragonite rods at room temperature. Proc Natl Acad Sci U S A, 115(30), 7670-7675.https://doi.org/10.1073/pnas.1718926115

Zhang, G., Lu, P., Zhang, Y., Tu, K., & Zhu, C. (2020). SUPPHREEQC: A program for generating customized PHREEQC thermodynamic datasets from SUPCRTBL and extending calculations to elevated pressures and temperatures. Computers and Geosciences, 143, 104560. https://doi.org/10.1016/j.cageo.2020.104560

Zhang, S., Nahi, O., Chen, L., Aslam, Z., Kapur, N., Kim, Y. Y., & Meldrum, F. C. (2022). Magnesium Ions Direct the Solid-State Transformation of Amorphous Calcium Carbonate Thin Films to Aragonite, Magnesium-Calcite, or Dolomite. Advanced Functional Materials, 32(25), 2201394. https://doi.org/10.1002/adfm.202201394

Zhao, H., and Darwin, D. (1990). Quantitative Backscattered Electron Analysis Techniques for Cement-Based Materials, SM Report No. 24 Research Grant AFOSR-89-0296, The Air Force Office of Scientific Research, 57 pp.

Zhou, G., & Yao, Q. (2014). Formation of Aragonite Mesocrystals and Implication for Biomineralization. American Mineralogist, 94(2-3), 293-302. https://doi.org/10.2138/am.2009.2957

Zhou, G.-T., Yao, Q.-Z., Fu, S.-Q., & Guan, Y.-B. (2010). Controlled crystallization of unstable vaterite with distinct morphologies and their polymorphic transition to

stable calcite. European Journal of Mineralogy, 22(2), 259–269. https://doi.org/10.1127/0935-1221/2009/0022-2008

Zou, Z., Habraken, W. J. E. M., Bertinetti, L., Politi, Y., Gal, A., Weiner, S., Addadi, L., & Fratzl, P. (2017). On the phase diagram of calcium carbonate solutions. Advanced Materials Interfaces, 4(1), 1600076. https://doi.org/10.1002/admi.201600076

Zou, Z., Polishchuk, I., Bertinetti, L., Pokroy, B., Politi, Y., Fratzl, P., & Habraken, W. J. E. M. (2018). Additives influence the phase behavior of calcium carbonate solution by a cooperative ion-association process. Journal of Materials Chemistry B, 6(3), 449–457. https://doi.org/10.1039/c7tb03170j